Design of Sustainable Cathodes for Li-ion Batteries

Understanding the redox behaviour of guaiacyl and catecholic groups in lithium organic system

Ivan Ilic

Univ.-Diss.

zur Erlangung des akademischen Grades

"doctor rerum naturalium"

(Dr. rer. nat.)

in der Wissenschaftsdisziplin "Polymerchemie“

eingereicht an der

Mathematisch-Naturwissenschaftlichen Fakultät

Institut für Chemie

der Universität Potsdam

und

Max-Planck-Institut für Kolloid- und Grenzflächenforschung

Hauptbetreuer/in: Prof. Dr. Markus Antonietti

Weitere Gutachter: Prof. Dr. Andreas Taubert
Prof. Dr. Christina Roth

Published online on the
Publication Server of the University of Potsdam:
https://doi.org/10.25932/publishup-48368
https://nbn-resolving.org/urn:nbn:de:kobv:517-opus4-483689

Contents

1. Motivation

All living creatures interact with their environment, using chemical processes to obtain energy, to grow and reproduce. Through this, living creatures also change the environment around them, e.g., by producing complex sugars from carbon dioxide or by assembling dry plants into nests to raise their offspring. The complexity of the creature tends to correlate with their impact on the environment. The impact of human beings, arguably the most complex creatures in the world, caused geologists to discuss a new epoch characterised by human influence, the so called "Anthropocene Epoch".[1]

Following the first industrial revolution at the end of the 18th century, this impact has been accelerating. Levels of carbon dioxide, the most important greenhouse gas, rose to unprecedented levels since the beginning of humankind resulting in global warming. Carbon dioxide is chiefly produced by humans through the burning of fuel; generating energy used for transportation or production. Therefore, by exchanging traditional carbon-based fuels with more sustainable energy sources, humankind could halt the increase in carbon dioxide levels and even reverse it.[2]

Sustainability, a term often used in everyday life as a blanket definition for many sustainable concepts, is a popular but ill-defined phrase.[3] However, in this thesis, the definition for sustainability will be based on the Brundtland report of 1987. Here, sustainable development was defined as: " …*development that meets the needs of the present without compromising the ability of future generations to meet their own needs…"*.[4] Therefore, a sustainable material in the context of this thesis, is a material that can be produced from replenishing resources' i.e., from biomass in quantities suitable for industrial applications without causing irreversible damage to nature.

Sustainable energy sources, such as wind, solar, and hydropower, produce mostly electrical energy as a result of natural phenomena. As a result, cloudy days can significantly reduce the output of a solar park while a windless day can completely halt energy production from a wind park. This electrical energy needs to be stored in special energy storage devices, unlike fossil fuels which can simply be transported and stored in tanks. Consequently, in order to build a mobile device, such as a car, powered by electricity from renewable sources one needs to design an electrical energy storage device. These problems can be solved by devices that can store large amounts of electrical energy; charging during times when production exceeds consumption only to release it during times of high demand and low supply.

The importance of this daunting task has been widely recognised, recently by the 2019 Nobel Prize in Chemistry, awarded to John B. Goodenough, M. Stanley Whittingham and Akira Yoshino "for the development of lithium-ion batteries." Lithium-ion batteries (LIBs) are one of the most widespread electrical energy storage technologies due to their excellent performance and low cost. Due to their prevalence in all of our mobile electrical devices, from our mobile phones and personal computers to cars, the modern world would not be the same without them. Nevertheless, the search for better energy storage devices is far from over, visible with the rising trend of scientific publications containing "electrical energy storage" as a topic (Figure 1.).

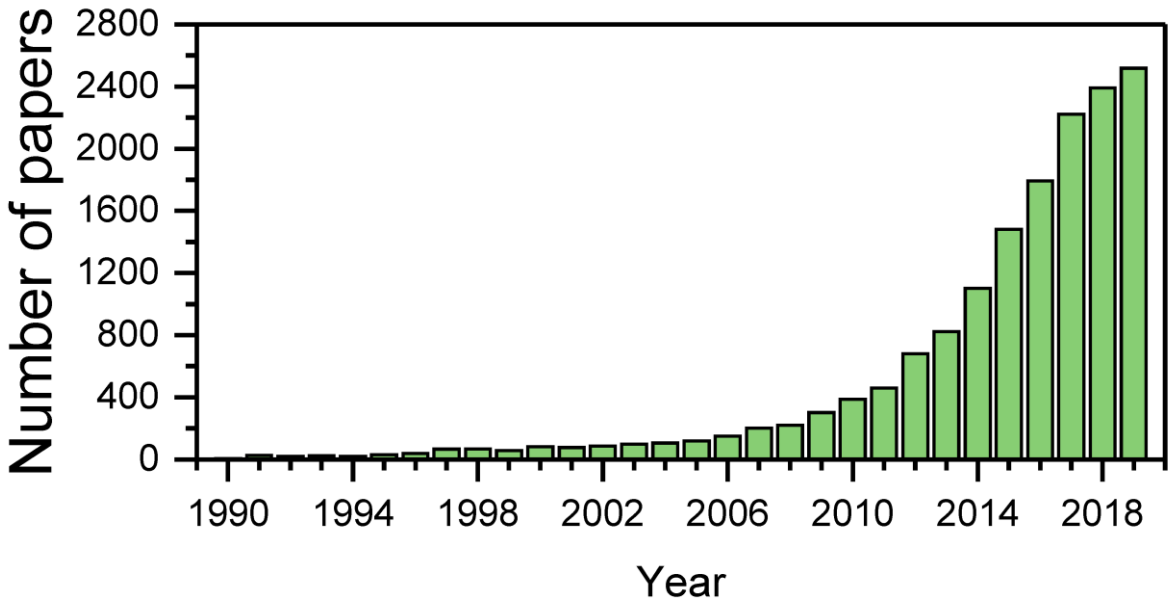

Figure 1. Number of scientific publications containing "electrical energy storage" as a topic from 1990 to 2019. Data taken from Web of Science database on 23rd January 2020.

Considering the challenges within lithium-ion batteries, the cathode is one of the most important. Current commercial cathodes are based on toxic and unsustainable heavy metals such as lithium cobalt oxide. Production of cobalt like all other heavy metals requires mining, a process that creates a negative environmental impact. Today, more than half of the cobalt mined in the world comes from the Democratic Republic of the Congo, as it contains almost half of the cobalt reserves on earth. DR Congo, being in a politically unstable region, is not a reliable supplier of cobalt as the price can vary during insurgencies.[5] Furthermore, serious concerns were reported about the use of slaves and child labour in the mining of cobalt as well as fueling the civil war in DR Congo- where mining profits ends up in the hands of the warlords. These concerns could be met by the design of cathodes produced from cobalt-free materials, e.g., other inorganic electrodes such as iron phosphates. Finally, such cathodes may

be made from organic materials, with the most sustainable ones being based on organic biowaste, as this waste material is produced in virtually all the parts of the world.

2. Introduction

2.1. Charge storage devices

Electrical energy storage is in essence the storage of electrons at higher potential than their thermodynamic equilibrium. The two main elements of any device used for electrical energy storage are electrodes. An electrolyte is used to bridge both electrodes, allowing for the passage of ions needed for charge equilibration as a result of electron flow. When the device stores no energy, or when the device is "empty", electrodes are in thermodynamic equilibrium, and, upon introduction to an electrical circuit, have no electron flow. However, if external potential is applied, or when the device is being "charged", electron flow occurs from one electrode, the cathode, to another electrode, the anode. Upon completion of the process, or when the device is fully charged, no more electrons can flow under applied voltage from cathode to anode. Now, the system is not in thermodynamic equilibrium, and when the cathode and anode are connected with a wire, electron flow will occur in the opposite direction, from the anode to the cathode. During this process the system relaxes towards thermodynamic equilibrium and the released energy can be used to perform a specific task, such as lighting a bulb.

The mechanism of electron storage can be Faradaic, based on chemical redox reactions which store electrons, or non-Faradaic, based on physical adsorption of electrically charged particles which form an electrical double layer on the electrode surface. Devices which utilise non-Faradaic mechanisms are called capacitors while those that utilise Faradaic mechanisms are called batteries. Due to the importance of understanding the underlying principles of these devices, they will be explained in detail within the following two sections.

2.1.1. Electrical double layer capacitors

A capacitor is a basic element of many electronic circuits which stores electrical energy in an electric field. It consists of two conductive elements, separated by a non-conductive region. Upon applying charge to one conductor, according to Coulomb's law, it polarises the other conductor attracting opposite charges, and thus storing electric energy. Capacitance is defined as the change of charge, dq, divided by the change of voltage, dV. From a physical perspective, capacitance is proportional to the area of the electrodes, A, and the dielectric constant of the insulator, ε, while being inversely proportional to the distance between the conductors.

$$C = \frac{\mathrm{d}q}{\mathrm{d}V} = \frac{\varepsilon A}{d}$$

However, traditional capacitors were never regarded as energy storage devices due to the low amount of energy these devices can store.[6] Nonetheless, porous materials with high surface areas and low distance between pores could result in devices capable of storing huge amounts of charge. Indeed new porous materials with surface areas of several thousand square meters per gram and pores sizes in the range of a nanometer have been utilised to construct a new generation of capacitors.

Porous materials have interconnected pores distributed within in their structure. These pores represent the phase boundary between the material and the environment, and therefore porous materials are characterised with large surface areas. Properties of porous materials are usually determined through sorption experiments with inert gases at cryogenic temperatures, most commonly via nitrogen sorption at 77 K. Further details on the gas sorption experiments be found in the appendix.

Microporous materials can be used as capacitors due to their high surface and small pore width, ultimately resulting in high capacity. The mechanism of storage in these devices is called electrical double layer capacitance (EDLC), due to a layer of negatively charged electrons found on the surface of the microporous material followed by a second layer of positively charged ions which ensures charge neutrality. As mentioned before, materials for capacitors must be conductive, therefore the most suitable class of materials for this application are microporous carbons due to their conductive nature and high surface areas.[7]

2.1.2 Batteries

Batteries utilise chemical reaction to produce energy. Although Alessandro Volta designed the firstly battery, John Frederic Daniell upgraded his design creating the first battery that could be used as a practical source of electricity. He connected a zinc electrode and a copper electrode immersed in solution of their respective sulphates connected via salt bridge. Electron flow occurred from the zinc electrode to the copper electrode due to zinc's more negative standard electrode reduction potential. During the discharging of the battery, the zinc electrode is reduced while the copper electrode is oxidised:

$$Zn(s) \rightarrow Zn^{2+}(aq) + 2\ e^-$$

$$Cu^{2+}(aq) + 2\ e^- \rightarrow Cu(s)$$

These two reactions can be combined resulting in:

$$Zn(s) + Cu^{2+}(aq) \rightarrow Zn^{2+}(aq) + Cu(s)$$

Therefore, when the electron flow occurs from the higher potential to the lower potential, the zinc electrode is shrinking in size while copper electrode is enlarged. This flow produces energy (E) equal to the product of charge (q) and the potential difference (ΔV):

$$E = q * \Delta V$$

Flow that produces electrons is the underlying principle of all batteries.[8]

In principle, by applying the right potential to the electrochemical cell, every cell reaction can be reversed — charging the battery and allowing it to be reused. However, some constraints such as the mixing of cations, make the recharging of cells impossible. Cells that are subject to cation mixing are called primary batteries. As primary batteries are single use only, in contrast to the rechargeable secondary battery, they will not be discussed in further detail due to their high cost and environmental hazard when disposed of improperly.[9]

Depending on the location of the redox active species, modern batteries can be divided into two main groups: solid electrode batteries, where the redox active species are located on the electrodes, and redox flow batteries, where the redox active species are located in the electrolyte. Although redox flow batteries hold great promise for large energy storage problems, the focus of this thesis lies within metal-ion batteries with solid electrodes, as they are the most common type of electrical energy storage devices. The basic design of these batteries does not differ fundamentally from Daniell's design, with the difference of materials chosen for electrodes and electrolyte. Anode (negative electrode) and cathode (positive electrode) are separated by a separator (semiporous membrane that prevents short circuiting) filled with electrolyte (media filled with metal ions that travel rather quickly to ensure charge balance at cathode and the anode). Similar to Daniell's batteries, all the batteries operate at a constant voltage that is equal to the potential difference between anode and cathode. Operational principles of such a device will be explained on the example of lithium-ion batteries due to their aforementioned importance (Figure 2.1).[10]

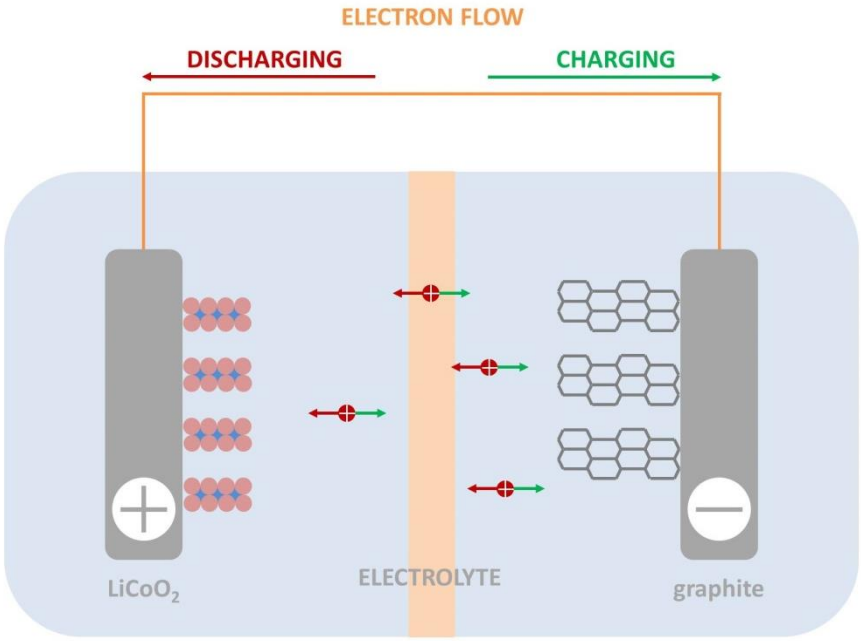

Figure 2.1. Basic operational principle of lithium-ion batteries. (Inspired[11])

First, the worth of lithium as a current metal of choice for batteries should be considered. Amongst metals, lithium has the smallest molecular weight and one of the most positive reduction potentials — low molecular weight and great charge carrier properties ensure a high charge density per mass and the most positive reduction potential ensures high operational voltage. Nevertheless, the journey from the first proposal of LIBs in 1976[12] to their commercial applications was daunting and long, as lithium-ion batteries consist of many elements that had to be refined for a specific application. Therefore, a short summary of these elements and their development is needed.[13]

The anode of LIBs is the site of reduction (during charging) or oxidation (during discharging) of lithium. Therefore lithium metal, comparable to zinc in Daniell's battery, is the simplest anode for LIBs. However, during charging, reduced lithium ions form lithium metal, which crystallises on the surface of the anode. Due to an uneven nucleation, nanowire structure called dendrites are formed.[14] These structures cause the malfunction of LIBs and can even result in an explosion due to overheating. Nevertheless, developments in intercalation technologies have allowed lithiated graphite to be used as an anode, hindering formation of dendrites during cycling as a result of the intercalation of lithium atoms between the graphite layers.[13,15,16]

The cathode of LIBs is the site of oxidation (during charging) or reduction (during discharging) of cathodic material that usually deintercalates and intercalates lithium ions during the process. A good example of a cathodic material for LIBs is Goodenough's cathode,

Li_xCoO_2 where x = 0 in a fully discharged and x = 1 in a fully charged state. However, stable operation is only possible between x = 0 and x = 0.5. During discharging of the battery, cobalt is reduced from Co(IV) to Co(III) and the charge balance is preserved by intercalation of lithium ions. The opposite process occurs during charging, where cobalt is oxidised while lithium is deintercalated from the cathode.[17]

Different types of electrolytes are currently under investigated for LIBs, namely organic, solid-state and polymeric. Aqueous electrolytes are not suitable as long as neutral lithium is used on the anode due to the harsh reaction of lithium with water, although methods have been developed to circumvent this problem.[18] Due to this limitation, commercial batteries mostly use organic electrolyte. Finding a suitable electrolyte for lithium ion batteries was a daunting task, due to the low reduction potential of lithium which can easily reduce organic compounds. However, different carbonate-based solvents, such as ethylene carbonate or diethyl carbonate can successfully withstand these conditions. Furthermore, salts used to make an electrolyte need to be resistant to oxidation as well as have good solubility in carbonates. Lithium salts with fluorinated anions, such as $LiPF_6$ presented good performance in such a system. Commercial electrodes rely on stable solid electrolyte interphase (SEI) formation. SEI occurs upon decomposition of organic electrolyte on the electrode surface, creating a layer of passivated material which conducts ions. SEI is considered stable if it protects the electrolyte from further decomposition.[19] Ultimately, the main task of the electrolyte is to ensure charge balance within electrodes, transporting lithium ions from one electrode to another, or from cathode to anode during charging and vice versa during discharging.[13]

Capacitors and batteries operate with fundamentally different electron storage mechanisms. However, both mechanisms have certain advantages and disadvantages, outlined in the following sections. In order to compare capacitors and batteries, one needs to be acquainted with the performance metrics commonly employed.

2.1.3. Performance metrics for capacitors and batteries

Traditionally, the most important metrics for describing performance of capacitors are capacitance, operating potential, cycling stability, coulombic efficiency, maximum power and energy density.

Capacitance (C [F]) is the amount of charge stored in a device, usually calculated from galvanostatic charge-discharge experiments, but it can also be calculated from cyclic

voltammetry or electrochemical impedance spectroscopy. Capacitance is proportional to the current (i [A]) and inversely proportional to the rate voltage changes ($\mathrm{d}V\,(\mathrm{d}t)^{-1}$ [V s^{-1}]):

$$C = \frac{i}{\frac{\mathrm{d}V}{\mathrm{d}t}}$$

However, capacitance based comparison of devices is inconvenient, more commonly, specific capacitance is used; where capacitance is reported per mass (gravimetric), volume (volumetric) or area (areal capacitance) of the active material.

Cycling stability describes the rate of degradation of a capacitor during charging and discharging. Usually, capacitors have high cycling stabilities, able to cycle for several thousand cycles limited degradation. A related metric, coulombic efficiency, provides an insight into the reversibility of cycling. Coulombic efficiency is calculated by dividing discharging specific capacitance with the charging specific capacitance (from the same cycle), and it is expected to be close to 100%. The operating potential of a capacitor is the voltage range where the cell is stable. High operating voltages are desirable as both maximum power (P_{max} [W]) and gravimetric energy density [J g^{-1}] have exponential relationship with voltage:

$$P_{max} = \frac{{V_i}^2}{4mR_s}$$

$$\text{Energy density} = \frac{1}{2}C_g V^2$$

where V_i [V] is the initial voltage of the device, R_s [Ω] is the equivalent series resistance, C_g [F g^{-1}] is the gravimetric capacitance, and V [V] is the voltage of the capacitor.

Commonly, batteries are described using a similar set of metrics, namely capacity, oxidation and reduction potential, cycling stability and coulombic efficiency. Cycling stability and coulombic efficiency are calculated in the same manner as for capacitors.

Capacity (C [mAh g^{-1}]) represents the amount of charge stored in a battery. It is proportional to current (I [A]) and the change of time (Δt [s]):

$$C = \frac{i\Delta t}{3.6}$$

An important metric for battery performance is theoretical capacity (C_{theor} [mAh g^{-1}]), which gives the maximum charge that a material can hold with respect to its mass. Therefore if a device reaches its theoretical capacity, no additional improvements are possible. Theoretical

capacity is proportional to the number of charges a molecule of a studied material can hold, and inversely proportional to the molecule's molar mass:

$$C_{theor} = \frac{nF}{3.6 * M}$$

If the polymer is an active material, one usually considers the number of charges per repeat unit as well as the molar mass of the repeat unit.

Potentials of cathodic and anodic redox reactions are important, as the voltage of a battery is equivalent to the difference between the potentials of the cathode and anode. For a battery, it is desirable to have a high voltage, where the cathodic reaction has a high potential and the anodic reaction has a low potential.[10]

Furthermore, it is important to note that the performance of an electrical energy storage device is codependent on every component of the device. Therefore, in order to study a specific element of a cell, such as a cathode, a so-called half-cell measurement is used. For example, tests for LIB cathodes are usually performed by utilising the experimental material as the cathode, elemental lithium as the anode, with a known separator, and a known electrolyte. Testing is performed at an extended voltage range which depends on the electrolyte of choice and desired cathodic voltage.

2.1.4. Capacitors and batteries – comparison and beyond

Although capacitors and batteries are both used for electrical energy storage, they are suitable for fundamentally different applications. Capacitors have higher power densities and lower energy densities than batteries a behaviour presented in a plot of power density to energy density, also known as Ragone's plot (Figure 2.2). For practical applications, capacitors tend to be used when a large quantity of energy is needed in a short time, conversely batteries are more suitable for applications where moderate quantities of energy are needed over a long period of time. For example, capacitors are used in the mechanism of emergency doors of airplanes while batteries are more suitable for electric cars.[20]

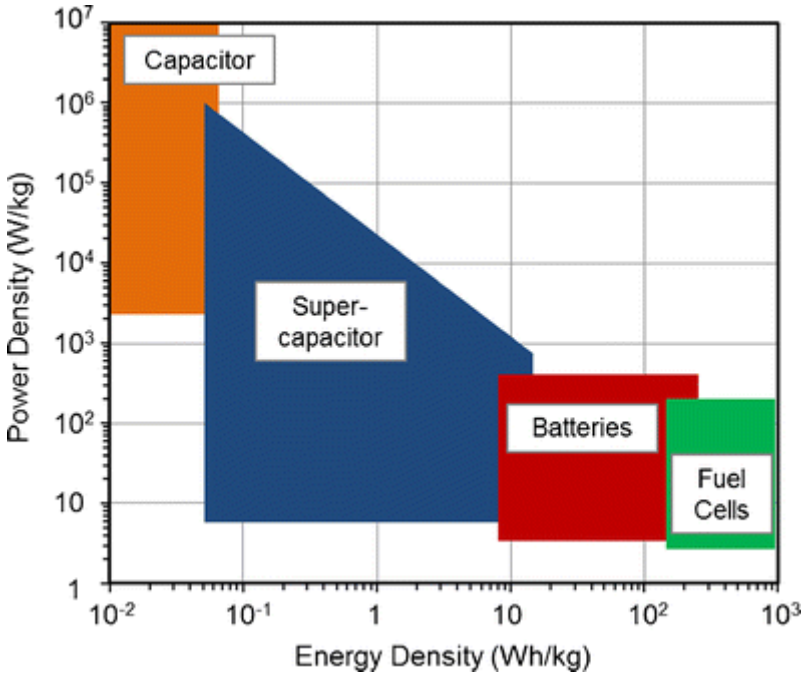

Figure 2.2. Ragone's plot for electrical energy storage and conversion devices. Reprinted by permission from Spinger Nature: Springer Biomedical Microdevices A flexible super-capacitive solid-state power supply for miniature implantable medical devices, Chuizhou Meng et al, Copyright 2013.[21]

Also commonly compared to capacitors and batteries are two other devices, namely fuel cells, a conversion device that will not be discussed in detail, and supercapacitors, in this context defined as a type of capacitor that harnesses both EDL mechanism and pseudocapacitance, fast and reversible redox reactions at the electrode surface.[21] However, pseudocapacitance in many materials is the source of much confusion and debate,[22] and will be discussed in detail later after further establishment of the distinction between a capacitor and a battery electrode. Furthermore, it is worth noting that the term supercapacitor does not have a uniform meaning within literature and is often used to depict a capacitor with a simple EDL mechanism. Therefore, in order to avoid confusion, devices with pseudocapacitive electron storage mechanisms will be labelled as pseudocapacitors, following definition of Lukatskaya et al.[23]

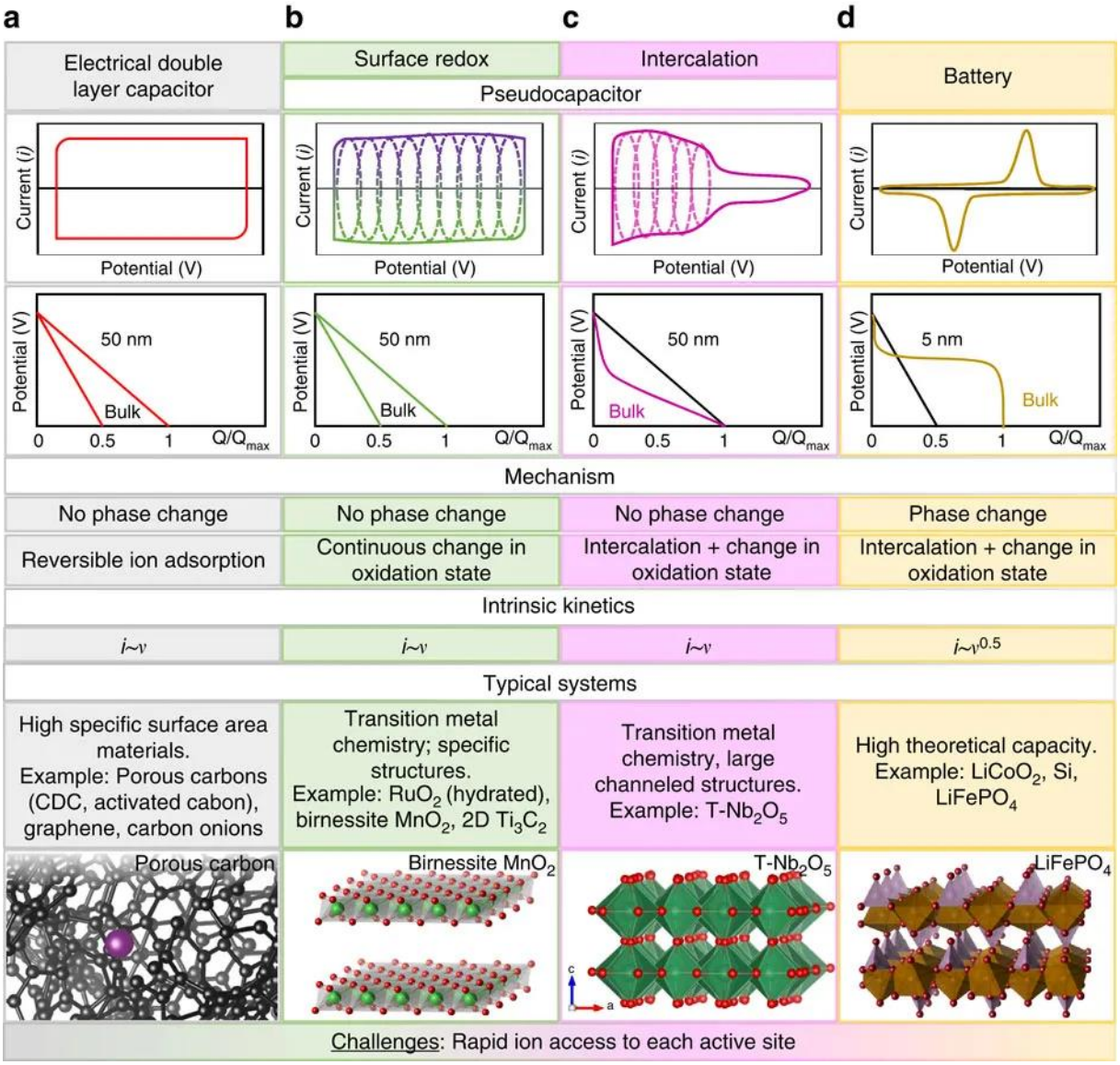

Figure 2.3. Comparison of devices utilising Faradaic and capacitive energy storage. (a) Capacitors, (b) surface redox pseudocapacitors, (c) intercalation pseudocapacitors and (d) batteries. Reproduced from *Nature Communications*, published open access under a CC BY license (Creative Commons Attribution 4.0 International License).[23]

The difference between a capacitor, a pseudocapacitor and a battery electrode can be rather easily established by comparing their cyclic voltammograms and charging-discharging curves (Figure 2.3). Cyclic voltammograms of capacitor electrodes tend to have a rectangular shape, while those of battery electrodes tend to have two pronounced symmetrical peaks at a certain voltage. Different positions of oxidation and reduction peaks are a consequence of surpassing the activation energy, called overpotential, as a redox reaction does not occur in the point of thermodynamic equilibrium — but after overpotential.[24] Furthermore, charging-discharging curves of capacitor electrodes form a triangle, while electrodes of batteries are characterised by plateau-like behaviour. Therefore, capacitor electrodes release captured electrons symmetrically during the entire range of discharging potential while electrodes of batteries

release the bulk of captured electrons at a particular potential. Hybrid electrodes, benefiting both from EDL mechanisms and redox reactions at a defined potential are characterised by mixed cyclic voltammograms, generally shaped as rectangles with peaks. Their charge-discharge curves are comparable to those of capacitor electrodes, but with a pronounced belly around the redox potential. However, Gómez-Romero et al. refer to this behaviour as pseudocapacitance,[6] Long *et al. c*laim pseudocapacitor electrodes are characterised by cyclic voltammograms and charging-discharging curves similar to capacitors,[22] while Lukatskaya et al. claim the existence of two pseudocapacitor subtypes, namely surface redox and intercalation subtypes.[23] Surface redox pseudocapacitors undergo continuous change in the oxidation state while intercalation pseudocapacitors undergo intercalation and change in the oxidation state. In this thesis, the definition of Lukatskaya et al. will be employed, while the electrodes described by Gómez-Romero et al. as pseudocapacitor electrodes, which benefit both from EDL and a redox reaction at defined voltage, will be regarded as hybrid electrodes.

Redox active cathodes mentioned in previously include only inorganic materials. However, as mentioned earlier, inorganic, heavy-metal based electrodes do not meet modern standards of sustainability. Therefore, in search for more sustainable materials, redox-active organic materials will be introduced in the next section.

2.2. Organic cathodes

Similar to inorganic materials, organic materials can also undergo redox reactions, and therefore can be utilised as battery or hybrid cathodes. Furthermore, organic materials have simpler redox reactions that do not include intercalation, allowing high rate performance and long life cycles. While inorganic materials undergo valence changes in one or more of their constituents, organic materials undergo a change in state of the electroactive group. Ever growing demand for lighter, smaller, and flexible portable electronic devices push the development of organic cathodes due to their ease of fabrication for flexible devices.[25] Significantly lower toxicity of organic compounds compared to heavy metals allows for the safer and easier disposal of organic batteries, decreasing environmental impact.[26]

Since the first attempt to design a battery based on organic material, doped polyacetylene,[27] the field attracted great attention. Many organic materials, from small molecules to polymers, have been investigated as cathode materials. Small molecules often exhibit high solubility in electrolytes due to their low molecular weight, therefore, focus will be given to polymers that display better resistance to dissolution in electrolytes due to their high molecular weight;

ultimately resulting in better cycling stabilities.[10] Organic polymers can be classified in two main groups: conjugated and nonconjugated polymers. Due to the fundamentally different underlying mechanisms these two groups use for redox reactivity, conjugated and nonconjugated polymers will be studied separately in the next two sections.

2.2.1. Conjugated polymers

Conjugated polymers, such as the aforementioned polyacetylene, have semiconductive properties due to the band structure generated by the overlapping adjacent π-orbitals. Upon doping, conjugated polymers can become conductive, allowing the electrons to pass from redox-active centres to current collectors, and reverse. However, their conjugated structure brings a great disadvantage; as connected redox centres influence each other. Therefore, redox transformation in one centre changes the redox potential of other redox moieties, ultimately resulting in a sloppy discharging behaviour compared to plateau formed during discharging of nonconjugated redox active groups (Figure 2.4.). Ideally, conjugated polymers can store one charge per repeat unit, however in practice, the proximity of repeat units limit the charge storage to 0.3-0.5 charges per repeat unit, causing significant discrepancies between the measured and theoretical capacity.[28]

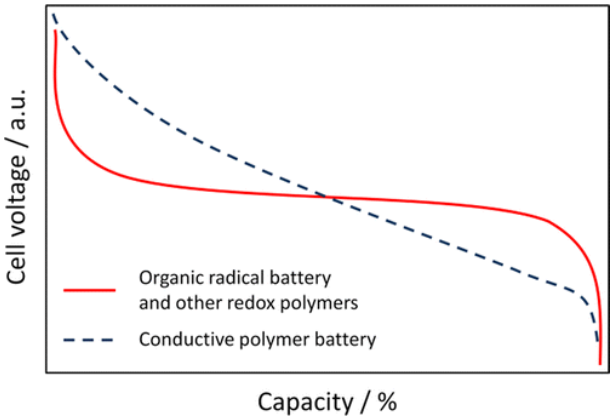

Figure 2.4. Discharging curves of a conductive conjugated polymer and non-conjugated polymer. Reprinted with permission from *Chem. Rev.* 2016, 116, 16, 9438-9484. Copyright 2016 American Chemical Society.[26,29]

Most common examples of conjugated polymers utilised as cathode materials include polyindole, polythiophene, polyaniline and, the most studied example, polypyrrole. However, precursors of conjugated polymers are not easily found in nature, and therefore need to be synthesised from oil-derived chemicals inherently limiting their sustainability.

2.2.2. Nonconjugated polymers

Contrary to conjugated polymers, nonconjugated polymers do not benefit from an overlap of π-orbitals, and subsequent semiconductive properties. However this behaviour also allows for a discharging curve with a plateau, resulting in batteries with a defined potential. Due to their insulating nature, nonconjugated polymers need to be mixed with conductive additives in order to ensure electron flow from redox centre to current collector and backwards. Therefore, conductive additives will be introduced in detail at the end of this chapter.

Depending on the chemical nature of the active groups, nonconjugated polymers can be either radical, where oxidised or reduced specie is a radical, or non-radical, where neither oxidised nor reduced specie is a radical. As radical redox active polymers are rather rare in nature, focus will be given to non-radical polymers. They comprise polymers bearing many different functional groups such as organosulfur, carbazole, triphenylamine, and viologen groups. However, focus will be given to carbonyl containing polymers due to their abundance in nature.[26]

Carbonyl polymers can be separated into three groups based on the stabilisation mechanism upon reduction: vicinal carbonyls which form stable enolates upon reduction, aromatic carbonyl derivates that are stabilised by charge dispersion through the aromatic ring and quinones that are stabilised due to aromaticity that is generated upon their reduction.[30] Quinones, being the most promising of the three, were first studied in 1972 as cathode materials in rechargeable batteries.[31] However, upon introduction to lithium-ion conventional electrolytes, molecular quinones exhibit good solubility ultimately causing poor stability of the cathodes. Therefore, research efforts have been concentrated on reducing the solubility of quinones, both by the reduction of small molecule stability,[32,33] and by the introduction of quinones in polymeric systems.[34,35] While polymeric quinones include systems with mostly *p*-quinone moieties[26,30,36,37] there are notable examples where *o*-quinone moieties[35,38] are utilised.

To conclude, quinones contacting polymers are broad and diverse group. However, they are specifically interesting as hydroquinones are commonly found in nature, and it could be possible to design cathodic materials sustainably, based on naturally occurring moieties. Significant efforts have already been undertaken, but due to the importance of this work, it will be outlined later in further detail.

2.2.2.1. Conductive additives

As previously mentioned, nonconjugated polymers display no intrinsic conductivity and hence conductive additives are required. Commonly used conductive additives include conductive polymers previously discussed and nanostructured carbons.

Conductive polymers can be used either as a polymer backbone, whereas they significantly increase the conductivity of the polymer,[39–41] or in a composite with redox active polymers.[42,43] Although introduction of redox active moieties on conductive backbones can be advantageous to mere composite formation, problems arise due to the formation of multiple redox centres. Furthermore, even conductive polymers are often mixed with nanostructured carbons to increase conductivity.[42,43]

The most common nanostructured conductive additives are graphene and carbon nanotubes, due to their high conductivity and surface area. However, their high cost and difficulty to sustainably produce hinder their applicability in industry. Therefore, carbon particles and porous carbons provide a valid alternative.[26] As previously mentioned, carbons can be synthesised from sustainable sources allowing for the formation of sustainable composites.

Nevertheless, sustainable composites require not only sustainable conductive additives but more importantly sustainable active materials. Therefore in the next chapter, the concept of sustainability will be introduced along with previous efforts to design sustainable materials for cathodes.

2.3. Sustainable cathodes

Naturally occurring polymers bearing phenolic groups are common. A plethora of redox active biomolecules such as dopamine are available, but do to their low abundance in nature they cannot meet an industrial demand and as a result are not deemed sustainable. Therefore, the focus will only be given to chemicals obtainable at larger quantities.

Many naturally occurring sustainable polyphenols, such as lignin and tannic acid, contain catecholic, guaiacyl, pyrogallolic and syringyl groups that can undergo oxidation forming redox active quinones (Scheme 1.).

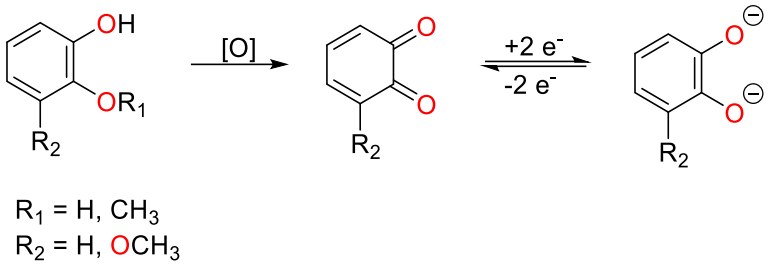

Scheme 2.1. Redox activity of catecholic, guaiacyl, pyrogallolic and syringyl groups.

As discussed previously, different catecholic polymers have been previously incorporated in cathode materials for LIBs successfully. Therefore, the challenge remains to employ lignin and tannic acid as cathode materials for LIBs. In the next two chapters previous efforts and challenges in doing so will be discussed.

2.3.1. Lignin

Lignin is the most abundant naturally occurring polyphenol, and along with cellulose and hemicellulose, one of the main components of wood.[44] It is a waste material in many industries, most notably the paper industry, where this polymer is used as a low-value fuel.[45] However, in recent years it has attracted great interest as a source for high value aromatic chemicals,[45,46] materials,[47] and as a precursor for functional materials.[48–50]

2.3.1.1. Structure, isolation and depolymerisation of lignin

Lignin is a polyphenol, whose phenolic moieties are *p*-hydroxylphenolic, guaiacyl, and syringyl. They are interconnected using a variety of bonds including esters and aliphatic carbon-carbon bonds. However, the structure of lignin depends on the source material as well as isolation method. For example, grasses contain all three phenolic moieties while softwood lignin contains primarily guaiacyl, and hardwood lignin contains significant amounts of both guaiacyl and syringyl moieties. Therefore, two batches of lignin do not contain the same structure hindering its widespread applications in industry.

Isolation of lignin comprises the separation of lignin from cellulose, hemicellulose and other minor components of wood. The oldest process for lignin isolation is called the sulphite process. Delignification occurs as a consequence of sulphonation via sulphite salts. Resulting lignin becomes water soluble due to the high amount of charged sulphite groups on the surface, called lignosulphonate. The Kraft process is a newer process predominantly used today, characterised by a high degree of delignification in basic conditions, resulting in lignin with low molecular mass and high solubility in water due to deprotonated phenols.[51]

Lignin can be depolymerised in order to produce a plethora of aromatic chemicals. Furthermore, different catalytic conditions can produce different chemicals.[52] However, the most interesting chemical for material synthesis is vanillin, a derivate of benzaldehyde with guaiacyl functional group and used as the main ingredient of vanilla sugar.[53,54] The interesting structure of vanillin allows for the formation of many functional materials and plastics while its widespread usage in food industry guarantees low toxicity.

2.3.1.2. Lignin based cathodes

Lignin-based cathodes have attracted great attention since their initial report by Inganäs et al. in 2012. They have successfully prepared a lignin-polypyrrole composite via electrochemical polymerisation of polypyrrole in lignosulphonate containing solution. The formed composite showed great electrochemical performance in aqueous 0.1 M $HClO_4$. Galvanostatic charging-discharging measurements (GCDM) showed a capacity of around 75 mAh g^{-1} at 0.83 A g^{-1} for the 0.5 µm thick electrode. However, when the thickness of electrode increased to 1.9 µm, the capacity dropped significantly to ~45 mAh g^{-1}, indicating inherent problems due to the low surface area of the electrode.[55] It is worth mentioning that parallel to this discovery a group in Russia published a paper about the usage of lignin as a cathode material in primary batteries followed by further studies.[56–59] However, as their work is oriented towards non rechargeable batteries, it will not be discussed further.

Milczarek et al. were the first to prepare a lignin cathode with nanostructured carbon as a conductive additive. Firstly, lignosulphonate was exchanged with Kraft lignin, a more common waste product of the paper industry, and carbon nanotubes were used as conductive additives. Furthermore, composite was prepared via a solution casting method allowing the process to be scalable and presented excellent performance. The composites exhibited a clear redox behaviour in CV, and a capacitance of around 185 F g^{-1} at a current density of 1 A g^{-1}, as calculated from GCDM between 0.1 and 0.65 V in 0.5 H_2SO_4 with the capacity retention of above 90% after 500 cycles.[60]

Park et al. Prepared a composite of sodium lignosulphonate with graphene oxide using solution casting. The formed composite showed capacitance of around 350 F g^{-1}, as calculated from GCDM at 1 A g^{-1} in 0.1 M $HClO_4$ between 0.2 and 0.8 V.[61] Composites between Kraft lignin and bioderived porous carbon allowed for the formation of the first fully biowaste derived cathode containing lignin. The composites produced exhibit great charge storage

properties with capacities of around 45 mAh g^{-1}, as calculated from GCDM at 0.75 A g^{-1} in 1 M $HClO_4$ between -0.1 and 0.8 V.[62]

Due to the complicated structure of lignin, understanding the mechanism of underlying charge storage proves difficult. Nevertheless, Admassie et al. studied a set of subtropical lignins to determine the content of syringyl and guaiacyl groups, groups postulated to be electrochemically active in lignin. Upon electrochemical preparation lignin composites with polypyrrole, their capacities were compared via cyclic voltammetry and galvanostatic charging-discharging measurements. They concluded that higher content of syringyl groups in lignin increases the charge storage properties.[63] Inganäs et al. performed an in-situ infrared spectroelectrochemical investigation of lignosulphonate-polypyrrole composites during electrochemical cycling in 0.1 M electrolyte. With this, they proved the proposed reaction (Scheme 2.1) happens during electrochemical cycling: as the intensity of carbonyl bands increases during electrochemical oxidation, only to decrease during electrochemical reduction.[64]

Not only lignin, but also lignin-derived molecules have been successfully incorporated in electrical energy storage devices. Nilsson et al. showed that hardwood and softwood Kraft lignins modified via addition of guaiacol, syringol and *p*-hydroquinone displayed better capacities in composites with polypyrrole compared to unmodified lignins, even though density of the aromatic groups did not always increase, as determined from ^{31}P NMR. The best performance was observed for a composite of hydroquinone modified softwood lignin, 69 mA g^{-1}, as calculated from GCDM at 1 A g^{-1} between 0.1 and 0.7 V in 0.1 M $HClO_4$.[65] In another study, Inganäs et al. prepared homopolymers and copolymers from syringol and guaiacol by phenol-formaldehyde condensation. Afterwards the polymers were introduced in a composite with polypyrrol via electropolymerisation and the electrochemical performance of the composites was tested. Compared to pure polypyrrol, the composites showed extraordinary improvement in capacity, namely 49, 62 and 57 mAh g^{-1} for polyguaiacol, polysyringol and copolymer, respectively, compared to 30 mAh g^{-1} for polypyrrole at 0.1 A g^{-1}, as calculated from GCDM between 0.1 and 0.7 V in 0.1 M $HClO_4$. Interestingly, a copolymer of guaiacol, syringol and hydroquinone was also formed and it showed an extraordinary capacity of 94 mAh g^{-1} under the same conditions.[66]

Poly(3,4-ethylenedioxythiophene) – lignosulphonate was evaluated as a cathode material in lithium and sodium ion batteries. Nevertheless, this work will not be studied in depth as there is no proof of lignin activity in the composite except the higher capacity of the composite as

compared to pure poly(3,4-ethylenedioxythiophene).[67] However, there are previous reports of increased charge storage of conductive polymers upon introduction of redox inactive polymers.[68]

Substantial efforts have been undertaken to form cathodes from lignin-derived materials. Those efforts are hindered by low structural integrity of lignin, as the structure of lignin changes on batch to batch basis. Therefore, polymerisation of lignin derived small molecules holds a great promise for the future of lignin derived electrodes.

2.3.2. Tannic acid

Tannic acid, like lignin, is a naturally occurring polyphenol and hydrolysable tannin. As a result, it exhibits good solubility in water, allowing easy extraction from wood waste using aqueous based solvents.[69] Although the structure of tannic acid is often described as glucose pentagallolyl gallate, tannic acid is in fact a mixture of different isomers of partially gallolylated glucose (Figure 2.5.).

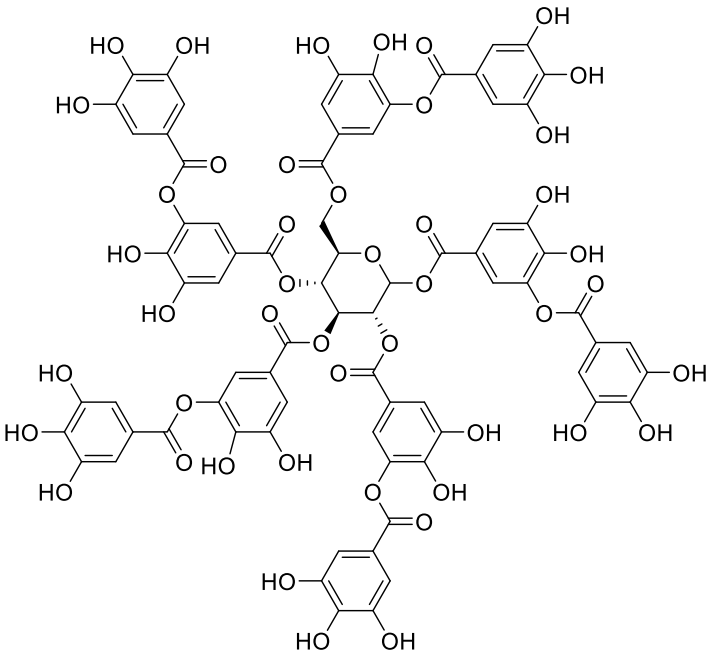

Figure 2.5. Idealised structure of tannic acid.

2.3.2.1. Tannic acid cathodes

Compared to lignin, the development of the tannic acid cathodes propagated less quickly, with the first work on the topic being published in 2017. This delay can be attributed to the aforementioned good solubility of tannic acid in acidic aqueous systems, contrary to lignin,

allowing the dissolution of tannic acid in aqueous electrolytes. Park et al. have solved the solubility problem through the crosslinking of tannic acid via phenolic-iron coordination bonds. These structures were assembled on the surface of carbon nanotubes, enhancing the conductivity of the composite. The resulting composite demonstrated good charge storage properties, achieving capacities of ~35 F g^{-1}, as calculated from GDCM at 1 A g^{-1} between -0.2 and 1.0 V in 1 M H_2SO_4.[70]

Yoon et al. improved this strategy through the functionalisation of nanoporous carbon with polydopamine — a good adhesive rich in catecholic groups that was subsequently used for the growth of a tannic acid layer connected with the aforementioned phenolic-iron coordination bond. These composites achieved improved performance in comparison to nanoporous carbon coated with polydopamine, with more than 240 F g^{-1} as calculated from CV experiments at 5 mV s^{-1} between 0.0 and 1.0 V in 1 M H_2SO_4.[71] Concurrently, Zhu et al. used a different strategy to reduce the solubility of tannic acid, immobilising it in the polypyrrole network, as has previously been done by Inganäs et al. to immobilise lignin.[55] This strategy afforded a material with the capacity around 280 F g^{-1} as calculated from GCDM at 1 A g^{-1} between 0.1 and 0.7 V in 0.1 M $HClO_4$. However, the prepared material had an inherent problem as a result of polypyrrole composites exhibiting a significant drop in gravimetric capacitance upon growth of thicker films on the electrode.[72]

Jin et al. devised a similar strategy for tannic acid immobilisation, as described previously by Zhong et al. for lignin.[73] Tannic acid was autoclaved at 180° with graphene oxide forming hydrogels which benefited from π-π interactions between the aromatic moieties of tannic acid and graphene oxide. Such composites exhibited excellent capacitance of 480 F g^{-1} as calculated from GCDM at 1 A g^{-1} between -0.2 and 0.8 V in 1 M H_2SO_4. Furthermore, they exhibited excellent cycling stability with a capacitance retention of 84.6% after 8000 cycles.[74] A similar strategy was used to immobilise tannic acid on graphene oxide, without the use of autoclaving and high temperatures. The resulting composite reached a capacitance of around 115 F g^{-1} as calculated from galvanostatic charging-discharging experiments at 1 A g^{-1} between 0.0 and 1.0 V in 1 M H_2SO_4.[75]

Zhong et al. formed a composite of graphene oxide and tannic acid by autoclaving at 180 °C in the presence of different metal cations. Formed composites had varying morphologies which were influenced by the cation used. The highest capacitance was exhibited by copper(II) crosslinked tannic acid composite, namely 460.4 F g^{-1} as calculated from GCDM at 1 A g^{-1} between -0.2 and 0.8 V in 1 M H_2SO_4.[76]

There are many examples of cathodes based on tannic acid. However, high solubility of tannic acid in polar solvents in hindering the development of these electrodes. Current efforts to reduce solubility include crosslinking with heavy metals and high temperature composite formation, limiting the sustainability of formed cathodes.

3. Outline

The objective of this thesis was the design of sustainable cathodes and their application for charge storage in lithium-organic system. Herein, different active materials derived from vanillin and tannic acid are explored in porous carbon composites.

Different pathways to synthesise vanillin-based materials are presented in chapter 4, and their viability as cathodes in a lithium organic electrolyte is investigated. Reductive grafting of vanillin on chitosan, a naturally occurring amine rich polysaccharide, results in a polymer with promising charge storage properties in aqueous electrolytes. However, compared to chitosan, it presented no beneficial properties for energy storage in the lithium organic electrolyte. Therefore, another material, a vanillin-based network, was prepared via catalytic trimerisation of bisvanillonitrile. During trimerisation, it is evident that the catalyst also demethylates guaiacyl groups forming catecholic groups. This material displayed excellent charge storage properties in the lithium organic electrolyte, although had rather low redox peaks and sloppy charging-discharging curves.

Chapter 5 focuses on the exploration of redox behaviour of catecholic and guaiacyl groups in lithium organic electrolyte, as well as different effects that increase charge storage. First, protocatechuic aldehyde is grafted onto polyallyamine — an amine rich synthetic polymer, forming a stable polymer network via imine links. The excellent electrochemical performance of the formed polymer is compared to an analogous polymer, which bears redox inactive resorcinolic groups instead of catecholic. The difference between the two polymers is attributed to the redox active reaction occurring in the former. Furthermore, it was observed that the composite of the carbon and the redox inactive polymer displayed much higher capacity compared to the carbon itself, which was ascribed to the hydrophilicity of the polymers, which allowed improved wettability of the carbon surface. Secondly, vanillin was grafted onto the same polymer for the comparison of electrochemical performance between catecholic and guaiacyl groups. Results of this experiment indicate slow demethylation of guaiacol in lithium organic electrolyte as opposed to the same reaction in an aqueous system that occurs rapidly in the first cycle. Finally, polymer bearing catecholic groups was introduced into composites with a set of bioderived porous carbons with similar microporosities and surface chemistries, but significantly different mesoporosities. It was found that mesopores of conductive carbon heavily influence charge storage in the formed carbon composites with redox active polymers.

Finally, a truly sustainable cathode based on tannic acid and bioderived porous carbon is presented in chapter 6. All the solvents used in cathode preparation exhibit low toxicity and are obtainable from biowaste. The formed material performs marvellously in lithium organic electrolyte, holding great promise for the future of lithium-based charge storage devices and their sustainable production.

4. Development of vanillin based cathode materials for lithium based electrical energy storage devices

Vanillin, as previously mentioned, is a molecule that can easily be produced from biowaste, from lignin. Vanillin is a great precursor for materials for sustainable energy storage as it has low molecular weight and a guaiacyl group that can undergo irreversible oxidation forming *ortho*-quinone. However, as a small molecule it is well soluble in most of the conventional electrolytes and therefore it must be polymerised to form poorly soluble macromolecules. Due to the combination of aldehyde, phenolic and methoxy functionalities vanillin can be easily introduced in polymers.[77] However, only a fraction of vanillin based polymers contains original guaiacyl group making them suitable for cathode materials.

Therefore, in this chapter two different approaches to develop sustainable, vanillin based cathode materials will be explored. Finally, their electrochemical performance for lithium based electrical energy storage will be evaluated.

Part of this chapter is adapted from my original work:

1) Ilic, I. K.; Meurer, M.; Chaleawlert-umpon, S.; Antonietti, M.; Liedel, C. Vanillin decorated chitosan as electrode material for sustainable energy storage. *RSC Adv.* **2019**, *9*, 4591-4598 (This article is licensed under a Creative Commons Attribution 3.0 Unported Licence)
2) Ilic, I. K.; Leus, K.; Schmidt, J.; Hwang, J.; Maranska, M.; Eigler, S.; Liedel, C. Polymerization in Carbone: A Novel Method for the Synthesis of More Sustainable Electrodes and Their Application as Cathodes for Lithium−Organic Energy Storage Materials Based On Vanillin. *ACS Sustainable Chem. Eng.* **2020**, *8*, 3055−3064 (This article is published under a Creative Commons Attribution (CC-BY) License, which permits unrestricted use, distribution and reproduction in any medium, provided the author and source are cited)

4.1. Vanillin decorated chitosan as electrode material for sustainable energy storage

Various work employing lignin as a material for cathodes has been presented. However, as previously mentioned, lignin's structure hinders its commercial application as it varies, not only with the method of extraction and lignin source applied, but also from one batch to another. This chapter presents a lignin-like material named ChiVan. ChiVan is formed by reductive addition of vanillin on chitosan, the second most abundant polysaccharide in the world. Compared to lignin, the structure of this polymer is highly defined, leading to better product security, making ChiVan more suitable for commercial applications than lignin. With over 60% of saccharide units in chitosan functionalised by vanillin, the concentration of redox functionalities in the polymer is significantly higher than in lignin materials. Composites with carbon black require no further binders or additives to be used as electrode material and show reversible charge storage up to 55 mAh g^{-1} as calculated from GCDM at 1 A g^{-1} in the potential range from -0.1 to 1.0 V in 1 M $HClO_4$ aqueous electrolyte.

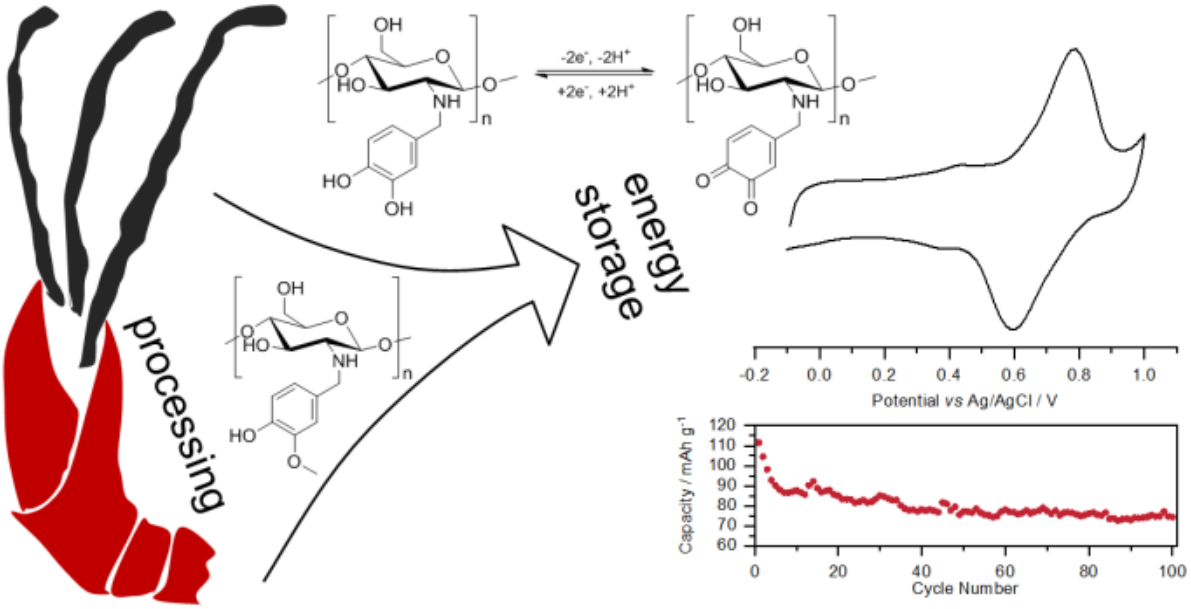

Figure 4.1. To replace dangerous and rare components in battery electrodes, more sustainable energy storage materials made from biowaste and wood-based vanillin are presented.

Saowaluk Chaleawlert-umpon helped with the design and interpretation of electrochemical experiments, while Maren Meurer performed the preliminary experiments.

4.1.1. Synthesis and characterisation of ChiVan

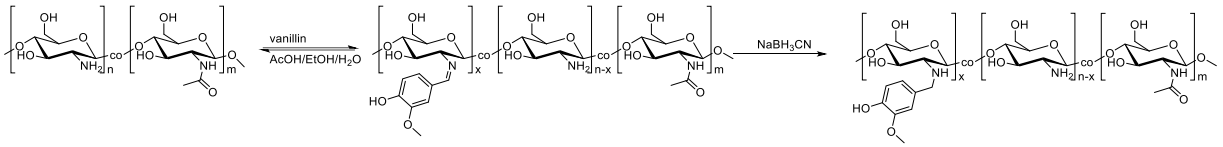

Scheme 4.1. Formation of chitosan-vanillin graft copolymer; n ≈ 85%, m ≈ 15% and x ≈ 62%.

Synthesis of the chitosan-vanillin graft copolymer (ChiVan) was performed according to a modified literature procedure (Scheme 4.1.).[78,79] Chitosan, which naturally contains acetamide groups as well as primary amines due to incomplete deacetylation of chitin, was first dissolved in diluted acetic acid due to the good solubility of chitosan in aqueous diluted solution of weak organic acids upon protonation of amine groups and subsequent polarisation of chitosan chains.

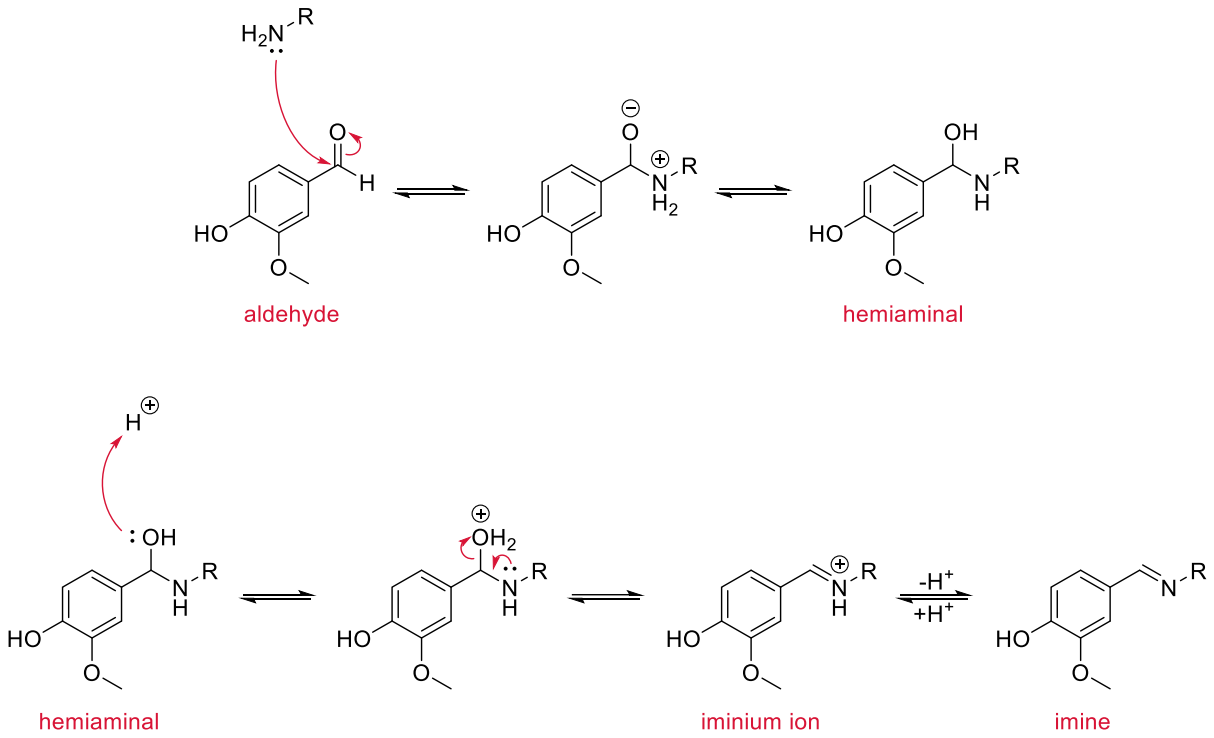

Scheme 4.2. Mechanism of hemiaminal formation (top) and of subsequent dehydratation (bottom).[80]

Upon addition of vanillin to chitosan, imine bonds form between the primary amines and vanillin in a slow reversible reaction. Firstly, nucleophilic amine attacks carbonyl group forming hemiaminal intermediate upon proton exchange. Acidic catalyst slows down this step as it protonates amine forming nonnucleophilic salt. However, acidic catalyst is needed in the second step, dehydratation of hemiaminal, allowing for the formation of imine product (Scheme 4.2). Therefore, acidic catalyst is necessary and a compromise needs to be made. As

the first step is slow at pH values lower than 4 and the second step is slow at pH values higher than 6, usually pH values between 4 and 6 are used.[80]

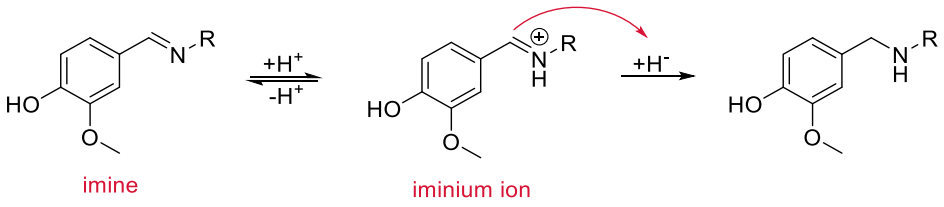

Scheme 4.3. Mechanism of reduction of imines in acidic conditions

The most common electrolytes for lignin-based cathodes are aqueous acidic solutions. Imine bonds, although they are strong covalent bonds, can be easily hydrolysed in the presence of water. Therefore, the imines were irreversibly and selectively reduced to secondary amines upon addition of sodium cyanoborohydride. Sodium cyanoborohydride, unlike other commonly used reducing agents such as sodium borohydride, can withstand aqueous solvents with negligible hydrolysis at pH higher than 3 due to electron withdrawing effect of cyano group. Furthermore, it is a selective reducing agent preferably used for imine reduction in aqueous solutions as it can reduce imines at slightly acidic pH while being unable to reduce carbonyl groups in significant amounts at pH greater than 4. Therefore, while maintaining pH between 4 and 7 one can selectively reduce imine bond between vanillin and chitosan. It is important to note that imine group does not get reduced directly, but rather iminium salt that gets formed upon reversible protonation of nitrogen. Hydride, upon deatachment from sodium cyanoborohydride performs a nucleophilic attack on carbon atom of protonated imine forming resultant secondary amine (Scheme 4.3).[81]

Upon stirring overnight, a white precipitate formed due to the rise of pH as a consequence of imine reduction that consumes protons.[78,79] The redissolved polymer by acidification was purified and characterised using nuclear magnetic resonance (NMR) and Fourier-transform infrared (FT-IR) spectroscopy.

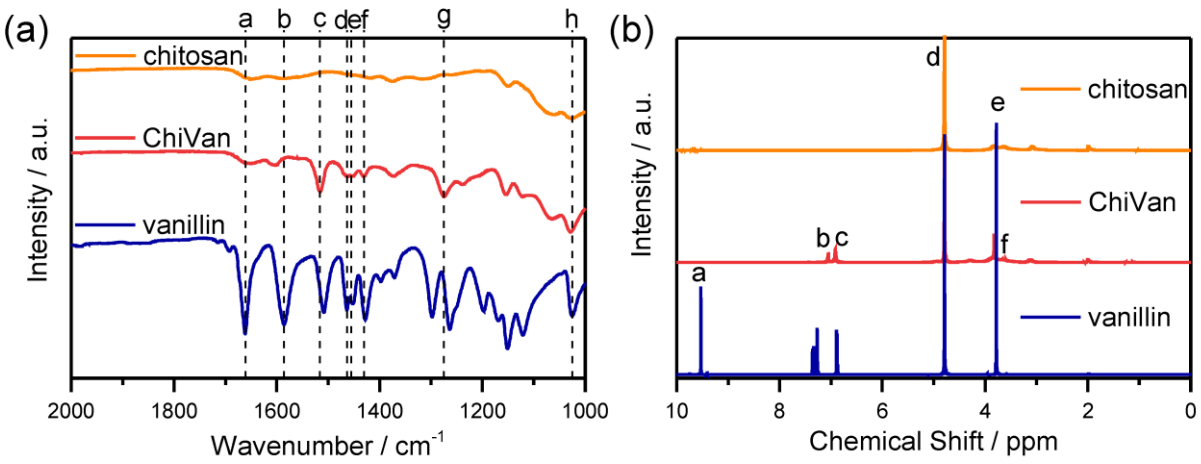

Figure 4.2. (a) FT-IR and (b) ^{1}H NMR spectra of chitosan, ChiVan, and vanillin in 1% solution of deuterated acetic acid in deuterated water.

FT-IR measurements were performed on chitosan, ChiVan, and vanillin (Figure 4.2.a). In vanillin, the C=O stretching vibration can be observed clearly at 1661 cm^{-1} (a), while this band does not appear in the spectrum of ChiVan, confirming the reaction of the aldehyde group in vanillin and successful removal of any excess vanillin. A weak band in the spectra of chitosan and ChiVan at a similar position can be ascribed to the C=O stretching vibrations of acetylated groups in chitosan (Scheme 4.1). Also the band at 1586 cm^{-1} (b) in the spectrum of vanillin, which represents a conjugated interaction between the aromatic ring and the carbonyl group, does not appear in the spectrum of ChiVan. The absence of any other band in ChiVan between 1600 and 1700 cm^{-1} points to the successful reduction of imine bonds in ChiVan. Proofs that the vanillin functionalities were successfully incorporated in ChiVan can be seen at 1516 cm^{-1} (c, aromatic C-C vibrations), 1463 cm^{-1} and 1430 cm^{-1} (d and f, asymmetrical CH_3 deformation vibrations), 1455 cm^{-1} (e, symmetrical CH_3 deformation vibrations), 1275 cm^{-1} (g, rocking vibrations for CH_3 groups), and 1025 cm^{-1} (h, mode of O-CH_3 group vibration).[82]

Furthermore, ChiVan was investigated by ^{1}H NMR spectroscopy and compared its spectrum to the ones of chitosan and vanillin (Figure 4.2b and A1). The sharp peak at 4.79 ppm (d) corresponds to deuterated water.[83] No free vanillin is left inside ChiVan as confirmed by the disappearance of the aldehyde proton peak at 9.53 ppm (a). Peaks at 7.05 and 6.91 ppm (b and c, aromatic protons) and at 3.82 ppm (e, methoxy proton) as well as peaks in the range of 3-4 ppm (f, protons at the saccharide rings) indicate successful formation of a polymer, in which vanillin-derived guaiacyl groups are grafted onto a chitosan backbone. NMR spectroscopy further proves the successful reduction of imines as no signals at higher chemical shift than

the aromatic proton peaks, where imine protons in chitosan-vanillin imines would be expected, can be detected in ChiVan.

By comparing the integral of the aromatic proton peaks to the anomeric proton peak at 4.29 ppm, functionalisation of 62% of saccharide rings by guaiacyl groups is calculated which agrees well with previous literature.[79] The remaining 38% of saccharide rings do not contain grafted vanillin units but either acetamide functionalities (up to 15% according to the vendor of chitosan) or unreacted primary amines. Given that 62% of saccharide units are functionalized with vanillin derived guaiacyl groups in the final polymer, the concentration of free guaiacyl groups in the bioderived polymer is 2.46 mmol g^{-1}, which is significantly higher than in common lignins.[63]

4.1.2. Synthesis and characterisation of C/ChiVan

ChiVan is a non-conductive material and therefore a composite with carbon black has been prepared to enable charge transport. The method of electrode preparation can significantly alter the properties of an electrode. As a method of choice, the composite of carbon black and ChiVan (C/ChiVan(pre)) was grinded in a ball mill with propylene glycol and ethanol as a sustainable dispersion agent.[84] Details of the experimental procedures are summarised in the Experimental Part. No binder was used in the electrode preparation as ChiVan acts not only as an active material but also as a binder. This binder-like behaviour has been previously reported both for chitosan[85] and polyphenolic polymers,[86] leading to the conclusion that ChiVan indeed exhibits binder-like behaviour. Omission of the binder simplifies the cathode material and increases its sustainability as binders like the most commonly used polyvinylidene difluoride (PVDF) are avoided.

For analysis, the prepared ink was dispersed in a large excess of ethanol. After centrifugation, the solid was dried at 80 °C overnight and investigated without further modifications. This procedure was done in order to remove remnants of propylene glycol which is hard to completely remove in vacuum due to its high boiling point. Thermogravimetric analysis (TGA) investigations in Figure A2 confirm the formation of a C/ChiVan composite, as its thermogravimetric behaviour resembles a combination of ChiVan and carbon black. Furthermore, elemental analysis matches well with the predicted results (Table A1) as it assumes chemical formula $C_{12.75}H_{17.80}NO_{6.48}$, compared to predicted $C_{11.26}H_{16.26}NO_{5.39}$.

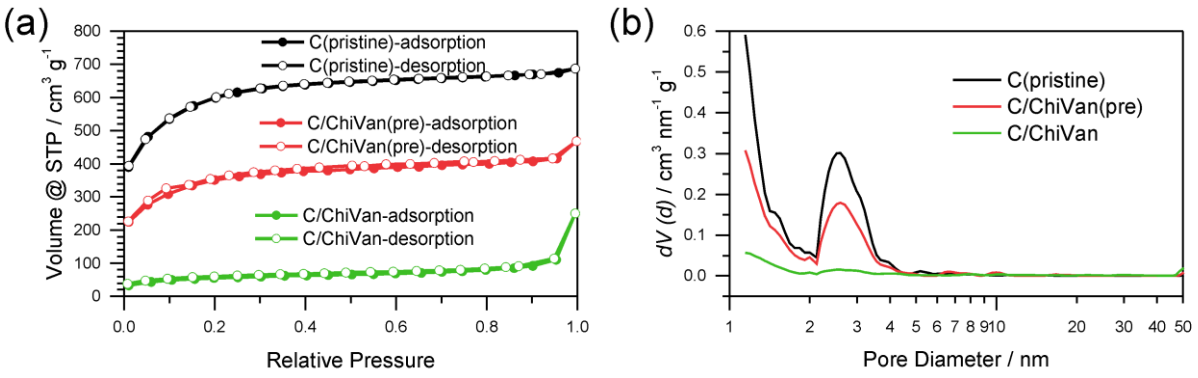

Figure 4.3. Nitrogen sorption measurement of C(pristine), C/ChiVan(pre), and C/ChiVan after grinding. (a) Isotherms and (b) pore size distribution.

Nitrogen sorption behaviour of carbon black and of the composite material before and after ball milling was studied (Figure 4.3). The apparent specific surface of pristine carbon black (2117 m^2 g^{-1}) drops after the introduction of ChiVan (1250 m^2 g^{-1}), most likely because of lower specific portion of porous material, and it drops even further after grinding (190 m^2 g^{-1}). Furthermore, carbon black is microporous with a significant amount of mesopores (diameter of 4 nm). After the introduction of ChiVan and even more significantly after ball milling, the apparent pore volume of micro- and mesopores decreases, while there are more macropores. Obviously, the surface area available for nitrogen adsorption decreases in the course of the process, which may be due to remaining solvent with a high boiling point in the pores, adhesion of ChiVan to the surface of the carbon black, gluing of the pores, or partly filling of the pores with ChiVan. The high pressure created by the impact with the ball during the grinding process may also influence the apparent surface area, for example by breaking the carbon black particles and increasing the surface area between individual small particles, which then increases external surface area. ChiVan binds different grains of carbon black, making them immobile.

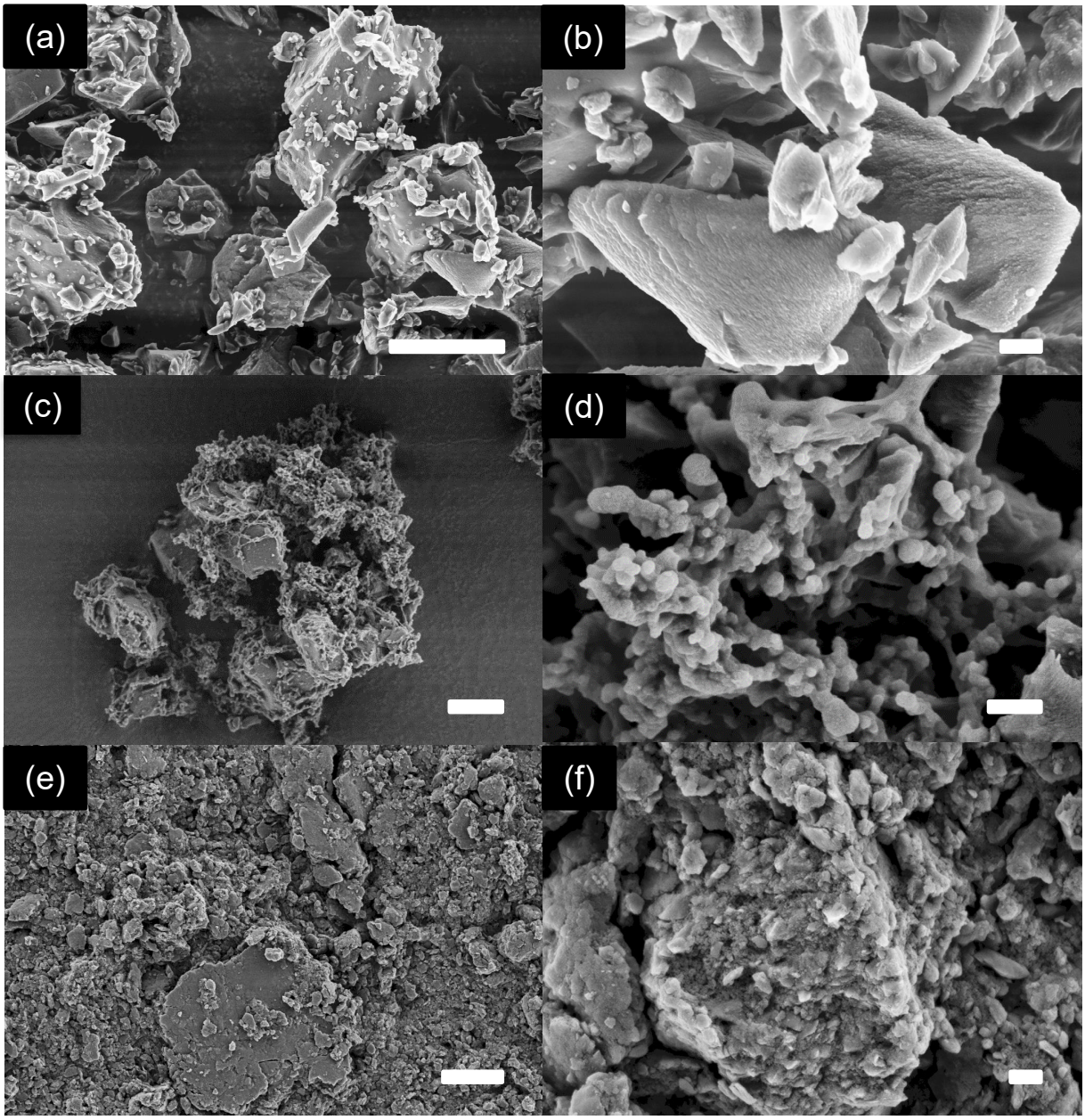

Figure 4.4. SEM images of carbon black (a,b) and C/ChiVan before (c,d) and after (e,f) grinding. The scale bars represent 6 µm (a, c, e) and 600 nm (b, d, f), respectively.

In order to gain more insight in the structure, the materials were investigated by means of scanning electron microscopy (SEM) (Figure 4.4) In all samples, carbon black particles can be observed in the range between few hundred to few thousands of nanometres, and energy dispersive X-ray spectroscopy (EDX) measurements detect only carbon, oxygen and small amounts of nitrogen (Figure A3). Upon addition of ChiVan, EDX measurements detect significant amounts of nitrogen that is concentrated to the regions of polymeric structure, a proof of ChiVan-CB composite formation. After ball milling, significantly smaller particles in the range of tens to hundreds of nanometres can be detected. No free polymer structures are

observable, which may confirm a good interaction of carbon black and ChiVan as indicated by nitrogen adsorption measurements. Furthermore, ball milling homogenises ChiVan, as can be seen by studying nitrogen and oxygen content using EDX, which are uniform through the sample and significantly higher than in the case of carbon black. ChiVan acting as binder is supposed to hold different carbon particles together. Such a tight composite should allow for an easy transport of electrons between the carbon black and ChiVan, making it a preferred material to be used in the batteries.

Ball milling using iron jars and balls may incorporate iron particles into the final material. Consequently, the iron contamination was investigated using inductively coupled plasma - mass spectrometry (ICP-MS). C/ChiVan has 0.040 (std. dev. 0.0002) mg g^{-1} of iron in it before grinding, while after grinding it has 1.54 (std. dev. 0.023) mg g^{-1}. These low levels of contamination are expected due to the softness of milled material,[87,88] however, they are assumed to be too low to have any significant influence on the electrochemical energy storage properties of the materials.

4.1.3. Electrochemical performance of C/ChiVan

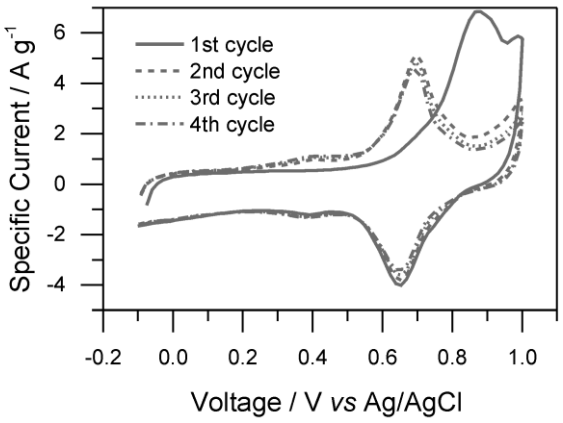

Figure 4.5. First four cycles of the cyclic voltammetry measurement of C/ChiVan. The CV was tested in 1 M $HClO_4$ aqueous solution (5 mV s^{-1}).

For investigating the electrochemical performance of the composite, the prepared ink was spread over graphite paper after ball milling. No washing with ethanol was performed as possible traces of remaining propylene glycol were not expected to negatively influence charge storage performance. It is important to note that ChiVan, just like lignin, undergoes electrochemical demethylation during the first oxidation step.[89] The demethylation is observable during the first cycle where during oxidation a peak appears at significantly higher voltage than during reversible oxidation reaction (Figure 4.5).

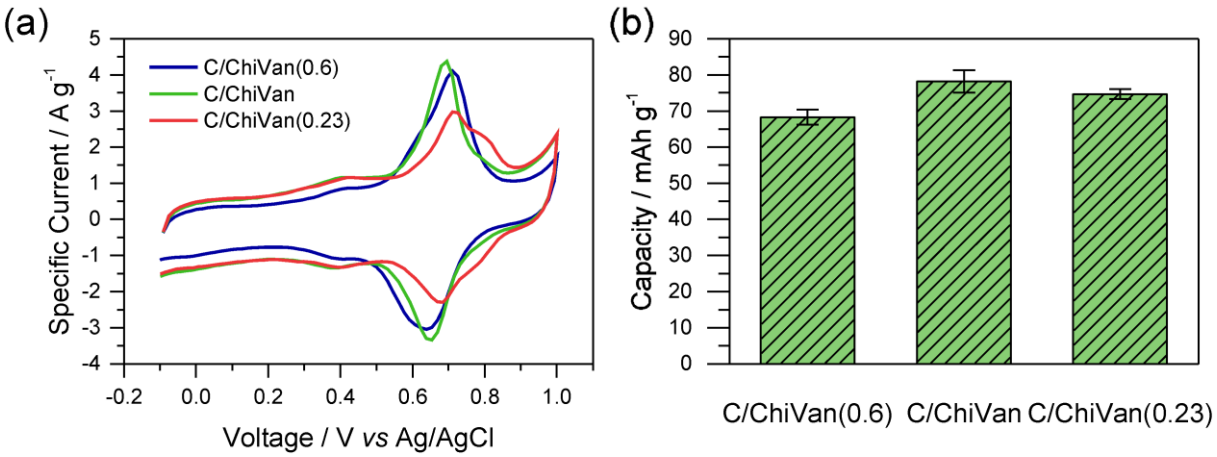

Figure 4.6. Cyclic voltammetry (a) and average capacities (b) as calculated from CV measurements for composites of carbon black and ChiVan prepared with different ratios of both constituents. All CVs were tested in 1 M $HClO_4$ aqueous solution (5 mV s^{-1}). The fifth cycle of the respective experiment is displayed.

Composites of ChiVan and carbon black with different ratios of the constituents (40%, 67% and 77% of carbon black) were used to determine the optimal ratio between ChiVan and carbon black. Figure 4.6 summarises cyclic voltammograms (fifth cycle) and capacity as calculated by integration of CV curves of different compositions. All three composites show a rectangular background, characteristic for porous carbons due to the formation of an electric double layer, and a pronounced pair of redox peaks between 0.6 and 0.7 V *vs* Ag/AgCl, characteristic for polymers that undergo reversible o-quinone to o-hydroquinone transformation. Specific currents and specific capacities in the figure and throughout this thesis all refer to the mass of total composite electrode material including carbon black and not to the mass of active material alone as the shape of CV curves indicates a significant contribution of carbon black to charge storage. The composite C/ChiVan (approximately 67% CB in the composite electrode) shows the highest specific capacity, visible in cyclic voltammetry both in terms of the highest redox couple peak and the highest rectangular background, meaning that it has the optimal ratio of ChiVan to carbon black. C/ChiVan(0.23) (approximately 77% CB in the composite electrode) has too much carbon black in it, so the redox couple constitutes a lower proportion of the total mass, resulting in a less pronounced redox peak in CV curves and a lower specific capacity (calculated respective to the total mass of electrode material). The relatively increased amount of carbon black does not lead to a more pronounced rectangular background in CV curves representing non-Faradaic charge storage, probably due to limited accessibility to the electrolyte. C/ChiVan(0.6) (approximately 40% CB in the composite electrode) in contrast has too much ChiVan in it, leading to insufficient electron transport. As a result of lower relative amount of carbon black, the rectangular background in CV curves is less pronounced, leading to lower capacity.

Therefore, all further mentioned composites were made using approximately 67% CB during synthesis (33% ChiVan or other polymer in the composite electrode). It should be emphasised that both constituents contribute to charge storage and all specific capacities are calculated referring to the total mass of the electrode, not to the mass of ChiVan.

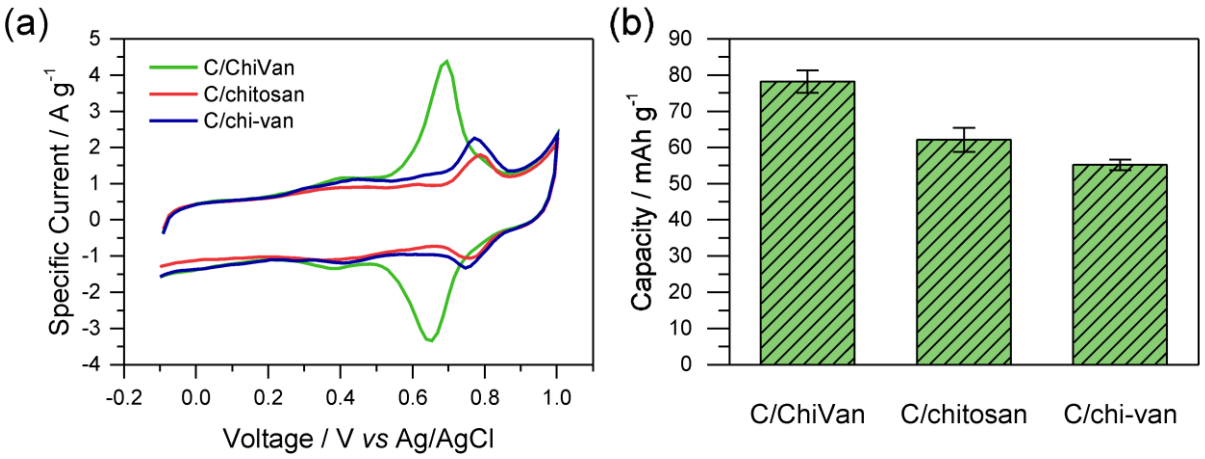

Figure 4.7. Cyclic voltammetry (a) and average capacities (b) as calculated from CV measurements for composites of carbon black with ChiVan, chitosan and nonreduced chitosan-vanillin adduct (chi-van). All CVs were tested in 1 M $HClO_4$ aqueous solution (5 mV s^{-1}). The fifth cycle of the respective experiment is displayed.

In order to asset the contribution of vanillin in ChiVan to charge storage and to investigate the necessity of imine reduction during synthesis, composites of the organic material and carbon black were prepared, however without the addition of vanillin (C/chitosan) or reduction step (C/chi-van) during synthesis, respectively (Figure 4.7). Composites without chitosan, which would be interesting to investigate the influence of the binding polymer backbone, could not be fabricated. When omitting addition of chitosan during synthesis, the resulting dispersion did not sediment during centrifugation, illustrating the necessity of chitosan due to its binding properties. In CV measurements of samples without vanillin, no redox couple between 0.6 and 0.7 V can be observed. This observation additionally proves that the redox pair in this range corresponds to the vanillin moiety in ChiVan. Samples which were synthesised without reducing the imine groups also do not show a redox couple in this region, probably due to the hydrolysis of imine bonds in the acidic electrolyte. These results demonstrate the versatility of the chitosan in ChiVan, on one hand as a binder of carbon black,[85] and on the other hand to prevent vanillin dissolution in the electrolyte.

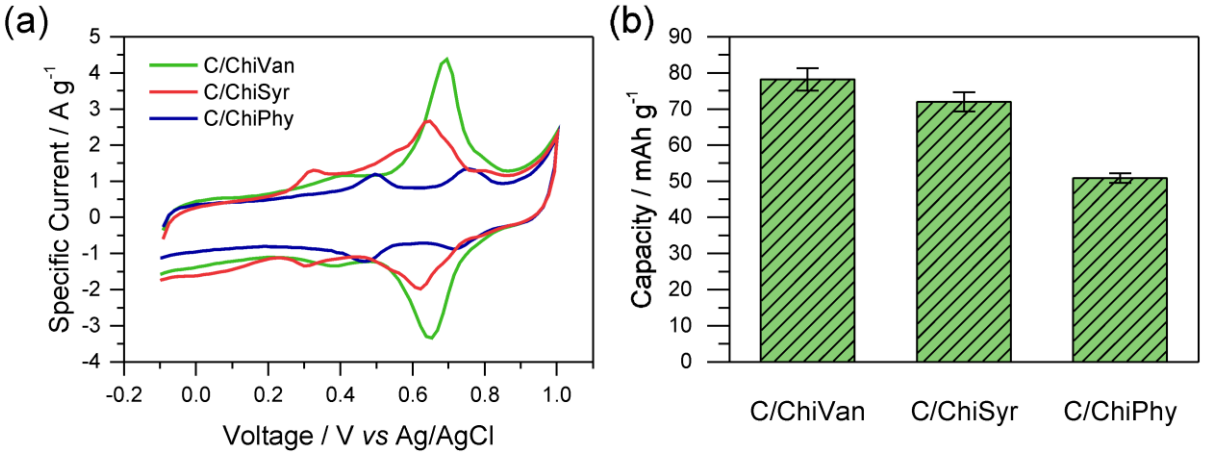

Figure 4.8. Cyclic voltammetry (a) and average capacities (b) as calculated from CV measurements for composites of carbon black with ChiVan, ChiSyr and ChiPhy. All CVs were tested in 1 M $HClO_4$ aqueous solution (5 mV s^{-1}). The fifth cycle of the respective experiment is displayed.

By using chitosan based polymers bearing redox functionalities of lignin instead lignin itself it is possible to investigate redox properties of different functional groups in lignin, simply by exchanging vanillin as the redox-active group to other aldehydes. In this regard, syringaldehyde (ChiSyr) and p-hydroxybenzaldehyde (ChiPhy) were studied (Figure 4.8.). C/ChiSyr shows similar CV curves to C/ChiVan however the orthoquinone redox couple is shifted to lower potential due to the electron donating effect of the additional methoxy group,[66] and the specific capacity is slightly lower. ChiPhy-CB shows no redox couple leading to lower specific capacity, as expected,[55] and the profile of the CV curve is similar to the one of C/chitosan.

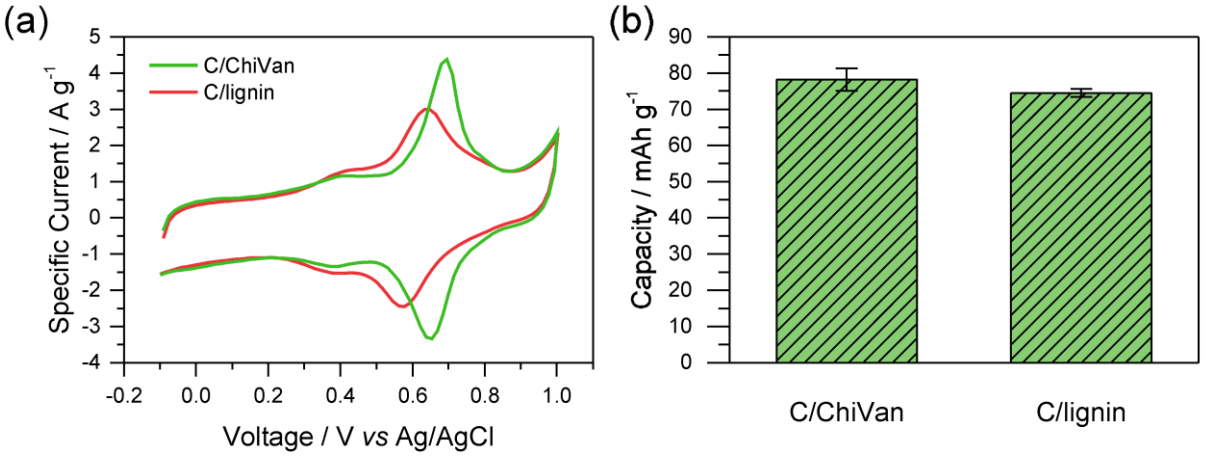

Figure 4.9. Cyclic voltammetry (a) and average capacities (b) as calculated from CV measurements for composites of carbon black with ChiVan and lignin. All CVs were tested in 1 M $HClO_4$ aqueous solution (5 mV s^{-1}). The fifth cycle of the respective experiment is displayed.

Additionally, the electrochemical performance of ChiVan was compared to the one of Kraft lignin (Figure 4.9) by generating a composite of Kraft lignin and carbon black with the equivalent procedure as for ChiVan and a similar carbon black-to-redox active polymer ratio.

Both CV profiles are similar, however with ChiVan's pair of redox peaks being shifted to a higher potential, in fact one of the highest reported for organic electrodes.[90] Also the redox peaks of ChiVan are more clearly defined compared to the ones of Kraft lignin as ChiVan has only one redox active unit (guaiacyl groups), while Kraft lignin has both guaiacyl and syringyl units. Furthermore, ChiVan has a significantly higher specific capacity. Interestingly, C/lignin shows main peak at the similar potential to C/ChiSyr, supporting the aforementioned observation of importance of syringyl groups in lignins used for charge storage.[63] Furthermore, guaiacyl rich lignins, unsuitable for energy storage devices[91] could be used for production of vanillin (and of chitosan-vanillin graft copolymers). One way to minimize the synthetic complexity and increase the sustainability of the electrodes would be to avoid the demanding separation steps of syringaldehyde from vanillin during vanillin synthesis and directly use a mixture of vanillin and syringaldehyde as obtained from lignin. The resulting capacity is expected to be similar to pure vanillin based electrodes.

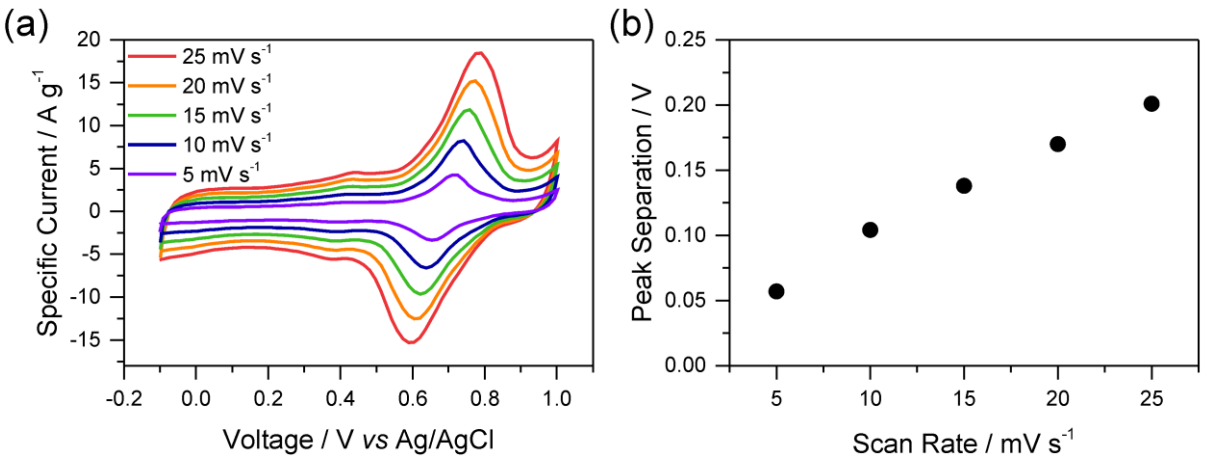

Figure 4.10. (a) Cyclic voltammetry of C/ChiVan at different scan rates. (b) Oxidation and reduction peak separation depending on the scan rate. The prepared electrodes were used as working electrodes, while platinum wire was used as a counter electrode, Ag/AgCl in saturated KCl was used as a reference electrode, and 1 M $HClO_4$ was used as electrolyte.

The reversibility of redox reactions was measured by measuring the peak separation of the two highest peaks in dependence of the scan rate (Figure 4.10). A linear dependence indicates a pseudoreversible redox reaction.[24]

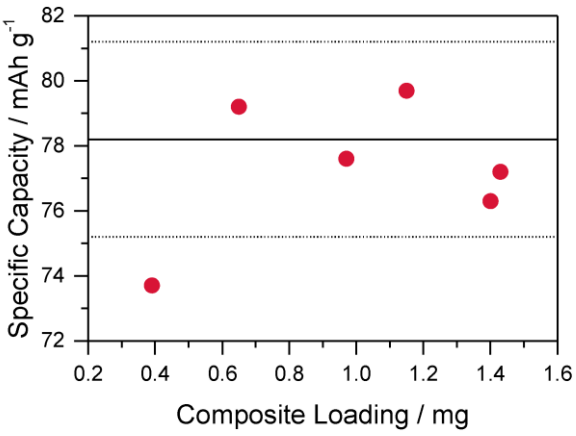

Figure 4.11. Capacity as calculated by integration of CV curves with different loadings on the working electrode. The full and dashed lines represent the average capacity and standard deviation of the capacity of C/ChiVan electrodes described above in Figure 4.6.

Additionally, the thickness-dependency of the capacity of C/ChiVan electrodes was investigated by adding different amounts of slurry (10-60 µL) to the current collector, resulting in different loading of the composite material (Figure 4.11). All the results, except the one with the lowest loading, fall in the limits of the standard deviation of the capacity of previous measurements with constant loading of 40 µL slurry. Electrodes featuring the lowest loading have significantly lower capacity probably due to the low amount of slurry that was put on the electrode (10 µL), not allowing to be spread well over the whole surface of the electrode. These results emphasise that in this case the mass loading does not significantly affect the capacity of the electrode, probably due to the porosity of the active material. Porosity allows the electrolyte to diffuse through the material, and therefore charge transfer can occur evenly throughout the electrode and not just on its outer surface.

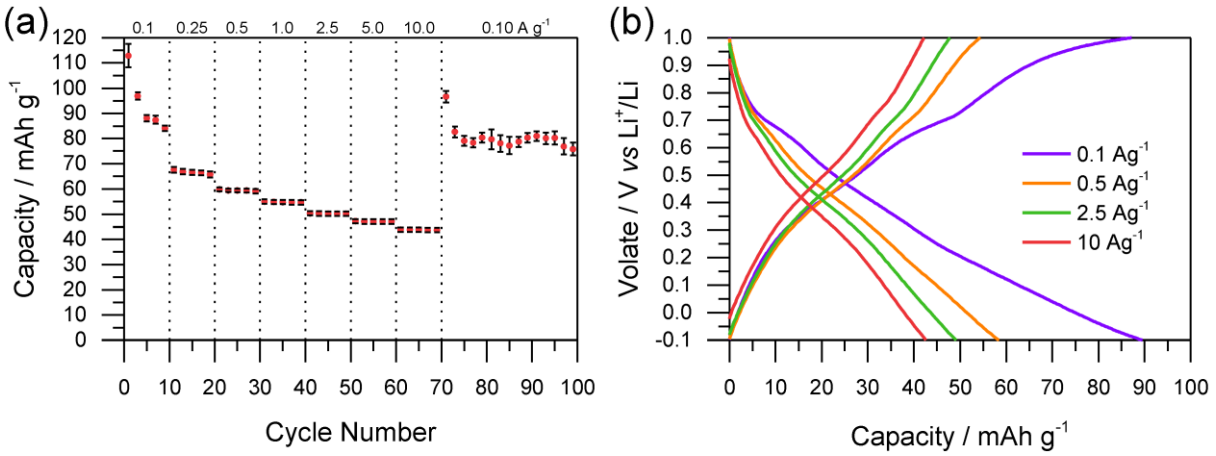

Figure 4.12. (a) Rate performance of C/ChiVan at different current densities (discharging capacity). Every second point is shown. (b) Galvanostatic charging-discharging curves at selected current densities. The prepared electrodes were used as working electrodes, while platinum wire was used as a counter electrode, Ag/AgCl in saturated KCl was used as a reference electrode, and 1 M $HClO_4$ was used as electrolyte.

The performance of the C/ChiVan electrodes was finally tested in galvanostatic charging-discharging measurements (Figure 4.12.). A nonlinear plot of potential as a function of capacity points to mixed battery-like charge storage along with capacitive charge storage, as expected for mixtures of an o-quinone containing polymer and high surface active carbon. Significantly pronounced capacity in the range of 0.6-0.8 V *vs* Ag/AgCl, corresponding to the reduction peak in CV measurements, is however only observable at slow discharging rate of 0.1 A g^{-1}. At higher discharging rate, the galvanostatic profile looks almost capacitor-like. The reason may be that charge transfer between quinone units and carbon black is kinetically hindered, possibly because of insufficient contact. Indeed, as visible in Figure 4.12a, capacity of C/ChiVan electrodes at high discharging rate is almost independent on the current density, indicating a surface confined charge storage behaviour.

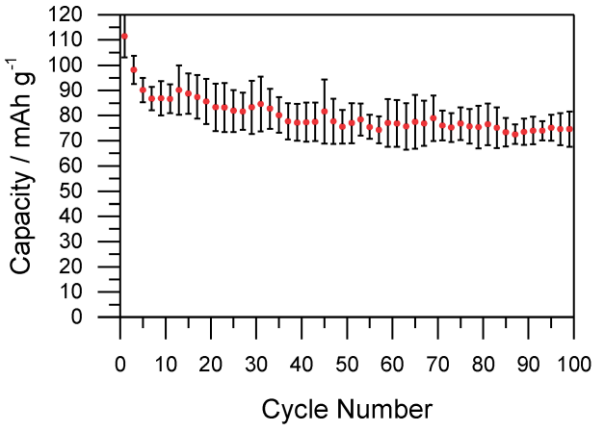

Figure 4.13. Rate performance for 100 cycles at a current density of 0.1 A g^{-1}. Every second point is shown. The prepared electrodes were used as working electrodes, while platinum wire was used as a counter electrode, Ag/AgCl in saturated KCl was used as a reference electrode, and 1 M $HClO_4$ was used as electrolyte.

Figure 4.13 further show that capacity of the electrode falls rapidly in the first few cycles but then is constant for 100 charging-discharging cycles, a phenomenon probably not connected with the low current density (0.1 A g^{-1}), but rather due to some irreversible reactions in the first cycles. Such reactions may include crosslinking reactions between oxidised vanillin units and partly decomposition of the chitosan backbone in the strongly acidic electrolyte.

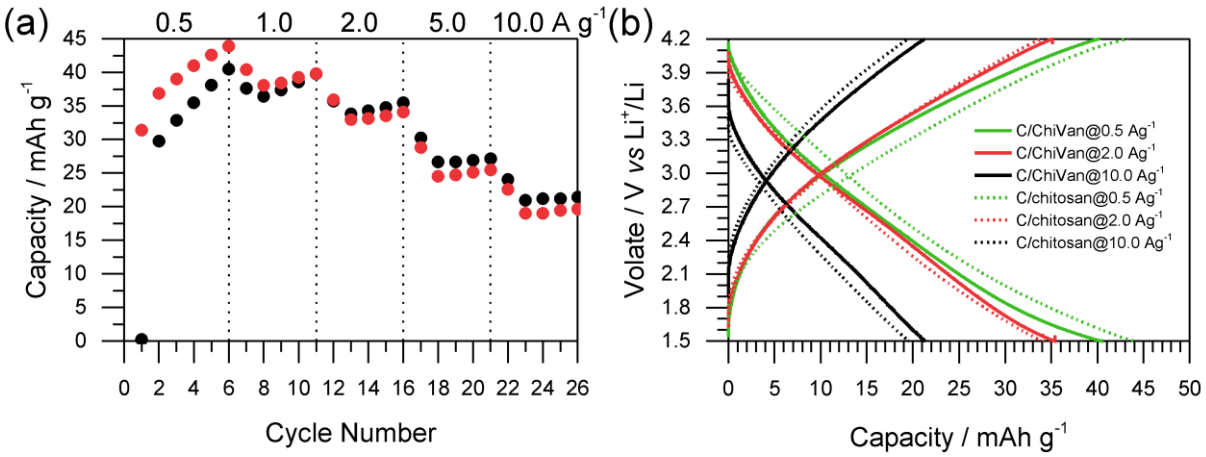

Figure 4.14. (a) Rate performance of C/ChiVan and C/chitosan at different current densities (discharging capacity). (b) Galvanostatic charging-discharging curves at selected current densities. The prepared electrodes were used as working electrodes, while lithium foil was used as a counter electrode, , and 1 M $LiPF_6$ in EC/DEC was used as electrolyte.

Lastly, C/ChiVan has been tested as a potential cathode material in lithium organic system, with 1 M $LiPF_6$ in EC/DEC as electrolyte and lithium foil as a counter electrode. It is important to note that these samples were prepared from pure polymers dispersed in the solvents rather than dissolved in the acidic solutions. However, there is no significant improvement of C/ChiVan compared to C/chitosan. Therefore, it can be concluded that, alike lignin, ChiVan is not suitable for formation of cathodes in lithium organic electrolytes.

4.1.4 Conclusion

To summarise, organic electrode materials based on low value biomass were successfully synthesised using only sustainable chemicals. The active polymer material was chitosan-derived, which is available from crab shell waste, with grafted vanillin units, deriving from lignin and as such from a low-value side product of paper industry. The polymer was characterised and composited with carbon black to form a tight composite. Nitrogen sorption measurements and electron microscopy indicate small structure sizes with the redox active biobased polymer and carbon black particles bound together. No other synthetic additives or fluorinated binders were used, significantly increasing the sustainability of such electrodes. The electrodes showed a combination of Faradaic and non-Faradaic charge storage in the range of up to 80 mAh g^{-1} (referring to the total electrode mass), resulting from the quinone-hydroquinone redox couple in the biobased polymer and carbon black, respectively. Being free of any synthetic polymer, metal, or halogenated binder, these electrodes are not only more sustainable than other electrodes but they show also one of the highest capacities of biobased polymer electrodes reported so far. However, their incorporation in a LIB setup and use in combination with lithium containing electrolytes was not successful.

4.2. Vanillin based network as a cathode material for lithium-organic energy storage materials

A novel vanillin derived electrode material for lithium-ion based energy storage systems is presented. In the presented approach, vanillin is first modified in two sustainable steps to afford bisvanillonitrile (BVN). The slurry for the electrodes is made from BVN and carbon black and is subsequently treated in the atmosphere of triflic acid in order to polymerise BVN. Used as cathode material in a lithium ion based energy storage device, the resulting material shows capacities up to 90 mAh g^{-1}. This extraordinary performance can be attributed to a combination of non-faradaic and faradaic charge storage, involving quinone units which are abundantly found in the polymer backbone. Therefore, omittance of aliphatic hydroxyl group allowed for a successful design of lithium ion based energy storage device. In contrast to conventional organic electrode materials, excellent contact to carbon as conductive additive is established by performing the polymerisation in a mixture with carbon (*in carbone*), allowing the omittance of additional unsustainable binder materials. Due to the sustainable synthesis and good performance, such sustainable electrodes may be applied in future energy storage devices.

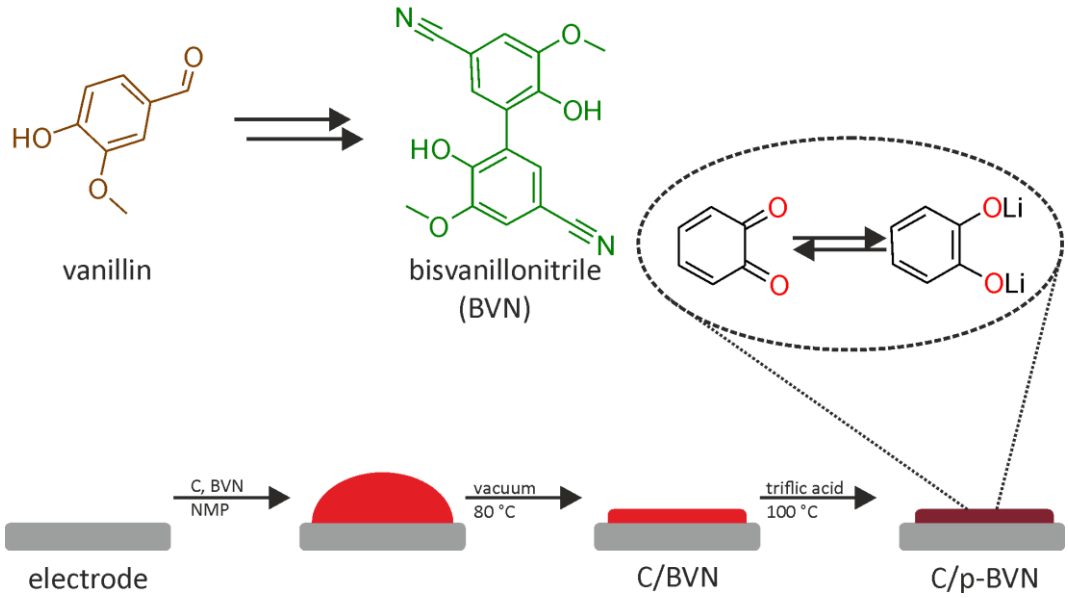

Figure 4.15. Polymerised bisvanillonitrile can be used as a cathode material in devices for storage of electrical energy bassed on lithium

Karen Leus helped with the design of the material (p-BVN). Johannes Schmidt performed the XPS measurement and helped with the interpretation of the obtained spectra. Jinyeon Hwang

helped with the design and performance of electrochemical experiments. Maria Maranska and Siegried Eigler performed and interpreted solid state NMR.

4.2.1. Synthesis and characterisation of BVN

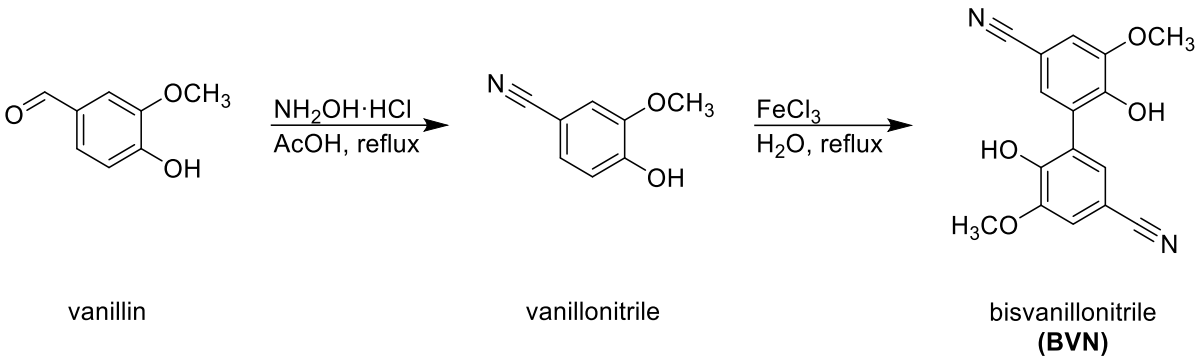

vanillin — vanillonitrile — bisvanillonitrile **(BVN)**

Scheme 4.4. Synthesis of BVN from vanillin

Bisvanillonitrile (BVN) was obtained from vanillin in two steps using rather sustainable reaction conditions and media (Scheme 4.4).

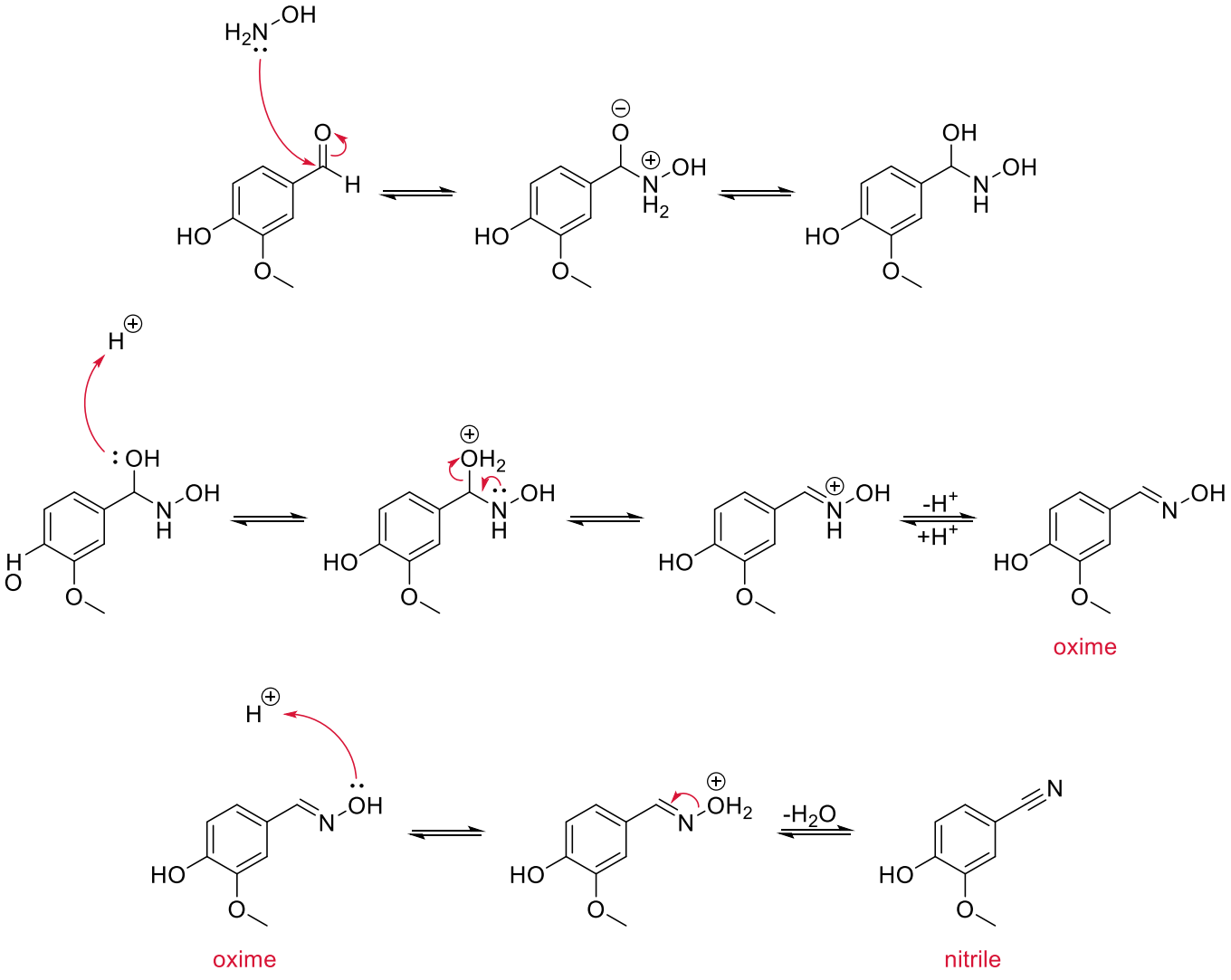

Scheme 4.5. Proposed mechanism of nitrile formation.

The first step, which concerns the substitution of the aldehyde with a nitrile group, was performed according to the previously reported procedure by Thompson et al.[92] Firstly, analogous to aforementioned imine formation from aldehyde and primary amine, hydroxylamine performs a nucleophilic attack on the carbonyl group of vanillin forming an intermediate. Upon catalytic protonation, this intermediate can undergo dehydration forming another intermediate, oxime.[80] Although the oximes are rather stable, they can undergo second dehydration under acidic condition and high temperature forming nitriles (Scheme 4.5). This reaction is analogous to imine formation (Scheme 4.2).

In the second step, the dimerisation of vanillonitrile, an oxidative coupling reaction mediated by iron(III) chloride, was used.[93,94] This reaction belongs to a class of Scholl reactions, reactions of two or more arenes promoted by Lewis acids, in this case iron(III) chloride or protons. The reaction mechanism is still under debate but the formation of radicals upon reduction of iron(III) to iron(II) was suggested.[95]

As iron cations may be strongly chelated by BVN, the product was extensively purified using soxhlet extraction with water, leaving a negligible iron contamination in the sample, 5.19 mg g^{-1} as determined from inductively coupled plasma - mass spectrometry (ICP-MS). The structure was confirmed by ^{1}H (Figure A5) and ^{13}C NMR (Figure A6) as well as MS (Figure A7).

4.2.2. Synthesis and characterisation of p-BVN

Trimerisation of aromatic polynitriles to create a network has been previously reported by Thomas et al. forming crystalline microporous polymers, named covalent triazine frameworks (CTFs) under high temperatures with zinc chloride as catalyst.[96] CTFs and related amorphous materials have been reported for many applications such as dye sorption,[97] catalyst support,[98] gas storage,[99] and electro-devices exhibiting a high versatility.[100–109] Later on, the low-temperature triflic acid-catalysed polymerisation of aromatic nitriles was used to obtain amorphous microporous polymers[110,111] and to prepare hard templated porous structures.[112] Besides, also nonporous structures are available which showed remarkable properties for applications such as photocatalysis.[113] BVN was polymerised *via* an acid vapour-assisted solid phase synthesis.[112] The resulting polymer was characterised by means of FT-IR, ss-NMR and XPS.

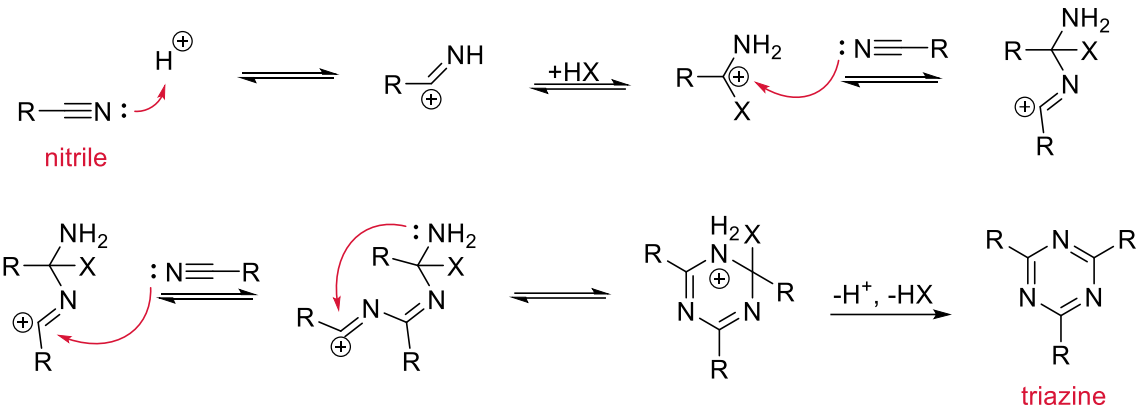

Scheme 4.6. Simplified mechanism or nitrile trimerisation with strong protic acid catalyst.

Trimerisation mechanism of nitriles catalysed with triflic acid is rather complicated. However, here a simplified mechanism as proposed by Komori et al. for trimerisation of nitriles in the presence of PCl_5-HCl catalyst is described (Scheme 4.6). First, nitrogen atom of nitrile gets protonated twice forming a salt. In the subsequent step, another nitrile performs a nucleophilic attack on the carbon atom of the formed salt. After another nucleophilic attack of imine an intermediate consisting of three nitriles is formed. Nucleophilic attack of terminal amine on the carbon bearing positive charge causes ring formation. The triazine is formed after subsequent double deprotonation.[114]

When comparing the FT-IR spectra of BVN and p-BVN (Figure 4.16a), the vibration at 3295 cm^{-1}, which corresponds to the hydroxyl vibrations, reduces in intensity and broadens after polymerisation. Furthermore a sharp band at 2230 cm^{-1}, which can be assigned to the nitrile groups, is present in BVN but disappears during the reaction. As suggested in the literature,[112] this observation points to the important role of nitrile groups in the polymerisation of BVN. A sharp band at 1640 cm^{-1} which appears in the spectrum after the polymerisation points to the formation of carbonyl groups, either in the form of amide groups upon hydrolysis of nitrile groups or as part of oxidised hydroxyl groups. Furthermore, a sharp vibration at 1270 cm^{-1} which almost completely disappears after polymerisation can be ascribed to methoxy groups and confirms demethoxylation upon polymerisation.[33, 39]

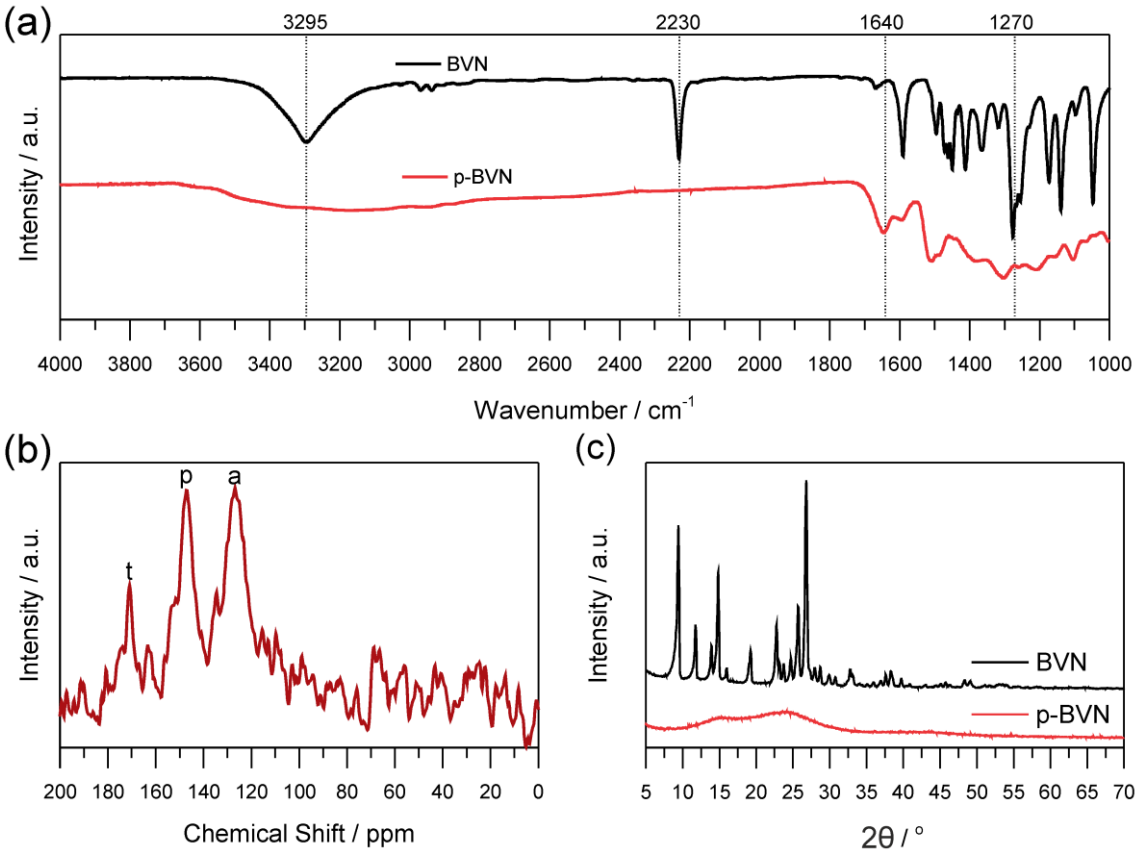

Figure 4.16. (a) FT-IR spectra of BVN and p-BVN. (b) Solid state ^{13}C NMR spectrum of p-BVN. (c) Powder XRD diffractogram of BVN and p-BVN.

The ^{13}C ss-NMR spectrum (Figure 4.16b) shows 3 signals in the range of 128, 147, and 170 ppm that can be assigned to aromatic carbons (a), the catechol unit (p) and triazine carbons (t), respectively. In contrast to the (starting) reference material BVN, no peak around 56 ppm can be identified indicating cleavage of the methyl group in the methoxy unit. Appearance of triazine carbons and cleavage of methoxy groups strongly supports the successful polymerisation.

Powder XRD was performed to compare BVN and p-BVN (Figure 4.16c). Sharp reflections of BVN indicate highly crystalline material, as is usually observed for small-molecules. On the contrary, p-BVN shows very low crystallinity with two broad reflexes centered around 15° and 24°. According to Bragg's law:

$$d = \frac{n\lambda}{2\sin\theta}$$

Assuming that n =1 and knowing that Cu-Kα (λ = 0.154 nm) X-ray source was used one can easily calculate that reflexes at 15° and 24° correspond to interatomic distances of 0.6 nm and 0.37 nm respectively. Later distance is similar to interlayer distance of graphite and can be ascribed to interlayer distance between the sheets of p-BVN.

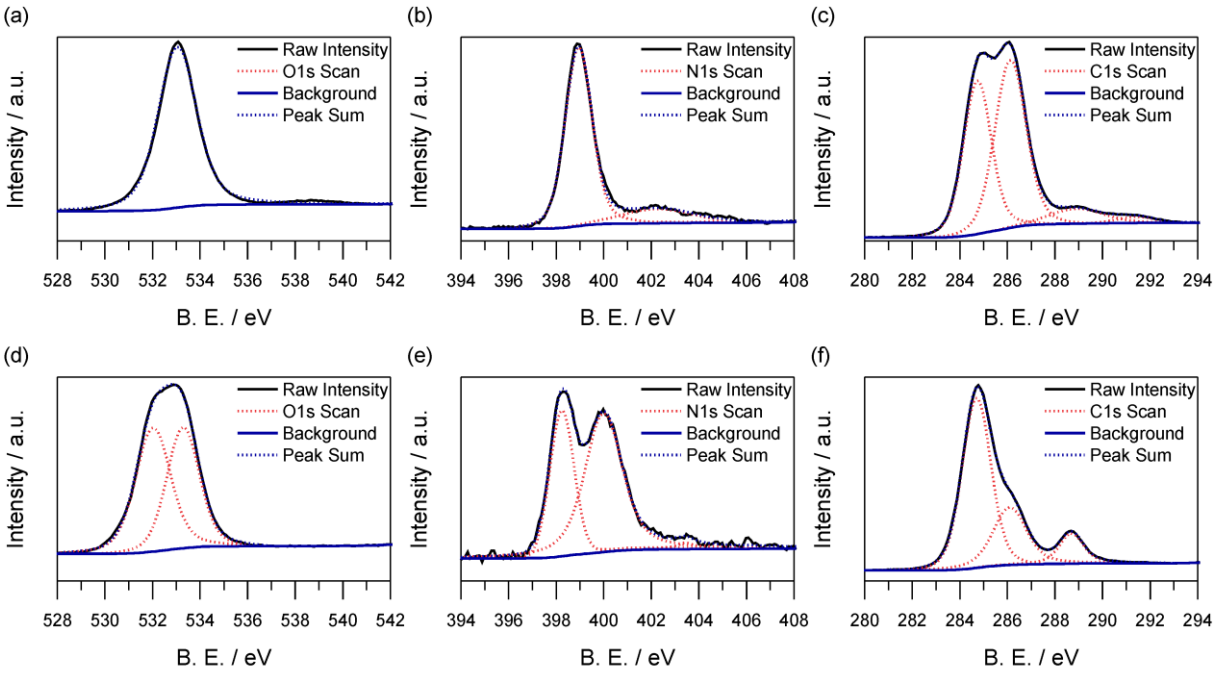

Figure 4.17. XPS spectra of BVN (a, b, and c) and p-BVN (d, e, and f). (a and d) O1s, (b and e) N1s, and (c and f) C1s.

In order to further investigate the polymerisation mechanism, XPS of the individual compounds was performed. In the energy range corresponding to oxygen 1s orbitals (Figure 4.17a), BVN has one observable peak at 533.04 eV which can be ascribed to oxygen that is bound to carbon via a single bond. After polymerisation, two peaks with similar area appear, one at 533.28 eV that can be ascribed to the aforementioned oxygen species and a second at 532.02 eV that can be ascribed to oxygen being part of a carbon-oxygen double bond, suggesting partial oxidation of the sample during polymerisation. As discussed above, such bonds can be formed either as amide groups or as quinones. The samples were not treated with any carbonyl containing solvent which might falsify the carbonyl signal at 532 eV.

In the energy range corresponding to nitrogen 1s orbitals (Figure 4.17b), BVN has two observable peaks. The most dominant one, at 398.94 eV, is characteristic for nitrogen in nitrile groups. A lower second peak at 402.24 eV is a satellite peak observable in molecules that have conjugated electron donors (hydroxyl and methoxyl groups) and acceptors (nitrile group). While this low intensity peak is still present after polymerisation, the main peak is completely transformed into two new peaks of similar size. The peaks at 398.24 eV and 399.99 eV can be ascribed to nitrogen in triazine and amide groups, respectively. These groups have been previously reported upon treatment of nitriles with triflic acid.[115] However, as no significant amide peak was observed in ss-NMR it can be concluded that amide formation is mainly a surface phenomenon.

In the energy range corresponding to carbon 1s orbitals (Figure 4.17c), BVN shows two dominant peaks and two peaks of low intensity. The dominant peaks at 284.74 eV and at 286.13 eV can be ascribed to carbon bound to other carbon atoms and oxygen/nitrogen heteroatoms, respectively. Two weak peaks at 288.92 eV and 291.4 eV indicate oxidised carbon and π-π interactions respectively. After polymerisation, the ratio of the first two peaks changes, so that the peak at 284.7 eV is significantly more intense than the peak at 286.1 eV. This effect may indicate demethylation of the methoxy groups present in BVN during the course of oxidation upon treatment with triflic acid, i.e., loss of heteroatom-bound carbon. The peak representing the oxidised carbon indeed gets significantly more intense during the polymerisation process, supporting the assumption of quinone formation in some of the aromatic groups as was discussed above. It is important to note though that the intensity of the carbon peaks in XPS analysis is often falsified by omnipresent carbon impurities.

Finally, elemental analysis additionally confirms the demethylation of the methoxy functionalities upon acid vapour-assisted solid phase synthesis as the carbon content significantly decreases when comparing BVN and p-BVN, as well as partial hydrolysis of nitrile groups as the oxygen content increases when comparing BVN and p-BVN (Table A2).

4.2.3. Synthesis and characterisation of CB/p-BVN

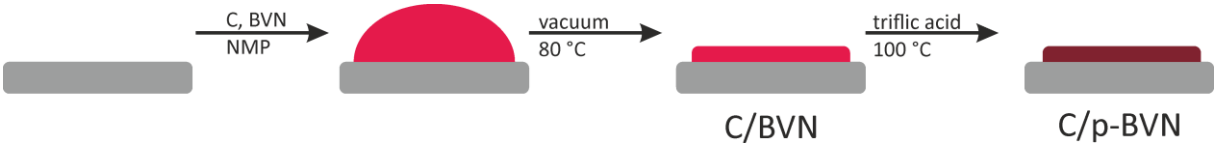

Scheme 4.7. *In carbone* polymersisation of BVN in the presence of carbon black. The grey rectangle represents the carbon paper, which is used as current collector in the experiments.

In order to increase the conductivity of the p-BVN, a hybrid material with conductive carbon black was prepared. For establishing a good contact between the active material and carbon, first a slurry of carbon and BVN was made and subsequently casted on the current collector, dried in vacuum, and the BVN was polymerised in the presence of carbon black (*in carbone*) in the same way as described above. The products after drying and after triflic acid treatment are denoted as C/BVN and C/p-BVN, respectively. This sequence of production steps makes later grinding of the hybrid material and blending with binders unnecessary. Scheme 4.7 shows the process.

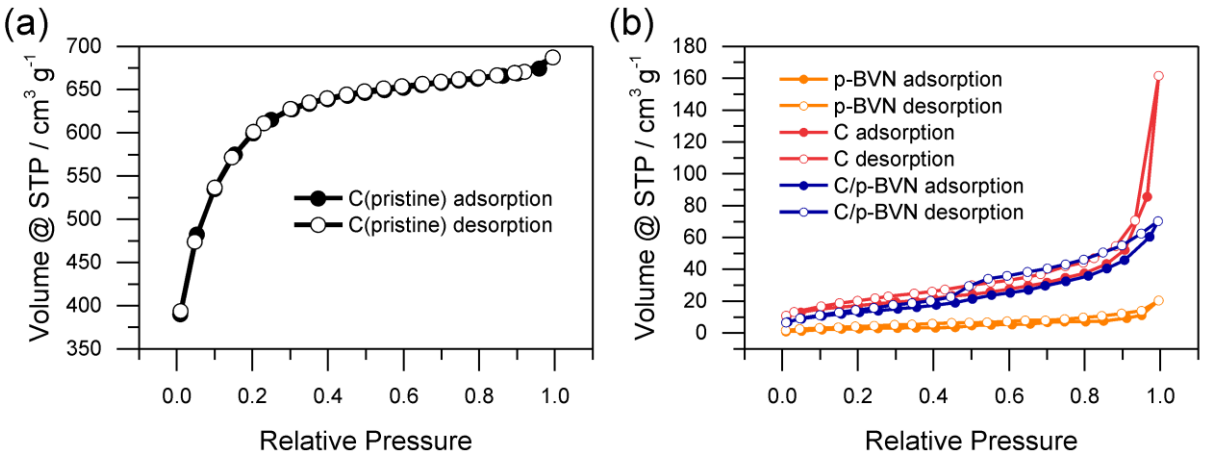

Figure 4.18. Nitrogen sorption isotherms of (a) C(pristine) and (b) p-BVN (orange), C (red) and C/p-BVN (blue).

Pristine carbon black has high surface area with both micropores and mesopores as discussed in previous chapter (Figure 4.18a) However, it gets significantly reduced after grinding (C), exhibiting BET surface area of 61.2 $m^2 g^{-1}$ (Figure 4.18b) probably due to the presence of NMP during the grinding process, which blocks the majority of the micropores during the nitrogen sorption measurements due to its high boiling point. The isotherm indicates the presence of a small amount of micropores and a high external surface area. The BET surface area significantly drops during the C/p-BVN fabrication (46.7 $m^2 g^{-1}$) due to the incorporation of non-porous p-BVN. The incorporation of the polymer not only results in additional blocking of some micropores but especially holds carbon black particles together, reducing the external surface area. Nevertheless, the isotherm has a similar shape as C and indicates both micropores and a significant contribution of the external surface area to nitrogen sorption.

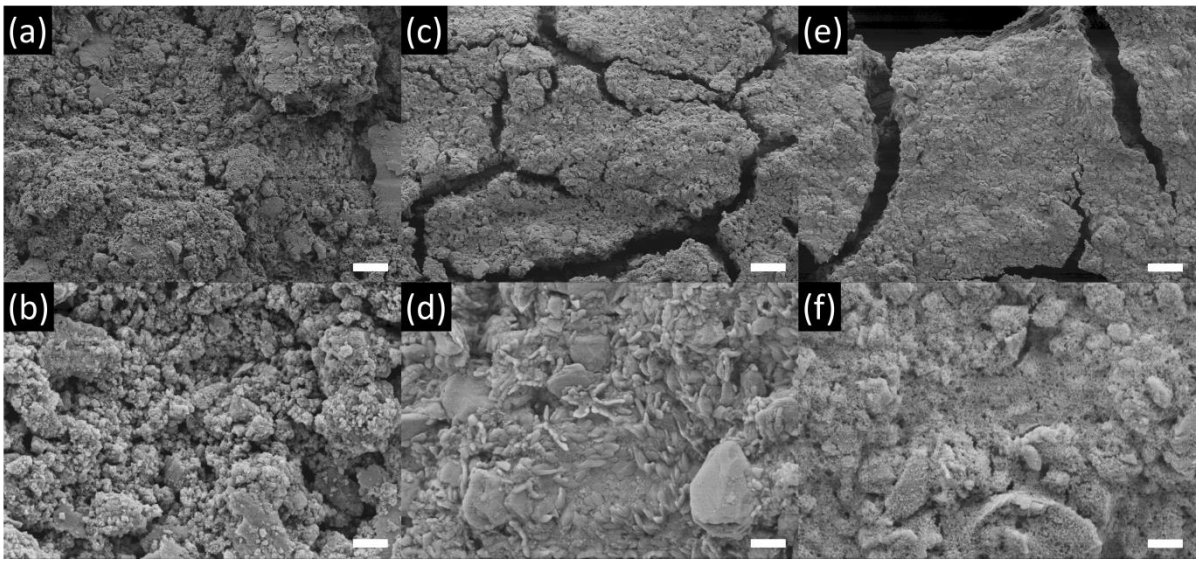

Figure 4.19. SEM images of C (a and b), C/BVN (c and d), and C/p-BVN (e and f). The scale bars represent 10 µm (a, c, and e) and 1 µm (b, d, and f), respectively.

SEM analysis provides further insights into the structure formation. As can be seen from Figure 4.19, C (grinded without the addition of any binder material) shows a grainy structure characteristic for carbon black. Upon the addition of BVN, rod/platelet-like particles appear between the grains, which can be identified as particles of BVN. Upon polymerisation, these structures disappear, and instead the grainy carbon black is covered with a web-like structure that can be ascribed to p-BVN, indicating good contact between C and p-BVN.

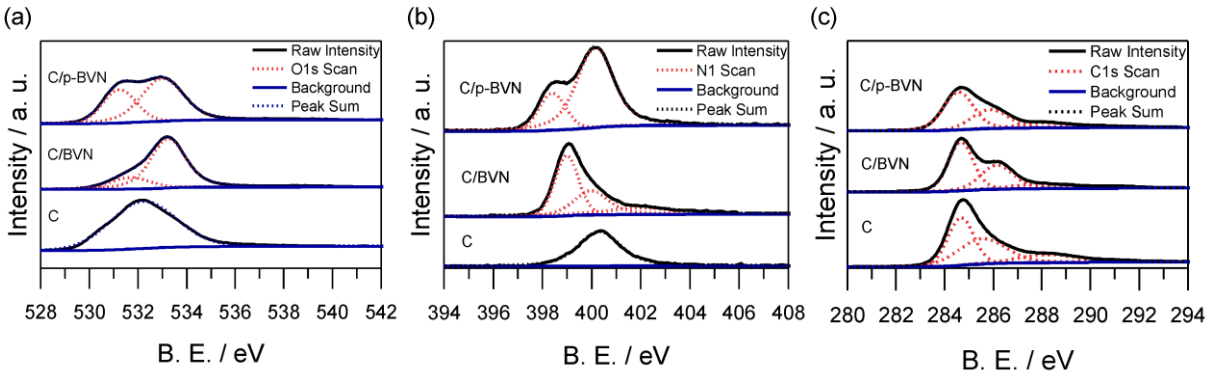

Figure 4.20. XPS spectra of C, C/BVN and C/p-BVN. (a) O1s, (b) N1s, and (c) C1s

XPS measurements of the hybrid materials confirm the formation of the same structures as discussed in the pristine organic material (Figure 4.20). The oxygen 1s peak at 532.22 eV in the sample of carbon black corresponds to oxygen on the carbon surface introduced as a consequence of ball milling.[116] In the C/BVN and C/p-BVN materials, this peak is also observed but overlaps with the above described peaks of BVN and p-BVN. A significantly increased intensity of the carbonyl oxygen peak of C/p-BVN in comparison to C/BVN supports the formation of quinones and amides in some of the aromatic and nitrile groups,

respectively, during acid vapour-assisted solid phase synthesis. Nitrogen on the carbon surface introduced from NMP during ball milling is observed in the energy range corresponding to the nitrogen 1s orbital at 400.32 eV. Also here, the observed peaks are in correspondence to the samples without carbon black. Carbon black finally shows three dominant peaks at 284.67 eV, 285.55 eV, and 288.22 eV in the energy range corresponding to the carbon 1s orbital, which also dominate the carbon 1s spectra of C/BVN and C/p-BVN, overlapping with the above indicated peaks of BVN and p-BVN.

Furthermore, thermogravimetric analysis was carried out (Figure A8). It was observed that upon grinding, the thermal stability of carbon black is reduced, which can be ascribed to the high oxygen content in C (Table A2) that is a consequence of the modification of carbon upon ball milling. The TGA curve of C/p-BVN can be seen as a combination of C and p-BVN and does not show a significant weight loss in the range of 400 °C (decomposition temperature of BVN). This observation confirms the polymerisation of BVN in the presence of carbon black and the formation of a hybrid material of C and p-BVN.

4.2.4. Energy storage of C/p-BVN

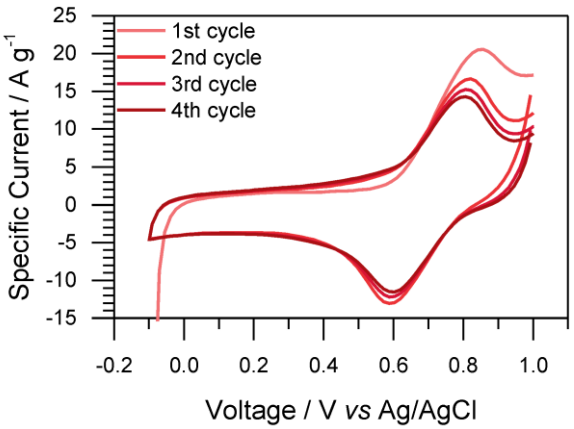

Figure 4.21. First four cyclic voltammograms of C/p-BVN. The CV was tested in 1 M $HClO_4$ aqueous solution (25 mV s^{-1}).

Firstly, performance of C/p-BVN has been investigated in aqueous electrolyte. First 4 cycles of cyclic voltammetry have been compared (Figure 4.21), and insignificant difference between them has been observed contrary to lignin or ChiVan (Figure 4.5). This further confirms hypothesised demethylation of BVN during network formation. Additionally, clear oxidation and reduction peaks occur at similar voltages as in C/ChiVan suggesting the same redox reaction for these two systems.

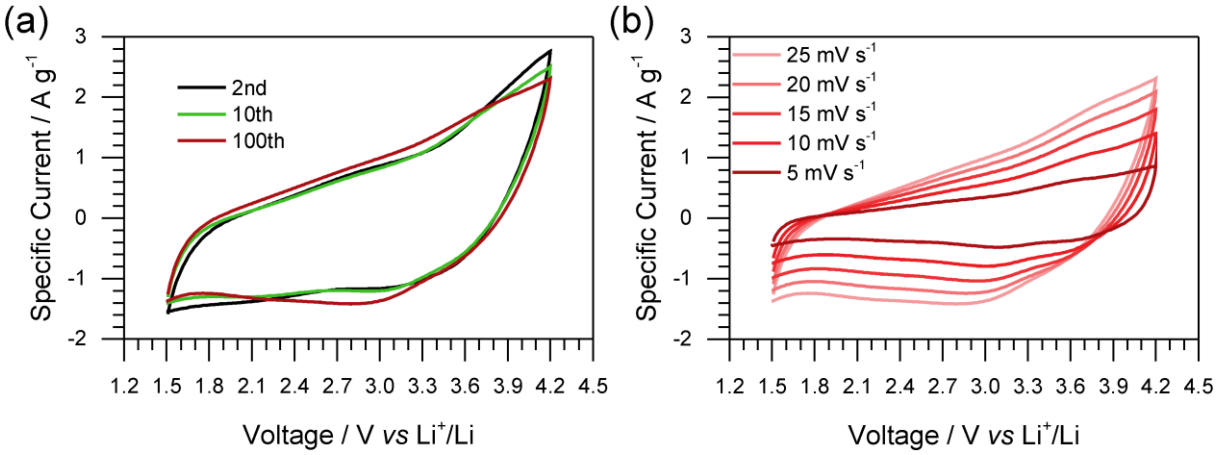

Figure 4.22. Cyclic voltammetry of C/p-BVN in a lithium half-cell setup with lithium counter electrode and 1 M $LiPF_6$ in EC/DEC (1/1) as electrolyte. (a) Different cycles at 25 mV s^{-1} and (b) different sweep rates.

Furthermore, C/p-BVN was investigated in lithium organic system, namely using 1 M $LiPF_6$ in ED/DEC (1/1) as an electrolyte and lithium foil as counter/reference electrode. The cyclic voltammetry of CB@p-BVN initially shows very weak peaks (Figure 4.22a). However, with prolonged cycling an oxidation peak around 3.7 V and a reduction peak around 2.8 V become visible. The increasing intensity of the redox couple peak and high overpotential can be explained by the necessary migration of Li^+ cations and bulky PF_6^- anions inside the electrode resulting in a rearrangement of the C/p-BVN composite. Furthermore, before p-BVN can contribute to the capacity by reversible redox reactions, its o-hydroquinone moieties (and possible quinone moieties formed upon polymerisation as described above) have to be lithiated. Cycling CB@p-BVN at different sweep rates suggests semireversible behaviour (Figure 4.22b).

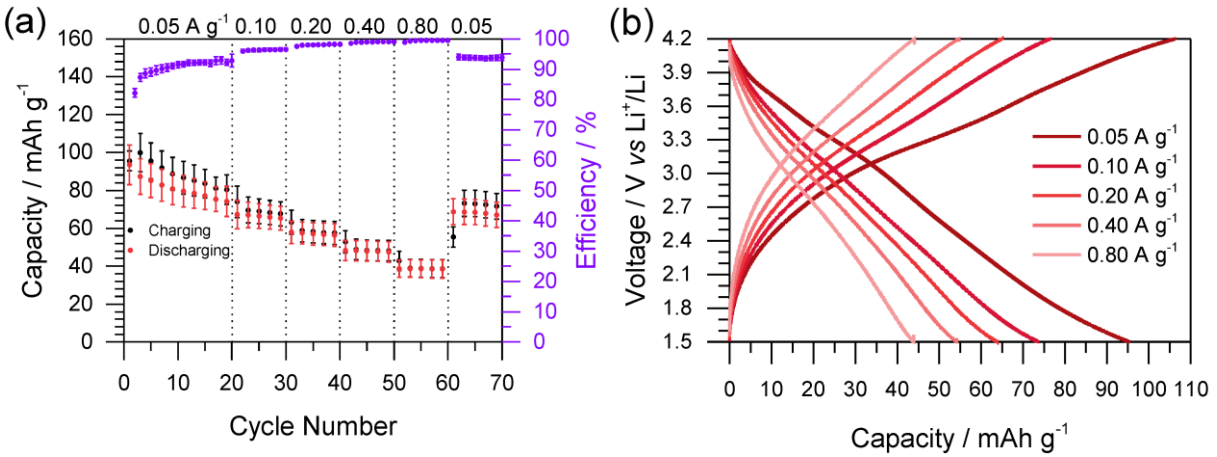

Figure 4.23. Electrochemical performance of CB@p-BVN in a lithium-ion half-cell setup. (a) Discharging capacities as calculated from charging-discharging tests at different current densities. Every second data point is omitted for clarity. (b) Charging-discharging tests at selected current densities.

Charging and discharging of C/p-BVN (Figure 4.23) at different current densities shows belly shaped galvanostatic discharging curves, characteristic for devices that store charge in a combination of battery-like and capacitor-like reactions.[6] The slope of the discharging curves is the lowest around 3 V, which corresponds well to the discharging peak in cyclic voltammograms. Figure 4.23a shows the rate capability of the C/p-BVN electrodes, calculated from the charging and discharging curves at different current densities. The initial discharging capacity of 85.2 mAh g^{-1} at a moderate current density of 0.05 A g^{-1} decreases to 66.4 mAh g^{-1}, 57.1 mAh g^{-1}, 47.8 mAh g^{-1}, and 38.5 mAh g^{-1} at current densities of 0.1 A g^{-1}, 0.2 A g^{-1}, 0.4 A g^{-1}, and 0.8 A g^{-1}, respectively, and retains 80% of the initial capacity (68.5 A g^{-1}) once the current density is restored to 0.05 A g^{-1} (capacities represent the 5th cycle at the respective current density). The decrease in the discharging capacity at 0.05 A g^{-1} within 60 cycles, some of them at higher current density, can be ascribed to the instability of the electrodes, e.g., by over-oxidation, as in general organic materials show a relatively low stability during electrochemical cycling as compared to inorganic electrodes.

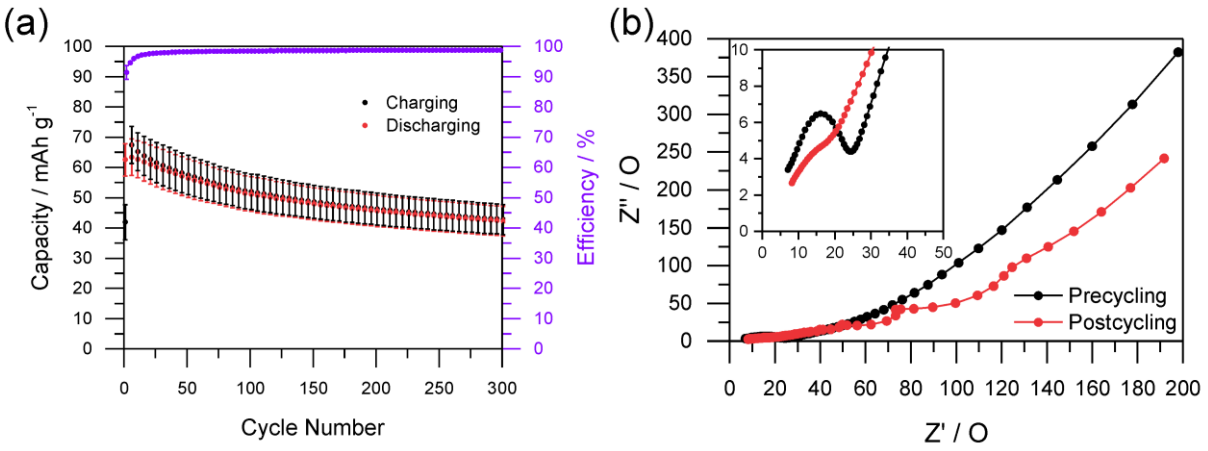

Figure 4.24. Electrochemical performance of C/p-BVN in a lithium half-cell setup with lithium as counter electrode and 1 M $LiPF_6$ in EC/DEC (1/1) as electrolyte. (a) Capacity of CB@p-BVN at 0.2 A g^{-1} as calculated from charging-discharging tests. Every fifth data point is displayed for clarity. (b) EIS of CB@p-BVN before and after cycling.

Similarly, charging and discharging for 300 cycles at a constant current density of 0.2 A g^{-1} results in a constant decrease of the discharging capacity with the exception of only the first six cycles, for which a slight increase is noted (Figure 4.24a). Capacity retention is relatively high, retaining 66.7% of the discharging capacity after 300 cycles. Comparing EIS before and after cycling (Figure 4.24b) clearly shows that during cycling new interfaces form. The Nyquis-plots show a complex behaviour with hints of multiple semicircles after cycling, denoting to the degradation of structures, macroscopic rearrangements, and the loss of contact, as indicated by decreasing capacity. The exact mechanism of p-BVN degradation remains unclear. When comparing samples which were simply immersed in the electrolyte to

samples which were charged and discharged for 300 cycles, a significant incorporation of fluorine at the expense of oxygen is apparent in cycled samples. Thus, EDX measurements indicate that oxygen is partly exchanged by fluorine from the electrolyte during cycling. Additionally, SEM images show flatter surface in cycled samples probably due to volumetric changes upon cycling (Figure A9).

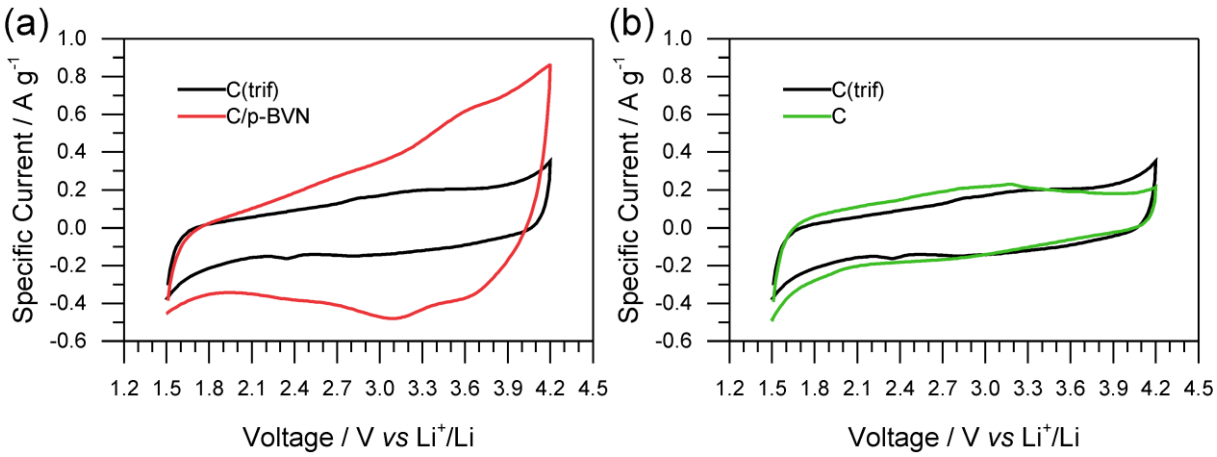

Figure 4.25. Cyclic voltammetry at 5 mV s^{-1} in a lithium half-cell setup with lithium as counter electrode and 1 M $LiPF_6$ in EC/DEC (1/1) as electrolyte. (a) C(trif) and C/p-BVN. (b) C(trif) and C.

The electrodes without p-BVN were used to estimate the contribution of p-BVN to the overall capacity of the C/p-BVN electrodes. These p-BVN free electrodes (further denoted as C(trif)) contain only carbon black (and 10% of PVDF as binder) and are treated in the same way as the C/p-BVN electrodes for better comparison, i.e., are also exposed to triflic acid during electrode formation. Such C(trif) electrodes however show significantly lower performance in cyclic voltammetry without any redox peaks in the cyclic voltammograms (Figure 4.25a), demonstrating the importance of p-BVN for a reversible redox behaviour of the electrodes. Furthermore, comparison of carbon black with and without triflic acid treatment shows no significant effect of triflic acid treatment on electrochemical performance of carbon black.

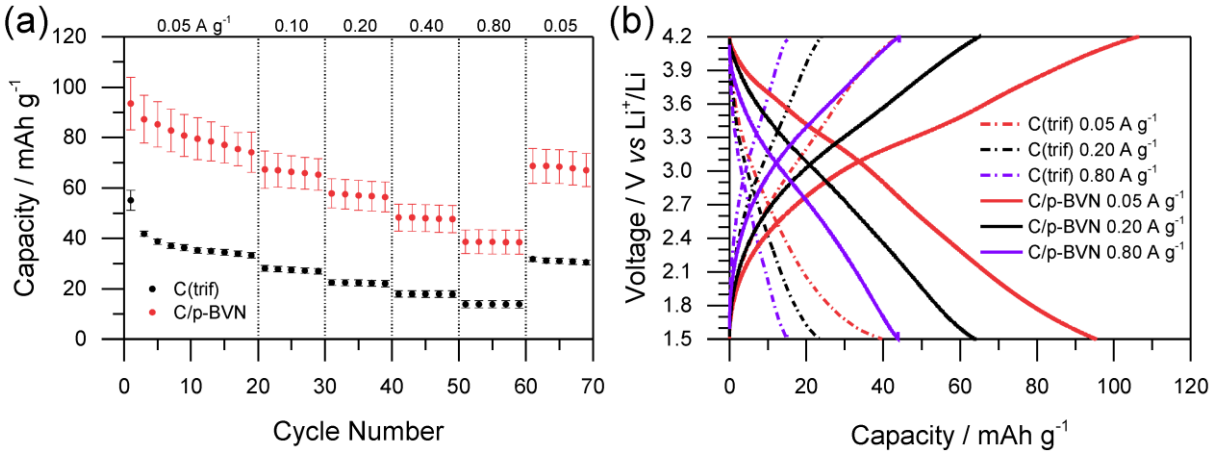

Figure 4.26 Galvanostatic charging-discharging behaviour of C(trif) and C/p-BVN at different current densities in a lithium half-cell setup with lithium as counter electrode and 1 M $LiPF_6$ in EC/DEC (1/1) as electrolyte. (a) Capacities. Every second point is omitted for clarity. (b) GCDC curves.

Galvanostatic charging-discharging measurements at different current densities have been used to quantify the difference between C(trif) and C/p-BVN (Figure 4.26). In contrast to C/P-BVN, C(trif) shows triangular galvanostatic charging-discharging curves, which indicates purely capacitor-like charge storage. The capacity of C(trif) is 38.7 mAh g^{-1} compared to 85.2 mAh g^{-1} for C/p-BVN (5th cycle, 0.05 A g^{-1}) which proves that p-BVN is the main contributor to charge storage in C/p-BVN.

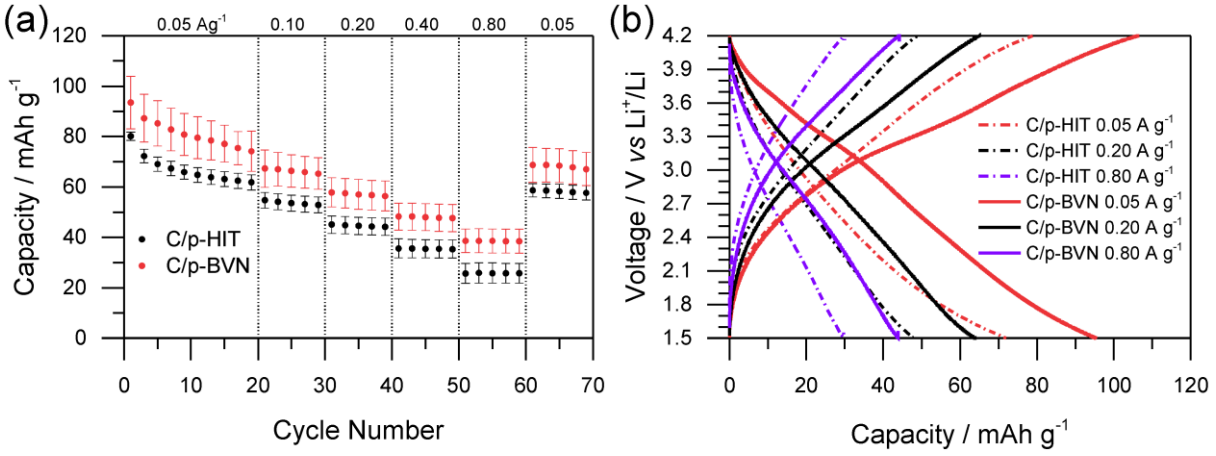

Figure 4.27. Galvanostatic charging-discharging behaviour of C/p-HIT and C/p-BVN at different current densities in a lithium half-cell setup with lithium as counter electrode and 1 M $LiPF_6$ in EC/DEC (1/1) as electrolyte a. (a) Capacities. Every second point is omitted for clarity. (b) GCDC curves.

In order to even more clearly demonstrate the significance of p-BVN for charge storage, BVN in the synthesis of C/p-BVN was exchanged by a similar compound, namely 5-hydroxyisophthalonitrile (HIT), which however does not provide quinones for charge storage capability. C/p-HIT was prepared analogous to C/p-BVN and its electrochemical performance has been tested under the same conditions (Figure 4.27). Charging-discharging tests at different current densities clearly indicate significantly better performance of C/p-BVN and

the absence of a belly shaped discharging behaviour in C/p-HIT. The surplus capacity of C/p-BVN when compared to C/p-HIT in the range of 20 mAh g^{-1} clearly indicates the contribution of quinones for charge storage, albeit with significantly lower capacity than theoretically predicted. The deviation is likely caused by contribution of phenolic groups to crosslinking as discussed above, irreversible oxidation reactions, and limited accessibility of active groups to the electrolyte. Still, quinone groups in C/p-BVN enhance the charge storage properties of this triazine containing network significantly. Enhanced charge storage of C/p-HIT when compared to CB(trif) may be explained by increased hydrophilicity[68,116,117] upon introduction of heteroatoms to carbon. This complex and interesting phenomenon will be further described in the Chapter 5.

In the past, triazine rings were thought to significantly contribute to the energy storage in CTFs and related materials used as cathodes in lithium-organic batteries,[101,109] but this assumption was disproved later.[108] Therefore, the triazine rings in the material do not contribute significantly to energy storage in CB@p-BVN but rather reduce the solubility of p-BVN by acting as crosslinking centres. As a mechanism of Faradaic charge storage in the case of CB@p-BVN the reversible redox-reaction between *ortho*-hydroquinone and *ortho*-quinone is suggested as shown for similar systems in aqueous [55,61,72] and organic lithium containing electrolytes[38].

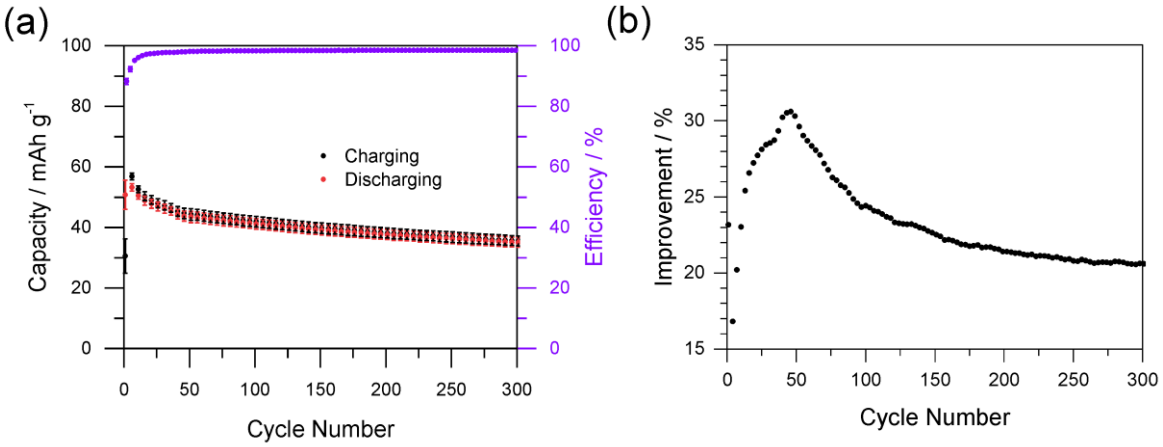

Figure 4.28. Electrochemical performance of C+p-BVN+PVDF in a lithium half-cell setup with lithium as counter electrode and 1 M $LiPF_6$ in EC/DEC (1/1) as electrolyte. (a) Capacity of C+p-BVN+PVDF at 0.2 A g^{-1} as calculated from charging-discharging tests. Every fifth data point is displayed for clarity. (b) Performance ratio of C/p-BVN to C+p-BVN+PVDF.

Finally, the importance of the polymerisation *in carbone*, i.e., in the presence and in tight contact to carbon is emphasised. In order to quantify the necessity of the polymerisation process, the CB@p-BVN electrodes are compared to conventionally fabricated organic electrodes having the same active material and carbon support in the same ratio on the current

collector with a similar loading. The capacity of these conventional electrodes, in which a slurry of the active material p-BVN (45%), carbon black (45%), and PVDF as binder (10%) is prepared by means of ball milling, is summarised in Figure 4.28 (denoted C+p-BVN+PVDF). The discharging capacity of C/p-BVN grossly outperforms C+p-BVN+PVDF. In early cycles, the improvement in the capacity by the polymerisation *in carbone* fluctuates between 17% and 32% and soon stabilises around 21%. This magnitude greatly exceeds the expected improvement of 10% due to the omission of binder and is explained by the better contact between the components after polymerisation *in carbone*.

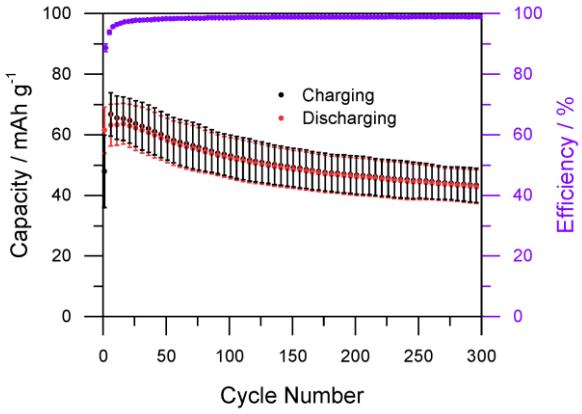

Figure 4.29. Electrochemical performance of PVDF containing C/p-BVN in a lithium half-cell setup with lithium as counter electrode and 1 M $LiPF_6$ in EC/DEC (1/1) as electrolyte. Capacity as calculated from charging-discharging tests at 0.2 A g^{-1}. Every fifth data point is displayed for clarity.

It is important to note that upon polymerisation *in carbone,* in the presence of the same binder, the resulting PVDF-containing electrodes (made of 45% BVN, 45% carbon black, and 10% PVDF) behave similarly to C/p-BVN (Figure 4.29.). The presence of a binder is therefore neither important for stability reasons nor is the lower capacity in binder-containing electrodes after conventional manufacturing a result of the binder content. In contrast, the CB@p-BVN electrodes may easily be fabricated without any fluorinated chemicals, increasing the sustainability of the process while simultaneously increasing the capacity.

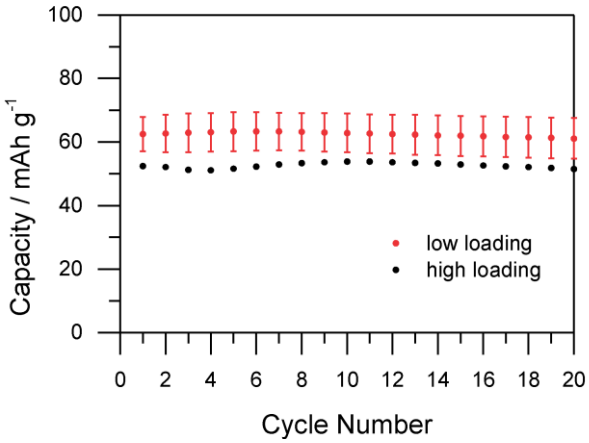

Figure 4.30. Difference in discharge capacities of C/p-BVN electrodes depending on loading. Low loading is around 2 mg cm^{-2} while high loading is around 5.5 mg cm^{-2}.

C/p-BVN electrodes showed great potential to be used as cathodes in lithium organic system. However, all the tested electrodes has active material loading of around 2 mg cm^{-2} while real life applications require values greater than 5 mg cm^{-2}. Therefore loading of the active material was increased and obtained electrodes were compared by their discharge capacities to aforementioned ones (Figure 4.30). During the first 20 cycles the electrodes show negligible drop in discharging capacities and therefore C/p-BVN holds a great promise in practical applications.

4.2.5. Conclusion

A novel cathode material derived from lignocellulosic biomass was presented. Specifically, vanillin, which can industrially be synthesised from lignin, was modified in two easy and sustainable steps affording bisvanillonitrile. The latter has a high density of redox active groups as well as two nitrile functionalities allowing the formation of a highly crosslinked aromatic network upon trimerisation of the nitrile groups in the presence of triflic acid. For the fabrication of the electrodes, a novel approach was developed in which first a composite of monomer and carbon black was formed. Upon polymerisation, tight interactions in the hybrid material were obtained. Not only did this method allow for the omission of binder, as the redox active polymer is formed around the grains of carbon black and thus served as an efficient binder itself, but it also allowed for a better contact between the carbon black and polymer, significantly improving the charge storage performance. To the best of my knowledge, the presented hybrid energy storage material is the first report of a lignin derived cathode for lithium-ion based energy storage and may hence contribute to more sustainable energy storage devices in the future. However, sloppy discharge curve along with low capacity compared to theoretical capacity must be investigated further.

5. Towards understanding of lithium based electrical energy storage in catecholic and guaiacyl cathode materials

In the previous chapter two vanillin derived cathode materials were successfully synthesised. One of them showed promising properties for lithium based electrical energy storage. In order elucidate mechanisms underlying vanillin energy storage different polymers bearing redox active catecholic and guaiacyl as well as redox inactive resorcinolic groups will be compared. Furthermore, interface between the model polymers with the porous carbons with similar surface chemistry but varying porosities will be studied in detail to help designing the optimal carbon to be used as conductive additive.

Part of this chapter is adapted from my original work:

1) Ilic, I. K.; Perovic, M.; Liedel, C. The interplay of porosity, wettability, and redox activity as determining factors for lithium-organic electrochemical energy storage using biomolecules. *ChemSusChem* **2020**, *13*, 1856-1863 (This article an open access article under the terms of the Creative Commons Attribution License, which permits use, distribution and reproduction in any medium, provided the original work is properly cited.)

5.1. Synthesis of model polymers bearing catecholic and guaiacyl groups

Polymers bearing primary amines have attracted great attention although their synthesis is rather difficult. Polyallyamine (PAAm), a primary amine containing polymer with high nitrogen content, around 25%, is a commercially available polymer purchasable in aqueous solutions. Its ability to immobilise aldehydes in shape of Schiff bases, by grafting of aldehydes on the polymer backbone, was first recognised long time ago and the obtained materials were utilised for the formation of separation membranes based on reverse osmosis.[118–121] Therefore, by grafting different aldehydes on polyallyamine one can prepare polymers that bear different functionalities such as catecholic and guiacyl groups and compare their properties. High amount of primary amines on polyallylamine allows for the formation of polymers with high density of desired functional groups.

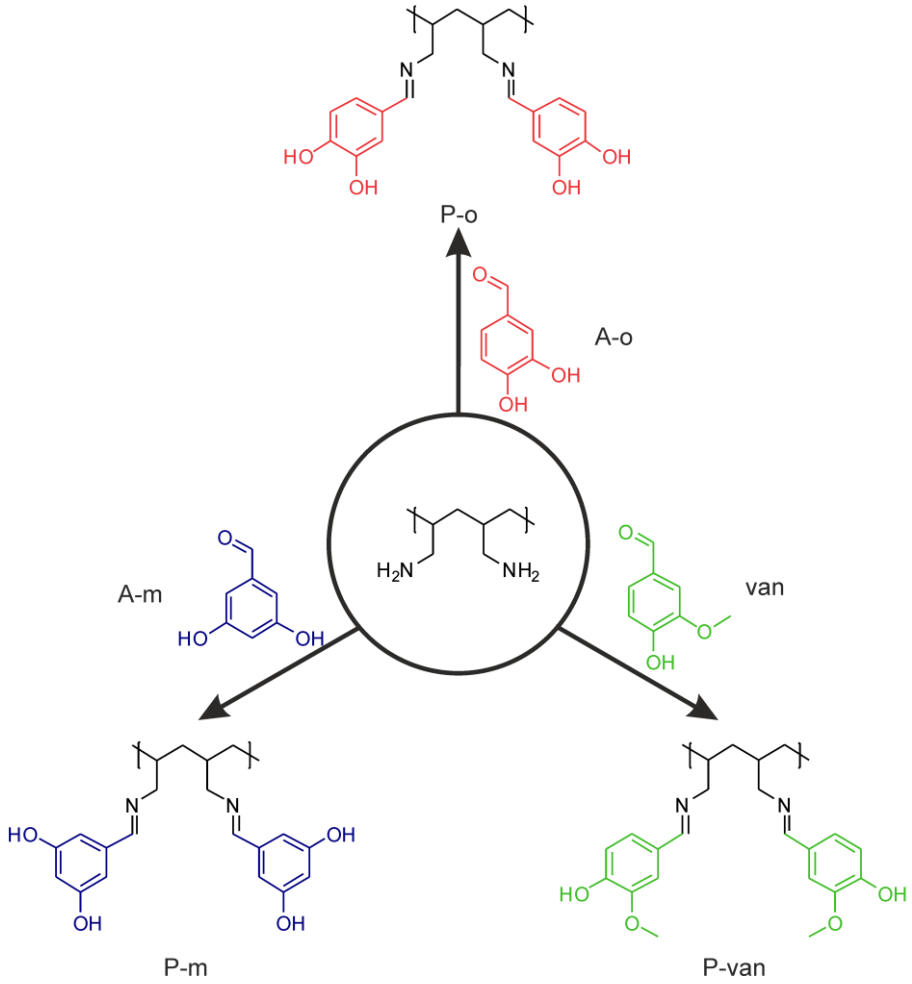

Figure 5.1. Polyallylamine can be easily functionalised by grafting aldehydes.

5.1.1. Synthesis and characterisation of pollyallylamine Schiff bases

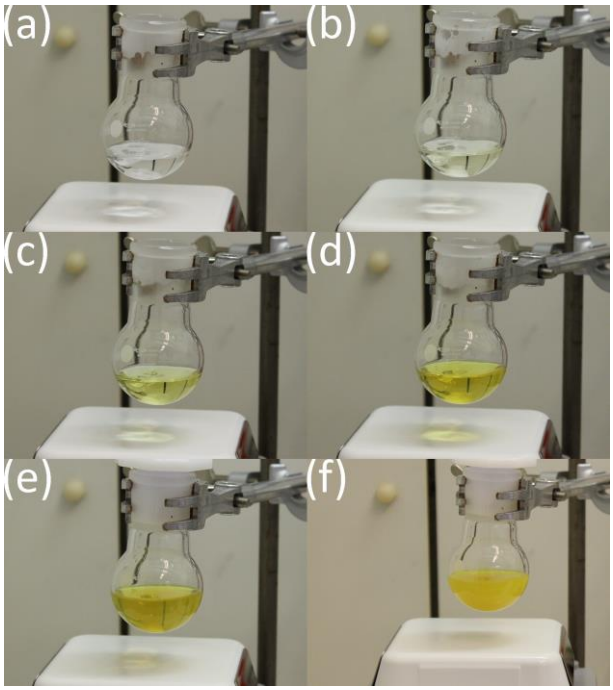

Figure 5.2. Reaction of polyallylamine (PAAm) with protocatechuic aldehyde (A-o). Before adding the A-o containing solution (a), after adding 10% (b), 20% (c), 50% (d) and 100% (e) of the A-o containing solution, and after additional stirring for 1 h (f).

Schiff bases of polyallylamine (PAAm) and different aldehydes, namely vanillin (van), protocatechuic aldehyde (A-o), and 3,5-diyhdroxybenzaldehyde (A-m), were synthesised by simple mixing of reactants in ethanolic solution. Addition of aldehydes to PAAm results in an immediate colour change as expected for the formation of Schiff bases, followed by precipitation (Figure 5.2) due to the interaction of leftover amine groups with acidic phenolic groups.[118] Subsequently the solvent was removed under vacuum and the powder was further dried under vacuum at elevated temperature as it is known that drying promotes formation of Schiff bases.[122] Successive washing with anhydrous ethanol yields the pure modified polymers. Mechanism of Schiff base formation was studied in detail in Chapter 4. (Scheme 4.2). Contrary to ChiVan, no reduction is necessary as desired application of these polymers is in water free organic lithium electrolyte making the reduction step obsolete as a result of irreversibility of imine formation in water free conditions.

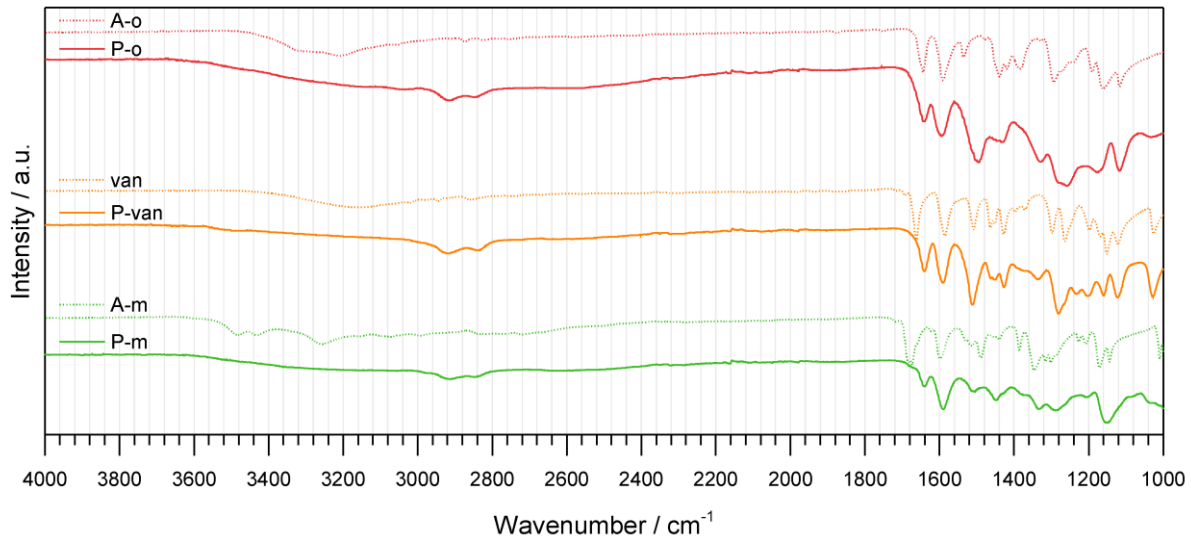

Figure 5.3. Infrared spectra of P-o, van, P-m, and their corresponding Schiff bases with PAAm.

Successful formation of Schiff bases is confirmed by infrared spectroscopy (Figure 5.3), as the resulting polymers contain the functional groups from the respective phenyl ring. Broad bands above 3000 cm^{-1}, from hydroxyl groups, are retained both in the spectra of polymers and aldehydes confirming retention of hydroxyl groups during synthesis. Two new bands appear in the spectra of polymers around 2840 and 2920 cm^{-1} indicating C-H stretching vibrations from the polyallylamine backbone.[123] No aldehyde groups are detectable in the polymers, but new bands at lower wavenumbers than aldehydes represent imine functionalities in all three samples, which confirms both successful reaction as well as successful removal of any unreacted aldehydes.[124] Intriguingly, the shift between the imine and aldehyde peak is very pronounced in the case of van/P-van and A-m/P-m but is rather subtle in the case of A-o/P-o, only by few cm^{-1}, which origins from the different wavenumber of aldehyde carbonyl vibrations in A-o, van, and A-m.

Table 5.1. Substitution rates of PAAm-aldehyde Schiff bases.

Polymeric Schiff base	N / wt %	Substitution rate / %
P-o	8.69-8.98	82.4-86.7
P-van	7.78-7.80	91.3-91.7
P-m	7.70-7.72	103.6-103.9

Table 5.1 summarises the resulting substitution rates in the samples as calculated using the amount of nitrogen determined from elemental analysis (Table A3) according to the equation:

$$w_N = \frac{m_N}{m_{polymer}} = \frac{Mr_N}{Mr_{PAAm} * (1 - \mu) + Mr_{P-x} * \mu}$$

$$\frac{Mr_N}{w_N} = Mr_{PAAm} - Mr_{PAAm} * \mu + Mr_{P-x} * \mu$$

$$\frac{Mr_N}{w_N} - Mr_{PAAm} = \mu * (Mr_{P-x} - Mr_{PAAm}) = \mu * (Mr_{A-x} - Mr_{water})$$

$$\mu = \frac{\frac{Mr_N}{w_N} - Mr_{PAAm}}{Mr_A - Mr_{water}}$$

where μ is the substitution rate, w_N is the nitrogen content, Mr_N is the molar mass of nitrogen, Mr_{PAAm} is the molar mass of PAAm, $Mr_{P\text{-}x}$ is the molar mass of PAAm-X, $Mr_{A\text{-}x}$ is the molar mass of the aldehyde and Mr_{water} is the molar mass of water.

The apparent substitution rate of P-m, which exceeds 100%, is a result of limitations of this method of analysis, but other methods unfortunately also overestimated substitution rates of Schiff bases on PAAm in the past.[118,120] This overestimation could be ascribed to a small amount of water present in the samples, as is visible from the TGA of the polymers (Figure A10). Several indications such as the deviation between multiple measurements and the pretended occurrence of sulfur in the samples show that these results are not precise. Their main point is to assure comparability between the samples which they do. Similar substitution rates allow us to compare differences caused by the redox-active and inactive functional groups.

5.1.2. Conclusion

Model polymers bearing variety of functional groups were prepared by simple, catalyst free grafting of aldehydes on the amine rich polyallyamine with only water as a side product. The choice of aldehyde mandates the functional groups the polymer is bearing. Therefore, redox active protochatecuic aldehyde was grafted on polyallyamine, as well as its redox inactive isomer 3,5-dihydroxybenzaldehyde. Furthermore, guaiacyl groups were introduced by grafting vanillin. Electrochemical behaviour of these model polymers will be investigated in the next chapter.

5.2. The interplay of porosity, wettability, and redox activity as determining factors for lithium-organic electrochemical energy storage using biomolecules

Biowaste derived cathode materials described in the 4. Chapter hold a great promise for sustainable energy storage. In order to gain a deeper understanding of the charge storage mechanism, the influences on charge storage in model systems based on biomass-derived, redox-active compounds and comparable structures were investigated. Hybrid materials composed of these model polymers and porous carbon were compared in order to precisely determine causes of exceptional capacity in lithium-organic systems. It was found that not only redox activity, but also hydrophilicity greatly influences capacity of the composites. Furthermore, in addition to bio-derived molecules with catechol functionalities, which are commonly described as redox-active species in lithium-bioorganic systems, these guaiacyl groups are described as a promising alternative and compared to the catecholic units.

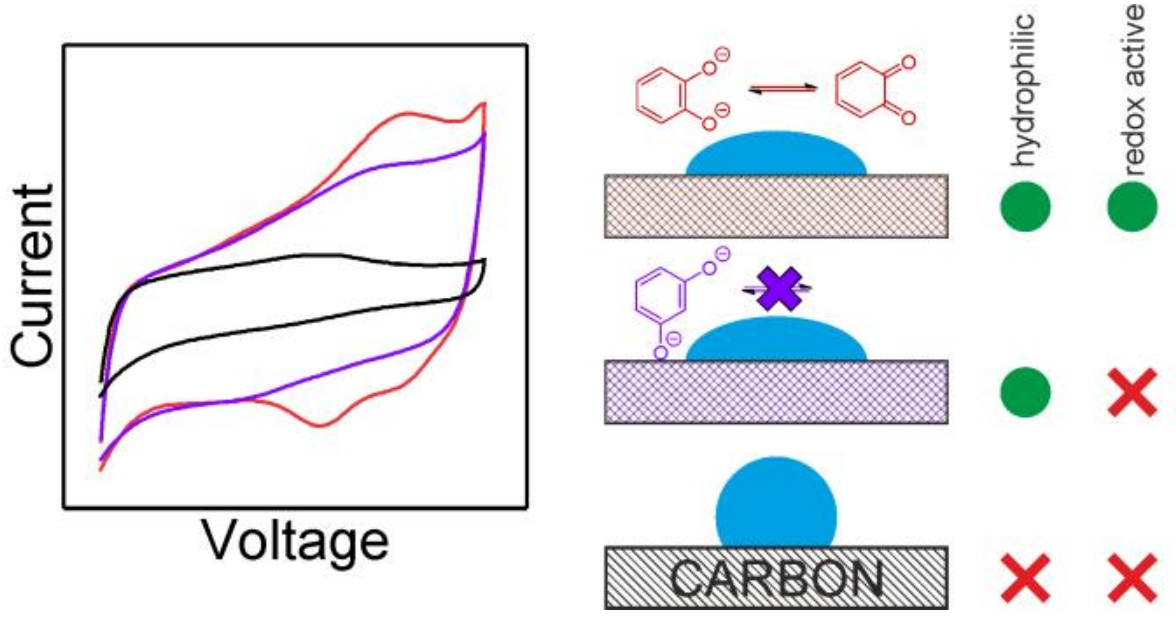

Figure 5.4. In bio-based materials for electrochemical energy storage, influences of redox activity, kind of functional group, and hydrophilicity are evaluated.

Milena Perovic performed and interpreted water vapour physisorption measurements.

5.2.1. Synthesis and characterisation of C/P-o

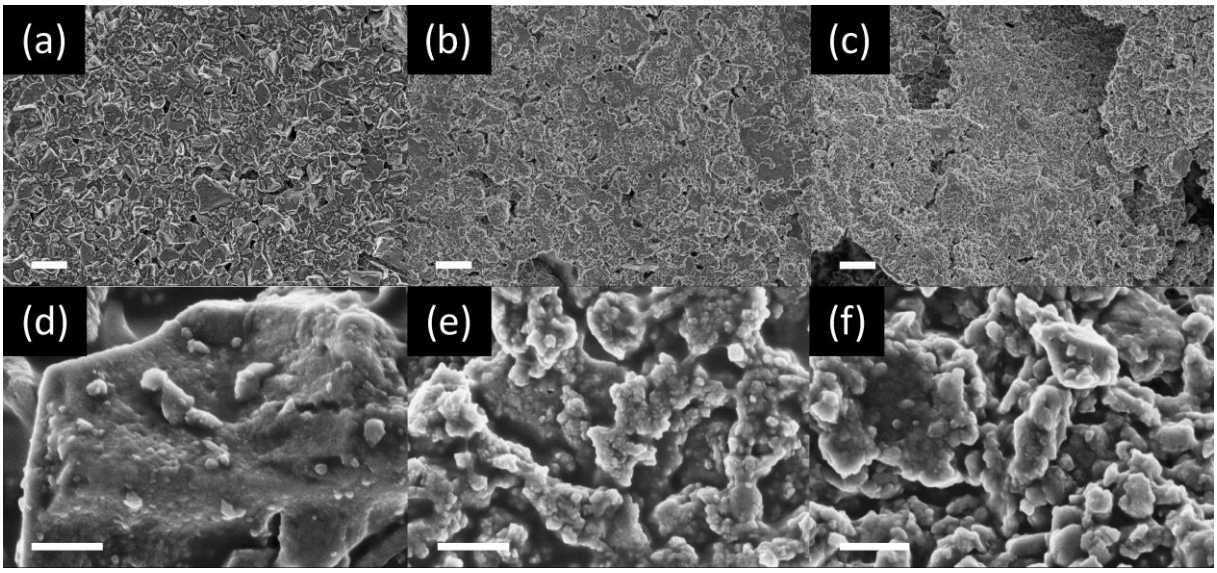

Figure 5.5. SEM images of C(pristine) (a, and d), C (b, and e), and C/P-o (c, and f). The scale bars represent 10 µm (a, b, and c) and 1 µm (d, e, and f), respectively.

Hybrid cathode materials were formed by combining the model biopolymers and porous carbon and will be further labeled as C/P-x where P-x is the abbreviation of the corresponding Schiff base polymer. Scanning Electron Microscopy shows the morphology of the obtained materials before (C(pristine)) and after ball-milling (C and C/P-o) (Figure 5.5). Upon prolonged milling, big particles of conductive carbon become smaller. The morphologies of both C/P-o and the neat carbon after ball-milling are similar due to the tight composite between the polymer and the conductive carbon.

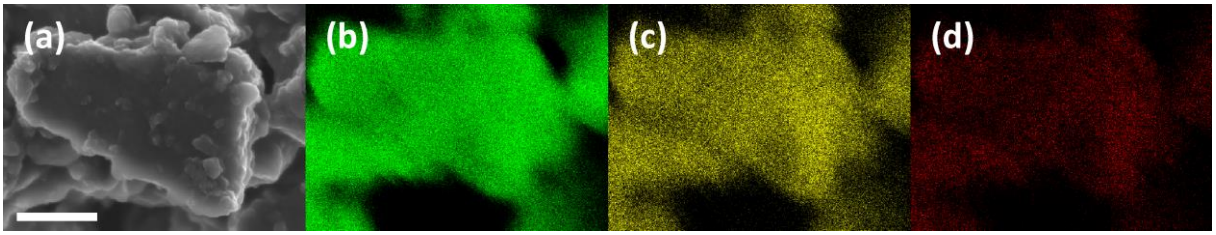

Figure 5.6. SEM image of C/P-o (a; scale bar 1 µm) and carbon (b), oxygen (c), and nitrogen (d) mapping by EDX.

Energy Dispersive X-ray mapping, showing a homogeneous dispersion of carbon, oxygen, and nitrogen, confirms this observation (Figure 5.6).

5.2.2. Optimisation of C/P-o for energy storage

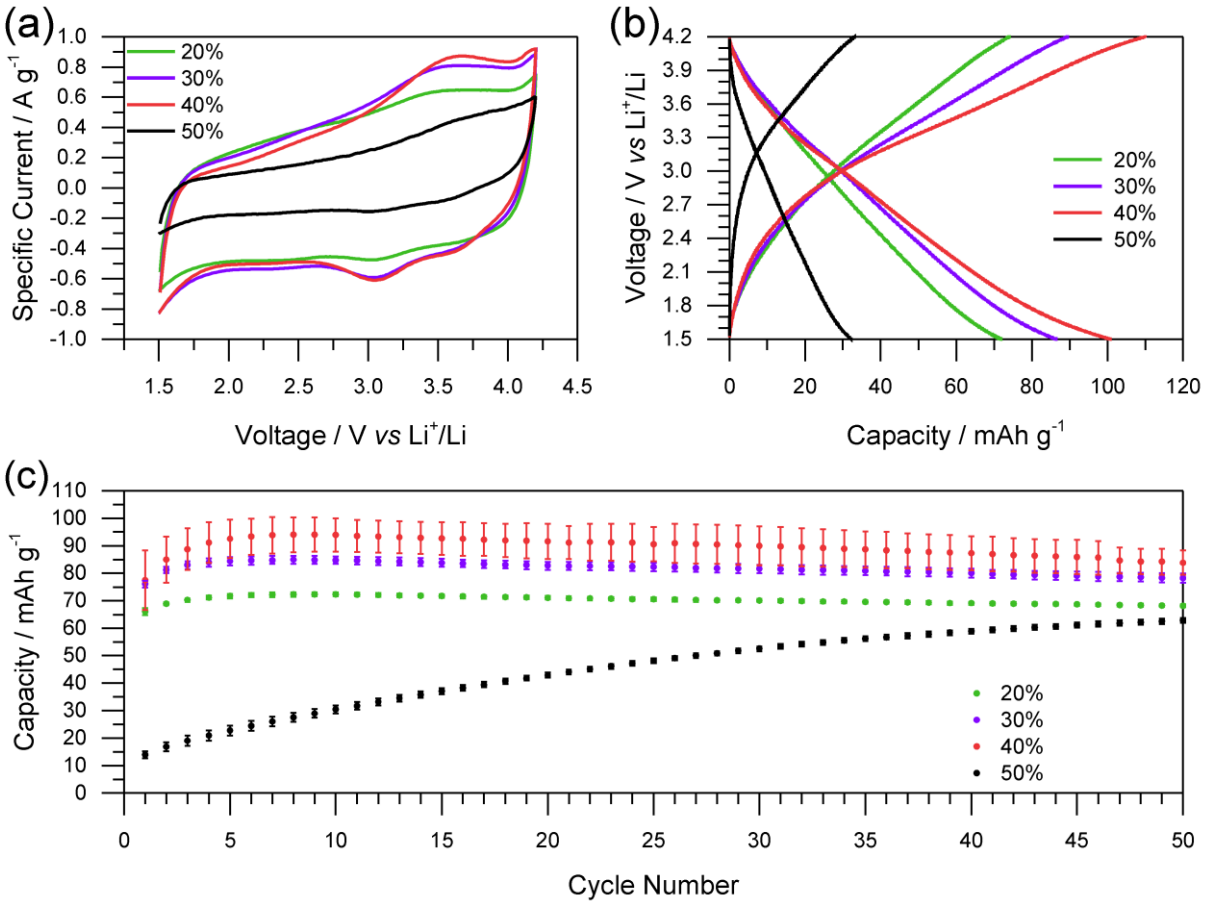

Figure 5.7. Electrochemical performance of different hybrid materials of P-o polymers with carbon and binder (C/P-o), where the percentage represents the amount of P-o, while the amount of PVDF is constant (10%), and the rest is conductive carbon. The test was performed in a lithium half-cell setup with lithium as counter electrode and 1 M $LiPF_6$ in EC/DEC (1/1) as electrolyte. (a) Cyclic voltammetry at 5 mV s^{-1}, 10th cycle. (b) Charging-discharging test at 0.2 A g^{-1}, 10th cycle each. (c) Discharging capacities as calculated from charging-discharging tests at 0.2 A g^{-1}.

In order to optimise the composition of P-o and conductive carbon multiple hybrid materials were prepared and compared electrochemically using cyclic voltammetry and charging-discharging tests (Figure 5.7). Capacity in the hybrid materials gradual increases from P-o contents between 20% and 40% and significantly decreases when increasing the amount of P-o to 50%. This behaviour can be explained by a combination of gradual increase of electrochemically active groups as well as hydrophilic groups, as will be explained in the course of this chapter, (Figure 5.7a,b) and sharp reduction of conductivity as a result of the high content of nonconductive polymer. Additionally, combinations with up to 40% active polymer material achieve maximum capacity after only a few cycles while the material with the higher active polymer content does not achieve the full capacity even after 50 cycles (Figure 5.7c). This behaviour may be ascribed to reorganisation of polymer-bound functionalities that happens upon cycling, allowing for a better conductivity between carbon

and polymer and subsequently higher utilisation of redox-active groups and wetting of the carbon material with the electrolyte. Due to the peak performance of 40% composite, all the experiments with different polymers have been performed using 40% of the corresponding polymer, 50% of conductive carbon, and 10% of PVDF.

5.2.3. Energy storage performance of redox active and inactive polyphenols – importance of wettability

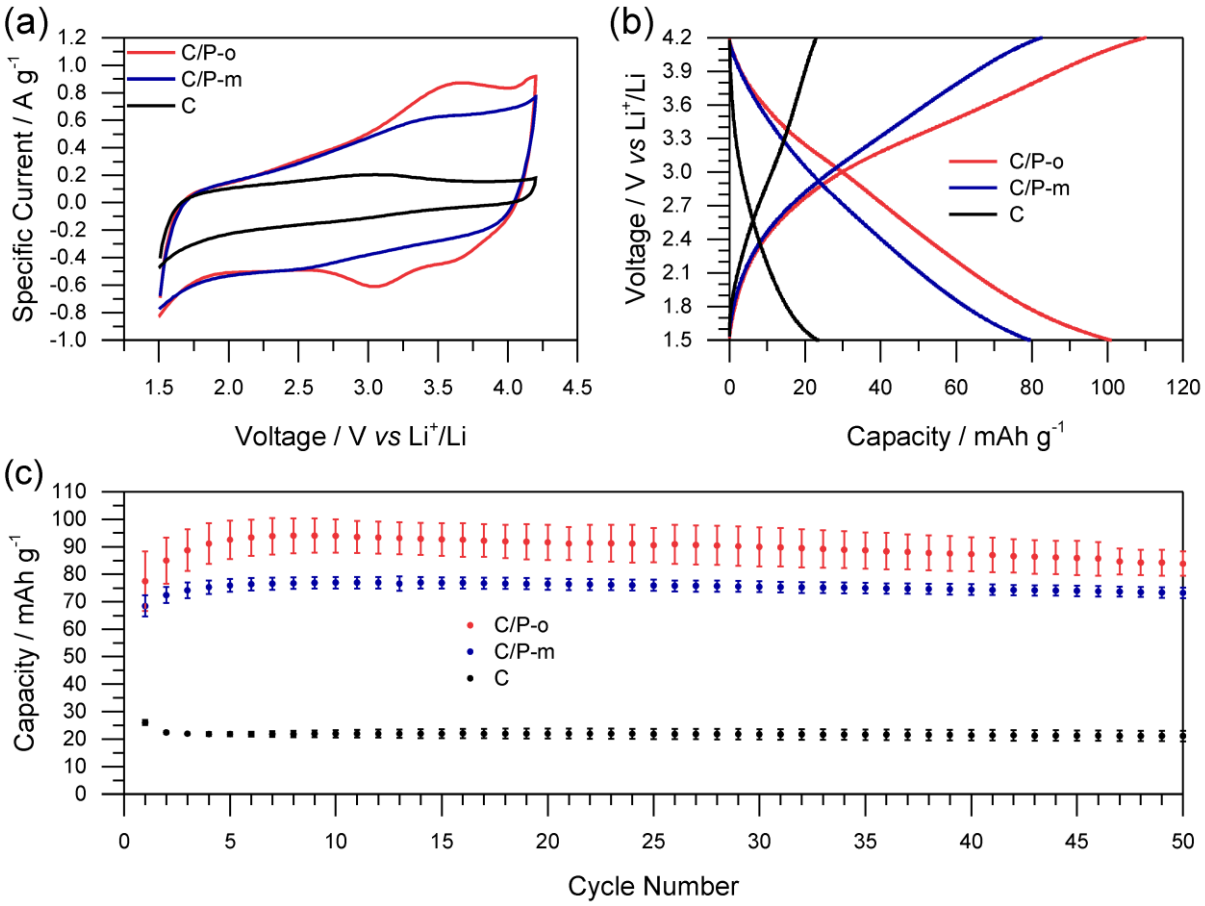

Figure 5.8. Comparison of the electrochemical performance of C/P-o, C/P-m, and porous carbon (C). The tests were performed in a lithium half-cell setup with lithium as a counter electrode and 1 M $LiPF_6$ in EC/DEC (1/1) as electrolyte. (a) Cyclic voltammograms at 5 mV s^{-1}, 10th cycle. (b) Charging-discharging tests at 0.2 A g^{-1}, 10th cycle. (c) Discharging capacities as calculated from charging-discharging tests at 0.2 A g^{-1}.

Figure 5.8 compares C/P-o, C/P-m, and microporous carbon in terms of their electrochemical performance during cyclic voltammetry and charging-discharging tests. Redox-activity of C/P-o is clearly detectable in cyclic voltammograms through peaks in the range of 3.3 V vs. Li^+/Li (Figure 5.8a). In the low voltage region, the voltammograms of C/P-o and C/P-m match fairly well, but there are no redox peaks around 3.3 V vs. Li^+/Li observable in the latter, as expected. Similarly, the absence of redox peaks is characteristic for purely microporous carbon.

Capacity of the microporous carbon in galvanostatic charging-discharging experiments is very low. Upon addition of P-m and even more so upon addition of P-o (C/P-m and C/P-o, respectively) it increases significantly. Upon prolonged cycling, C and C/P-m retain the capacity while C/P-o shows subsequent decay (Figure 5.8c) as will be discussed later. The higher capacity of C/P-o when compared to C/P-m can easily be explained by an additional redox contribution to capacity, resulting in a slightly belly-shaped galvanostatic discharging behaviour of C/P-o (Figure 5.8b) in agreement with the shape of cyclic voltammograms. Peaks in the latter correspond to the redox transformation of catecholic groups, and the reduction curves in galvanostatic cycling exhibit increased capacity in the same voltage range of 3-3.5 V vs. Li^+/Li. No belly-shaped behaviour can be observed for C and C/P-m (Figure 5.8b).

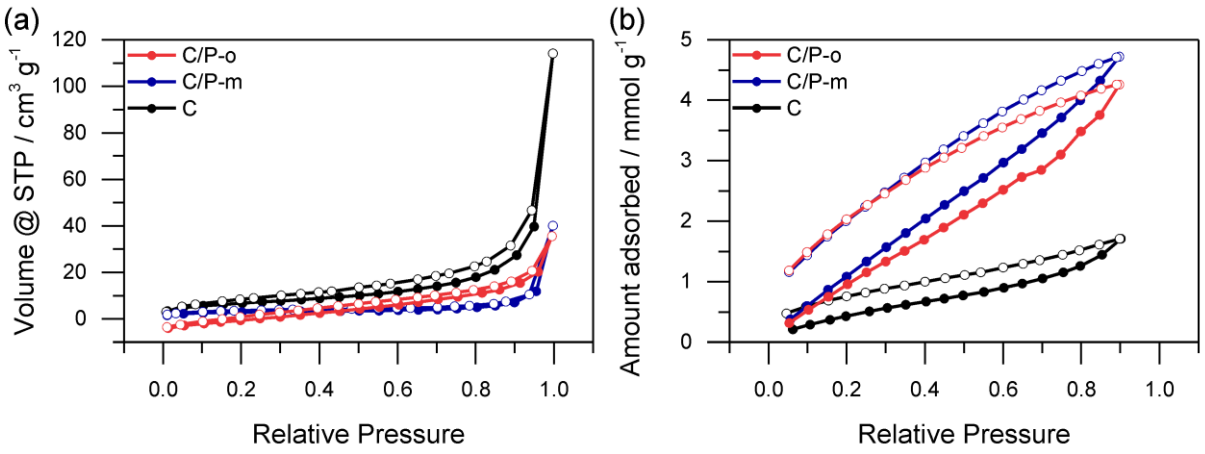

Figure 5.9. Nitrogen (77 K) (a) and water vapour (298 K) (b) physisorption isotherms of C/P-o, C/P-m, and C. Full dots represent adsorption while empty ones represent desorption.

The difference in capacity between C/P-m and microporous carbon however cannot be explained by redox reactions. C/P-m shows much higher capacity compared to carbon despite not being redox-active. A possible explanation for this phenomenon is increased hydrophilicity of the hybrid material upon introduction of a heteroatom-rich polymer to microporous carbon. Consequently, the nitrogen and water vapour physisorption behaviour is discussed in order to asset hydrophilicity of the prepared hybrid materials (Figure 5.9).

During ball-milling, carbon (C) loses most of its internal surface area probably due to a combination of high energy ball milling and blocking of pores by the binder (cf. physisorption behaviour of the pristine microporous carbon in Figure A11). The BET surface areas of hybrid materials with model polymers (C/P-o and C/P-m) are even lower, possibly both due to the relatively lower amount of microporous carbon in the hybrid material and due to

additional blocking of pores by the active polymers. All samples exhibit high external surface areas due to loose packing of particles.

Water vapour physisorption does not follow the same trend as established by nitrogen gas physisorption. In contrast, water vapour uptake in C/P-o and C/P-m is similarly high, with the carbon material adsorbing significantly less water vapour than both over the entire range of relative pressures. As the elemental composition of P-o and P-m is the same, this behaviour may be ascribed to abundant hydroxyl groups in the polymers, resulting in mixed carbon-polymer materials with similar hydrophilicity. Hydrophilicity is significantly higher than in case of the unmodified carbon material, causing the material to be better wettable not only by water but also by polar solvents such as in battery electrolytes. With the electrolyte reaching a larger part of the internal volume of microporous carbon, the contribution of energy storage by formation of the electric double layer increases. More charge can be stored on the surface, both in case of C/P-o and C/P-m compared to carbon, causing higher capacity. A similar behaviour was previously described in aqueous solutions of polypyrrole with and without chitosan, where the redox inactive chitosan significantly increased the capacity of polypyrrole.[68] It is important to note that ball milling tends to increase the hydrophilicity of carbons as well, although to a lesser extent.[116]

5.2.4. Energy storage performance – comparison of guaiacyl and catecholic redox centres

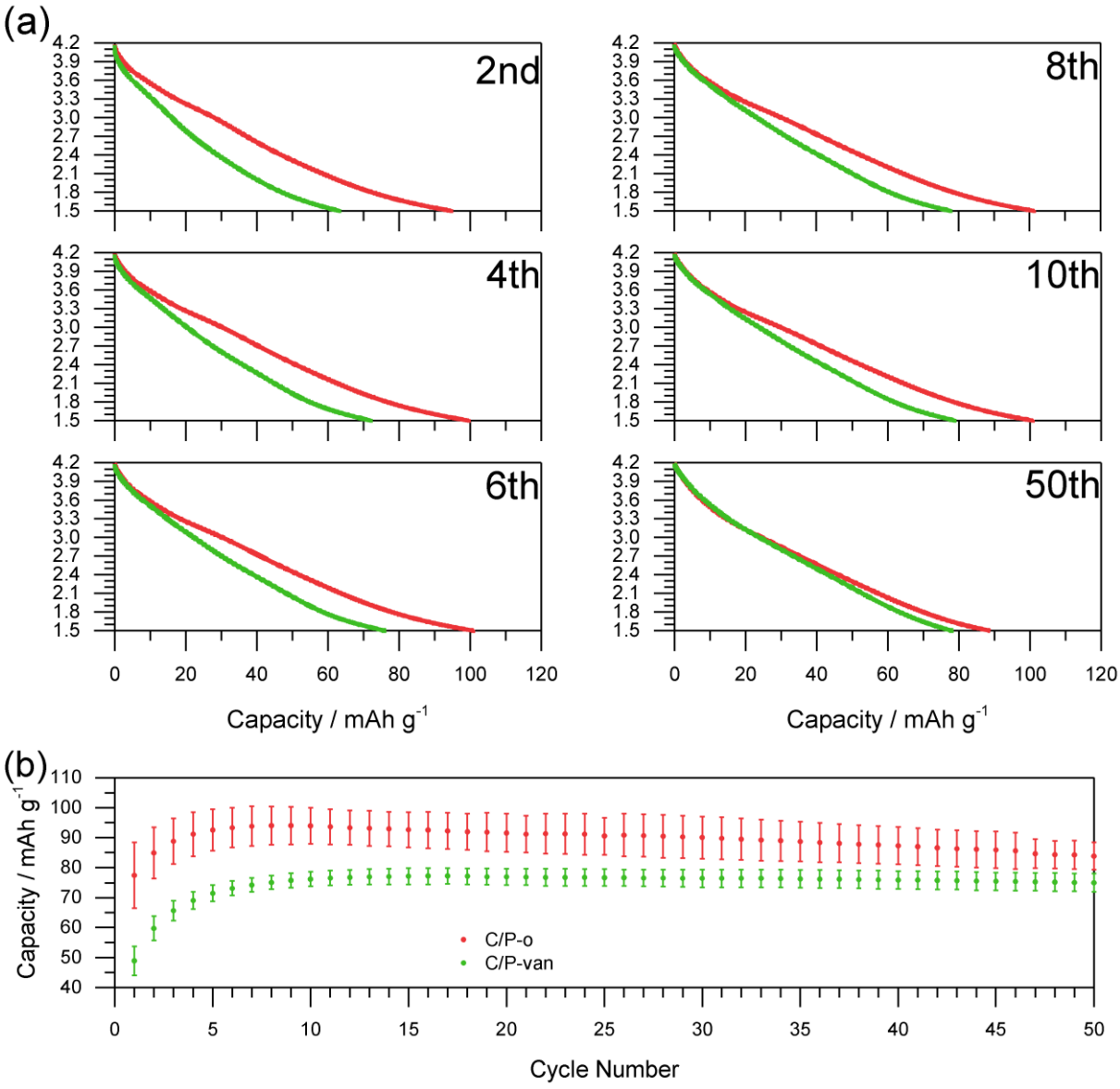

Figure 5.10. Charging-discharging tests of C/P-o and C/P-van. The tests were performed in a lithium half-cell setup with lithium as counter electrode and 1 M $LiPF_6$ in EC/DEC (1/1) as electrolyte. (a) Discharging curves at 0.2 A g^{-1} of different cycles, where charging and discharging were performed between 4.2 V and 1.5 V. (b) Discharging capacities at 0.2 A g^{-1}.

Catecholic groups in hybrid materials with microporous carbons consequently contribute to overall capacity both through increased hydrophilicity and redox activity. Still, catecholic groups are rather rare in nature, notable exception being dopamine. In contrast, guaiacyl groups are abundant in nature, for example in low-value biogenic materials such as lignin. To my knowledge, such materials have never been used in secondary lithium ion batteries to date. Thus, the focus will be on such materials, by comparing the electrochemical performance of C/P-o and C/P-van (Figure 5.10). Discharging curves greatly differ initially,

both in terms of overall capacity as well as in terms of shape, but become more similar with the progressing cycles. Unlike C/P-o, C/P-van discharging curves show no belly-shape in the beginning. With progressing cycles, the shape changes, ultimately almost matching the shape of C/P-o discharging curves after approx. 50 charging-discharging cycles.

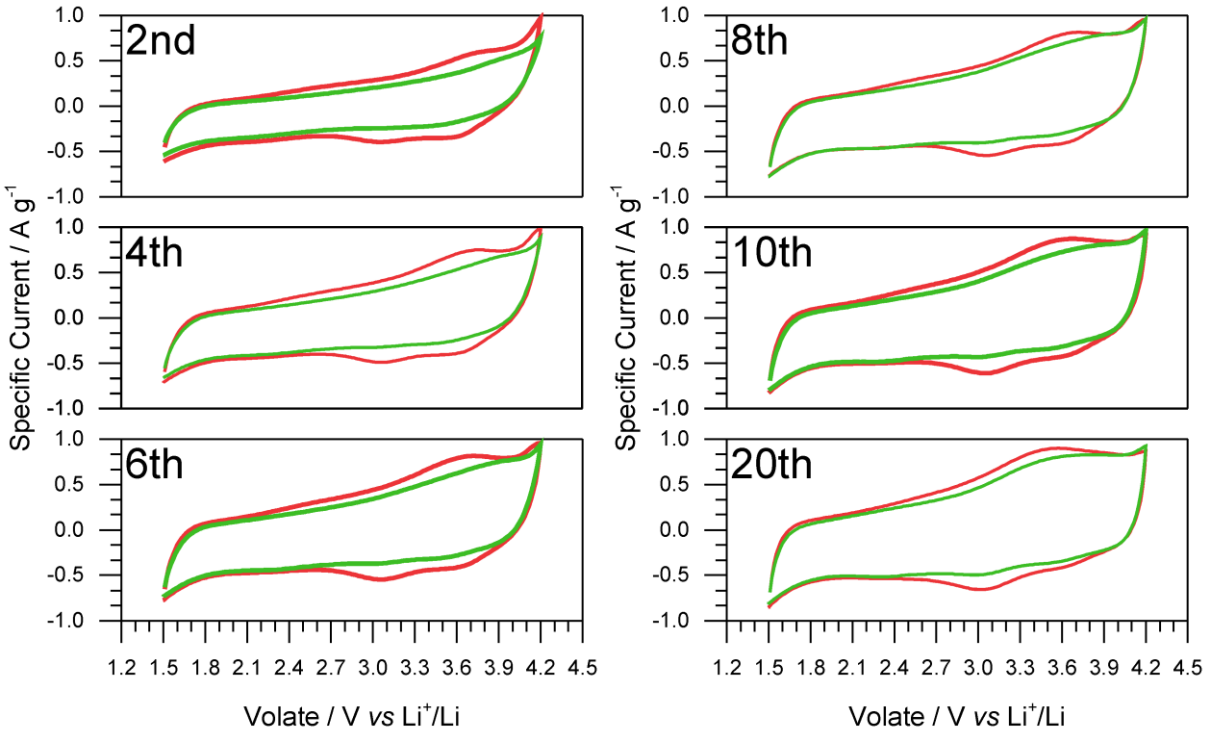

Figure 5.11. Cyclic voltammetry of C/P-o and C/P-van at 5 mV s^{-1}, selected cycles. The test was performed in a lithium half-cell setup with lithium as a counter electrode and 1 M $LiPF_6$ in EC/DEC (1/1) as electrolyte.

The same behaviour is apparent in cyclic voltammetry (Figure 5.11). While no clear redox peaks are observable in early cycles of C/P-van, such peaks at similar potential as in C/P-o appear with continuing cycling, and the cyclic voltammograms of C/P-van and C/P-o start to resemble each other.

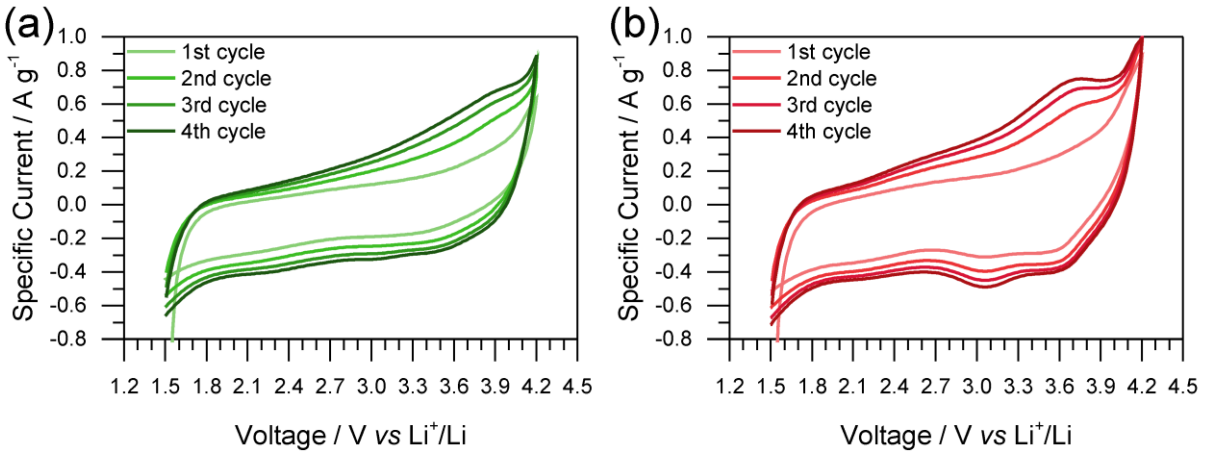

Figure 5.12. First four cycles of cyclic voltammograms of C/P-van (a) and C/P-o (b). Cyclic voltammograms were measured at 5 mV s^{-1} in a lithium half-cell setup with lithium as counter electrode and 1 M $LiPF_6$ in EC/DEC (1/1) as electrolyte.

In aqueous systems, as discussed in previous chapter, demethylation occurs in the first oxidation step, expressed by the high current in cyclic voltammetry curves at voltages approximately 0.2 V higher than the reversible redox peak which evolves in the next cycle (Figure 4.5). A quinone-hydroquinone redox-pair thus can easily be formed also in molecules which initially contain guaiacyl groups. As this mechanism requires the presence of water, it is impossible in a lithium-ion containing setup in water-free organic electrolytes. Consistently, no such first irreversible oxidation peak is observable in cyclic voltammetry in this setup. Still, galvanostatic and cyclic voltammetry curves of C/P-van indicate formation of the same quinone-hydroquinone redox couple as in C/P-o with prolonged cycling (Figures 5.10 and 5.11) probably due to the slow demethylation that exposes redox-active functionalities. The mechanism for the involved demethylation process is unclear; however a similar mechanism to the one found in aqueous systems is suggested, with the difference that fluoride anions serve as nucleophiles instead of water, forming fluoromethane in the process. As no significant irreversible oxidation peak is observable in a distinct early cycle of cyclic voltammetry measurements (Figure 5.11), unlike in the case of similar polymers in aqueous systems (Figure 4.5), leading to the conclusion that demethylation requires several charging-discharging cycles in a lithium half-cell setup. Irreversible oxidation, usually resulting in diminishing capacity with prolonged cycling, is common in organic battery materials.[125]

Notably, C/P-van reaches constant capacity after approx. 10 charging-discharging cycles at current density of 0.2 A g^{-1}. After reaching the maximum, capacity is constant within 50 charging-discharging cycles, in contrast to the case of C/P-o where capacity slowly decreases immediately after reaching the maximum. The behaviour of both during continuous charging and discharging can be explained by a model in which both materials are passing through

three phases: sleeping, living, and dead phases as established for lithium/sulfur batteries by Risse et al.[126] In this case, the sleeping phase represents all the guaiacyl groups that did not undergo initial oxidation yet and all the hydroquinone groups that are unreachable to the electrolyte. The living phase represents all the quinone-hydroquinone redox-pairs that undergo redox reactions in that step and is the only phase that contributes to Faradaic charge storage of the material. Finally, the dead phase represents all the degraded groups that cannot undergo a redox reaction anymore. During cycling units can irreversibly change from sleeping to living phase or from sleeping/living to dead phase.

The different charge storage behaviour with continuous cycling may be explained by differences in sleeping phases between both materials. Oxidation of hydroquinone groups happens much faster than oxidation of guaiacol groups, resulting in complete transition of C/P-o from the sleeping phase to the living phase within few cycles. The subsequently fading capacity indicates a slow transition to the dead phase. In contrast, the constant capacity of C/P-van after reaching the maximum may be ascribed to continuous slow transition of some guaiacyl groups from sleeping to living phase at a similar rate as the transition of other active groups from living phase to dead phase. It consequently does not necessarily indicate higher stability of the material during cycling. Ultimately, the maximum capacity is lower in C/P-van compared to C/P-o as partial demethylation (formation of the living species) continues after the maximum capacity is reached. Only after approx. 50 cycles capacities of C/P-van and C/P-o become similar because of the formation of quinone groups in C/P-van and irreversible oxidation of C/P-o. The final apparent specific capacity in C/P-van is still slightly lower than in C/P-o because the specific capacity is calculated based on the initial mass of the hybrid material, including methyl groups in P-van. Demethylation of guaiacol groups slightly reduces the weight of the polymer material, thus leaving the assumed gravimetric capacity an underestimation.

5.2.5. Energy storage properties of C/P-o

Next, the electrochemical behaviour of the best performing material, C/P-o, will be evaluated in detail. Upon comparing the charge storage behaviour of C/P-o to C/P-m and C (Figure 5.8), influences of carbon, redox activity, and changes in hydrophilicity may be estimated. Contributions to charge storage (i) of the conductive carbon's electrical double layer, (ii) of the influence of enhanced hydrophilicity of conductive carbon, increasing its accessibility by the electrolyte and thus facilitating capacitive charge storage, and (iii) of the redox activity of

o-quinone functionalities was calculated by comparing the capacities of C, C/P-m and C/P-o. Capacity of C, divided by 9/5 (as there is 90% of conductive carbon in C compared to 50% in C/P-m and C/P-o), was divided by the total capacity of C/P-o in order to obtain the percentaged contribution of the capacitive charge storage of ball-milled carbon. Furthermore, the difference between capacities of C/P-o and C/P-m was divided by the capacity of C/P-o to obtain the percentaged contribution of redox activity. The rest of capacity is due to enhanced formation of an electrical double layer of carbon that becomes accessible to the electrolyte due to enhanced hydrophilicity. According to these calculations, after 10 cycles at 0.2 A g^{-1}, reversible redox reactions contribute to only 18.1 % of charge storage. With only 13.0 % deriving from capacitive charge storage on the surface of the unmodified carbon material, changes in hydrophilicity of the surfaces have the major influence to the charge storage (68.9 %). Abundant phenolic functionalities and imines result in significantly enhanced hydrophilicity, facilitating capacitive charge storage. These results point to the importance of selecting appropriate binders and carbons when designing electrode materials from renewable resources.

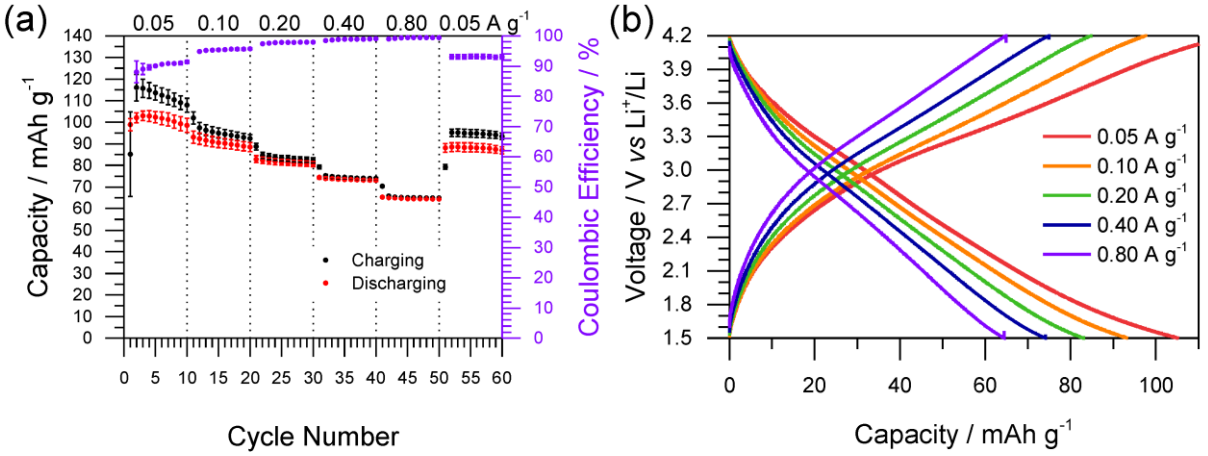

Figure 5.13. (a) Charging-discharging tests of C/P-o at different current densities as indicated. (b) Galvanostatic charging-discharging curves (5th, 15th, 25th, 35th, and 45th cycle from (a)). The test was performed in a lithium half-cell setup with lithium as a counter electrode and 1 M $LiPF_6$ in EC/DEC (1/1) as an electrolyte.

Charging-discharging tests at different current densities (Figure 5.13a) were performed between 0.05 A g^{-1} and 0.80 A g^{-1}. Within the first three cycles, capacity increases and slowly starts to decrease afterwards, as already discussed above. At higher charging-discharging rates up to 0.80 A g^{-1}, capacity is only moderately decreased and restored to almost initial values after the current density returns to 0.05 A g^{-1} again, prominently supporting diffusion- and surface-controlled charge storage. Discharging curves at different current densities (Figure 5.13b) generally appear as almost straight lines with slight indication of a belly shape

indicating dominant capacitive behaviour with some added distinct quinone-hydroquinone redox reactions, respectively.

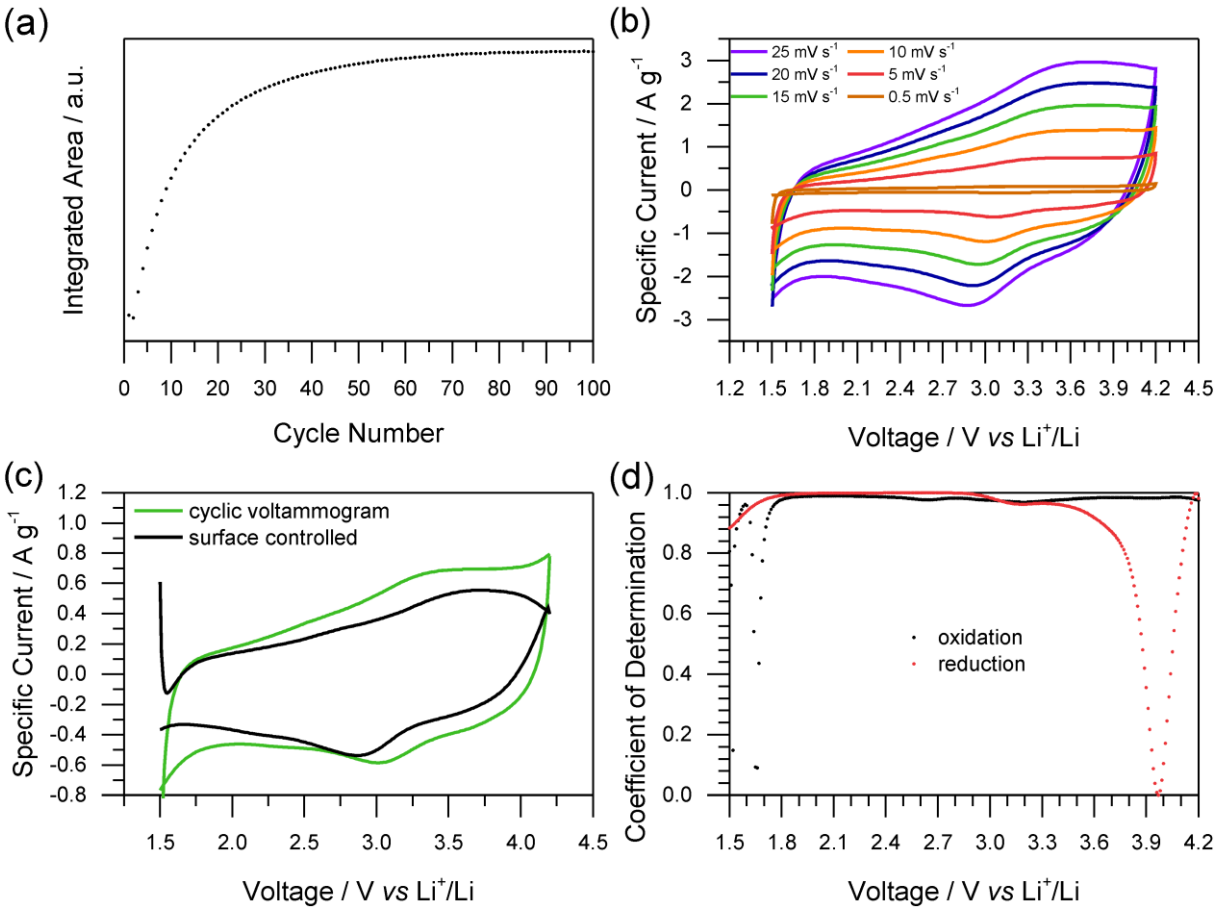

Figure 5.14. (a) Integrated area of cyclic voltammograms of C/P-o at 25 mVs^{-1}. (b) Cyclic voltammetry at different rates as indicated. (c) Surface controlled contributions to capacity at 5 mV s^{-1} as calculated from cyclic voltammetry at different rates. (d) Coefficient of Determination (*aka* R^2 value) for calculation of surface and diffusion controlled contributions to charge storage as calculated from data presented in (c). The test was performed in a lithium half-cell setup with lithium as counter electrode and 1 M $LiPF_6$ in EC/DEC (1/1) as electrolyte.

As the integrated area of cyclic voltammograms is slowly increasing within some tens of cycles (Figure 5.14a), for better comparability the hybrid material was first cycled for 100 cycles at 25 mV s^{-1} followed by cycling at 20, 15, 10, 5 and 0.5 mV s^{-1} for one cycle each. Figure 5.14b shows cyclic voltammetry curves of C/P-o at different rates. CV curves show clear oxidation and reduction peaks at 3.6 and 2.8 V respectively, matching the range of belly-shaped behaviour in galvanostatic charging-discharging curves. Using the performance at different cycling speeds, the ratio of surface and diffusion controlled charge storage was calculated.[127–129] The current response (I) at a certain potential can be separated into two contributions: surface controlled (proportional to scan rate v) and diffusion controlled (proportional to square root of scan rate SQRT(v)). Upon linearization of this reaction one obtains:

$$\frac{I}{\sqrt{v}} = k_1\sqrt{v} + k_2$$

Therefore, by measuring the current response at different scan rates one can calculate diffusion and surface controlled current response and subsequently Farradaic and capacitive contributions to overall energy storage.[23,127–129]

Except for the limits between which cyclic voltammetry experiments were performed, the resulting curve for the capacitive contribution to charge storage (Figure 5.14c, black curve) resembles the cyclic voltammogram of C/P-m (Figure 5.8a, blue curve). In both cases, capacity is roughly 80 % as high as in case of C/P-o (84.8 % comparing Figure 5.8a, blue and red curve, and 74.8 % comparing Figure 5.14c black and green curve, respectively), confirming the importance of the effect of hydrophilicity on charge storage and matching the results of galvanostatic experiments (redox-reactions in C/P-o responsible for 18.1 % of charge storage). Addition of P-o to carbon clearly not only introduces the possibility of Faradaic charge storage but also facilitates capacitive charge storage. The notable differences between the calculated capacitive contribution to charge storage in Figure 5.14c and charge storage in C/P-m (Figure 5.8a, blue curve) at low and high voltages can be ascribed to limitations of the assumed model, expressed by a low coefficient of determination (*aka* R^2 value, Figure 5.14d) due to the sudden increase or decrease in current density at the edges of cyclic voltammograms. Slight differences between capacitive charge storage in C/P-m and calculated capacitive contribution to C/P-o as denoted above can be primarily ascribed to the aforementioned collapse of the model at the edges of cyclic voltammograms.

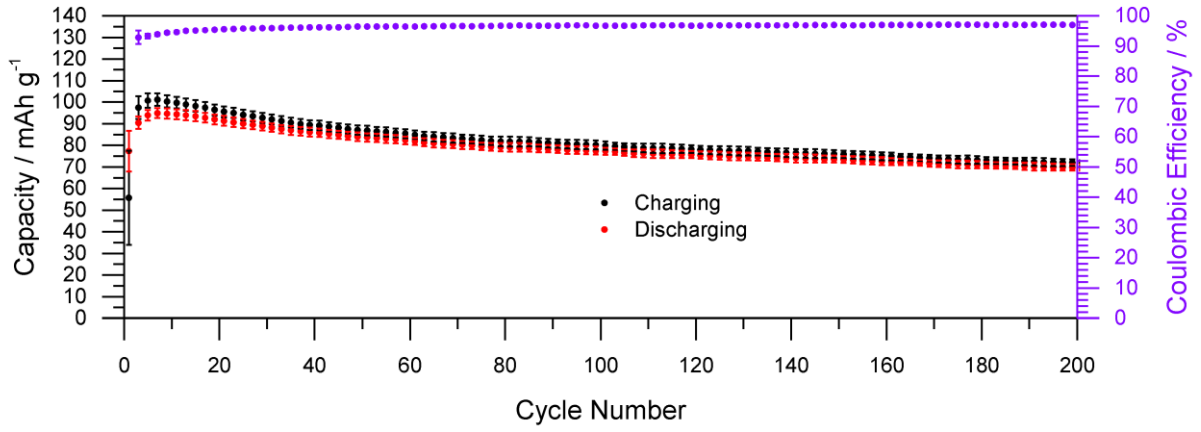

Figure 5.15. Long-term stability test at 0.1 A g^{-1} (every third data point is shown). The test was performed in a lithium half-cell setup with lithium as counter electrode and 1 M $LiPF_6$ in EC/DEC (1/1) as electrolyte.

During long term cycling at 0.1 A g^{-1} (Figure 5.15), capacity slowly decreases as is generally observed for organic systems (see discussion above). However, a remarkable retention of 73.5 % is observed after 200 cycles (in average 0.13% decay of capacity per cycle). The high coulombic efficiency of approximately 97% makes P-o a promising polymer for electrochemical energy storage applications.

5.2.6. Conclusion

Polymers made from polyallylamine and redox-active and inactive aldehydes were used as model compounds of biogenic polymers in order to elucidate different contributions to electrochemical energy storage in future bio-based batteries and lithium ion capacitors. In the systems under investigation, which included carbon, binder, and the active or inactive polymer, only 18.1 % of the capacity could be ascribed to distinct redox reactions. The samples with the inactive polymer still showed significantly higher capacity than microporous carbon itself, and the difference was ascribed to increased hydrophilicity of the capacitive hybrid material that causes better wettability by the electrolyte as well as lithium transport behaviour. Therefore, it can be concluded that a significant portion of capacity of electrochemical energy storage devices based on natural polyphenols stems from capacitive charge storage on hydrophilic surfaces in addition to redox activity. Furthermore, electrochemical performance in a lithium organic system of model polymers containing redox-active catecholic groups was compared to such with naturally abundant guaiacyl groups. Both showed similar performance after prolonged cycling, with slower initial rise in capacity for guaiacyl-containing polymers due to slow demethylation processes. Based on these findings a biomass derived hybrid material was prepared that showed excellent properties for electrochemical energy storage in lithium-organic systems with capacity of over 100 mAh g^{-1} at 0.05 A g^{-1} and capacity retention of 73.5% after 200 cycles at 0.1 A g^{-1}.

5.3. Influence of carbon porosity on the performance of redox active polymer – carbon hybrid materials

Activated carbons, due to their low price, derivability from biowaste, and good conductivity hold great promise for electrochemical energy storage as part of hybrid materials with bioderived polymers. However, as demonstrated in the previous chapter, porous carbons cannot be simply regarded as passive elements of the hybrid material, as their properties are influenced by the chemical nature of the polymers. Therefore, it is of great interest to study the interface of these two components. To the best of my knowledge, only one such a study has been conducted in which the compared carbons had fundamentally different surface chemistries, hampering reliable conclusions.[130] In contrast, porosity of carbons has been recognised as an important feature for the design of carbon based EDLC capacitors. In those systems, it was found that total surface area does not linearly correlate with capacitance, while the hierarchical structure of carbons is more important.[7,131–133] In this chapter, influence of carbon mesoporosity on the electrochemical performance of carbon polymer hybrid material will be investigated.

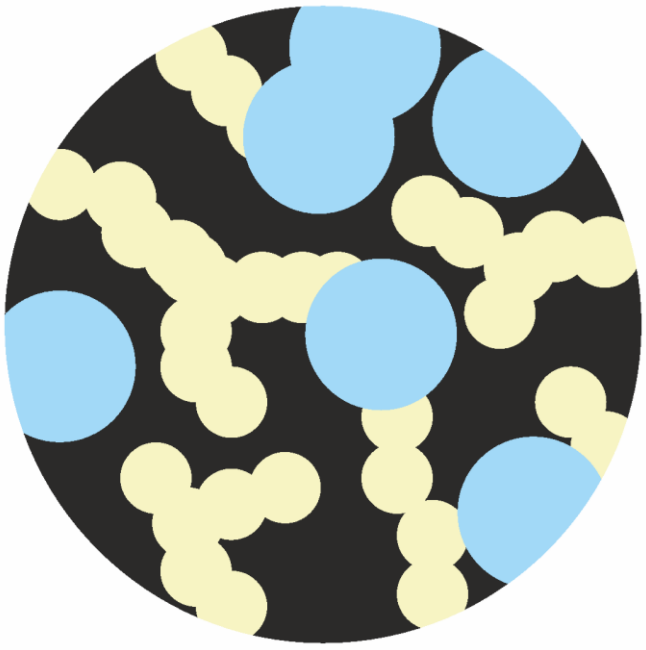

Figure 5.16. Most of the carbons containing high surface area are characterised with external surface area (white-black interface), mesopores (blue-black interface) and micropores (yellow-black interface). Understanding of interface between a carbon and a polymer is needed.

Milena Perovic synthesised carbons STC-1, STC-2, STC-4 and STC-8 and she characterised them *via* nitrogen physisorption measurements.

5.3.1. Synthesis of a set of porous carbons

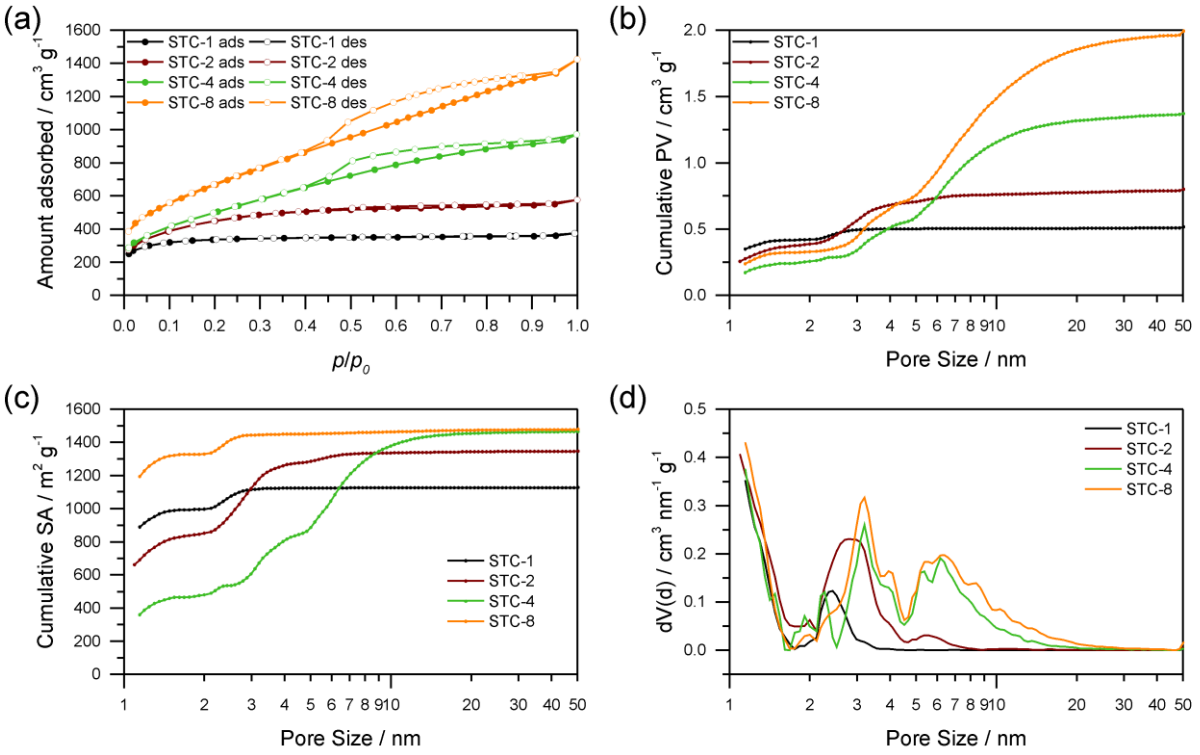

Figure 5.17. Nitrogen sorption measurements for different STCs. (a) Isotherms. (b) Cumulative pore volume. (c) Cumulative surface area. (d) Pore size distribution.

Salt-templated carbons (STCs) with varying pore structures were prepared by carbonisation of sucrose in the presence of the different amounts of zinc chloride as a template that was washed out afterwards. All carbons were named STC-X where X denotes the mass ratio of zinc chloride to sucrose before carbonisation.[133] As indicated in Figure 5.17 and Table 5.2, this zinc chloride to sucrose ratio determines the amount of mesopores in STCs, while the amount of micropores is similar in all the carbons. STC-1 had a very small amount of mesopores with uniform pore size around 2.4 nm. In STC-2, both the amount and size of mesopores are only slightly larger (around 2.8 nm). STC-4 and STC-8 however were significantly different from the aforementioned STCs: both have a bimodal size distribution of mesopores, with most abundant pore sizes in the range of 3.2 and 6.3 nm. The main difference between STC-4 and STC-8 is the additional occurrence of even larger mesopores, larger than 10 nm, in STC-8. This significant difference of pore size distributions between the STCs make them a great candidate to compare influences of mesoporosity on the contact between the redox active polymer and the porous carbon.

Table 5.2. Nitrogen sorption measurements for different STCs.

Name	SSA_{BET} / m^2 g^{-1}	V_{micro} / cm^3 g^{-1}	V_{meso} / cm^3 g^{-1}	V_{total} / cm^3 g^{-1}	Avg. size / nm
STC-1	1272	0.42	0.14	0.58	1.82
STC-2	1610	0.39	0.46	0.89	2.22
STC-4	1821	0.25	1.20	1.51	3.31
STC-8	2429	0.33	1.75	2.21	3.64

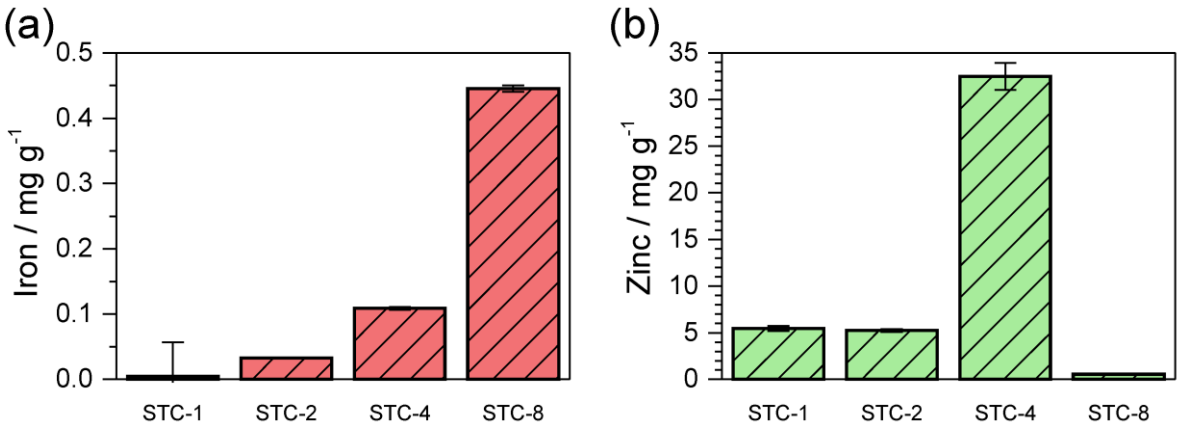

Figure 5.18. Iron (a) and zinc (b) content in the different STCs as calculated from ICP-MS.

Combustive CNHS elemental analysis of the prepared samples (Table A4) indicate that the samples are made primarily of carbon as expected, and high amount of sulphur. Sulphur contamination can be explained by sulphuric acid used during synthesis for dehydratation of sucrose. ICP-MS data (Figure 5.18) suggests low levels of iron contamination in prepared samples along with varying levels of zinc contamination. Zinc contamination in STC-1 and STC-2 is low, around 0.5% and even lower for STC-8, around 0.1%. Although STC-4 contains around 3% of zinc, it is still negligible and interaction with the electrochemical measurements is not expected.

In order to exclude falsification of results caused by changes of hydrophilicity, not only hybrid materials of STCs with the redox active polymer P-o but also with redox inactive P-m (STC-x/P-o and STC-x/P-m, respectively) were prepared. Conductive additives and binder were added to all compositions to further exclude influences of conductivity or stability of the different STCs on the hybrid materials' performance. As P-m is not redox active, capacities of different STC/P-m samples indicate the difference between the STCs.

5.3.2. Electrochemical behaviour of hybrid materials containing redox active and inactive polymers and porous carbons

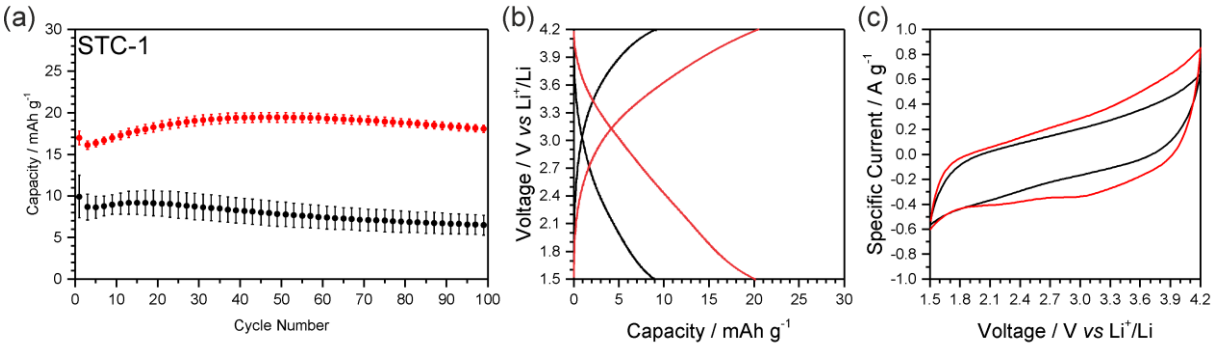

Figure 5.19. Electrochemical behaviour of STC-1/P-o and P-m. (a) Capacity as derived from charging-discharging measurements at 0.2 A g^{-1} for 100 cycles. (b) 50th charging-discharging cycle for said measurements. (c) Cyclic voltammogram (30th cycle) at 25 mV s^{-1}.

STC-1/P-o shows significantly higher capacity than STC-1/P-m (Figure 5.19). However, the reason for this behaviour might not be redox activity as both cyclic voltammogram and discharge curve show redox activity only in traces. Furthermore, both composites show rather low capacity as described previously, due to the inability of electrolyte to effectively diffuse through the micropores.

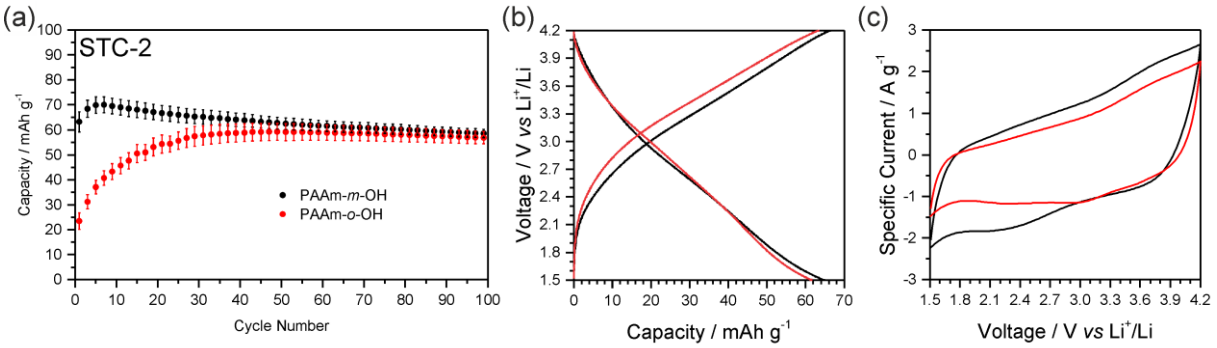

Figure 5.20. Electrochemical behaviour of STC-2/P-o and P-m. For details see caption 5.19.

Surprisingly, STC-2/P-o shows significantly lower capacity than STC-2/P-m (Figure 5.20). However, upon prolonged cycling the capacities reach similar level. STC-2 hybrid materials show much higher capacities than STC-1 due to significantly increased amount of mesopores. However, STC-2/P-o does not show significant contribution of redox active moieties.

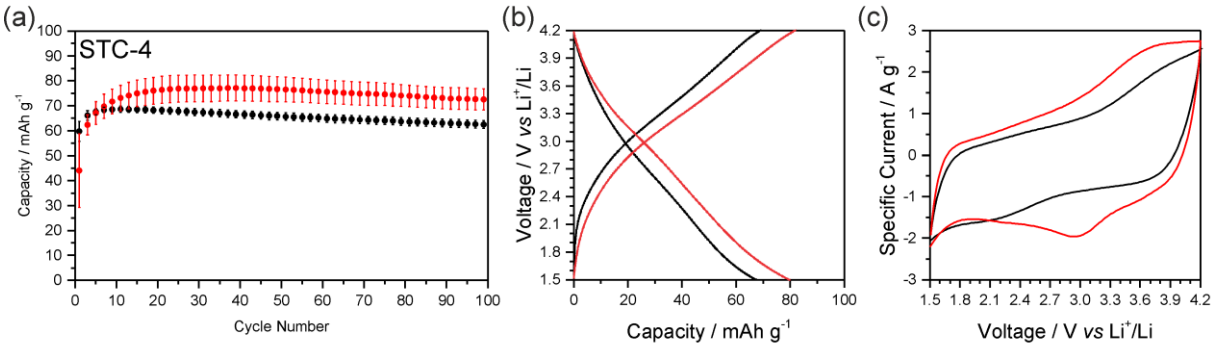

Figure 5.21. Electrochemical behaviour of STC-4/P-o and P-m. For details see caption 5.19.

STC-4/P-o shows much higher capacity than STC-4/P-m (Figure 5.21). However, in this case the reason can be attributed to redox activity of P-o as both discharging curve and cyclic voltammetry clearly indicate redox activity around 3.3 V.

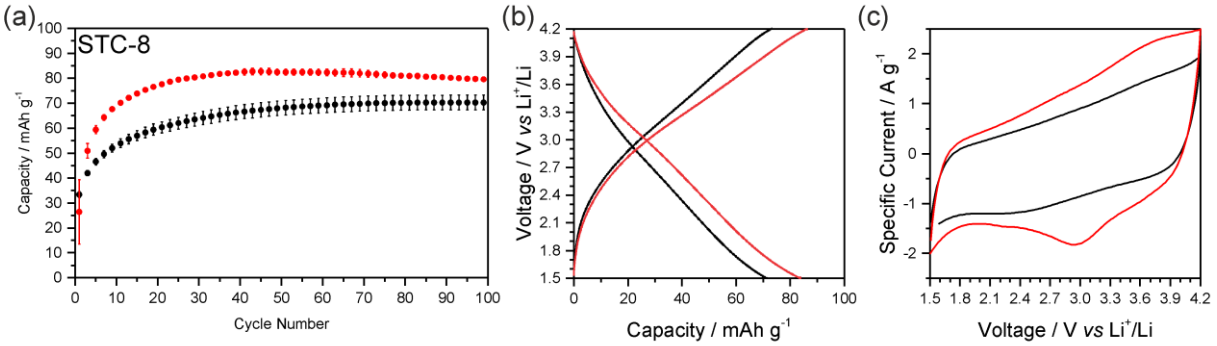

Figure 5.22. Electrochemical behaviour of STC-8/P-o and P-m. For details see caption 5.19.

Similar to the case of hybrid materials based on STC-4, STC-8/P-o shows much higher capacity than STC-8/P-m (Figure 5.22). Furthermore, both discharge curves and cyclic voltammograms indicate clear redox behaviour. Interestingly, in contrast to the rest of the hybrid materials containing P-m, there is slow increase in capacity of STC-8/P-m during all 100 cycles.

5.3.3. Interface between the carbon and polymer – importance of the mesopores

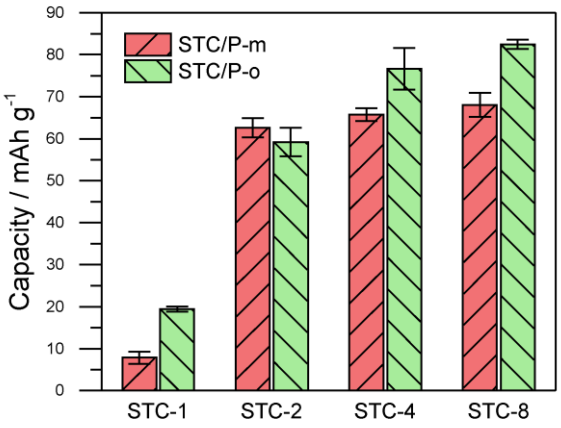

Figure 5.23. Summary of the electrochemical behaviour of hybrid materials containing different STCs and P-o or P-m, 50th discharging cycle as calculated from aforementioned charging-discharging measurements.

Figure 5.23 contains a summary of different hybrid material behaviors as presented before. Differences in capacities and redox contribution between different hybrid materials remain to be explained. This phenomenon was described for STC-1 previously in an ionic liquic electrolyte, explained by the low mesoporosity of STC-1.[133] Accessibility of micropores by the electrolyte in STC-1 is hindered but greatly increases with the introduction of mesopores (STC-2/3/4) where mesopores serve as a connection between micropores.

All hybrid materials with redox active polymers show a significant increase in capacity within the first cycles. Capacity in hybrid materials with the redox inactive material in contrast slowly decreases, except for STC-8/P-m. This behaviour can be explained by the larger mesopores of STC-8 in contrast to other STCs that allows the material to tangle inside allowing for the better passage of electrolyte.

The highest redox activity, observed for STC-4/P-o and STC-8/P-o, correlates with the high amount of large mesopores they contain. The presence of large mesopores during formation of the hybrid material in general offers the possibility for the polymer to enter the carbon material. Such a tight composite allows for the easy exchange of electrons between the carbon and the polymer, facilitating efficient redox reactions. This layout may also help to prevent dissolution of the polymer as the pores serve as a protective layer for the polymer. Furthermore, increased redox capacity in STC-8 as compared to STC-4 correlates with the higher amount of large mesopores found in STC-8, supporting the assumption of the importance of mesopore volume for efficient redox activity.

In contrast, hybrid materials containing STC-2 show almost the same capacity after prolonged cycling. Increasing capacity of STC-2/P-o with cycling, similar to the other hybrid materials with redox active polymer, may indicate similar behaviour and redox activity, but neither cyclic voltammogramas nor the shape of charging-discharging curves support this assumption, due to almost triangular discharging curves, and very small redox peaks in the cyclic voltammogram.

Figure 5.24. Proposed model of interaction between carbon (black), micropores (small holes), mesopores (big pores) and polymer (red)

STC-2 behaviour is complex and hard to explain, however a following model is proposed. In comparison to STC-4 and STC-8, STC-2 has a lower amount of mesopores, which are also smaller, enabling only a small fraction of polymer to enter the carbon material and preventing efficient charge transfer. The polymer chains which enter the pores may get anchored inside them, preventing dissolution in the electrolyte. Additionally, the hydrophilicity of the polymers increases the wettability of external surfaces of carbon, allowing for a better contact with the electrolyte. Therefore, there is no significant difference in performance of STC-2/P-o and STC-2/P-m upon prolonged cycling.

However, this behaviour does not explain the significantly higher capacity observed for STC-1/P-o compared to STC-1/P-m. This behaviour could be ascribed to the redox activity in P-o but charging-discharging curves show no trace of a belly and there are no clear redox peaks distinguishable in voltammogram. Therefore, this abrupt increase in capacity must have another explanation, and the crosslinking of P-o during partial oxidation is suggested as a cause. Condensation of quinones during chemical oxidation occurs as a result of the homocoupling of aromatic rings in ortho position to the aromatic centre.[134] Therefore, P-o lying on the external surface of the STC-1 particles is partially oxidised, forming dimers that crosslink P-o and thus binding P-o around the external surface. Furthermore, due to its

electrophilic nature in contrast to PVDF, Po helps the electrolyte to wet the external surface of STC-1 ultimately increasing the capacity of the composite. In contrary, P-m has no redox active moieties and therefore it does not undergo oxidation nor dimerisation, failing to form a crosslinked network on the external surface, and ultimately does not contribute to the capacity of STC-1/P-m. However, this theory requires additional evidence.

5.3.4. Conclusion

Various hybrid materials containing porous carbons and redox active and inactive polymers have been prepared. Produced hybrid materials display rather complex redox behaviour that requires further investigation. However, correlation between the amount of mesopores and redox activity is observed. The proposed model suggests that polymers are residing in the pores or, if there is small amount of pores, are entangled disabling charge transfer between the polymer and carbon and consequently the redox activity. Furthermore, with no mesopores present the polymers reside on the surface without significant redox activity. However, at the moment there is not enough evidence to support these theories and the further investigations are needed.

6. Truly sustainable cathode materials for lithium based electrical energy storage devices

In the previous chapters various redox active materials derived from vanillin and protocathecuic aldehyde were presented. Although the redox-active moieties of these materials come from biowaste, from lignin, and therefore are sustainable, other catalyst and reagents, such as triflic acid and polyallyamine, reduce the sustainability of the resulting cathodes. However, from the lessons learned in the previous chapters it is possible to use naturally occurring polymers to synthesise truly sustainable cathodes. Furthermore, previous chapter described a biobased carbon rich in mesopores, STC-8, which showed an optimal performance in hybrid materials with biobased redox active model polymer.

Part of this chapter is adapted from my original work

1) Ilic, I. K.; Tsouka, A.; Perovic, M.; Hwang, J.; Heil, T.; Loeffler, F. F.; Oschatz, M.; Antonietti, M.; Liedel, C. Sustainable Cathodes for Lithium-Ion Energy Storage Devices Based on Tannic Acid—Toward Ecofriendly Energy Storage. *Adv. Sustainable Syst.* **2020**, 2000206 (This article is licensed under a Creative Commons Attribution 4.0 International)

6.1. Sustainable Cathodes for Lithium Ion Energy Storage Devices based on Tannic Acid – Towards Eco-Friendly Energy Storage

Tannic acid is a good choice for design of truly sustainable cathodes due to its natural abundance and richness in redox active groups. Furthermore, tannic acid contains pyrogallolic groups that, due to similarity to catecholic group, represent the best naturally derived redox active centres. Synthesis of an organic cathode material from tannic acid and microporous carbon derived from biomass is reported. Sustainable, crosslinked, binder-free hybrid material by ball-milling and drying is prepared without any further chemical treatment. All constituents including redox active material and carbon additive are available from renewable resources. The low cost, eco-friendly material shows outstanding performance with capacity above 105 mAh g^{-1}, at 0.1 A g^{-1} in lithium-ion electrolyte. With the redox couple at approximately 3.4 V vs. Li^+/Li, the cells also feature one of the highest reversible redox potentials reported for biomolecular cathodes so far.

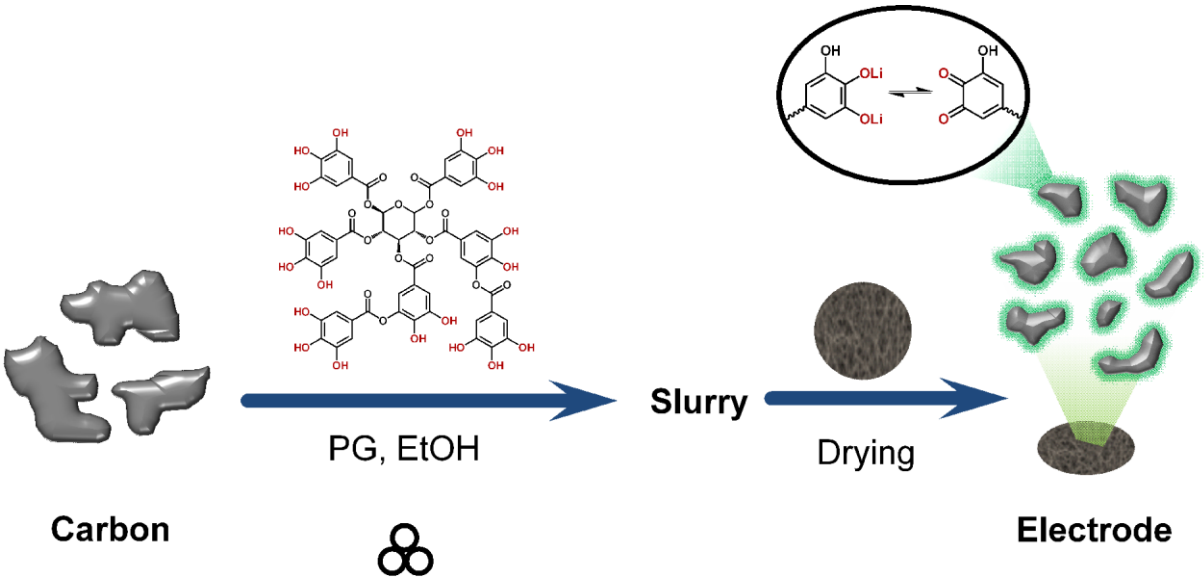

Figure 6.1. Redox activity of tannic acid can be utilised for the formation of cathodes

Jinyeon Hwang helped designing the electrochemical experiments and interpreting them. Additionally, Figures 6.1 and 6.3 are based on his design. Milena Perovic synthesised the carbon and she characterised it *via* nitrogen physisorption measurement. Tobias Heil made the TEM measurements and he helped with their interpretation.

6.1.1. Synthesis and characterisation of carbon - tannic acid hybrid material

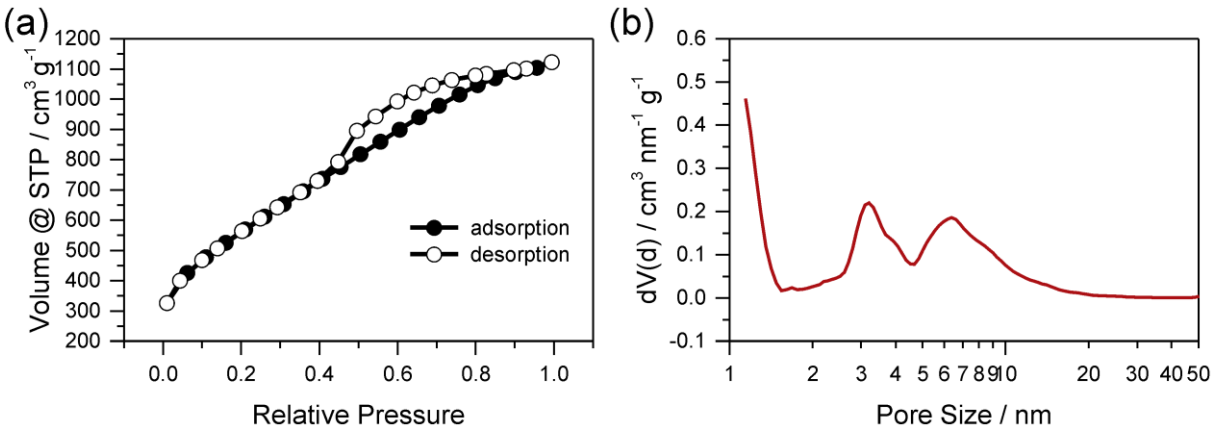

Figure 6.2. Nitrogen physisorption of synthesised carbon at 77 K. (a) Isotherm. (b) Pore size distribution.

Firstly, a sucrose derived carbon STC-8 was synthesised as described previously and additionally reduced in order to increase conductivity.[135] As this is the only carbon used in this chapter, furthermore, it will be referred to as carbon (C(pristine)). The porosity of the carbon was investigated using nitrogen sorption at 77 K (Figure 6.2.). Alike nonreduced STC-8, obtained carbon is microporous with significant portion of mesopores.

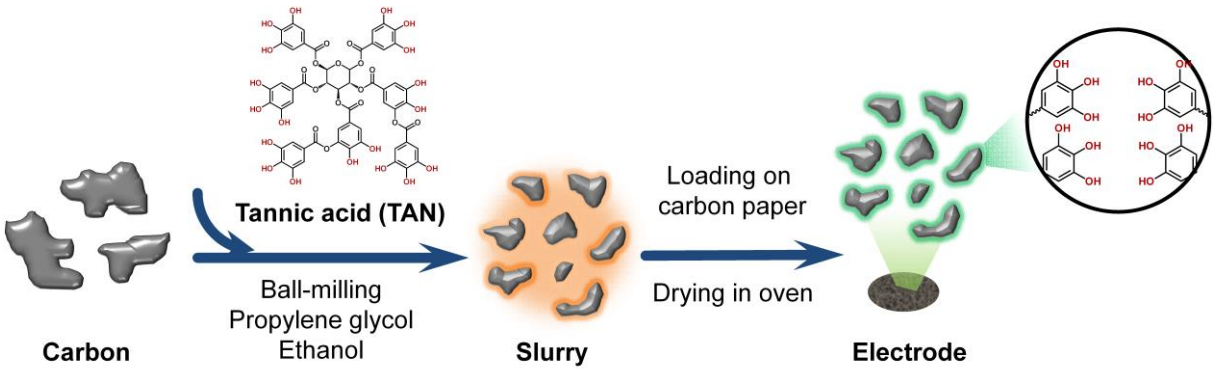

Figure 6.3. In order to assure good contact between tannic acid and carbon both were ball milled facilitating formation of the hybrid material.

Good solubility of tannic acid in water and polar organic solvents of low toxicity, such as ethanol, allows for an easy extraction from plant-based waste such as bark.[69] However, the same also implies solubility in conventional electrolytes, limiting tannic acid's applicability in electrochemical devices where in principle it has great potential due to its abundant redox active groups, low price, and natural abundance. In order to mitigate solubility and increase conductivity, which is another issue of many organic active materials including tannic acid (TAN), it was mixed with the prepared carbon (C(pristine)). Preparation of the hybrid material was facilitated with ball milling, yielding hybrid materials with the good contact

between the components. Not only does this approach prevent dissolution of tannic acid, but tannic acid also acts as a binder in the formed composite electrodes, allowing for the omittance of halogenated binders and increasing the sustainability of the material.[136] Similarly, graphene sheets that stabilise tannic acid by π-π interactions between tannic acid and graphene were used previously.[136] However, graphene is rather expensive and hard to produce from renewable resources and therefore not suitable for truly sustainable electrodes. High surface area carbon additives in general enable the stable fixation of redox-active organic materials onto the carbon support and maximize the exposed reaction sites located at the interface to the electrolyte.[137] Biowaste derived carbons with high surface area are rather appealing in terms of sustainability.

Table 6.1. Different ball milling procedures of C(pristine) and TAN.

Name	C(pristine) / mg	TAN / mg	Grinding method
C(50 min)	54	0	neat grinded for 50 min
C(50 min)/TAN	36	24	C(pristine) was neat grinded for 50 min, and afterwards TAN dissolved in PG was added for 10 more min
C/TAN	36	24	C(pristine) and TAN were neat grinded for 50 min, and afterwards PG was added for 10 more min
C/TAN(PG)	36	24	C(pristine) and TAN were mixed with PG and grinded for 60 min

For optimal stabilisation of TAN by establishing π-π interactions between tannic acid and carbon, a number of combinations of neat grinding and liquid assisted-grinding were investigated (Table 1).

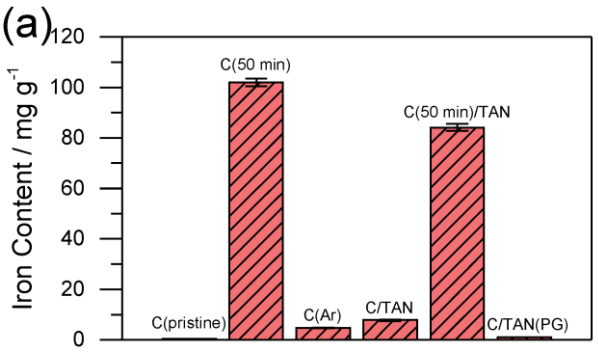

Figure 6.4. Iron content of C(pristine), C(50 min) and different hybrid materials of C and TAN prepared in a ball mill.

Stainless steel jars equipped with stainless steel balls were used for the preparation of hybrid materials resulting in incorporation of iron into the materials, as examined by ICP-MS (Figure 6.4), and of oxygen, as examined by elemental analysis (Table A5). While the bio-derived carbon C(pristine) contains almost no heteroatoms, during neat grinding it incorporates approximately 10% of iron (C(50 min)) and around 13% of oxygen. In order to understand these contaminations the same sample was prepared and ballmilled in argon atmosphere (C(Ar)). Surprisingly, the iron contamination is negligible, around 0.5% while the oxygen increase remains the same. As a conclusion, oxygen atmosphere enhances iron leakage in the sample while the oxygen modification appears in the later stage, upon exposure of grinded carbon to oxygen from air, probably due to the highly reactive grinded carbon species. Upon subsequent addition of tannic acid (C(50 min)/TAN), the iron content may be slightly reduced but still remains rather high. In samples in which TAN and carbon are grinded together, both with initial addition of solvent and with addition of solvent after 50 min of grinding, iron contamination gets significantly reduced (C/TAN(PG) and C/TAN, respectively). These results indicate that iron, in these samples, indeed is not only complexed by tannic acid as described in the literature.[70,71] More importantly, the results suggest that carbon gets activated during ball milling and reacts with iron from the stainless steel jars and balls. In the presence of tannic acid or solvent, reactive surfaces of carbon may rather interact with these organic materials, resulting in drastically reduced incorporation of carbon into the final material. Such reactions of carbons during ball milling have been previously described in the literature.[116,138–140] The carbon content of C(50 min) is significantly decreased compared to C(pristine) while the oxygen content increases, suggesting further reaction of carbon with oxygen from the air.

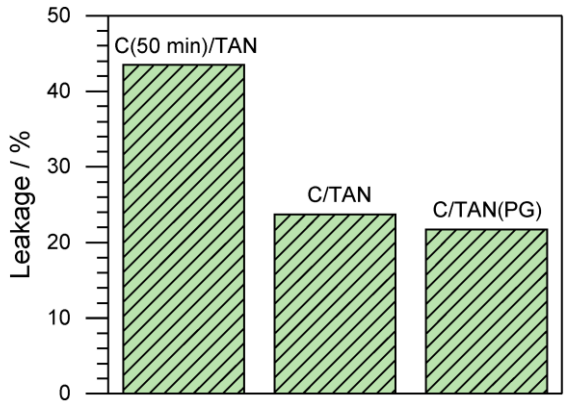

Figure 6.5. Leakage of tannic acid from different C and TAN hybrid materials as determined by UV/Vis.

Crosslinking of TAN with iron salts is the most studied method of tannic acid immobilisation for electrochemical energy storage.[70,71] Incorporation of iron from ball milling into tannic acid based composites may have a similar effect on the stability, and therefore the influence of iron content on the leakage of tannic acid from the hybrid materials using UV-Vis spectroscopy will be discussed next. In this regard, hybrid materials C(50 min)/TAN, C/TAN, and C/TAN(PG) were ultrasonicated with ethanol, and afterwards solids (carbon and stable hybrid material) were removed by filtration. By calibrating with solutions of tannic acid of known concentration (Figure A12), the amount of leaked tannic acid was determined (Figure 6.5). These results indicate that leakage does not correlate with the iron content leading to the conclusion that iron contamination from stainless steel jars and balls does not act as a crosslinking agent for tannic acid. Instead, it can be concluded that through grinding carbon in a ball mill the highly active new surfaces strongly interact with tannic acid forming a rather stable hybrid material. The apparently still rather high leakage levels are caused by rather harsh treatment (ultrasonication) in an exceptionally good solvent for tannic acid, resulting in dissolution of more material than would be the case during battery cycling.

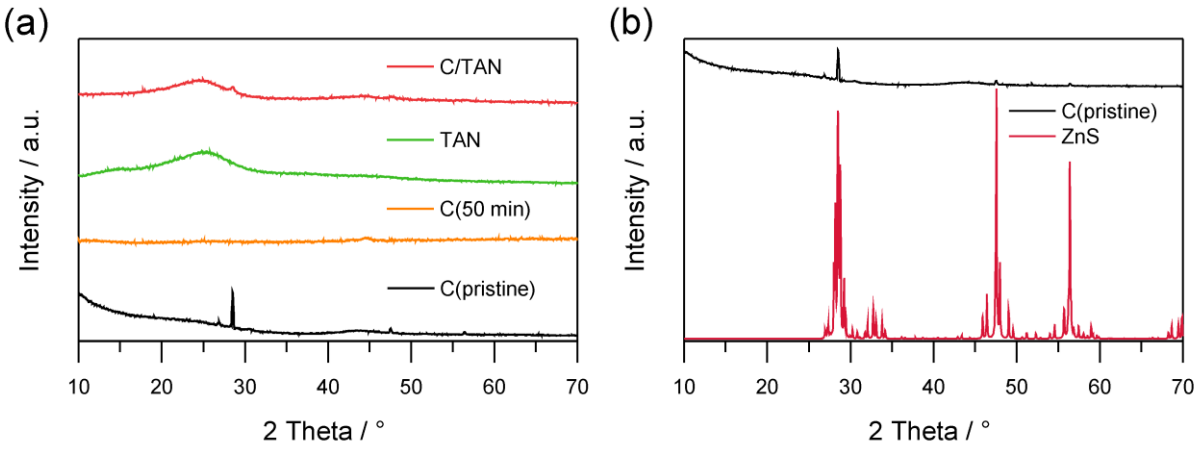

Figure 6.6. (a) Powder XRD measurements of C(pristine), C(50 min), TAN, and C/TAN. (b) Comparison of C(pristine) and zinc sulphide, as calculated from monocrystalline data.

The nature of interaction between carbon and TAN, iron, or oxygen will be discussed next. Figure 6.6a shows diffractograms of XRD measurements. C(pristine) shows multiple sharp diffraction lines indicating contamination with a highly crystalline species, identified as zinc sulphide[141] (which may be formed during the synthesis of sustainable carbons from leftover zinc chloride and sulphuric acid upon reduction (Figure 6.6b)) in an amorphous carbon matrix. The contamination is rather minor though as ICP shows only 8.87 (std. dev. 0.168) mg of zinc per gram of C(pristine). Zinc sulphide is not visible in C(50 min), which also does not include any diffraction lines which would indicate crystalline domains. Especially, no diffraction lines denoting to crystalline iron compounds are observable despite the rather high iron content after ball milling, controverting physical interactions between carbon and iron particles and rather denoting to chemical reactions between carbon and iron during ball milling. In C/TAN, broad diffraction lines denoting zinc sulphide are observable as expected for smaller crystallites after ball milling with increased lattice-microstrain.[87] A characteristic broad diffraction line in the range of 25° results from π-π stacking of tannic acid molecules in the hybrid material, as also visible in the diffractogram of TAN, suggesting the perseverance of intermolecular interactions of the tannic acid in the hybrid material.

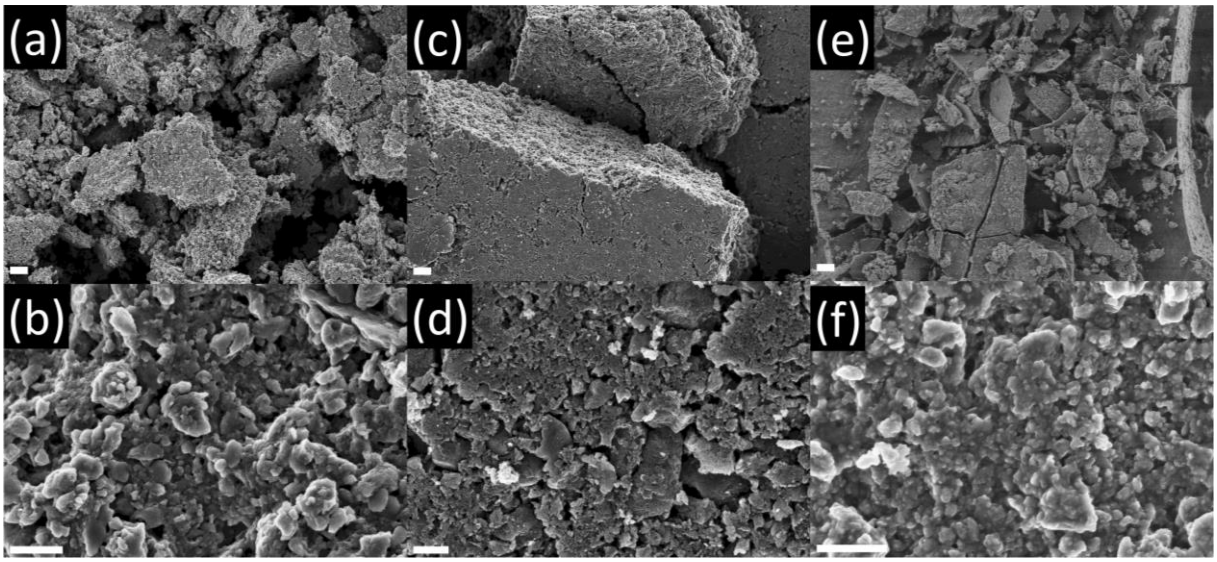

Figure 6.7. SEM images of C/TAN (a,b), C/TAN(PG) (c,d) and C(50min)/TAN (e,f). Scale bars are 10 µm (a,c,e) or 1 µm (b,d,f).

Morphology of different hybrid materials was compared using SEM (Figure 6.7). All the hybrid materials consist of aggregates of smaller particles. The size of the smaller particles remains the same through all the samples. However, density of their packing is higher for C/TAN(PG) and C(50 min)/TAN compared to C/TAN. Ultimately, this leads to larger aggregates in the two former cases making the C/TAN optimal for electrochemical investigation as lower density of particles allows for the better flow of electrolyte.

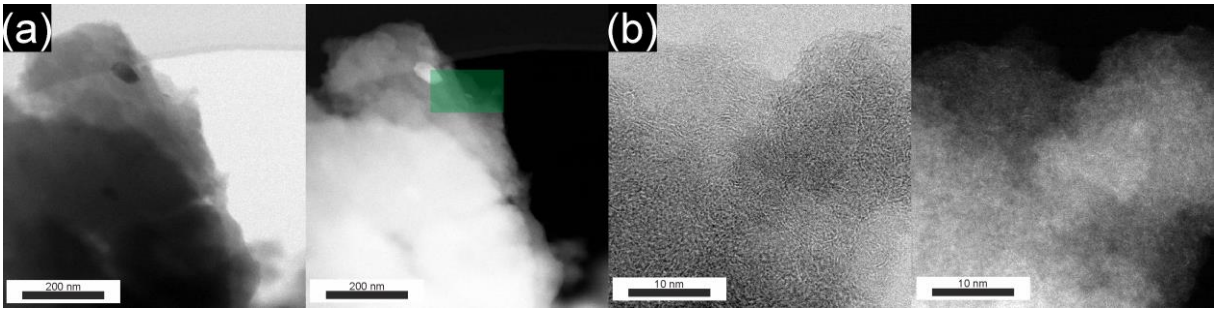

Figure 6.8. STEM images of C/TAN. (a,b) brightfield (left) and darkfield images at different magnifications.

Investigations of C/TAN by STEM are used in order to further characterise the hybrid material (Figure 6.8). The sample under investigation mainly consists of amorphous sheet structures with visible near-range order. In order to determine the state of iron in the sample EELS was performed. Unfortunately, due to the low abundance of iron in this sample no conclusions could be made and therefore EELS of C(50 min) was performed showing two peaks at 705.5 and 706.5 eV indicating presence of iron(0) and iron(II) respectively (Figure A13).

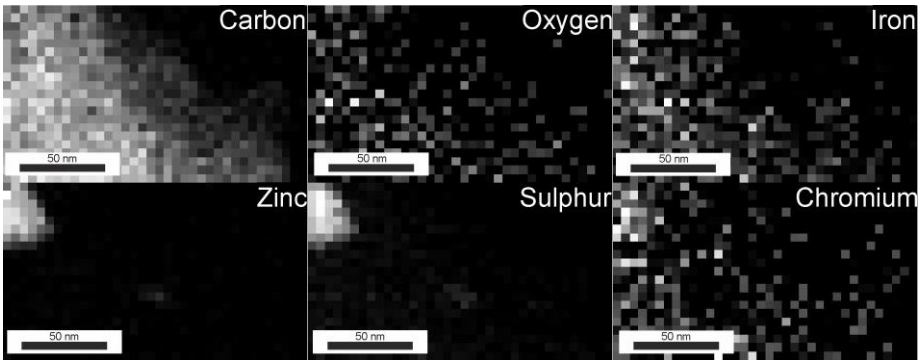

Figure 6.9. EDX imaging of the region highlighted in green in Figure 6.8a for different elements.

The sample is mostly composed of C and O and also show traces of Fe and Cr (from stainless steel), Zn and S (from zinc sulphide), but also of Ca, Na, and Si (from glassware). EDX mapping in Figure 6.9 illustrates the presence of these elements. Carbon, oxygen, iron and chromium can be found regularly distributed across the same area. This observation confirms the conclusion of a carbon-tannic acid hybrid material with small amounts of iron and chromium impurities not organised into big particles but rather being scattered across the sample and thus explains why no iron or chromium compounds are visible in XRD measurements. Zinc and sulphur in contrast are localised exclusively in visible particles, confirming the occurrence of crystallites of zinc sulphide rather than being scattering across the sample.

6.1.2. Electrochemical performance of C/TAN

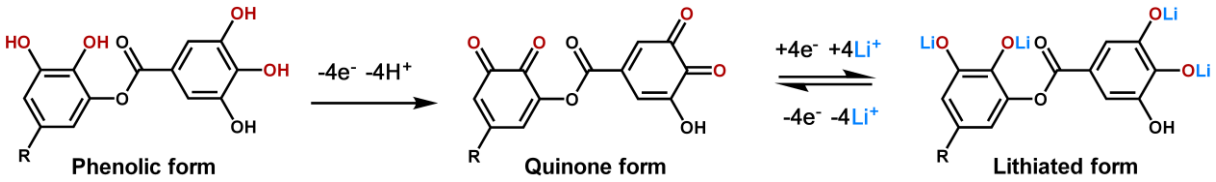

Scheme 6.2. Electrochemical performance of tannic acid.

Due to abundance of electroactive pyrogallolic groups C/TAN was tested as a cathode material in lithium organic system (Scheme 6.2).

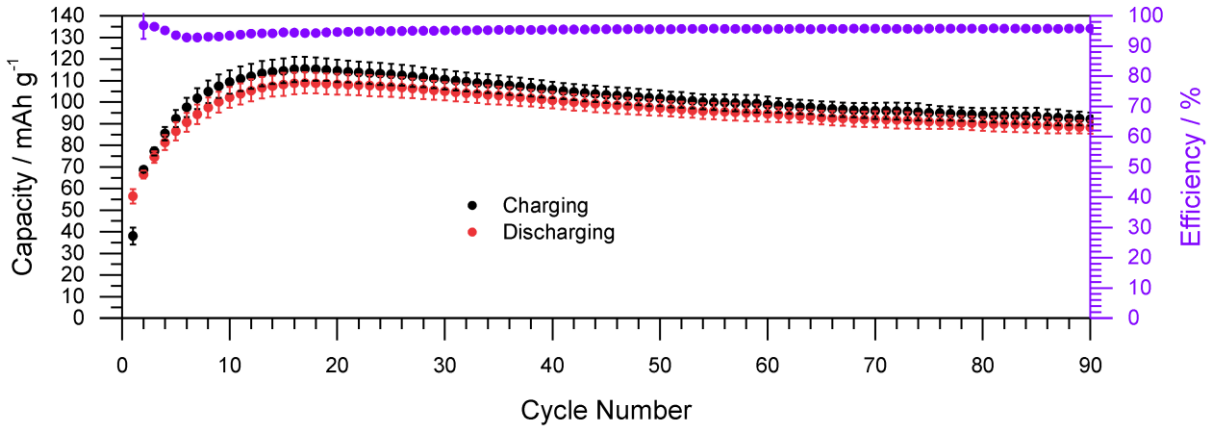

Figure 6.10. Charging-discharging test of C/TAN at 0.1 A g^{-1}.

The electrochemical performance was investigated using charging-discharging tests and cyclic voltammetry: During the first 17 cycles of long term cycling at 0.1 A g^{-1}, capacity is rising and slowly decreases afterwards (Figure 6.10). The initial increase can be ascribed to gradual oxidation of TAN as well as reorganisation of the polymer during cycling which leads to better interaction between TAN and C. The subsequent decrease can be primarily ascribed to deactivation of redox active groups and leakage of tannic acid.[72]

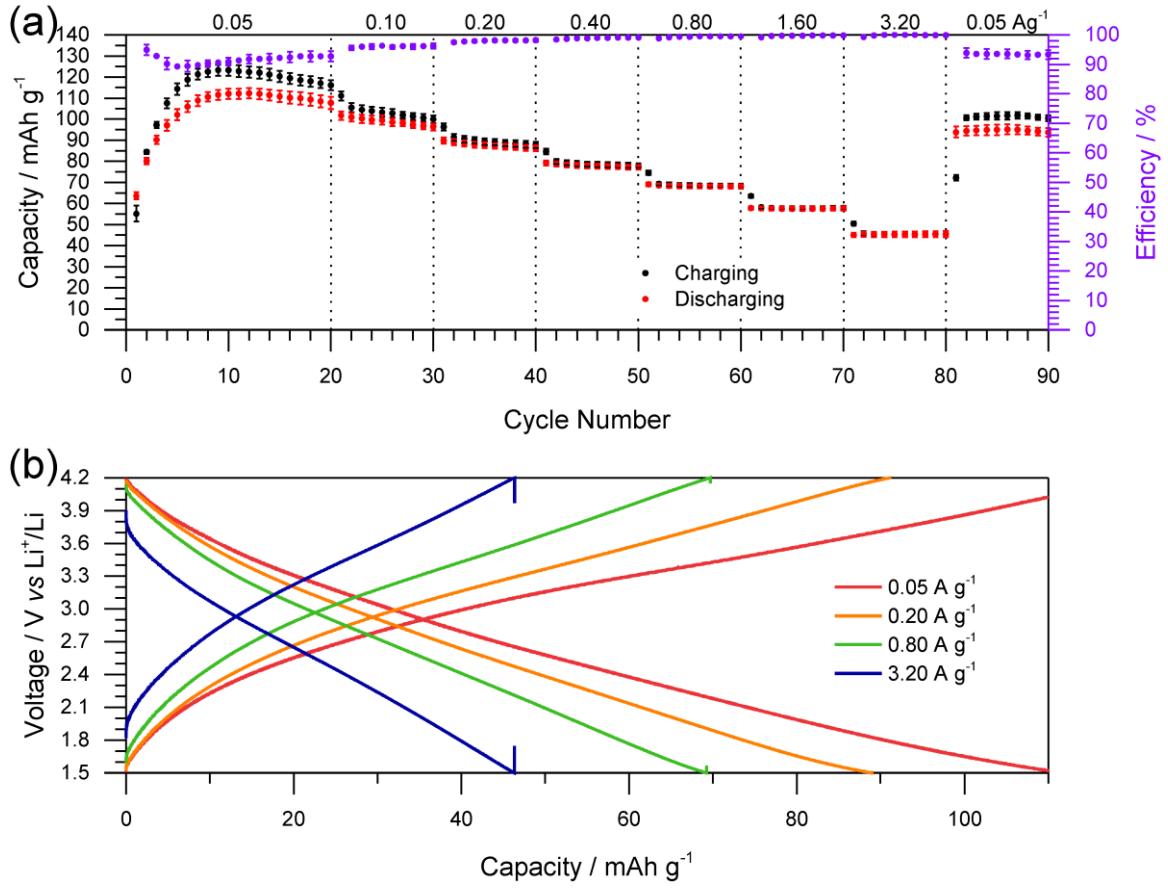

Figure 6.11. Electrochemical performance of C/TAN during charging-discharging tests at different current densities. (a) Cycling. (b) Curves at selected current densities.

This decrease of capacity is comparably low, with 81.1 % retention of capacity after 90 cycles. Furthermore, charging-discharging tests were performed at varying current densities, starting at 0.05 A g^{-1} for 20 cycles followed by increase to 0.1, 0.2, 0.4, 0.8, 1.6 and 3.2 A g^{-1} for 10 cycles each only to be ultimately decreased to 0.05 A g^{-1} for 10 cycles (Figure 6.11). As expected, initially the capacity is rising for 12 cycles to 112.3 mAh g^{-1} only to start to slowly decrease as observed before. At high current density of 3.2 A g^{-1}, still comparably high capacity of 45 mAh g^{-1} is retained. Upon subsequent reduction of the current density to 0.05 A g^{-1} capacity increases again to around 95 mAh g^{-1}. Therefore, it can be concluded that C/TAN can withstand current densities between 0.05 A g^{-1} and 3.2 A g^{-1} without significant degradation.

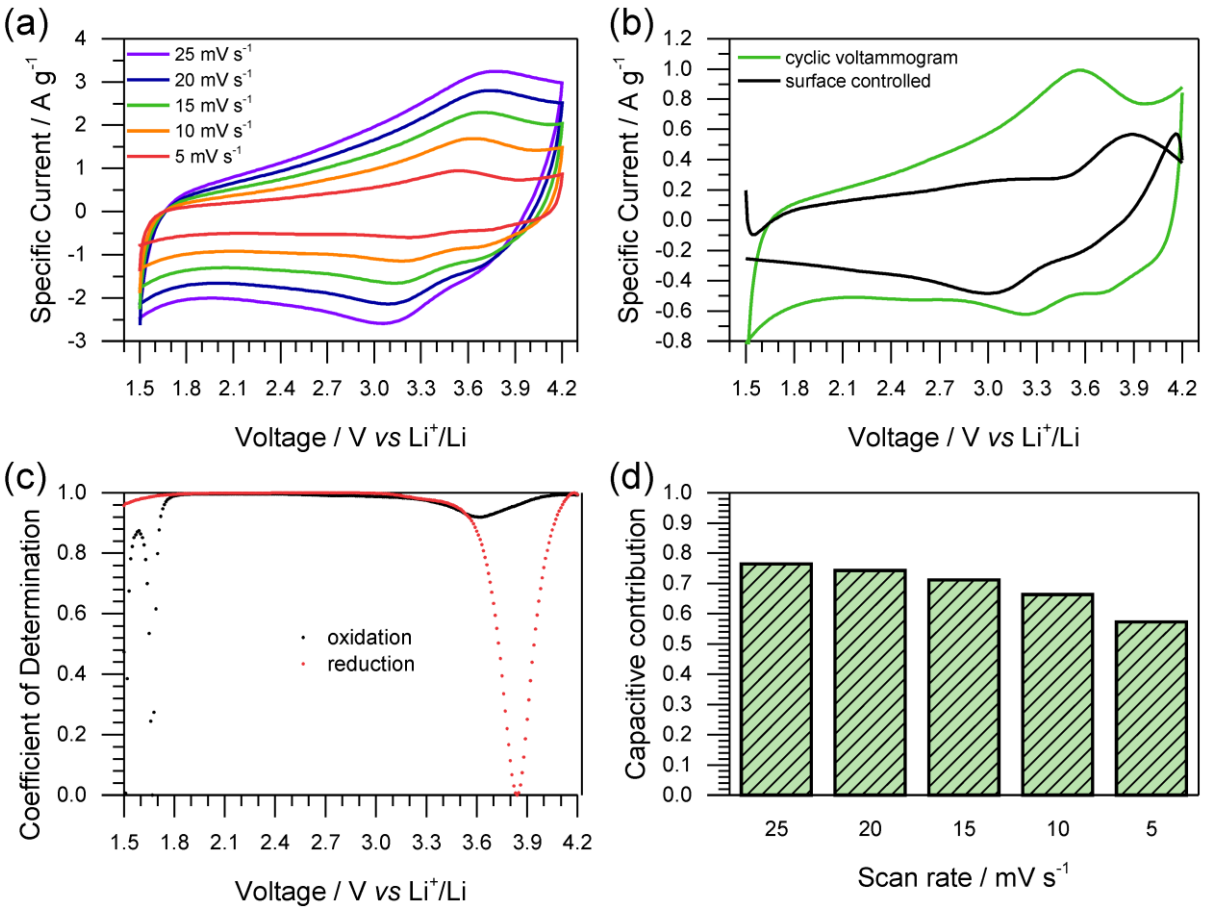

Figure 6.12. (a) Cyclic voltammetry at different scan rates. (b) Surface controlled contributions to capacity at 5 mV s^{-1} as calculated from cyclic voltammetry. (c) Coefficient of Determination (*aka* R^2 value) for calculation as presented in (b). (d) Capative contribution at different scan rates. The test was performed in a lithium half-cell setup with lithium as counter electrode and 1 M $LiPF_6$ in EC/DEC (1/1) as electrolyte.

Cyclic voltammetry of C/TAN (Figure 6.12a) clearly shows oxidation and reduction peaks. The voltage difference between the peaks decreases with the decreasing scan rate indicating semireversible behaviour. The averaged redox potential is at 3.4 V (vs. Li^+/Li) which is

relatively high compared to conventional organic materials and outstanding when compared to other electrodes from regrown biomass. This high redox potential can be attributed to a synergistic interplay of chemical (ester bonds leading to increased redox potential) and physical (hybrid material with high-surface active carbon) characteristics of the material. Especially electron withdrawing groups like electronegative ester bonds increase the redox potential. Furthermore, Faradaic and non-Faradaic contributions to capacity have been evaluated by separating current density in cycling voltammetry weather it is linear with scan rate or square root of scan rate as described in Chapter 5.2.5. This model works well except in the region of high and low voltages as can be seen from R^2 value and easily explained by abruptly rising and falling currents on the very low and high voltages (Figure 6.12c). As expected, Faradaic contribution occurs at the potentials where oxidation and reduction peaks are found (Figure 6.12b). By integrating non-Faradaic voltammogram and dividing it by integrated area of overall voltammogram one can determine the non-Farradaic contribution (Figure 6.12d) and subsequently Faradaic. Faradaic contribution is rather high, between 23.5 % (at 25 mV s^{-1}) and 42.8 % (at 5 mV s^{-1}).

6.1.3. Conclusion

Using tannic acid as an abundant, bio-derived starting material and an eco-friendly ball milling process, sustainable cathode materials for organic lithium based energy storage devices were prepared. Sucrose derived conductive carbon was used as a conductive component that, upon ball milling, forms stable hybrid material with tannic acid. The resulting structures and electrochemical behaviour were extensively characterised, and the hybrid electrodes showed discharging capacities of 112.3 mAh g^{-1} at 0.05 A g^{-1}. No oil-derived binder or carbon additives were used, and electrode slurries were prepared in a benign solvent, demonstrating the truly sustainable nature of the presented electrodes.

7. Conclusion and outlook

The primary objective of this thesis was the development of sustainable cathodes for energy storage in a lithium organic system. Previously reported lignin and tannic acid derived cathodes served as a starting point, due to their prevalence as materials for sustainable cathodes. Therefore, redox active functionalities, guaiacyl and catecholic groups, were introduced in polymers, producing promising cathode materials.

First, vanillin, a guiacyl containing benzaldehyde derivate synthesised from lignin, was grafted via reductive amination onto chitosan, a biowaste derived polyamine. The generated polymer was mixed with microporous carbon, forming a hybrid material with suitable conductivity for electrochemical applications. This composite displayed exceptional electrochemical properties in aqueous acidic solutions, with the redox reaction occurring at higher potentials in comparison to Kraft lignin. Additionally, improved gravimetric capacities over Kraft lignin were ascribed to a higher density of guaiacyl groups. Furthermore, the modularity of the polymer allowed for the introduction of other aromatic groups commonly found in lignin utilizing two aldehydes, namely syringaldehyde and 4-hydroxybenzaldehyde. As expected, 4-hydroxybenzaledehyde based polymer showed no redox activity while syringaldehyde derived polymer displayed redox activity at lower potentials than vanillin as a result of the electron donating effect of the adjacent methoxy group. However, the poor performance of vanillin-based polymer in the lithium organic system could probably be attributed to aliphatic hydroxyl groups that are found in the chitosan backbone.

This problem was solved with the synthesis of the second vanillin-based material outlined in this thesis. A two-step, sustainable synthesis was utilised to modify vanillin to bisvanillonitrile, a molecule containing two fused guaiacyl rings and two nitrile groups. Upon exposure of this molecule to triflic acid vapour bisvanillonitrile polymerised, forming a redox active polymer. Although the details of this polymerisation remain unclear, trimerisation of nitrile functionalities along with demethylation of guaiacyl groups have been observed, indicating the formation of crosslinked catecholic groups containing polymer. Upon introduction of bisvanillonitrile to the porous carbon prior to polymerisation, good contact between the resulting polymer and carbon is achieved with the minimum dissolution, due to interpenetrating networks which allow for the easy transport of electrons through the hybrid material. The formed material displayed excellent properties in the lithium organic system exhibiting charge storage capacities more than twice as high as pure porous carbon. In

addition, this material presented good stability with clear redox behaviour observed at high potentials, even though the redox activity contributes to only a fraction of the polymers charge storage.

In order to elucidate various effects which contribute to the performance of sustainable polymers — a model porous carbon polymer hybrid material was developed. A number of benzaldehyde derivatives were grafted onto polyallylamine, utilising a simple imine forming reaction. This approach allowed for a simple tuning of the functional groups on the benzene ring, and therefore testing of the electrochemical properties of a variety of functional groups. Grafting of protocatechuic aldehyde yielded a catecholic rich model polymer. Furthermore, redox inactive isomers of protocatechuic aldehyde, 3,5-dihydroxybenzaldehyde were grafted onto polyallylamine to produce a redox inactive polymer with similar chemical composition. Upon mixing of the polymer with porous carbon the electrochemical properties of the resulting hybrid materials were tested in a lithium organic system.

These hybrid materials allowed for the detailed studies of the electrochemical contribution of redox activity, leading to the conclusion that around 20% of the charge storage in hybrid materials can be attributed to redox activity. However, the hybrid material of the redox inactive polymer showed significant increase in the charge storage compared to the porous carbon, attributed to the increasing wettability of the carbon network as heteroatom rich polymer is introduced in the hydrophobic carbon network. Furthermore, a guaiacyl rich model polymer was prepared by grafting vanillin on polyallylamine and comparing the subsequent hybrid material to the catechol rich one. Guaiacyl groups exhibit the same redox behaviour as the catecholic groups, but the first irreversible oxidation step occurs slowly during cycling in contrast to the fast oxidation of guaiacyl groups in the aqueous acidic electrolyte.

Further elucidation of sustainable polymer and carbon interfaces was made through the comparison of hybrid materials of redox active or inactive polymers with porous carbons of different porosities. A set of four carbons with the similar surface chemistry and microporosity, but significantly different mesoporosity, wered prepared and resulting hybrid materials compared. Further investigation of the precise mechanism is required, however the importance of carbon mesoporosity for hybrid materials with model polymers was established.

Lastly, drawing from these investigations, a combination of methods were employed to create a truly sustainable hybrid material for charge storage. Due to the superiority of catecholic to

guaiacyl groups, tannic acid was used as redox active material in addition to its wide availability as a biopolymer. Sucrose derived porous carbon with high fraction of mesoporosity was employed as a conductive network. The hybrid material was formed via carefully studied ball milling method, and the resulting material displayed good stability to tannic acid leakage. Furthermore, prepared composites require no additional binder as tannic acid acts as one, further increasing the sustainability of the formed hybrid material. The material presented excellent properties as the cathode material with high charge storage and good stability.

Therefore, in this thesis sustainable cathodes applicable in lithium organic system were developed along with the in depth understanding of the behaviour of the common naturally occurring redox active groups; namely guaiacyl and catecholic, in lithium organic system. Furthermore, different contributions to the overall charge storage properties of the hybrid materials with porous carbon and sustainable polymer were clarified highlighting the importance of capacitive network wettability. Additionally, porosity tuning of the carbons was investigated, indicating the importance of carbon mesoporosity for the formation of carbon – polymer hybrid materials.

Further endeavours should focus on the synthesis of novel biowaste derived redox active polymers for energy storage applications, mainly synthesis of guaiacyl or catechol containing polymers from vanillin and other lignin derived small molecules. Special interest should be given to conductivity of such polymers, as the reduction of conductive additive can simplify the process of hybrid material preparation. Additionally, polymerised bisvanillonitrile is of great commercial interest, as vanillin-based polymers with surviving phenolic groups are a great industrial challenge. However, polymerisation was catalysed using triflic acid, a hazardous substance which should be exchanged when considering sustainability. Therefore, a more sustainable polymerisation catalyst is required for this reaction.

Herein developed model polymers, bearing different sustainable groups, should be further developed due to the simplicity of their synthesis. These model polymers could be used for the evaluation of potential redox active moieties, as virtually any moiety could be introduced if attached to some derivative of benzaldehyde. This approach could lead to a plethora of novel bioderived redox active moieties, and therefore more sustainable polymers. Furthermore, the importance of mesopores in porous polymers used for preparation of hybrid materials with sustainable polymers should be investigated further. Importance of such an investigation lies in the development of a model which can predict the charge storage

properties of different hybrid materials. Additionally, degradation mechanisms of catecholic groups in lithium organic system should be investigated in detail, as better understanding of the degradation mechanism grants the opportunity to create stable polymers.

Finally, many sustainable polymers with redox active groups remain untested for their charge storage properties, leaving potential candidates unexplored. As previously mentioned, guaiacyl groups are common in nature, most commonly found in biowaste polymer lignin. Synthesis of the lignin derived hybrid materials for charge storage should be a priority.

When considering sustainable energy as a whole, this thesis stands as a first step toward more sustainable energy storage. Sustainable energy production is one of the main foundations of a sustainable society, but on a global scale, it is worth little if energy produced cannot be stored in a sustainable fashion. Therefore, this thesis demonstrated the design of biowaste derived cathodes usable in lithium ion system as an important next step in the development of a sustainable society.

8. Appendix

8.1. Methods

As I have used many techniques in my previous work, they were already reported previously in my internship report (Free University Berlin, 2017, Synthesis and Characterisation of Crown Ether Based Porous Polymers for Applications in Gas Adsorption and Catalysis – namely NMR) and master thesis (Free University Berlin, 2017, ZIF-11 templated synthesis of polymeric carbon nitride quantum dots for energy applications) and herein presented techniques are based on my previous writing.

8.1.1. Nuclear magnetic resonance (NMR)

Nuclear magnetic Resonance is a spectroscopy technique based on the interaction of the electromagnetic field with the atomic nuclei. Only atomic nuclei with the spin of n + 0.5, where n is a natural number, are NMR active. Equivalent nuclei with different spin don not differ in energy unless put in magnetic field. Based on this principle, NMR distinguishes nuclei in different chemical environment, by putting nucleus in the magnetic field. Nuclei that are most often probed in NMR are ^{1}H and ^{13}C.

Solution NMR is the strongest analytic tool in a synthetic organic chemistry, where products can usually be dissolved in common organic solvents (deuterated, as deuterium is not NMR active). Unfortunately, it can't be used to study materials (as they are usually insoluble), but it is still useful for study of organic precursors of the materials. However, for the insoluble materials solid state NMR (ss NMR) can be used. The underlying principle is the same as for solution NMR but the sample homogenisation technique is different. While liquid NMR relies on homogeneity of solution of sample in the deuterated solvent, solid state NMR is based on spinning of the solid powder that homogenises the sample.

The samples for liquid ^{1}H and ^{13}C NMR were prepared by dissolving the material (10 mg) in the mixture of D_2O (1 mL) and D_3CCOOD (10 µL) in the case of chitosan, vanillin and ChiVan or DMSO (d_6, 0.65 mL) in the case of VN and BVN. The spectra were measured using an Ascend 400 MHz NMR spectrometer (Bruker).

^{13}C solid-state nuclear magnetic resonance (ss-NMR) spectrum was measured at static magnetic field 14.1 T (600 MHZ) with a JEOL JNM-ECZ600R/M1 spectrometer (Japan). ^{13}C single-pulsed NMR experiment was performed at a MAS rate of 16 kHz using ZrO_2 3,2 mm MAS probe. The temperature of VT (variable temperature) cooling air was set to 275 K at a

flow rate of 1070–1335 L/h. Nominal pulse angle 90 °, pulse length 2.13 µs, direct pulse, no CP, no decoupling. The ^{13}C measurement ran with relax delay of 300 s over 100 scans. The spectrum was referenced to external tetramethylsilane (TMS) at 0 ppm as a secondary reference.

8.1.2. Fourier transform infrared spectroscopy (FTIR)

Infrared spectroscopy gives the information about the absorption of the molecule in the IR region (wavenumber between 400 and 4000 cm^{-1}). Electromagnetic radiation in aforementioned energetic region excites vibrations in the molecule and, therefore, from the IR spectra on can gain information about vibrational levels in the sample. As every chemical bond has specific vibrational levels the IR spectroscopy gives information about the bond types in a sample. Fourier transform is a method of data analysis used in the most of the modern IR spectrometers.

Sample preparation for this technique is easy, solid samples can be analysed as powders, without further modifications, by using the attenuated total reflectance (ATR) sampling technique making the ATR FTIR spectroscopy a fast and valuable technique for analysis of the samples, especially of the organic samples where usually multiple bonds can be seen.[142]

FT-IR measurements were performed using a Nicolet iS 5 FT-IR Spectrometer (ThermoFisher Scientific).

8.1.3. Mass spectrometry

Mass spectrometry is an analytical technique that determines the mass to charge ratio of ionised sample. It can be applied to identify organic and inorganic samples both qualitatively and quantitatively.

Firstly, the sample is ionised upon exposure to irradiation. Rapid ions are introduced in a chamber with magnetic field. As ions are charged, magnetic field exerts a force on them proportional to their charge while inertia, proportional to their mass, provides resistance to change of path. Based on this ratio a ratio m/z is determined and therefore the sample can be identified.[143]

Mass spectrometry of BVN was performed by dissolving BVN in acetonitrile. Eluent used was methanol/isopropanol (80/20) with 0.1% formic acid. Mass spectrometer used was LC-MS Agilent 1260.

8.1.4. Inductively coupled plasma atomic emission spectroscopy

Inductively coupled plasma atomic emission spectroscopy (ICP-OES) is a coupled technique. ICP is an ionisation source, operating at high temperatures. OES is an analytical technique that is capable of identifying range of chemical elements from their emission spectra both qualitatively and quantitatively.[144]

ICP-OES was conducted using a Horiba Ultra 2 instrument equipped with a photomultiplier tube detection. The samples were dissolved in aqua regia and filtered prior to analysis.

8.1.5. Gas adsorption and desorption isotherms

Apparent surface area of a material is usually measured by determining adsorption isotherms of a non-reactive gas at cryogenic temperatures. Prior to measurement, measured material should be activated, meaning that all the residual reactants that are left in the pores after synthesis should be removed along with the solvent residues. Usually the activation is performed by washing the material with ethanol and then drying it in vacuum oven at an elevated temperature. Different gasses can be used for the measurement and the nitrogen gas at the 77 K is the most commonly used. Appropriate method for data analysis should be used. The most popular model for gas adsorption is Brunauer–Emmett–Teller (BET) theory. It is based on Langmuir adsorption model, applicable only for monolayers, by assuming that the gas adsorbs on the surface in the infinite number of non-interacting multilayers that can be modelled as Langmuir monolayers. Although it was initially made for flat surfaces, it gives very good results for porous materials. The BET equation:

$$\frac{p/p_0}{n(1-p/p_0)} = \frac{1}{n_m C} + \frac{C-1}{n_m C}\left(\frac{p}{p_0}\right)$$

where n is amount of the nitrogen adsorbed, p is the pressure, p_0 is the saturation pressure, n_m is the monolayer capacity and C is a BET constant. Linearisation of this equation can be done by plotting $\frac{p/p_0}{n(1-p/p_0)}$ vs $\left(\frac{p}{p_0}\right)$. An analysed area should be based on Rouquerol's criteria:

- C should be positive
- region of the plot should be linear
- n_m should correspond to the pressure in the limits of the data
- calculated value for the monolayer formation $1/(\sqrt{C}+1)$ should be approximately equal at n_m

Shape of the isotherm provides valuable information about the interaction of gas molecules and the investigated material. IUPAC distinguishes 6 main isotherm types.

Adsorption isotherm of type I indicate that the material is microporous, with the pore size smaller than 0.7 nm (type I(a)) or 0.7-2 nm (type I(b)). Type II is common for non-porous and macroporous materials, as a consequence of the multilayers created on the surface. Isotherms III and V indicate weak interactions between gas molecules and the material. Type IV isotherm indicated mesoporous material, with pores either smaller (type IV(b)) or larger (type IV(a)) than 4 nm. Isotherm type VI is also a consequence of the multilayer formation, similar to type II.[145]

Prior to all physisorption measurements, the samples were degassed under vacuum at 80 °C for 16 h (hybrid materials) or at 150 °C for 20 h (pure carbon materials). Nitrogen physisorption measurements were performed on a Quantachrome Quadrasorb SI physisorption instrument at 77 K, while water vapour physisorption was measured on Quantachrome Autosorb IQ physisorption instrument at 298 K.

8.1.6. Electron microscopy (EM)

Electron microscopy is analogous to optical microscopy but instead of light, electron beams are used, due to much higher maximum resolution of the electrons compared to the photons. Therefore, the parts of an electron microspore are analogous to the parts found in an optical microscope. Transmission electron microscope (TEM) is a special geometry of an electron microscope where an electron beam passes through the sample as opposed to the scanning electron microscope (SEM) where the electron beam gets reflected from the sample. Therefore, a sample for TEM needs to be very thin, up to 100 nm while not for SEM. TEM provides very good resolution, up to 0.1 nm, meaning that single atomic rows can be observed.

Energy dispersive X-ray spectrometry (EDX or EDS) is an analytical technique commonly coupled with the electron microscopes. High-energy electron beam needed for imaging using electron microscopy induces ionisation of the inner electrons of an element. Generated holes are filled with the electrons from outer shells releasing energy in the process as photons. As the released energy depends on the element, energies of the observed photons can be used to determine the elemental composition of the imaged sample.[146]

Electron energy loss spectroscopy (EELS) is another technique commonly coupled with electron microscopy, namely TEM. Upon interaction of electrons with the matter inelastic

scattering occurs and the electrons lose energy. As the energy loss depends on the element and its oxidation state it is possible to gain precise knowledge of the elements present in the sample as well as their oxidation state.[147]

The morphology at the surface was investigated by means of SEM and TEM. SEM used was Zeiss Leo Gemini 1550 microscope, and the atomic distribution of different elements was mapped by energy-dispersive X-ray spectroscopy (EDX, X-Max, Oxford instruments). The STEM images were acquired using a double-Cs-corrected Jeol ARM200F, equipped with a cold field emission gun. The microscope is further equipped with an EDS detector and a Gatan Quantum GIF energy-filter, which were utilized for the EDS and EELS measurements. For all investigation, the acceleration voltage was set to 80kV.

8.1.7. Thermal gravimetric analysis (TGA)

Thermogravimetric analysis is a method based on the change in the mass as a function of temperature. A sample is placed in a small inert container along with a reference, an empty container. The measurements can be performed in different gasses and the most commonly they are performed in the inert nitrogen or synthetic air. Both containers are heated parallelly and the mass difference between the two is the result of the theromogravimetrical analysis, represented as the thermogravimetric curve. Every step on it consists of two temperatures: initial temperature, where the change of the mass begins, and the final temperature, where the change of the mass ends. This techniques is very useful for the determination of the thermal stability of the compounds, as well as the amount of the residual solvent inside the pores of a porous materials.[142]

TGA measurements were performed using a thermo microbalance TG 209 F1 Libra (Netzsch, Selb, Germany). A platinum crucible was used for the measurement of 10 +/- 1 mg of samples in a nitrogen flow of 10 ml min^{-1} and a purge flow of 10 ml min^{-1}. The samples were heated with a heat rate of 10 K min^{-1} to 1000 °C. Data was recorded and analyzed by the Proteus (6.1.0) and Quadstar (7.03, MID modus) software package.

8.1.8. Combustion elemental analysis

Combustion elemental analysis is the most common technique employed to determine the elemental composition of organic samples. Upon exposure of organic sample to elevated temperature in the oxidising environment the common organic building blocks, namely carbon, hydrogen, nitrogen and sulphur, form gaseous oxides. Detection of these oxides gives

information about the amount of respective elements in the tested sample. Detection of oxygen is done in a separate mode as oxygen is converted to carbon oxides under special conditions and determination of the amount of carbon monoxide gives the information about the oxygen content in the sample.[148]

Elemental analysis was performed with a vario MICRO cube CHNOS Elemental Analyzer (Elementar Analysensysteme GmbH, Langenselbold, Germany) in the CHNS mode and a 2mgChem80s method or in the O mode with 2mg sample mass and WLD detector.

8.1.9. X-ray photoelectron spectroscopy (XPS)

X-rays are electromagnetic waves with the wavelengths between 0.01 and 10 nm and are capable of pushing the core-level electrons out of its atomic orbitals as the free electrons. As the energy of the x-rays is known, and the kinetic energy of the emitted electrons is measured, the binding energy can easily be calculated according to the conservation energy equation:

$$E_{binding} = E_{X-rays} - (E_{kinetic} + \phi)$$

Where ϕ is the work function that depends on both the spectrometer and the sample measured. As binding energies of the electrons depend on every atom, an elemental composition can be determined this way. The binding energy of the electrons also depends on the oxidation state of an atom and on its chemical environment. Therefore, one can also derive this information from the XPS.

In order to understand the XPS data deconvolution is needed, which means that the experimentally obtained curve needs to be approximated by a number of smaller curves. Each of those curves represents an atom of an element in a specific chemical environment and the relative surface of each curve represents the amount of the atoms in that specific environment.

XPS analyses only the outermost atomic layers of a surface, namely the electrons on the depth of around 10 nm and less.[149]

X-ray photoelectron spectroscopy (XPS) measurements were performed using a ThermoScientific K-Alpha$^+$ X-ray Photoelectron Spectrometer. All samples were analyzed using a microfocused, monochromated Al K α X-ray source (1486.68 eV; 400 µm spot size). To prevent any localised charge buildup during analysis the K-Alpha$^+$ charge compensation system was employed at all measurements. The samples were mounted on conductive carbon tape the resulting spectra analyzed using the Avantage software from ThermoScientific.

8.1.10. Powder X-ray diffraction (PXRD)

Aforementioned X-rays can scatter off the atom's nuclei and when they scatter off the atoms whose interatomic distances are larger than the X-rays' wavelength their scattering can be described by the Bragg's law:

$$n\lambda = 2d \sin\theta$$

where n is an integer, λ is a wavelength of the X-rays, d is a distance between atomic planes and θ is an angle between incident wave and an atomic plane.

In monocrystalline samples, this scattering gives a pattern that can be used to determine the crystal structure. When the sample is polycrystalline, it has numerous monocrystals with different orientations and the monocrystalline patterns overlap forming circles at diffracting angles, with every circle having certain intensity. Powder x-ray diffractogram (also PXRD pattern) is obtained when the cross section of these circles is taken, so that position and intensity of every peak corresponds to the position and intensity of the circle.

Sharpness of the peaks in a PXRD pattern depend on the uniformity of the positions of the atoms in a sample, therefore highly crystalline samples give sharp peaks while the samples with the low crystallinity give broad peaks. When the atoms are randomly distributed in a material (amorphous material) no peaks can be observed. Exposure time needed to obtain spectra is inversely proportional to the crystallinity of the material. Therefore, nanostructured materials, with many surface atoms, need longer exposure time than their bulk counterparts.[142]

Degree of crystallinity can be calculated from the PXRD patterns[150,151] as broadness of the diffractive indices depends on the uniformity of atomic distances. Therefore, high crystalline samples have narrow diffractive indices, unlike broad ones observed for amorphous samples.

Powder XRD measurements were performed on a Bruker D8 diffractometer with Cu-Kα (λ = 0.154 nm) X-ray source and equipped with a scintillation counter-Scinti-Detector. The diffraction data was recorded in the 2θ range between 3 and 70° with an angular resolution of 0.03°. Prior to plotting the data has been smoothened using Savitzky-Golay method with 10 points of window and second polynomial order.

8.1.11. Absorbance UV-VIS spectroscopy

UV-Vis light has a wavelength between 10 and 750 nm. If shone by the light of an appropriate wavelength, a molecule undergoes a transition from the ground state ψ_0 to the excited sate ψ_1 absorbing the energy. The light needs to have the energy equal to the

difference between ψ_0 and ψ_1. Later it can emit the absorbed energy going back from ψ_1 to ψ_0. The wavelength of the emitted energy corresponds to the difference in energy between ψ_1 and ψ_0.[152]

The Beer-Lambert law describes the absorbance of a material as a sum of the absorbance of all the components in the sample:

$$A = A_i = \sum_{i=1}^{N} \varepsilon_i c_i l$$

where A is absorbance, ε is absorptivity and l is the path length of the light through the sample.

The samples for the UV-Vis spectroscopy can be liquid (pure liquid phase, solution or dispersion) or solid. During the measurement of a liquid sample a reference is used, that only contains the solvent used in the sample.

UV-Vis spectroscopy can be used to determine the concentration of a sample with known qualitative properties. Multiple spectra of the same molecule at different concentrations are measured and their maximum absorbance is linearised according to:

$$A = xc$$

where x is a constant for a given system. By measuring absorbance of the sample with the unknown concentration the concentration can be calculated from the equation above.

Absorption spectra were recorded with a T70+ UV/Vis Spectrometer (PG Instruments Ltd).

8.1.12. Electrochemical methods

Electrochemical techniques rely on the flow of electrons to induce chemical changes.

The electrochemical measurements performed in the three-electrode setup with aqueous acidic electrolyte (Figure A4) were performed as following: 1 M $HClO_4$ (50 mL) was used as an electrolyte with a platinum wire counter electrode and an Ag/AgCl reference electrode in saturated KCl solution. Three electrode system allows for the precise determination of the potential as it is determined as a difference between the working and the reference electrode.

The electrochemical measurements performed in lithium organic system were performed in Swagelok type cells. Lithium foil, Celgard 2325 (13 mm in diameter, 25 µm thick), and 1 M $LiPF_6$ in ethylene carbonate and diethyl carbonate (volumetric ratio 1:1, 100 µL, solution used

as obtained from Sigma-Aldrich) were used as counter electrode, membrane, and electrolyte, respectively. A circular carbon current collector covered with the active material was used as working electrode. The electrolyte was chosen as it is one of the most common choices for carbonyl based organic lithium-ion batteries, along with similar electrolytes.[153] All Swagelok type cells were assembled in a glovebox with low water and oxygen levels. Due to simplicity of the measurements, two electrode system, meaning that no reference electrode was used and the voltage was determined as a difference between the working and the counter electrode.

Redox reactions occur when two chemical species get in contact, provided that one species has higher HOMO orbital than the others LUMO orbital. Therefore, upon contact an electron or more transfers form HOMO of one species to the LUMO of another. Voltammetry works on the same principle, by varying the potential it allows for the flow of electrons either from the sample (oxidation) or to the sample (reduction). Measuring of the electron flow, current, allows for the determination of these potentials as electrons are released during oxidation of the sample and consumed during reduction. Therefore by plotting the current at different potential certain peaks are visible, regions where current increases or decreases abruptly, indicating regions of electron transfer.

8.1.11.1. Voltammetry

Voltammetry techniques measure the current as the response to the changing voltage. Cyclic voltammetry is the most common variation of voltammetry used. Lowest and highest potentials need to be chosen carefully not to induce degradation of the electrolyte or unwanted degradations of the sample. First voltammetry is performed from the starting potential to the desired potential and then the process is reversed. Upon returning to the starting potential the process can be repeated as many times as desired providing the information about the samples stability during cycling.[24]

During half-cell tests of the cathodes the redox reactions are visible as aforementioned peaks. Redox potential is a point where oxidation and reduction reactions are in equilibrium. However, peaks are always observed at higher (oxidation) or lower potentials (reduction) as overpotential is needed to overcome activation energy of the reaction. Potential of the reaction is calculated as the average of the oxidation and reduction potentials.

Scan rate is the speed at which the potential changes during the measurement. Varying scan rate can give valuable information about the tested sample, providing information about reversibility of the reaction as well as Faradaic and non-Faradaic contribution to capacity.

Furthermore, capacity of the electrode can be determined from the cyclic voltammetry according to the formula:

$$C = \int \frac{I\,dV}{v} * \frac{1}{2\Delta V}$$

where C is capacity of the tested electrode, I is current, V is potential, ΔV is the potential range in which the experiment was performed and v is the scan rate.

8.1.11.2. Galvanostatic measurements

Galvanostatic, or amperostatic, measurements are performed at varying potential but constant current. Galvanostatic charging-discharging measurements are commonly used for cathode and anode evaluation as they are simulating the charging and discharging cycles of the electrode during cycling of energy storage device. Usually, cycling is performed at certain current density but changing of the current density during cycling is a useful way for determination of stability of the electrode material at higher and lower current densities.[154] Capacity of the electrode during a certain charging or discharging cycle can be calculated according to formula:

$$C = \frac{It}{3.6}$$

Where C is capacity, I is current and t is duration of charging or discharging.

Obtained data is usually plotted as potential to capacity. Pure Faradaic devices are recognised by a discharge capacity curve where at a certain point slope equals 0, meaning that the charging and discharging occur at a certain potential, the same potential where the peaks in cyclic voltammetry are observed. On contrary, pure capacitive devices are characterised by triangular shape as electrons enter the capacitor at constant rate during charging.[23]

8.1.11.3. Electrochemical impedance spectroscopy

Electrochemical impedance spectroscopy (EIS), alternatively called dielectric spectroscopic testing, measures the response of the system as impedance of a power cell by alternating low-amplitude voltage. Although other methods of data analysis can be used, usually, the obtained data is expressed as a Nyquist plot showing imaginary and real parts of the impedance of the cell. The Nyquist plot is characterised by a semicircle, representing an interface, that ends with a straight line. Conductivity of the interface can be roughly determined from the semicircle as the diameter of the circle is inversely proportional to the conductivity while the

kinetics of the cell can be determined from the slope of the line, where faster diffusion is characterised by larger slope. Additionally, multiple semicircles indicate multiple interfaces and are usually a sign of the problems of the cell. However, they can also indicate formation of SEI. EIS is commonly used to ensure good assembly of the cell, to compare similar samples and to follow degradation of the cell during cycling.[154]

8.2. Materials

Chitosan with an average molecular weight of 15 kDa and with minimum 85% degree of deacetylation (Polysciences, Inc.), vanillin (Sigma-Aldrich), syringaldehyde (Acros Organics), 4-hydroxybenzaldehyde (Sigma-Aldrich), sodium cyanoborohydride (Acros Organics), sodium carbonate (Carl Roth), Kraft lignin from southern pine trees (Domtar), carbon black AB-520 (MTI Corporation), hydroxylammonium chloride (Sigma-Aldrich), iron (III) chloride (Fluka), magnesium sulphate (Acros Organics), triflic acid (TCI), sodium hydroxide (Sigma-Aldrich), 5-hydroxyisophthalonitrile (TCI), protocatechuic aldehyde (A-o, Carl Roth), 3,5-dihydroxybenzaldehyde (A-m, Fischer), aqueous solution (15 %) of polyallylamine with average molecular weight of 15,000 g mol-1 (PAAm, Polysciences, Inc.), carbon EQ-AB-520Y (CC, MTI Corporation), hydrolysable tannic acid (molecular weight of 1701.23 g mol^{-1} as indicated by the supplier, Acros Organics), sucrose (Sigma Aldrich), zinc chloride (Alfa Aesar), sulphuric acid (Alfa Aesar) and carbon paper Spectracarb 2050A-0550 (Fuel Cell Store) were used as received. Solvents acetic acid (VWR International), ethanol (Fisher), propylene glycol (Acros Organics), NMP (PanReac AppliChem), toluene (Fluka), diethyl ether (Fluka) and ammonia (25%, Fluka) and deuterated solvents water (Sigma-Aldrich) and acetic acid (Sigma-Aldrich) were used without further purification.

It is important to note that when referring to carbon or carbon black, in the Chapter 4. it is referring to carbon black AB-520, in Chapter 5. to carbon EQ-AB-520Y and in Chapter 6. to reduced STC-8. Due to similar properties of these carbons I decided not to make distinction between them.

8.3. Synthetic procedures

Synthesis of C/ChiVan: Chitosan (0.5 g) was dissolved in 0.2 M acetic acid (35 mL) and stirred for 2 h. A solution of vanillin (0.48 g in 35 mL ethanol) was then added to the mixture. After 1 h of additional stirring at room temperature, $NaBH_3CN$ (0.77 g) was added and the reaction stirred further for 17 h. A precipitate formed which was dissolved by addition of glacial acetic acid (3 mL). After 1 h of further stirring, carbon black (1.5 g), that was previously grinded in an agate mortar, was added and stirred for 24 h. The mixture was neutralised using a 15% aqueous solution of Na_2CO_3 and stirred for 2 hours. The product was centrifuged by splitting the dispersion in two centrifugation tubes (max capacity 50 mL) and subsequently washed two times with water and two times with ethanol (each centrifugation was done at 4000 rpm for 3 minutes). The obtained solid was dried at 60 ^{0}C overnight.

Synthesis of C/ChiVan(0.6): Chitosan (0.5 g) was dissolved in 0.2 M acetic acid (35 mL) and stirred for 2 h. A solution of vanillin (0.48 g in 35 mL ethanol) was then added to the mixture. After 1 h of additional stirring at room temperature, $NaBH_3CN$ (0.77 g) was added and the reaction stirred further for 17 h. A precipitate formed which was dissolved by addition of glacial acetic acid (3 mL). After 1 h of further stirring, carbon black (0.5 g), that was previously grinded in an agate mortar, was added and stirred for 24 h. The mixture was neutralised using a 15% aqueous solution of Na_2CO_3 and stirred for 2 hours. The product was centrifuged by splitting the dispersion in two centrifugation tubes (max capacity 50 mL) and subsequently washed two times with water and two times with ethanol (each centrifugation was done at 4000 rpm for 3 minutes). The obtained solid was dried at 60 ^{0}C overnight.

Synthesis of C/ChiVan(0.23): Chitosan (0.5 g) was dissolved in 0.2 M acetic acid (35 mL) and stirred for 2 h. A solution of vanillin (0.48 g in 35 mL ethanol) was then added to the mixture. After 1 h of additional stirring at room temperature, $NaBH_3CN$ (0.77 g) was added and the reaction stirred further for 17 h. A precipitate formed which was dissolved by addition of glacial acetic acid (3 mL). After 1 h of further stirring, carbon black (2.5 g), that was previously grinded in an agate mortar, was added and stirred for 24 h. The mixture was neutralised using a 15% aqueous solution of Na_2CO_3 and stirred for 2 hours. The product was centrifuged by splitting the dispersion in two centrifugation tubes (max capacity 50 mL) and subsequently washed two times with water and two times with ethanol (each centrifugation was done at 4000 rpm for 3 minutes). The obtained solid was dried at 60 ^{0}C overnight.

Synthesis of C/chitosan: Chitosan (0.5 g) was dissolved in 0.2 M acetic acid (35 mL) and stirred for 2 h. Ethanol (35 mL) was then added to the mixture. After 1 h of additional stirring at room temperature, $NaBH_3CN$ (0.77 g) was added and the reaction stirred further for 17 h. Glacial acetic acid (3 mL) was added. After 1 h of further stirring, carbon black (1.5 g), that was previously grinded in an agate mortar, was added and stirred for 24 h. The mixture was neutralised using a 15% aqueous solution of Na_2CO_3 and stirred for 2 hours. The product was centrifuged by splitting the dispersion in two centrifugation tubes (max capacity 50 mL) and subsequently washed two times with water and two times with ethanol (each centrifugation was done at 4000 rpm for 3 minutes). The obtained solid was dried at 60 ^{0}C overnight.

Synthesis of C/chi-van: Chitosan (0.5 g) was dissolved in 0.2 M acetic acid (35 mL) and stirred for 2 h. A solution of vanillin (0.48 g in 35 mL ethanol) was then added to the mixture. The reaction was stirred further for 18 h. Glacial acetic acid (3 mL) was added. After 1 h of further stirring, carbon black (1.5 g), that was previously grinded in an agate mortar, was added and stirred for 24 h. The mixture was neutralised using a 15% aqueous solution of Na_2CO_3 and stirred for 2 hours. The product was centrifuged by splitting the dispersion in two centrifugation tubes (max capacity 50 mL) and subsequently washed two times with water and two times with ethanol (each centrifugation was done at 4000 rpm for 3 minutes). The obtained solid was dried at 60 ^{0}C overnight.

Synthesis of ChiVan: Chitosan (0.5 g) was dissolved in 0.2 M acetic acid (35 mL) and stirred for 2 h. A solution of vanillin (0.48 g in 35 mL ethanol) was then added to the mixture. After 1 h of additional stirring at room temperature, $NaBH_3CN$ (0.77 g) was added and the reaction stirred further for 17 h. A precipitate formed which was dissolved by addition of glacial acetic acid (3 mL). After 25 h of stirring the mixture was neutralised using a 15% aqueous solution of Na_2CO_3 and further stirred for 2 hours. The product was centrifuged by splitting the dispersion in two centrifugation tubes (max capacity 50 mL) and subsequently washed two times with water and two times with ethanol (each centrifugation was done at 4000 rpm for 3 minutes). The obtained solid was dried at 60 ^{0}C overnight.

Synthesis of C/ChiSyr: Chitosan (0.5 g) was dissolved in 0.2 M acetic acid (35 mL) and stirred for 2 h. A solution of Syringaldehyde (0.58 g in 35 mL ethanol) was then added to the mixture. After 1 h of additional stirring, at room temperature, $NaBH_3CN$ (0.77 g) was added and the reaction stirred further for 17 h. A precipitate formed which was dissolved by addition of glacial acetic acid (9 mL). After 1 h of further stirring, carbon black (1.5 g), that was previously grinded in an agate mortar, was added and stirred for 24 h. The mixture was

neutralised using a 15% aqueous solution of Na_2CO_3 and stirred for 2 hours. The product was centrifuged by splitting the dispersion in two centrifugation tubes (max capacity 50 mL) and subsequently washed two times with water and two times with ethanol (each centrifugation was done at 4000 rpm for 3 minutes). The obtained solid was dried at 60 ^{0}C overnight.

Synthesis of C/ChiPhy: Chitosan (0.5 g) was dissolved in 0.02 M acetic acid (35 mL) and stirred for 2 h. A solution of p-hydroxybenzaldehyde (0.39 g in 35 mL ethanol) was then added to the mixture. After 1 h of additional stirring at room temperature, $NaBH_3CN$ (0.77 g) was added and the reaction stirred further for 18 h. Carbon black (1.5 g), that was previously grinded in an agate mortar, was added and stirred for 24 h. The mixture was neutralised using a 15% aqueous solution of Na_2CO_3 and stirred for 2 hours. The product was centrifuged by splitting the dispersion in two centrifugation tubes (max capacity 50 mL) and subsequently washed two times with water and two times with ethanol (each centrifugation was done at 4000 rpm for 3 minutes). The obtained solid was dried at 60 ^{0}C overnight.

Electrode preparation (C/ChiVan and related): For the working electrode, different samples (60 mg) were grinded using a planetary ball mill PM100 (Retsch) equipped with stainless steel jars and balls for 50 min and for another 10 min together with 250 μL propylene glycol. Ethanol (750 μL) was added to the slurry, and samples were hand shaken and ultrasonificated for 5 min. 40 μL of the obtained slurry was spread across a carbon paper (1.5 cm^2). For electrodes with higher or lower loading, the volume of slurry to be spread on carbon paper was adjusted accordingly.

Electrode preparation (C/lignin): Kraft lignin (20 mg) and carbon black (40 mg) were grinded in a stainless steel jar using a planetary ball mill PM100 (Retsch). Propylene glycol (0.25 mL) and ethanol (0.75 mL) were used as solvent to prepare a processible slurry, which was further hand shaken and ultrasonicated before application. 40 μL of the obtained slurry was spread across a carbon paper (1.5 cm^2). The electrode was dried at 80 ^{0}C overnight.

Synthesis of vanillonitrile:[92] Vanillin (18.26 g, 120 mmol) and hydroxylammonium chloride (12.50 g, 180 mmol) were dissolved in acetic acid (100 mL). The resulting mixture was heated under reflux conditions for 2 h with the formation of an orange solution. After cooling down it was poured into diethyl ether (300 mL) and subsequently washed, once with water and twice with a 5% sodium hydroxide solution (150 mL in each step). The aqueous phases were cleaned once with diethyl ether (150 mL). The organic phases were combined and dried with $MgSO_4$. The solvent was removed under reduced pressure, and the product was

recrystallised from toluene and dried under vacuum at 80 °C overnight. The procedure yielded 15.19 g (84.9%) of pure vanillonitrile as confirmed by ^{1}H NMR and ^{13}C NMR.

^{1}H NMR (400 MHz, deuterated DMSO): d = 10.26 ppm (s, 1H, OH), 7.35 ppm (d, 1H, aromatic), 7.26 ppm (m, 1H, aromatic), 6.89 ppm (d, 1H, aromatic), 3.81 ppm (s, 3H, -CH_3).

^{13}C NMR (400 MHz, deuterated DMSO): d = 55.94 ppm (-CH_3), 100.94 ppm (aromatic), 115.24 ppm (aromatic), 116.09 ppm (aromatic), 119.67 ppm (nitrile), 126.50 ppm (aromatic), 147.98 ppm (aromatic), 151.46 ppm (aromatic).

Synthesis of bisvanillonitrile (BVN):[93,94] Vanillonitrile (10 g, 50.3 mmol) was mixed with water (240 mL), and a solution of iron (III) chloride (21.75 g, 100.6 mmol) in water (240 mL) was added. The mixture was heated under reflux conditions during 4 h and filtered afterwards. The precipitate was collected and purified using soxhlet extraction overnight with water as the purification solvent. The product was further cleaned with ethanol (three times centrifugation) and dried under vacuum at 80 °C overnight. The procedure yielded 4.77 g (48.0%) of pure bisvanillonitrile as confirmed by ^{1}H NMR, ^{13}C NMR and MS, and a low iron content of 5.19 (std. dev. 0.082) mg g^{-1} was confirmed with ICP-MS.

^{1}H NMR (400 MHz, deuterated DMSO): d = 9.86 ppm (s, 2H, OH), 7.42 ppm (s, 2H, aromatic), 7.23 ppm (s, 2H, aromatic), 3.89 ppm (s, 6H, -CH_3).

^{13}C NMR (400 MHz, deuterated DMSO): d = 56.39 ppm (-CH_3), 100.35 ppm (aromatic), 114.08 ppm (aromatic), 119.56 ppm (nitrile), 124.61 ppm (aromatic), 128.14 ppm (aromatic), 147.94 ppm (aromatic), 148.88 ppm (aromatic).

MS (solvent: ACN, eluent: methanol/isopropanol (80/20) with 0,1% formic acid): calculated: 296.08, measured: 296.0 (negative ion mode).

Synthesis of p-BVN:[112] A vial (10 mL) containing BVN (50 mg) was placed into a Schlenk tube (Figure S6 in the Supporting Information) with a volume around 120 mL. The tube was evacuated, and 100 mL of argon was added to it followed by 0.6 mL of triflic acid. The tube was heated to 100 °C for 22 h. Hereafter, the product was immersed in a 25% aqueous solution of ammonia for 1 h. Afterwards, the resulting polymer was centrifuged, washed with water and ethanol (2 times 50 mL of each solvent, 4000 rpm, 3 min), and dried in vacuum at 80 °C for 3 h.

Synthesis of C/p-BVN.[112] Carbon black (30 mg) and BVN (30 mg) were put into a stainless steel jar (12 mL) and grinded at 650 rpm for 50 min using a planetary ball mill PM100

(Retsch). Hereafter, NMP (1 mL) was added before further grinding for 10 min. 40 µL of the obtained slurry was spread across a circular piece of carbon paper (11 mm in diameter). The electrodes were dried in vacuum for 17 h at 80 °C before being placed inside a vial (5 mL). Two vials were put into a Schlenk tube with a volume of approximately 120 mL. The tube was evacuated, and 100 mL of argon was added to it followed by 0.6 mL of triflic acid. The tube was heated to 100 °C for 22 h. The electrodes were subsequently immersed into a 25% aqueous solution of ammonia, water, and ethanol for 1 h each. Finally, they were dried in vacuum at 80 °C for 3 h.

Synthesis of C/p-HIT.[112] Carbon black (30 mg) and HIT (30 mg) were put into a stainless steel jar (12 mL) and grinded at 650 rpm for 50 min using a planetary ball mill PM100 (Retsch). Hereafter, NMP (1 mL) was added before further grinding for 10 min. 40 µL of the obtained slurry was spread across a circular piece of carbon paper (11 mm in diameter). The electrodes were dried in vacuum for 17 h at 80 °C before being placed inside a vial (5 mL). Two vials were put into a Schlenk tube with a volume of approximately 120 mL. The tube was evacuated, and 100 mL of argon was added to it followed by 0.6 mL of triflic acid. The tube was heated to 100 °C for 22 h. The electrodes were subsequently immersed into a 25% aqueous solution of ammonia, water, and ethanol for 1 h each. Finally, they were dried in vacuum at 80 °C for 3 h.

Synthesis of P-o:[118] An aqueous solution of PAAm (0.33 g, 0.87 mmol of repeating units) was added to ethanol (10 mL) and stirred for 10 minutes. After the addition of A-o (0.12 g, 0.87 mmol) dissolved in ethanol (10 mL) the mixture was stirred for 1 h. Afterwards the solvent was removed at 60 °C at a pressure of 180 mbar which was lowered to 150 mbar shortly after the beginning of the solvent removal. After drying of the obtained polymer at 80 °C under vacuum for 2 h, it was washed with ethanol using centrifugation (4 times with 50 mL ethanol, 5 min). The sample was dried in vacuum oven overnight.

Synthesis of P-m[118]

An aqueous solution of PAAm (0.33 g, 0.87 mmol of repeating units) was added to ethanol (10 mL) and stirred for 10 minutes. After the addition of A-m (0.16 g, 0.87 mmol) dissolved in ethanol (10 mL) the mixture was stirred for 1 h. Afterwards the solvent was removed at 60 °C at a pressure of 180 mbar which was lowered to 150 mbar shortly after the beginning of the solvent removal. After drying of the obtained polymer at 80 °C under vacuum for 2 h, it

was washed with ethanol using centrifugation (4 times with 50 mL ethanol, 5 min). The sample was dried in vacuum oven overnight.

Synthesis of P-van:[118] An aqueous solution of PAAm (0.33 g, 0.87 mmol of repeating units) was added to ethanol (10 mL) and stirred for 10 minutes. After the addition of van (0.13 g, 0.87 mmol) dissolved in ethanol (10 mL) the mixture was stirred for 1 h. Afterwards the solvent was removed at 60 °C at a pressure of 180 mbar which was lowered to 150 mbar shortly after the beginning of the solvent removal. After drying of the obtained polymer at 80 °C under vacuum for 2 h, it was washed with ethanol using centrifugation (4 times with 50 mL ethanol, 5 min). The sample was dried in vacuum oven overnight.

Synthesis of hybrid materials of P-x with carbon black: P-x (24 mg) and conductive carbon (30 mg) were ball milled for 50 min in a stainless steel jar before a solution of PVDF in NMP (6 mg mL^{-1}) was added (1 mL) and the mixture was ball milled for additional 10 min. The slurry (30 µL) was spread across a circular piece of carbon paper (11 mm in diameter) and dried at 80 °C for 17 h. For physisorption measurements, the slurry was spread in a petri dish before drying. The collected powder was later washed twice with ethanol (50 mL each time) and dried for 3 additional hours.

Synthesis of STC-x:[133] $ZnCl_2$ was employed as the salt template for the synthesis of STC. 5 g of sucrose was dissolved in 15 mL of water, and 5x g of $ZnCl_2$ was dissolved in another 15 mL of water. The prepared solutions were mixed and 0.55 g concentrated sulfuric acid was added. The mixture was transferred to a Petri dish, dried at 100 °C for 6 h, and subsequently heated to 160 °C and kept for 6 h. The mixture was then transferred to a horizontal tubular furnace for carbonization at 900 °C for 2 h under N_2 flow with heating rate of 60 °C h^{-1}. Excess amount of inorganic salt was removed by stirring the mixture in 1 M HCl for 3 days, followed by filtration and washing with large amounts of water.

Synthesis of reduced STC-8: In order to reduce the content of oxygen-containing surface functionalities, STC-8 was treated under reducing atmosphere (5% H_2 in N_2) in a horizontal tubular furnace for 2 h on 600 °C (heating rate: 240 °C h_{-1}).

Synthesis of C/TAN: Ball-milling was performed using a Retsch PM 100 planetary ball mill, 12 mL stainless steel jars, and 5 stainless steel balls (10 mm). Sustainable carbon (36 mg) and tannic acid (24 mg) were neat grinded for 50 min at 650 rpm. Propylene glycol (0.25 mL) was added and grinded further for 10 min. Ethanol (0.75 mL) was added and the mixture was

ultrasonificated for 5 min resulted in a homogeneous ink. Ink was transferred in a Petri dish with the help of two times 1 mL ethanol and dried at 80 °C under vacuum for 17 hours.

Synthesis of C/TAN(PG): Ball-milling was performed using a Retsch PM 100 planetary ball mill, 12 mL stainless steel jars, and 5 stainless steel balls (10 mm). Tannic acid (24 mg), sustainable carbon (36 mg) and propylene glycol (0.25 mL) were grinded for 1 hour at 650 rpm. Ethanol (0.75 mL) was added and the mixture was ultrasonificated for 5 min resulted in a homogeneous ink. Ink was transferred in a Petri dish with the help of two times 1 mL ethanol and dried at 80 °C under vacuum for 17 hours.

Synthesis of C(50 min)/TAN: Ball-milling was performed using a Retsch PM 100 planetary ball mill, 12 mL stainless steel jars, and 5 stainless steel balls (10 mm). Sustainable carbon (36 mg) was neat grinded for 50 min at 650 rpm. Solution of tannic acid (24 mg) in propylene glycol (0.25 mL) was added and grinded further for 10 min. Ethanol (0.75 mL) was added and the mixture was ultrasonificated for 5 min resulted in a homogeneous ink. Ink was transferred in a Petri dish with the help of two times 1 mL ethanol and dried at 80 °C under vacuum for 17 hours.

Synthesis of C(50 min): Ball-milling was performed using a Retsch PM 100 planetary ball mill, 12 mL stainless steel jars, and 5 stainless steel balls (10 mm). Sustainable carbon (54 mg) was neat grinded for 50 min at 650 rpm.

Synthesis of C(Ar): Same as C/(50 min) but the carbon was put in jar and degassed in the glovebox for 5 days. The jar was closed in the glovebox and sealed with the parafilm. After grinding it was left to cool overnight before the jar was opened.

8.4. Supplementary Graphs and Tables

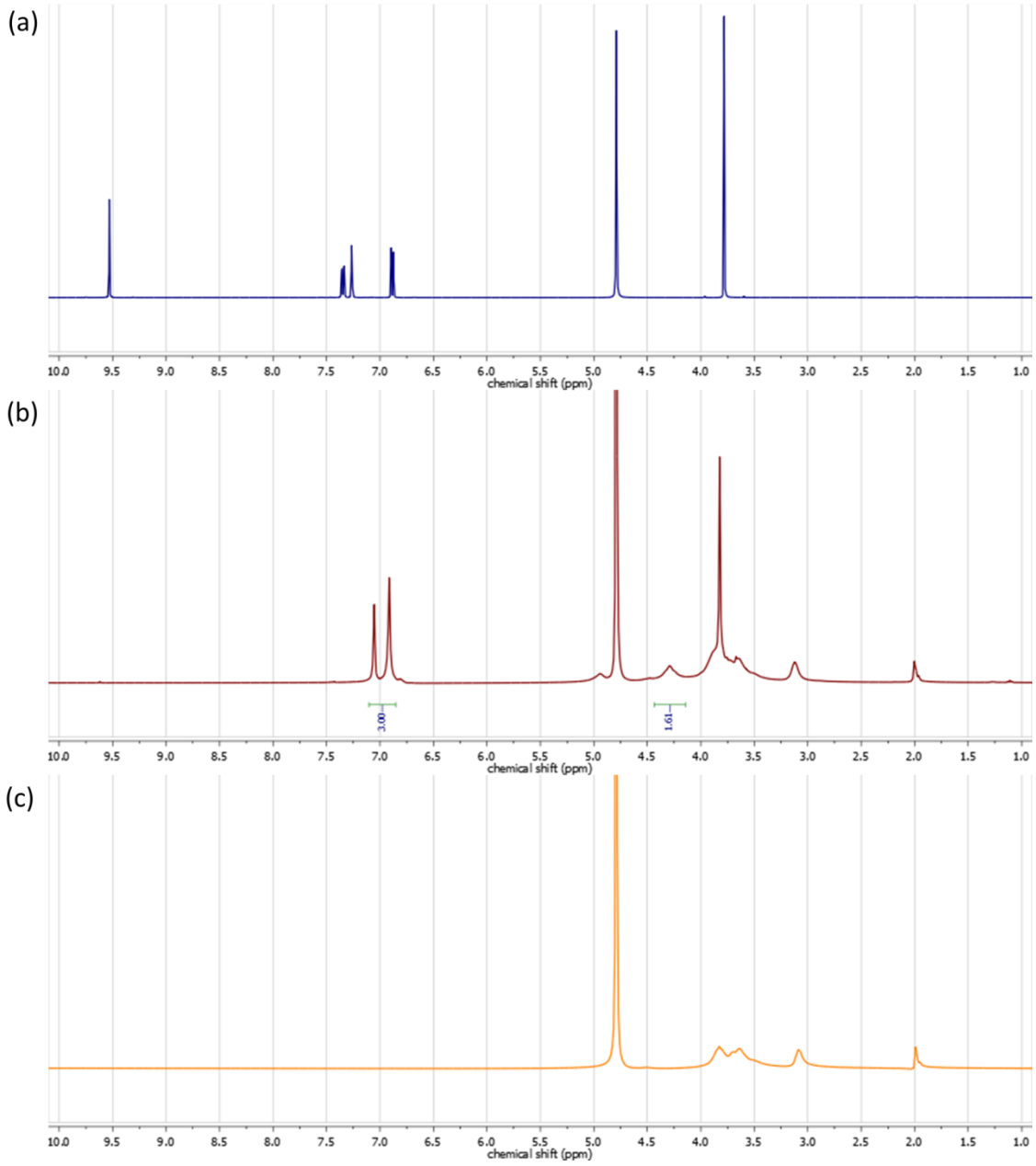

Figure A1. ^{1}H NMR spectra of (a) vanillin, (b) ChiVan, and (c) chitosan in 1% solution of deuterated acetic acid in deuterated water.

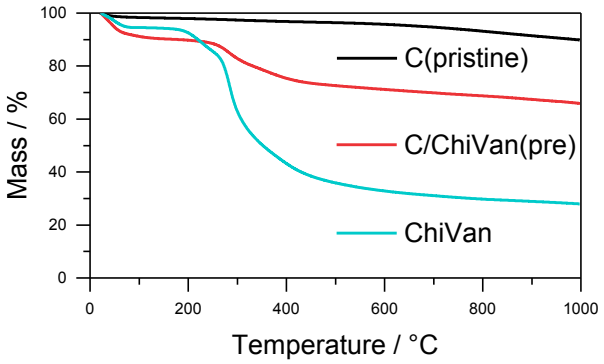

Figure A2. TGA of C(pristine), C/ChiVan(pre), and ChiVan with a heating rate of 10 K min^{-1} under nitrogen atmosphere.

Table A1. Combustive elemental analysis results of following samples. All the measurements were performed twice (first two rows) and the average is calculated. All the reported hybrid materials are unmodified (pre).

	N [%]	C [%]	H [%]	O [%]
Carbon black	0.18	93.41	1.239	5.726
	0.15	93.71	1.014	5.556
AVERAGE	0.165	93.56	1.1265	5.641
C/ChiVan(0.6)	2.85	67.71	4.119	22.96
	2.83	67.38	4.226	22.921
AVERAGE	2.84	67.545	4.1725	22.9405
C/ChiVan	1.53	75.58	2.998	15.976
	1.57	76.35	3.207	17.453
AVERAGE	1.55	75.965	3.1025	16.7145
C/ChiVan(0.23)	1.14	77.8	2.691	15.96
	1.14	79.2	2.904	14.84
AVERAGE	1.14	78.5	2.7975	15.4
ChiVan	4.84	52.72	6.148	35.485
	4.79	52.57	6.211	35.807
AVERAGE	4.815	52.645	6.1795	35.646
C/chi-van	1.56	76.26	2.706	18.023
	1.62	78.16	2.994	17.607
AVERAGE	1.59	77.21	2.85	17.815
C/ChiPhy	2.04	74.62	3.431	15.714
	2.91	64.4	3.993	16.371
AVERAGE	2.475	69.51	3.712	16.0425
C/ChiSyr	1.57	75.37	3.463	17.363
	1.43	73.86	3.048	17.363
AVERAGE	1.5	74.615	3.2555	17.363
C/chitosan	1.75	74.29	3.056	17.628
	1.76	75.58	3.07	17.49

AVERAGE	1.755	74.935	3.063	17.559
chitosan	7.28	40.59	6.47	42.82
	7.47	41.27	6.705	43.943
AVERAGE	7.375	40.93	6.5875	43.3815

(a)

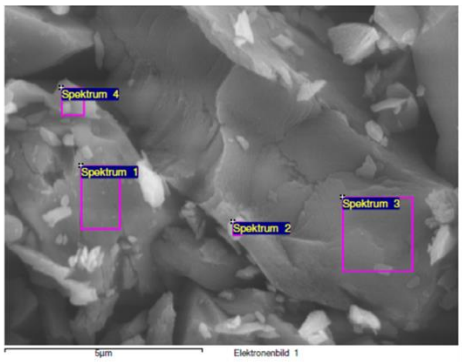

Processing option : All elements analysed (Normalised)

Spectrum	In stats.	C	N	O	Total
Spektrum 1	Yes	95.57	2.09	2.34	100.00
Spektrum 2	Yes	93.86	3.20	2.94	100.00
Spektrum 3	Yes	96.03	2.15	1.81	100.00
Spektrum 4	Yes	94.96	2.50	2.54	100.00
Mean		95.10	2.49	2.41	100.00
Std. deviation		0.94	0.51	0.47	
Max.		96.03	3.20	2.94	
Min.		93.86	2.09	1.81	

All results in weight%

(b)

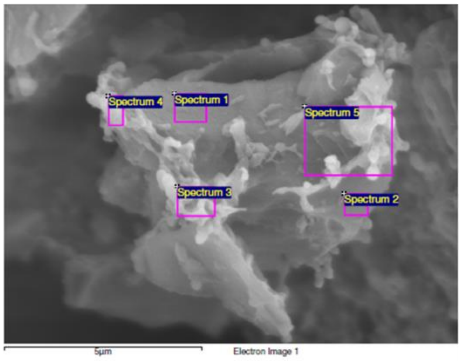

Processing option : All elements analysed (Normalised)

Spectrum	In stats.	C	N	O	Na	Total
Spectrum 1	Yes	92.09	3.74	3.87	0.31	100.00
Spectrum 2	Yes	93.54	2.91	3.19	0.36	100.00
Spectrum 3	Yes	85.72	7.35	6.45	0.48	100.00
Spectrum 4	Yes	85.51	6.16	7.66	0.67	100.00
Spectrum 5	Yes	89.71	4.59	5.28	0.42	100.00
Mean		89.31	4.95	5.29	0.45	100.00
Std. deviation		3.64	1.80	1.83	0.14	
Max.		93.54	7.35	7.66	0.67	
Min.		85.51	2.91	3.19	0.31	

All results in weight%

(c)

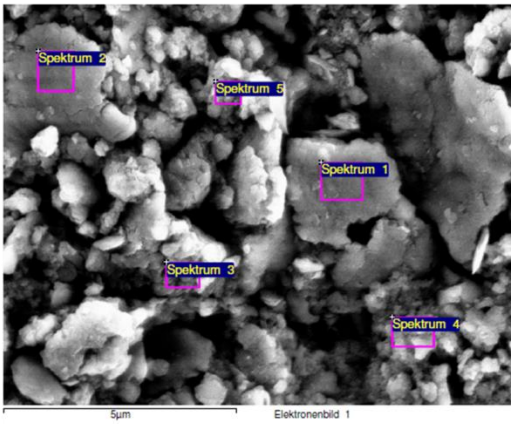

Processing option : All elements analysed (Normalised)

Spectrum	In stats.	C	N	O	Na	Total
Spektrum 1	Yes	87.83	4.64	6.97	0.56	100.00
Spektrum 2	Yes	86.78	5.15	7.60	0.46	100.00
Spektrum 3	Yes	88.55	4.65	6.32	0.48	100.00
Spektrum 4	Yes	85.95	5.93	7.50	0.61	100.00
Spektrum 5	Yes	87.84	5.05	6.65	0.46	100.00
Mean		87.39	5.08	7.01	0.52	100.00
Std. deviation		1.02	0.53	0.55	0.07	
Max.		88.55	5.93	7.60	0.61	
Min.		85.95	4.64	6.32	0.46	

All results in weight%

Figure A3. SEM images along with EDX measurements at different regions of (a) C(pristine), (b,c) C/ChiVan (b) before and (c) after grinding.

Figure A4. Cell used for electrochemical experiments in Chapter 4.

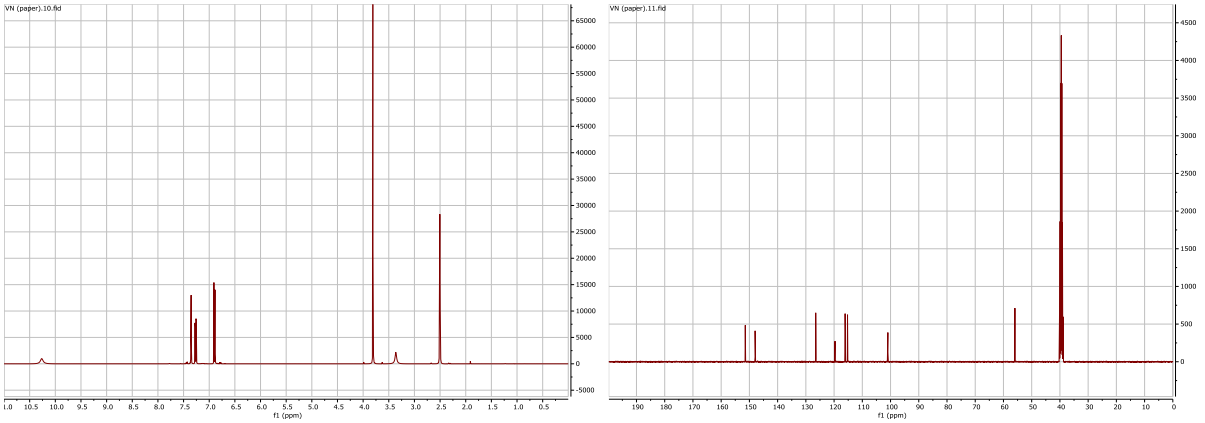

Figure A5. ^{1}H and ^{13}C NMR of as synthesised vanillonitrile.

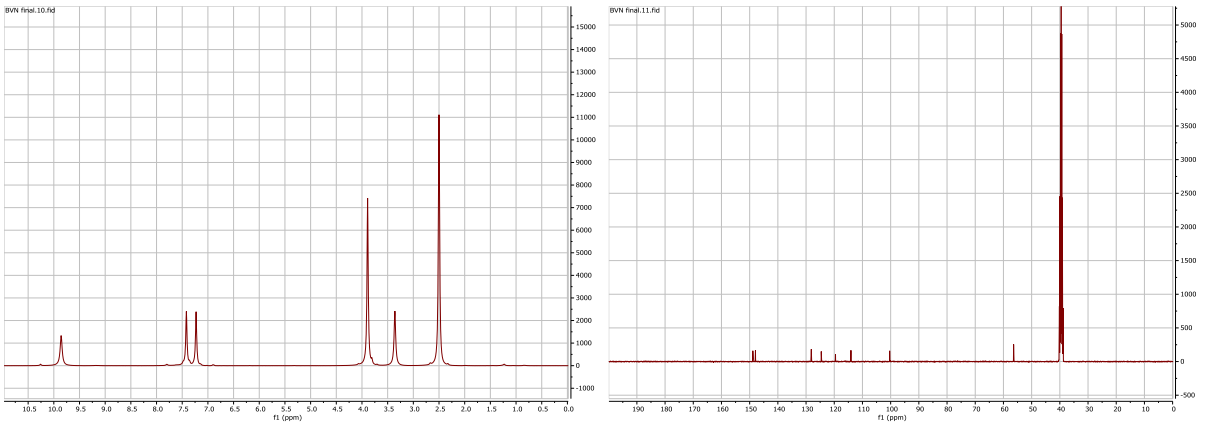

Figure S6. ^{1}H and ^{13}C NMR of as synthesised BVN.

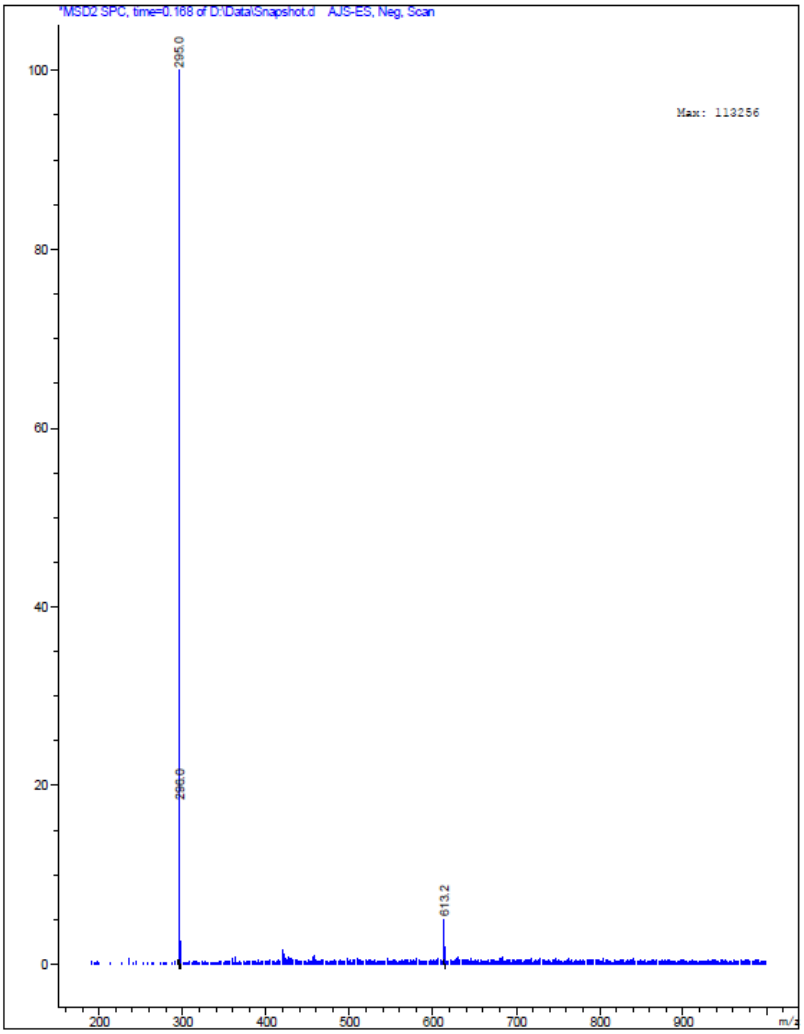

Figure A7. Mass spectrometry of BVN.

Table A2. Combustive elemental analysis of BVN, p-BVN, C(pristine), C and C/p-BVN. All the measurements were performed twice (first two rows) and the average is calculated.

	N [%]	C [%]	H [%]	S [%]	O [%]
BVN	9.14	63.81	4.09	0.85	23.25
	9.10	63.62	4.10	0.80	23.41
AVERAGE	9.12	63.72	4.10	0.82	23.33
p-BVN	9.17	56.87	4.30	1.21	26.53
	9.34	58.00	4.43	1.00	26.44
AVERAGE	9.26	57.44	4.37	1.10	26.48
C(pristine)	0.23	93.85	1.07	0.72	4.66
	0.21	93.66	1.05	0.73	4.79

AVERAGE	0.22	93.76	1.06	0.73	4.72
C	1.09	71.19	1.33	0.80	13.18
	1.10	71.03	1.30	0.76	13.23
AVERAGE	1.10	71.11	1.32	0.78	13.21
C/p-BVN	6.38	69.51	3.42	2.43	18.61
	6.37	69.69	3.37	2.30	18.98
AVERAGE	6.38	69.60	3.39	2.37	18.79

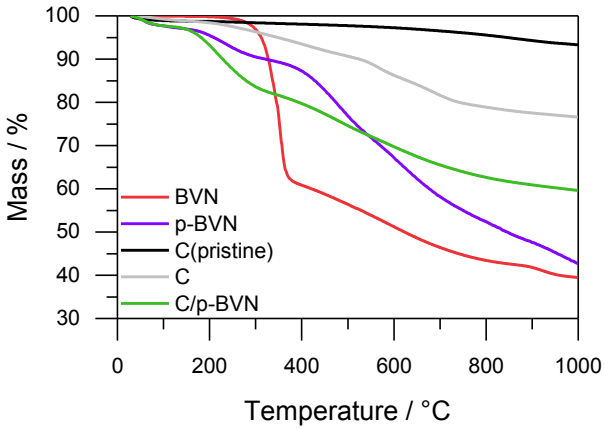

Figure A8. TGA of BVN, p-BVN, C(pristine), C and C/p-BVN

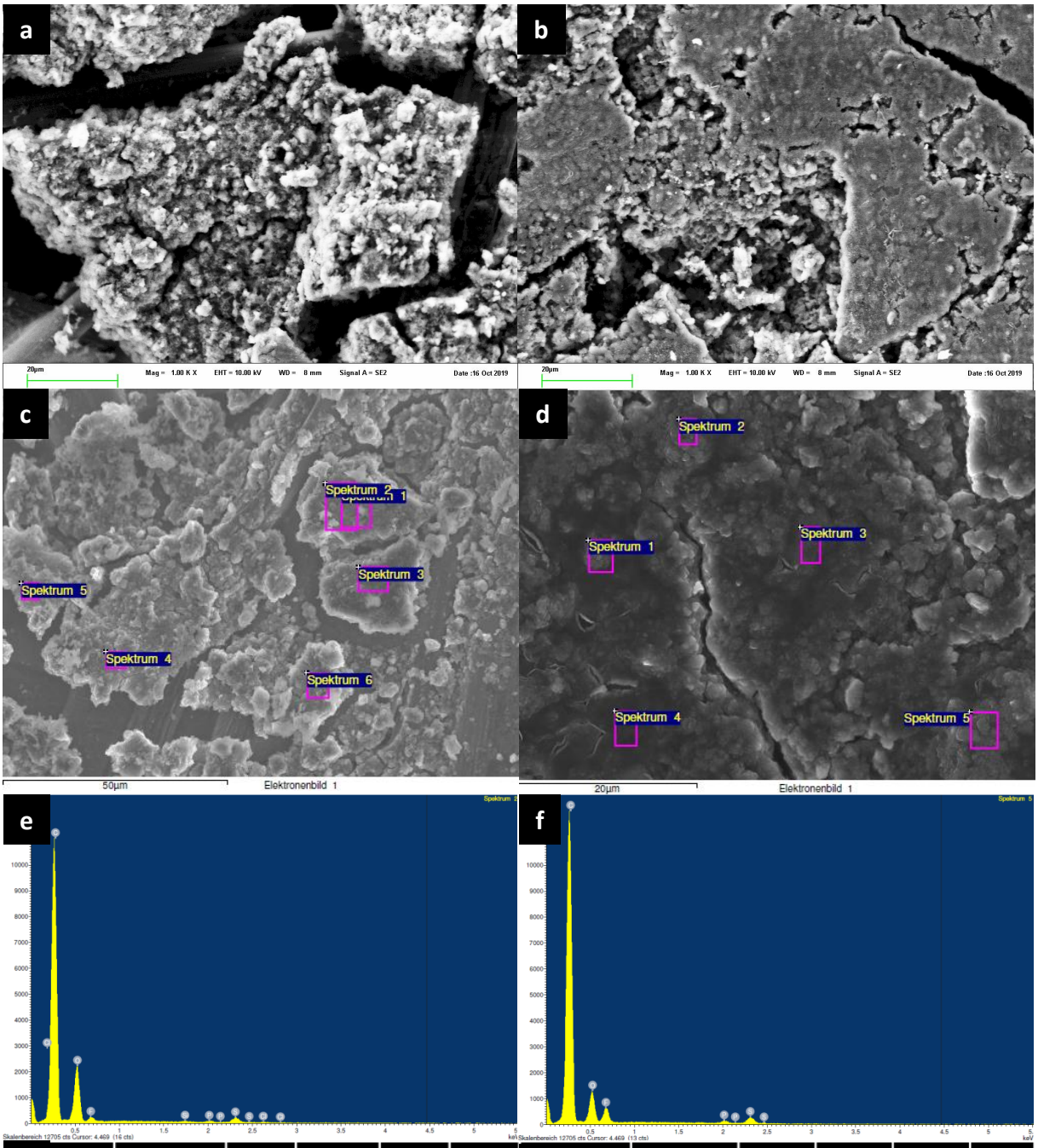

g

Spektrum	C [at. %]	N	O	F	S
2	67.28	6.48	23.35	1.98	0.91
3	63.75	7.09	26.66	1.78	0.73
4	67.33	5.96	23.36	2.62	0.73
5	63.76	8.23	25.26	2.01	0.74
6	61.07	5.37	30.40	2.32	0.84

h

Spektrum	C [at. %]	N	O	F	S
1	69.14	6.30	14.56	8.87	1.14
2	72.21	7.46	13.58	5.62	1.13
3	64.89	5.96	12.14	16.02	1.00
4	43.30	3.29	10.49	41.81	1.11
5	72.69	6.82	13.31	6.08	1.11

Figure A9. SEM images (a and b, scale bar 20 µm), SEM images with indication of areas for investigation by EDX spectroscopy (c and d), EDX spectra (e and f), and elemental analysis as obtained from EDX (g and h) for C/p-BVN(aged) (a, c, e, and g) and C/p-BVN(cycled) (b, d, f, and h).

Table A3. Combustive elemental analysis of Schiff bases of PAAm. All the measurements were performed twice (first two rows) and the average is calculated.

	N [wt %]	C [wt %]	H [wt %]	S [wt %]
P-o	8.98	64.87	7.061	1.023
	8.69	65.21	6.944	0.914
AVERAGE	8.84	65.04	7.003	0.969
P-van	7.78	67.32	7.180	0.815
	7.80	67.18	7.186	0.773
AVERAGE	7.79	67.25	7.183	0.794
P-m	7.70	65.66	6.476	0.907
	7.72	65.69	6.620	0.360
AVERAGE	7.71	65.68	6.548	0.634

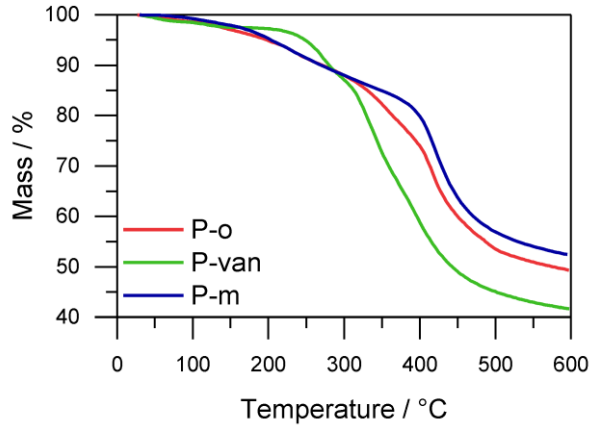

Figure 40. TGA of P-o, P-van and P-m.

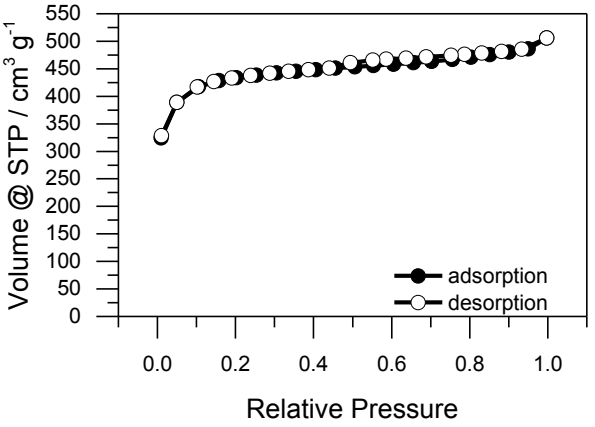

Figure A11. Nitrogen physisorption measurement of C(pristine).

Table A4. Combustive elemental analysis of the following samples. All the measurements were performed twice (first two rows) and the average is calculated.

Name	N/%	C/%	H/%	S/%
STC-1	0.11	81.30	0.74	4.01
	0.10	79.76	0.74	3.30
AVERAGE	0.11	80.53	0.74	3.66
STC-2	0.15	88.98	0.60	4.82
	0.12	90.09	0.59	4.34
AVERAGE	0.14	89.54	0.60	4.58
STC-4	0.20	88.98	0.84	6.40
	0.19	88.25	0.83	6.33
AVERAGE	0.20	88.62	0.84	6.37
STC-8	0.58	85.22	0.68	4.77
	0.64	87.06	0.69	4.89
AVERAGE	0.61	86.14	0.69	4.83
STC-1/P-m	4.39	68.83	4.04	1.83
	4.38	68.48	4.05	1.64
AVERAGE	4.39	68.66	4.05	1.74
STC-2/P-m	5.18	69.10	4.32	1.83
	5.32	71.52	4.51	1.89
AVERAGE	5.25	70.31	4.42	1.86
STC-4/P-m	4.86	66.27	4.21	2.28
	5.09	69.43	4.40	2.39
AVERAGE	4.98	67.85	4.31	2.34
STC-8/P-m	4.82	68.81	4.07	1.95
	4.79	68.66	4.05	1.95
AVERAGE	4.81	68.74	4.06	1.95
STC-1/P-o	4.62	67.92	4.19	1.65
	4.61	68.32	4.22	1.63
AVERAGE	4.62	68.12	4.21	1.64
STC-2/P-o	4.70	68.13	4.09	1.88
	4.57	66.84	4.02	1.84
AVERAGE	6.64	67.45	4.06	1.86
STC-4/P-o	4.71	68.25	4.09	2.48
	4.67	67.17	3.99	2.43
AVERAGE	4.69	67.71	4.04	2.46
STC-8/P-o	4.87	68.39	3.93	1.96
	5.00	70.30	4.04	2.04
AVERAGE	4.94	69.35	3.99	2.00
P-o	9.84	68.13	7.45	2.20
	9.11	64.47	6.71	0.12
AVERAGE	9.48	66.30	7.08	1.16
P-m	8.10	64.44	7.28	0.06
	8.25	64.78	7.40	0.05

AVERAGE	8.17	64.61	7.34	0.06

Table A5. Combustive elemental analysis.

Name	N/%	C/%	H/%	S/%	O/%
tannic acid	0.00	48.88	3.83	0.76	46.83
	0.00	48.90	3.87	0.72	47.59
AVERAGE	0.00	48.89	3.85	0.74	47.21
C(pristine)	1.02	92.66	1.35	2.63	3.05
	1.03	93.01	1.28	2.61	1.90
AVERAGE	1.03	92.84	1.32	2.62	2.48
C(50 min)	1.10	70.36	1.50	2.34	16.00
	1.09	70.24	1.44	2.30	15.51
AVERAGE	1.10	70.30	1.47	2.32	15.76
C(50 min)/TAN	1.18	61.37	2.86	1.75	26.34
	1.18	61.30	2.86	1.73	26.36
AVERAGE	1.18	61.34	2.86	1.74	26.35
C/TAN	1.30	69.85	3.23	1.88	24.95
	1.25	69.76	3.18	1.84	24.55
AVERAGE	1.27	69.81	3.21	1.86	24.75
C/TAN(PEG)	1.48	70.92	3.23	1.75	23.35
	1.46	70.78	3.48	1.76	23.89
AVERAGE	1.47	70.85	3.36	1.76	23.62
C(Ar)	0.61	76.17	4.00	1.55	15.29
	0.65	80.30	4.08	1.55	14.97
AVERAGE	0.63	78.24	4.04	1.55	15.13

cc

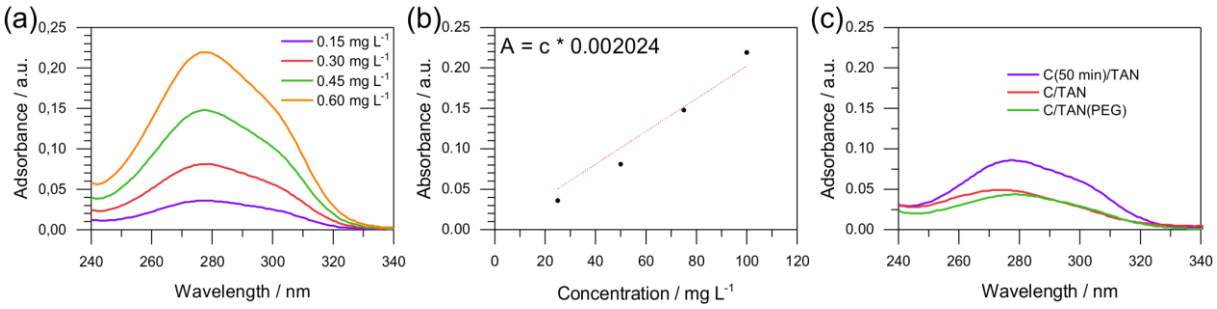

Figure A12. (a) UV/Vis spectra of tannic acid at different concentrations. (b) Calibration line. (c) UV/Vis spectra of tannic acid leaked from different composites.

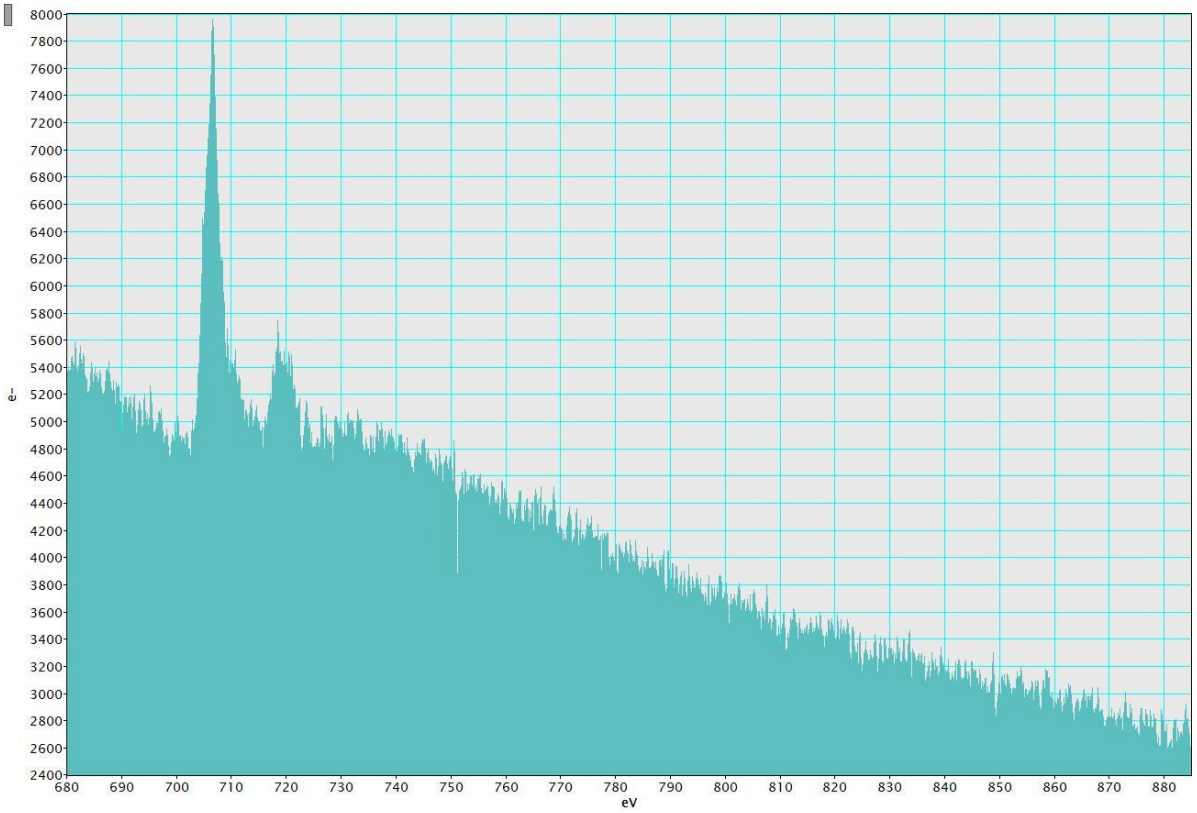

Figure A13. EELS of C(50 min).

8.5. Abbreviations

Avg. – average

BET - Brunauer-Emmett-Teller

BVN – bisvanillonitrile

CB – carbon black

CNHS – carbon, nitrogen, hydrogen and sulphur

CTF – covalent triazine framework

CV – cyclic voltammetry

DEC – diethyl carbonate

EC – ethylene carbonate

EDL(C) – electrical double layer (capacitance)

EDX – energy dispersive X-ray

EELS - electron energy loss spectroscopy

EIS - electrochemical impedance spectroscopy

FT-IR - Fourier-transform infrared spectroscopy

GCDM – galvanostatic charging discharging measurements

HIT - 5-hydroxyisophthalonitrile

ICP - inductively coupled plasma

LIB – lithium-ion battery

MS - mass spectrometry

NMP - N-methyl-2-pyrrolidone

NMR – nuclear magnetic resonance

OES – atomic emission spectroscopy

PAAm- polyallylamine

p-BVN – polymerised BVN

PG – propylene glycol

p-HIT – polymerised HIT

PVDF – polyvinylidene difluoride

SEI - solid electrolyte interphase

SEM – scanning electron microscopy

STC – salt-templated carbon

STEM - scanning transmission electron microscopy

TAN – tannic acid

TEM – transition electron microscopy

TGA – thermogravimetric analysis

UV – ultraviolet

Vis – visible

VN – vanillonitrile

XPS – X-ray photoelectron spectroscopy

(P)XRD – (powder) X-ray diffraction

8.5. Declaration

Die vorliegende Dissertation entstand im Zeitraum zwischen Oktober 2017 und Februar 2020 unter der Betreuung von Prof. Dr. Dr. h.c. Markus Antonietti am Max-Planck-Institut für Kolloid- und Grenzflächenforschung.

Hiermit erkläre ich, dass die vorliegende Arbeit selbständig angefertigt wurde und keine anderen als die angegebenen Hilfsmittel und Quellen verwendet wurden.

The present work was carried out and written during October 2017 and February 2020 at the Max Planck Institute of Colloids and Interfaces under the supervision of Prof. Dr. Dr. h.c. Markus Antonietti.

I declare that I have produced all the work using only literature and other aids as described here.

IVAN ILIC

POTSDAM, February 2020

8.6. Publication list

1) Ilic, I. K.; Meurer, M.; Chaleawlert-umpon, S.; Antonietti, M.; Liedel, C. Vanillin decorated chitosan as electrode material for sustainable energy storage. *RSC Adv.* **2019**, *9*, 4591-4598
2) Ilic, I. K.; Leus, K.; Schmidt, J.; Hwang, J.; Maranska, M.; Eigler, S.; Liedel, C. Polymerization in Carbone: A Novel Method for the Synthesis of More Sustainable Electrodes and Their Application as Cathodes for Lithium−Organic Energy Storage Materials Based On Vanillin. *ACS Sustainable Chem. Eng.* **2020**, *8*, 3055-3064
3) Ilic, I. K.; Perovic, M.; Liedel, C. The interplay of porosity, wettability, and redox activity as determining factors for lithium-organic electrochemical energy storage using biomolecules. *ChemSusChem* **2020**, *13*, 1856-1863
4) Ilic, I. K.; Tsouka, A.; Perovic, M.; Hwang, J.; Heil, T.; Loeffler, F. F.; Oschatz, M.; Antonietti, M.; Liedel, C. Sustainable Cathodes for Lithium-Ion Energy Storage Devices Based on Tannic Acid—Toward Ecofriendly Energy Storage. *Adv. Sustainable Syst.* **2020**, 2000206

9. References

(1) Hazen, R. M.; Grew, E. S.; Origlieri, M. J.; Downs, R. T. On the Mineralogy of the "Anthropocene Epoch." *Am. Mineral.* **2017**, *102* (3), 595–611. https://doi.org/10.2138/am-2017-5875.

(2) Tran, M.; Banister, D.; Bishop, J. D. K.; McCulloch, M. D. Realizing the Electric-Vehicle Revolution. *Nat. Clim. Chang.* **2012**, *2* (5), 328–333. https://doi.org/10.1038/nclimate1429.

(3) Yan, J.; Wei, T.; Fan, Z.; Qian, W.; Zhang, M.; Shen, X.; Wei, F. Preparation of Graphene Nanosheet/carbon Nanotube/polyaniline Composite as Electrode Material for Supercapacitors. *J. Power Sources* **2010**, *195* (9), 3041–3045. https://doi.org/10.1016/j.jpowsour.2009.11.028.

(4) Brundtland United Nations Commission. *Our Common Future*; Oxford University Press, 1987.

(5) Banza Lubaba Nkulu, C.; Casas, L.; Haufroid, V.; De Putter, T.; Saenen, N. D.; Kayembe-Kitenge, T.; Musa Obadia, P.; Kyanika Wa Mukoma, D.; Lunda Ilunga, J. M.; Nawrot, T. S.; et al. Sustainability of Artisanal Mining of Cobalt in DR Congo. *Nat. Sustain.* **2018**, *1* (9), 495–504. https://doi.org/10.1038/s41893-018-0139-4.

(6) Dubal, D. P.; Ayyad, O.; Ruiz, V.; Gómez-Romero, P. Hybrid Energy Storage: The Merging of Battery and Supercapacitor Chemistries. *Chem. Soc. Rev.* **2015**, *44* (7), 1777–1790. https://doi.org/10.1039/c4cs00266k.

(7) Borchardt, L.; Oschatz, M.; Kaskel, S. Tailoring Porosity in Carbon Materials for Supercapacitor Applications. *Mater. Horizons* **2014**, *1* (2), 157–168. https://doi.org/10.1039/c3mh00112a.

(8) Martins, G. F. Why the Daniell Cell Works! *J. Chem. Educ.* **1990**, *67* (6), 482. https://doi.org/10.1021/ed067p482.

(9) Smith, M. J.; Gray, F. M. Batteries, from Cradle to Grave. *J. Chem. Educ.* **2010**, *87* (2), 162–167. https://doi.org/10.1021/ed800053u.

(10) Schon, T. B.; McAllister, B. T.; Li, P.-F.; Seferos, D. S. The Rise of Organic Electrode Materials for Energy Storage. *Chem. Soc. Rev.* **2016**, *45* (22), 6345–6404. https://doi.org/10.1039/C6CS00173D.

(11) Bruning, A. Why Lithium-Ion Batteries Catch Fire. *Chemical & Engineering News*. 2016.

(12) Whittingham, M. S. Electrical Energy Storage and Intercalation Chemistry. *Science (80-.).* **1976**, *192*, 1126–1127. https://doi.org/10.1246/cl.2012.972.

(13) Winter, M.; Barnett, B.; Xu, K. Before Li Ion Batteries. *Chem. Rev.* **2018**, *118* (23), 11433–11456. https://doi.org/10.1021/acs.chemrev.8b00422.

(14) Ryou, M. H.; Lee, Y. M.; Lee, Y.; Winter, M.; Bieker, P. Mechanical Surface Modification of Lithium Metal: Towards Improved Li Metal Anode Performance by Directed Li Plating. *Adv. Funct. Mater.* **2015**, *25* (6), 834–841. https://doi.org/10.1002/adfm.201402953.

(15) Zanini, M.; Basu, S.; Fischer, J. E. Alternate Synthesis and Reflectivity Spectrum of Stage 1 Lithium-Graphite Intercalation Compound. *Carbon N. Y.* **1978**, *16* (3), 211–212. https://doi.org/10.1016/0008-6223(78)90026-X.

(16) Basu, S.; Zeller, C.; Flanders, P. J.; Fuerst, C. D.; Johnson, W. D.; Fischer, J. E. Synthesis and Properties of Lithium-Graphite Intercalation Compounds. *Mater. Sci. Eng.* **1979**, *38* (3), 275–283. https://doi.org/10.1016/0025-5416(79)90132-0.

(17) Mizushima, K.; Jones, P. C.; Wiseman, P. J.; Goodenough, J. B. LixCoO2 (0 < X < 1): A New Cathode Material for Batteries of High Energy Density. *Mater. Res. Bull.* **1980**, *15* (6), 783–789. https://doi.org/10.1143/jjap.42.6131.

(18) Chang, Z.; Li, C.; Wang, Y.; Chen, B.; Fu, L.; Zhu, Y.; Zhang, L.; Wu, Y.; Huang, W. A Lithium Ion Battery Using an Aqueous Electrolyte Solution. *Sci. Rep.* **2016**, *6*, 2–7. https://doi.org/10.1038/srep28421.

(19) Wang, A.; Kadam, S.; Li, H.; Shi, S.; Qi, Y. Review on Modeling of the Anode Solid Electrolyte Interphase (SEI) for Lithium-Ion Batteries. *npj Comput. Mater.* **2018**, *4* (1). https://doi.org/10.1038/s41524-018-0064-0.

(20) Jiang, H.; Lee, P. S.; Li, C. 3D Carbon Based Nanostructures for Advanced Supercapacitors. *Energy Environ. Sci.* **2013**, *6* (1), 41–53. https://doi.org/10.1039/c2ee23284g.

(21) Meng, C.; Gall, O. Z.; Irazoqui, P. P. A Flexible Super-Capacitive Solid-State Power Supply for Miniature Implantable Medical Devices. *Biomed. Microdevices* **2013**, *15* (6), 973–983. https://doi.org/10.1007/s10544-013-9789-1.

(22) Brousse, T.; Bélanger, D.; Long, J. W. To Be or Not To Be Pseudocapacitive? *J. Electrochem. Soc.* **2015**, *162* (5), A5185–A5189. https://doi.org/10.1149/2.0201505jes.

(23) Lukatskaya, M. R.; Dunn, B.; Gogotsi, Y. Multidimensional Materials and Device Architectures for Future Hybrid Energy Storage. *Nat. Commun.* **2016**, *7*, 1–13. https://doi.org/10.1038/ncomms12647.

(24) Elgrishi, N.; Rountree, K. J.; McCarthy, B. D.; Rountree, E. S.; Eisenhart, T. T.; Dempsey, J. L. A Practical Beginner's Guide to Cyclic Voltammetry. *J. Chem. Educ.* **2018**, *95* (2), 197–206. https://doi.org/10.1021/acs.jchemed.7b00361.

(25) Nishide, H.; Oyaizu, K. Toward Flexible Batteries. *Science (80-.).* **2008**, *319* (8), 737–738.

(26) Muench, S.; Wild, A.; Friebe, C.; Häupler, B.; Janoschka, T.; Schubert, U. S. Polymer-Based Organic Batteries. *Chem. Rev.* **2016**, *116* (16), 9438–9484. https://doi.org/10.1021/acs.chemrev.6b00070.

(27) Chiang, C. K. An All-Polymeric Solid State Battery. *Polymer (Guildf).* **1981**, *22*, 2454–1456.

(28) Snook, G. A.; Kao, P.; Best, A. S. Conducting-Polymer-Based Supercapacitor Devices and Electrodes. *J. Power Sources* **2011**, *196* (1), 1–12. https://doi.org/10.1016/j.jpowsour.2010.06.084.

(29) Janoschka, T.; Hager, M. D.; Schubert, U. S. Powering up the Future: Radical Polymers for Battery Applications. *Adv. Mater.* **2012**, *24* (48), 6397–6409. https://doi.org/10.1002/adma.201203119.

(30) Häupler, B.; Wild, A.; Schubert, U. S. Carbonyls: Powerful Organic Materials for Secondary Batteries. *Adv. Energy Mater.* **2015**, *5* (11). https://doi.org/10.1002/aenm.201402034.

(31) Alt, H.; Binder, H.; Köhling, A.; Sandstede, G. Investigation into the Use of Quinone Compounds-for Battery Cathodes. *Electrochim. Acta* **1972**, *17* (5), 873–887. https://doi.org/10.1016/0013-4686(72)90010-2.

(32) Tobishima, S. I.; Yamaki, J. I.; Yamaji, A. Cathode Characteristics of Organic Electron Acceptors for Lithium Batteries. *J. Electrochem. Soc.* **1984**, *131* (1), 57–63. https://doi.org/10.1149/1.2115542.

(33) Boschi, T.; Pappa, R.; Pistoia, G.; Tocci, M. On the Use of Nonylbenzo-Hexaquinone as a Substitute for Monomeric Quinones in Non-Aqueous Cells. *J. Electroanal. Chem.* **1984**, *176* (1–2), 235–242. https://doi.org/10.1016/S0022-0728(84)80321-6.

(34) Le Gall, T.; Reiman, K. H.; Grossel, M. C.; Owen, J. R. Poly(2,5-Dihydroxy-1,4-Benzoquinone-3,6-Methylene): A New Organic Polymer as Positive Electrode Material for Rechargeable Lithium Batteries. *J. Power Sources* **2003**, *119–121*, 316–320. https://doi.org/10.1016/S0378-7753(03)00167-8.

(35) Nokami, T.; Matsuo, T.; Inatomi, Y.; Hojo, N.; Tsukagoshi, T.; Yoshizawa, H.; Shimizu, A.; Kuramoto, H.; Komae, K.; Tsuyama, H.; et al. Polymer-Bound Pyrene-4,5,9,10-Tetraone for Fast-Charge and -Discharge Lithium-Ion Batteries with High Capacity. *J. Am. Chem. Soc.* **2012**, *134* (48), 19694–19700. https://doi.org/10.1021/ja306663g.

(36) Song, Z.; Zhan, H.; Zhou, Y. Anthraquinone Based Polymer as High Performance Cathode Material for Rechargeable Lithium Batteries. *Chem. Commun.* **2009**, No. 4, 448–450. https://doi.org/10.1039/b814515f.

(37) Liu, K.; Zheng, J.; Zhong, G.; Yang, Y. Poly(2,5-Dihydroxy-1,4-Benzoquinonyl Sulfide) (PDBS) as a Cathode Material for Lithium Ion Batteries. *J. Mater. Chem.* **2011**, *21* (12), 4125–4131. https://doi.org/10.1039/c0jm03127e.

(38) Patil, N.; Aqil, A.; Ouhib, F.; Admassie, S.; Inganäs, O.; Jérôme, C.; Detrembleur, C. Bioinspired Redox-Active Catechol-Bearing Polymers as Ultrarobust Organic Cathodes for Lithium Storage. *Adv. Mater.* **2017**, *29* (40), 1–9. https://doi.org/10.1002/adma.201703373.

(39) Acker, P.; Rzesny, L.; Marchiori, C. F. N.; Araujo, C. M.; Esser, B. π-Conjugation Enables Ultra-High Rate Capabilities and Cycling Stabilities in Phenothiazine Copolymers as Cathode-Active Battery Materials. *Adv. Funct. Mater.* **2019**, *1906436*, 1906436. https://doi.org/10.1002/adfm.201906436.

(40) Zhao, L.; Wang, W.; Wang, A.; Yuan, K.; Chen, S.; Yang, Y. A Novel Polyquinone Cathode Material for Rechargeable Lithium Batteries. *J. Power Sources* **2013**, *233*, 23–27. https://doi.org/10.1016/j.jpowsour.2013.01.103.

(41) Häringer, D.; Novák, P.; Haas, O.; Piro, B.; Pham, M. C. Poly(5-Amino-1,4-Naphthoquinone), a Novel Lithium-Inserting Electroactive Polymer with High Specific

Charge. *J. Electrochem. Soc.* **1999**, *146* (7), 2393–2396. https://doi.org/10.1149/1.1391947.

(42) Zhang, W.; Yang, F. K.; Pan, Z.; Zhang, J.; Zhao, B. Correction: Bio-Inspired Dopamine Functionalization of Polypyrrole for Improved Adhesion and Conductivity (Macromolecular Rapid Communications (2014), 35 (350-354)). *Macromol. Rapid Commun.* **2014**, *35* (20), 1808. https://doi.org/10.1002/marc.201400509.

(43) Zhang, W.; Pan, Z.; Yang, F. K.; Zhao, B. A Facile in Situ Approach to Polypyrrole Functionalization through Bioinspired Catechols. *Adv. Funct. Mater.* **2015**, *25* (10), 1588–1597. https://doi.org/10.1002/adfm.201403115.

(44) Arbenz, A.; Avérous, L. Chemical Modification of Tannins to Elaborate Aromatic Biobased Macromolecular Architectures. *Green Chem.* **2015**, *17* (5), 2626–2646. https://doi.org/10.1039/c5gc00282f.

(45) Esposito, D.; Antonietti, M. Redefining Biorefinery: The Search for Unconventional Building Blocks for Materials. *Chem. Soc. Rev.* **2015**, *44* (16), 5821–5835. https://doi.org/10.1039/C4CS00368C.

(46) Zakzeski, J.; Bruijnincx, P. C. A.; Jongerius, A. L.; Weckhuysen, B. M. The Catalytic Valorization of Lignin for the Production of Renewable Chemicals. *Chem. Rev.* **2010**, *110* (6), 3552–3599. https://doi.org/10.1021/cr900354u.

(47) Upton, B. M.; Kasko, A. M. Strategies for the Conversion of Lignin to High-Value Polymeric Materials: Review and Perspective. *Chem. Rev.* **2016**, *116* (4), 2275–2306. https://doi.org/10.1021/acs.chemrev.5b00345.

(48) Thakur, V. K.; Thakur, M. K.; Raghavan, P.; Kessler, M. R. Progress in Green Polymer Composites from Lignin for Multifunctional Applications: A Review. *ACS Sustain. Chem. Eng.* **2014**, *2* (5), 1072–1092. https://doi.org/10.1021/sc500087z.

(49) Liu, W. J.; Jiang, H.; Yu, H. Q. Thermochemical Conversion of Lignin to Functional Materials: A Review and Future Directions. *Green Chem.* **2015**, *17* (11), 4888–4907. https://doi.org/10.1039/c5gc01054c.

(50) Kai, D.; Tan, M. J.; Chee, P. L.; Chua, Y. K.; Yap, Y. L.; Loh, X. J. Towards Lignin-Based Functional Materials in a Sustainable World. *Green Chem.* **2016**, *18* (5), 1175–1200. https://doi.org/10.1039/c5gc02616d.

(51) Matsushita, Y. Conversion of Technical Lignins to Functional Materials with Retained

Polymeric Properties. *J. Wood Sci.* **2015**, *61* (3), 230–250. https://doi.org/10.1007/s10086-015-1470-2.

(52) Schutyser, W.; Renders, T.; Van Den Bosch, S.; Koelewijn, S. F.; Beckham, G. T.; Sels, B. F. Chemicals from Lignin: An Interplay of Lignocellulose Fractionation, Depolymerisation, and Upgrading. *Chem. Soc. Rev.* **2018**, *47* (3), 852–908. https://doi.org/10.1039/c7cs00566k.

(53) Fache, M.; Boutevin, B.; Caillol, S. Vanillin Production from Lignin and Its Use as a Renewable Chemical. *ACS Sustain. Chem. Eng.* **2016**, *4* (1), 35–46. https://doi.org/10.1021/acssuschemeng.5b01344.

(54) Pacek, A. W.; Ding, P.; Garrett, M.; Sheldrake, G.; Nienow, A. W. Catalytic Conversion of Sodium Lignosulfonate to Vanillin: Engineering Aspects. Part 1. Effects of Processing Conditions on Vanillin Yield and Selectivity. *Ind. Eng. Chem. Res.* **2013**, *52* (25), 8361–8372. https://doi.org/10.1021/ie4007744.

(55) Milczarek, G.; Inganas, O. Renewable Cathode Materials from Biopolymer/Conjugated Polymer Interpenetrating Networks. *Science (80-.).* **2012**, *335*, 1468–1471.

(56) Opra, D. P.; Gnedenkov, S. V.; Sinebryukhov, S. L.; Tsvetnikov, A. K.; Sergienko, V. I. Высокоэнергоемкие Литиевые Источники Тока На Основе Гидролизного Лигнина. *Bull Russ Acad Sci Chem* **2012**, *2*, 111–116.

(57) Gnedenkov, S. V.; Opra, D. P.; Sinebryukhov, S. L.; Tsvetnikov, A. K.; Ustinov, A. Y.; Sergienko, V. I. Hydrolysis Lignin-Based Organic Electrode Material for Primary Lithium Batteries. *J. Solid State Electrochem.* **2013**, *17* (10), 2611–2621. https://doi.org/10.1007/s10008-013-2136-x.

(58) Gnedenkov, S. V.; Opra, D. P.; Sinebryukhov, S. L.; Tsvetnikov, A. K.; Ustinov, A. Y.; Sergienko, V. I. Hydrolysis Lignin: Electrochemical Properties of the Organic Cathode Material for Primary Lithium Battery. *J. Ind. Eng. Chem.* **2014**, *20* (3), 903–910. https://doi.org/10.1016/j.jiec.2013.06.021.

(59) Gnedenkov, S. V.; Opra, D. P.; Zemnukhova, L. A.; Sinebryukhov, S. L.; Kedrinskii, I. A.; Patrusheva, O. V.; Sergienko, V. I. Electrochemical Performance of Klason Lignin as a Low-Cost Cathode-Active Material for Primary Lithium Battery. *J. Energy Chem.* **2015**, *24* (3), 346–352. https://doi.org/10.1016/S2095-4956(15)60321-7.

(60) Milczarek, G.; Nowicki, M. Carbon Nanotubes/kraft Lignin Composite:

Characterization and Charge Storage Properties. *Mater. Res. Bull.* **2013**, *48* (10), 4032–4038. https://doi.org/10.1016/j.materresbull.2013.06.022.

(61) Kim, S. K.; Kim, Y. K.; Lee, H.; Lee, S. B.; Park, H. S. Superior Pseudocapacitive Behavior of Confined Lignin Nanocrystals for Renewable Energy-Storage Materials. *ChemSusChem* **2014**, *7* (4), 1094–1101. https://doi.org/10.1002/cssc.201301061.

(62) Chaleawlert-umpon, S.; Berthold, T.; Wang, X.; Antonietti, M.; Liedel, C. Kraft Lignin as Electrode Material for Sustainable Electrochemical Energy Storage. *Adv. Mater. Interfaces* **2017**, *1700698*, 1–7. https://doi.org/10.1002/admi.201700698.

(63) Admassie, S.; Nilsson, T. Y.; Inganäs, O. Charge Storage Properties of Biopolymer Electrodes with (Sub)tropical Lignins. *Phys. Chem. Chem. Phys.* **2014**, *16* (45), 24681–24684. https://doi.org/10.1039/c4cp03777d.

(64) Ajjan, F. N.; Jafari, M. J.; Rębiś, T.; Ederth, T.; Inganäs, O. Spectroelectrochemical Investigation of Redox States in a Polypyrrole/lignin Composite Electrode Material. *J. Mater. Chem. A* **2015**, *3* (24), 12927–12937. https://doi.org/10.1039/c5ta00788g.

(65) Nilsson, T. Y.; Wagner, M.; Inganäs, O. Lignin Modification for Biopolymer/Conjugated Polymer Hybrids as Renewable Energy Storage Materials. *ChemSusChem* **2015**, *8* (23), 4081–4085. https://doi.org/10.1002/cssc.201500570.

(66) Rębiś, T.; Nilsson, T. Y.; Inganäs, O. Hybrid Materials from Organic Electronic Conductors and Synthetic-Lignin Models for Charge Storage Applications. *J. Mater. Chem. A* **2016**, *4* (5), 1931–1940. https://doi.org/10.1039/c5ta06821e.

(67) Navarro-Suárez, A. M.; Carretero-González, J.; Casado, N.; Mecerreyes, D.; Rojo, T.; Castillo-Martínez, E. Hybrid Biopolymer Electrodes for Lithium- and Sodium-Ion Batteries in Organic Electrolytes. *Sustain. Energy Fuels* **2018**, *2* (4), 836–842. https://doi.org/10.1039/c7se00551b.

(68) Gan, J. K.; Lim, Y. S.; Huang, N. M.; Lim, H. N. Boosting the Supercapacitive Properties of Polypyrrole with Chitosan and Hybrid Silver Nanoparticles/nanoclusters. *RSC Adv.* **2016**, *6* (92), 88925–88933. https://doi.org/10.1039/c6ra13697d.

(69) de Hoyos-Martínez, P. L.; Merle, J.; Labidi, J.; Charrier – El Bouhtoury, F. Tannins Extraction: A Key Point for Their Valorization and Cleaner Production. *J. Clean. Prod.* **2019**, *206*, 1138–1155. https://doi.org/10.1016/j.jclepro.2018.09.243.

(70) Oh, J. Y.; Jung, Y.; Cho, Y. S.; Choi, J.; Youk, J. H.; Fechler, N.; Yang, S. J.; Park, C.

R. Metal–Phenolic Carbon Nanocomposites for Robust and Flexible Energy-Storage Devices. *ChemSusChem* **2017**, *10* (8), 1675–1682. https://doi.org/10.1002/cssc.201700549.

(71) Lee, Y. A.; Lee, J.; Kim, D. W.; Yoo, C. Y.; Park, S. H.; Yoo, J. J.; Kim, S.; Kim, B.; Cho, W. K.; Yoon, H. Mussel-Inspired Surface Functionalization of Porous Carbon Nanosheets Using Polydopamine and Fe3+/tannic Acid Layers for High-Performance Electrochemical Capacitors. *J. Mater. Chem. A* **2017**, *5* (48), 25368–25377. https://doi.org/10.1039/c7ta08010g.

(72) Mukhopadhyay, A.; Jiao, Y.; Katahira, R.; Ciesielski, P. N.; Himmel, M.; Zhu, H. Heavy Metal-Free Tannin from Bark for Sustainable Energy Storage. *Nano Lett.* **2017**, *17* (12), 7897–7907. https://doi.org/10.1021/acs.nanolett.7b04242.

(73) Xiong, C.; Zhong, W.; Zou, Y.; Luo, J.; Yang, W. Electroactive Biopolymer/graphene Hydrogels Prepared for High-Performance Supercapacitor Electrodes. *Electrochim. Acta* **2016**, *211*, 941–949. https://doi.org/10.1016/j.electacta.2016.06.117.

(74) Xu, L.; Yu, H.; Li, Y.; Jia, M.; Yao, C.; Jin, X. Tannic Acid-Decorated Spongy Graphene for Flexible and High Performance Supercapacitors. *J. Electrochem. Soc.* **2018**, *165* (9), A1706–A1712. https://doi.org/10.1149/2.0871809jes.

(75) Jia, M.-Y.; Xu, L.-S.; Li, Y.; Yao, C.-L.; Jin, X.-J. Synthesis and Characterization of Graphene/carbonized Paper/tannic Acid for Flexible Composite Electrodes. *New J. Chem.* **2018**, *42* (17), 14576–14585. https://doi.org/10.1039/C8NJ02898B.

(76) Xiong, C.; Zou, Y.; Peng, Z.; Zhong, W. Synthesis of Morphology-Tunable Electroactive Biomass/graphene Composites Using Metal Ions for Supercapacitors. *Nanoscale* **2019**, *11* (15), 7304–7316. https://doi.org/10.1039/c9nr00659a.

(77) Fache, M.; Boutevin, B.; Caillol, S. Vanillin, a Key-Intermediate of Biobased Polymers. *Eur. Polym. J.* **2015**, *68*, 488–502. https://doi.org/10.1016/j.eurpolymj.2015.03.050.

(78) Desbrières, J.; Martinez, C.; Rinaudo, M. Hydrophobic Derivatives of Chitosan: Characterization and Rheological Behaviour. *Int. J. Biol. Macromol.* **1996**, *19* (1), 21–28. https://doi.org/10.1016/0141-8130(96)01095-1.

(79) Jagadish, R. S.; Divyashree, K. N.; Viswanath, P.; Srinivas, P.; Raj, B. Preparation of N-Vanillyl Chitosan and 4-Hydroxybenzyl Chitosan and Their Physico-Mechanical,

Optical, Barrier, and Antimicrobial Properties. *Carbohydr. Polym.* **2012**, *87* (1), 110–116. https://doi.org/10.1016/j.carbpol.2011.07.024.

(80) Clayden, J.; Greeves, N.; Warren, S. *Organic Chemistry*, Second Edi.; Oxford University Press, 2012.

(81) Lane, C. F. Sodium Cyanoborohydride - A Hihgly Selective Reducing Agent for Organic Functional Groups. *Syntesis* **1974**, 135–146.

(82) Balachandran, V.; Parimala, K. Vanillin and Isovanillin: Comparative Vibrational Spectroscopic Studies, Conformational Stability and NLO Properties by Density Functional Theory Calculations. *Spectrochim. Acta - Part A Mol. Biomol. Spectrosc.* **2012**, *95*, 354–368. https://doi.org/10.1016/j.saa.2012.03.087.

(83) Fulmer, G. R.; Miller, A. J. M.; Sherden, N. H.; Gottlieb, H. E.; Nudelman, A.; Stoltz, B. M.; Bercaw, J. E.; Goldberg, K. I. NMR Chemical Shifts of Trace Impurities: Common Laboratory Solvents, Organics, and Gases in Deuterated Solvents Relevant to the Organometallic Chemist. *Organometallics* **2010**, *29* (9), 2176–2179. https://doi.org/10.1021/om100106e.

(84) Isikgor, F. H.; Becer, C. R. Lignocellulosic Biomass: A Sustainable Platform for the Production of Bio-Based Chemicals and Polymers. *Polym. Chem.* **2015**, *6* (25), 4497–4559. https://doi.org/10.1039/C5PY00263J.

(85) Filip, J.; Šefčovičová, J.; Gemeiner, P.; Tkac, J. Electrochemistry of Bilirubin Oxidase and Its Use in Preparation of a Low Cost Enzymatic Biofuel Cell Based on a Renewable Composite Binder Chitosan. *Electrochim. Acta* **2013**, *87*, 366–374. https://doi.org/10.1016/j.electacta.2012.09.054.

(86) Ajjan, F. N.; Casado, N.; Rębiś, T.; Elfwing, A.; Solin, N.; Mecerreyes, D.; Inganäs, O. High Performance PEDOT/lignin Biopolymer Composites for Electrochemical Supercapacitors. *J. Mater. Chem. A* **2016**, *4* (5), 1838–1847. https://doi.org/10.1039/c5ta10096h.

(87) Štefanić, G.; Krehula, S.; Štefanić, I. The High Impact of a Milling Atmosphere on Steel Contamination. *Chem. Commun.* **2013**, *49* (81), 9245–9247. https://doi.org/10.1039/c3cc44803g.

(88) Štefanić, G.; Krehula, S.; Štefanić, I. Phase Development during High-Energy Ball-Milling of Zinc Oxide and Iron-the Impact of Grain Size on the Source and the Degree

of Contamination. *Dalt. Trans.* **2015**, *44* (43), 18870–18881. https://doi.org/10.1039/c5dt02498f.

(89) Milczarek, G. Lignosulfonate-Modified Electrodes: Electrochemical Properties and Electrocatalysis of NADH Oxidation. *Langmuir* **2009**, *25* (17), 10345–10353. https://doi.org/10.1021/la9008575.

(90) Song, Z.; Zhou, H. Towards Sustainable and Versatile Energy Storage Devices: An Overview of Organic Electrode Materials. *Energy Environ. Sci.* **2013**, *6* (8), 2280–2301. https://doi.org/10.1039/c3ee40709h.

(91) Admassie, S.; Nilsson, T. Y.; Inganäs, O. Charge Storage Properties of Biopolymer Electrodes with (Sub)tropical Lignins. *Phys. Chem. Chem. Phys.* **2014**, *16* (45), 24681–24684. https://doi.org/10.1039/c4cp03777d.

(92) Thompson, R.; Doggrell, S.; Hoberg, J. O. Potassium Channel Activators Based on the Benzopyran Substructure: Synthesis and Activity of the C-8 Substituent. *Bioorganic Med. Chem.* **2003**, *11* (8), 1663–1668. https://doi.org/10.1016/S0968-0896(03)00058-0.

(93) Wallis, P. J.; Booth, K. J.; Patti, A. F.; Scott, J. L. Oxidative Coupling Revisited: Solvent-Free, Heterogeneous and in Water. *Green Chem.* **2006**, *8* (4), 333. https://doi.org/10.1039/b518132a.

(94) Gang, H.; Lee, D.; Choi, K. Y.; Kim, H. N.; Ryu, H.; Lee, D. S.; Kim, B. G. Development of High Performance Polyurethane Elastomers Using Vanillin-Based Green Polyol Chain Extender Originating from Lignocellulosic Biomass. *ACS Sustain. Chem. Eng.* **2017**, *5* (6), 4582–4588. https://doi.org/10.1021/acssuschemeng.6b02960.

(95) Sarhan, A. A. O.; Bolm, C. Iron(iii) Chloride in Oxidative C–C Coupling Reactions. *Chem. Soc. Rev.* **2009**, *38* (9), 2730. https://doi.org/10.1039/b906026j.

(96) Kuhn, P.; Antonietti, M.; Thomas, A. Porous, Covalent Triazine-Based Frameworks Prepared by Ionothermal Synthesis. *Angew. Chemie - Int. Ed.* **2008**, *47* (18), 3450–3453. https://doi.org/10.1002/anie.200705710.

(97) Kuhn, P.; Krüger, K.; Thomas, A.; Antonietti, M. "Everything Is Surface": Tunable Polymer Organic Frameworks with Ultrahigh Dye Sorption Capacity. *Chem. Commun.* **2008**, No. 44, 5815–5817. https://doi.org/10.1039/b814254h.

(98) Palkovits, R.; Antonietti, M.; Kuhn, P.; Thomas, A.; Schüth, F. Solid Catalysts for the Selective Low-Temperature Oxidation of Methane to Methanol. *Angew. Chemie - Int.*

Ed. **2009**, *48* (37), 6909–6912. https://doi.org/10.1002/anie.200902009.

(99) Katekomol, P.; Roeser, J.; Bojdys, M.; Weber, J.; Thomas, A. Covalent Triazine Frameworks Prepared from 1,3,5-Tricyanobenzene. *Chem. Mater.* **2013**, *25* (9), 1542–1548. https://doi.org/10.1021/cm303751n.

(100) Hao, L.; Luo, B.; Li, X.; Jin, M.; Fang, Y.; Tang, Z.; Jia, Y.; Liang, M.; Thomas, A.; Yang, J.; et al. Terephthalonitrile-Derived Nitrogen-Rich Networks for High Performance Supercapacitors. *Energy Environ. Sci.* **2012**, *5* (12), 9747. https://doi.org/10.1039/c2ee22814a.

(101) Sakaushi, K.; Nickerl, G.; Wisser, F. M.; Nishio-Hamane, D.; Hosono, E.; Zhou, H.; Kaskel, S.; Eckert, J. An Energy Storage Principle Using Bipolar Porous Polymeric Frameworks. *Angew. Chemie - Int. Ed.* **2012**, *51* (31), 7850–7854. https://doi.org/10.1002/anie.201202476.

(102) Sakaushi, K.; Hosono, E.; Nickerl, G.; Gemming, T.; Zhou, H.; Kaskel, S.; Eckert, J. Aromatic Porous-Honeycomb Electrodes for a Sodium-Organic Energy Storage Device. *Nat. Commun.* **2013**, *4*, 1485. https://doi.org/10.1038/ncomms2481.

(103) Liao, H.; Ding, H.; Li, B.; Ai, X.; Wang, C. Covalent-Organic Frameworks: Potential Host Materials for Sulfur Impregnation in Lithium–sulfur Batteries. *J. Mater. Chem. A* **2014**, *2* (23), 8854–8858. https://doi.org/10.1039/C4TA00523F.

(104) Hao, L.; Ning, J.; Luo, B.; Wang, B.; Zhang, Y.; Tang, Z.; Yang, J.; Thomas, A.; Zhi, L. Structural Evolution of 2D Microporous Covalent Triazine-Based Framework toward the Study of High-Performance Supercapacitors. *J. Am. Chem. Soc.* **2015**, *137* (1), 219–225. https://doi.org/10.1021/ja508693y.

(105) Li, Y.; Zheng, S.; Liu, X.; Li, P.; Sun, L.; Yang, R.; Wang, S.; Wu, Z. S.; Bao, X.; Deng, W. Q. Conductive Microporous Covalent Triazine-Based Framework for High-Performance Electrochemical Capacitive Energy Storage. *Angew. Chemie - Int. Ed.* **2017**, 1–6. https://doi.org/10.1002/anie.201711169.

(106) Talapaneni, S. N.; Hwang, T. H.; Je, S. H.; Buyukcakir, O.; Choi, J. W.; Coskun, A. Elemental-Sulfur-Mediated Facile Synthesis of a Covalent Triazine Framework for High-Performance Lithium-Sulfur Batteries. *Angew. Chemie - Int. Ed.* **2016**, *55* (9), 3106–3111. https://doi.org/10.1002/anie.201511553.

(107) Je, S. H.; Kim, H. J.; Kim, J.; Choi, J. W.; Coskun, A. Perfluoroaryl-Elemental Sulfur S

N Ar Chemistry in Covalent Triazine Frameworks with High Sulfur Contents for Lithium-Sulfur Batteries. *Adv. Funct. Mater.* **2017**, *1703947*, 1703947. https://doi.org/10.1002/adfm.201703947.

(108) See, K. A.; Hug, S.; Schwinghammer, K.; Lumley, M. A.; Zheng, Y.; Nolt, J. M.; Stucky, G. D.; Wudl, F.; Lotsch, B. V.; Seshadri, R. Lithium Charge Storage Mechanisms of Cross-Linked Triazine Networks and Their Porous Carbon Derivatives. *Chem. Mater.* **2015**, *27* (11), 3821–3829. https://doi.org/10.1021/acs.chemmater.5b00772.

(109) Sakaushi, K.; Hosono, E.; Nickerl, G.; Zhou, H.; Kaskel, S.; Eckert, J. Bipolar Porous Polymeric Frameworks for Low-Cost, High-Power, Long-Life All-Organic Energy Storage Devices. *J. Power Sources* **2014**, *245*, 553–556. https://doi.org/10.1016/j.jpowsour.2013.07.007.

(110) Ren, S.; Bojdys, M. J.; Dawson, R.; Laybourn, A.; Khimyak, Y. Z.; Adams, D. J.; Cooper, A. I. Porous, Fluorescent, Covalent Triazine-Based Frameworks via Room-Temperature and Microwave-Assisted Synthesis. *Adv. Mater.* **2012**, *24* (17), 2357–2361. https://doi.org/10.1002/adma.201200751.

(111) Zhu, X.; Tian, C.; Mahurin, S. M.; Chai, S. H.; Wang, C.; Brown, S.; Veith, G. M.; Luo, H.; Liu, H.; Dai, S. A Superacid-Catalyzed Synthesis of Porous Membranes Based on Triazine Frameworks for CO 2 Separation. *J. Am. Chem. Soc.* **2012**, *134* (25), 10478–10484. https://doi.org/10.1021/ja304879c.

(112) Huang, W.; Wang, Z. J.; Ma, B. C.; Ghasimi, S.; Gehrig, D.; Laquai, F.; Landfester, K.; Zhang, K. A. I. Hollow Nanoporous Covalent Triazine Frameworks: Via Acid Vapor-Assisted Solid Phase Synthesis for Enhanced Visible Light Photoactivity. *J. Mater. Chem. A* **2016**, *4* (20), 7555–7559. https://doi.org/10.1039/c6ta01828a.

(113) Kuecken, S.; Acharjya, A.; Zhi, L.; Schwarze, M.; Schomäcker, R.; Thomas, A. Fast Tuning of Covalent Triazine Frameworks for Photocatalytic Hydrogen Evolution. *Chem. Commun.* **2017**, *53* (43), 5854–5857. https://doi.org/10.1039/C7CC01827D.

(114) Yanagida, S.; Yokoe, M.; Katagiri, I.; Ohoka, M.; Komori, S. Studies on Nitrile Salts. IV. Trimerization of Nitriles to 1,3,5-Triazines by the Combined Catalyst PCl5-HCl. *Bull. Chem. Soc. Jpn.* **1973**, *46*, 306–310.

(115) Ren, S.; Bojdys, M. J.; Dawson, R.; Laybourn, A.; Khimyak, Y. Z.; Adams, D. J.;

Cooper, A. I. Support Info - Porous, Fluorescent, Covalent Triazine-Based Frameworks via Room-Temperature and Microwave-Assisted Synthesis. *Adv. Mater.* **2012**, *24* (17), 2357–2361. https://doi.org/10.1002/adma.201200751.

(116) Vujković, M.; Matović, L.; Krstić, J.; Stojmenović, M.; Đukić, A.; Babić, B.; Mentus, S. Mechanically Activated Carbonized Rayon Fibers as an Electrochemical Supercapacitor in Aqueous Solutions. *Electrochim. Acta* **2017**, *245*, 796–806. https://doi.org/10.1016/j.electacta.2017.06.018.

(117) Kim, Y. T.; Mitani, T. Competitive Effect of Carbon Nanotubes Oxidation on Aqueous EDLC Performance: Balancing Hydrophilicity and Conductivity. *J. Power Sources* **2006**, *158* (2 SPEC. ISS.), 1517–1522. https://doi.org/10.1016/j.jpowsour.2005.10.069.

(118) Oikawa, E.; Yahata, K. Schiff's Bases of Polyallylamine - Synthesis and Membrane Properties for Reverse Osmosis. *Polym. Bull.* **1987**, *17* (4), 315–322. https://doi.org/10.1007/BF00955714.

(119) Oikawa, E.; Katoh, K.; Yahata, K. Reverse Osmotic Separation of Sodium Chloride and Cobalt(II) Chloride through Membranes Prepared from Schiff Bases of Polyallylamine. *Sep. Sci. Technol.* **1990**, *25* (1–2), 45–62. https://doi.org/10.1080/01496399008050320.

(120) Oikawa, E.; Katoh, K.; Aoki, T. Characteristics of Reverse Osmosis Membranes Prepared from Schiff Bases of Polyallylamine in Aprotic Solvents and Separation of Inorganic and Organic Solutes through the Membranes. *Sep. Sci. Technol.* **1991**, *26* (4), 569–584. https://doi.org/10.1080/01496399108050491.

(121) Oikawa, E.; Soyama, M.; Aoki, T. Separation Performances of the Membranes Prepared from Schiff Bases of Poly(allylamine) for Organic Solutes. *Polymer (Guildf).* **1994**, *35* (10), 2153–2159. https://doi.org/10.1016/0032-3861(94)90243-7.

(122) Saggiomo, V.; Lüning, U. On the Formation of Imines in Water-a Comparison. *Tetrahedron Lett.* **2009**, *50* (32), 4663–4665. https://doi.org/10.1016/j.tetlet.2009.05.117.

(123) Mondal, A.; Mandal, B. Synthesis and Characterization of Crosslinked Poly(vinyl alcohol)/poly(allylamine)/2-Amino-2-Hydroxymethyl-1,3-Propanediol/polysulfone Composite Membrane for CO2/N2 Separation. *J. Memb. Sci.* **2013**, *446*, 383–394. https://doi.org/10.1016/j.memsci.2013.06.052.

(124) Kovacic, J. E. The CN Stretching Frequency in the Infrared Spectra of Schiff's Base Complexes-I. Copper Complexes of Salicylidene Anilines. *Spectrochim. Acta Part A Mol. Spectrosc.* **1967**, *23* (1), 183–187. https://doi.org/10.1016/0584-8539(67)80219-8.

(125) Ilic, I. K.; Leus, K.; Schmidt, J.; Hwang, J.; Maranska, M.; Eigler, S.; Liedel, C. Polymerisation in Carbone: A Novel Method for the Synthesis of More Sustainable Electrodes and Their Application as Cathodes for Lithium-Organic Energy Storage Based on Vanillin. *Prep.*

(126) Risse, S.; Angioletti-Uberti, S.; Dzubiella, J.; Ballauff, M. Capacity Fading in Lithium/sulfur Batteries: A Linear Four-State Model. *J. Power Sources* **2014**, *267*, 648–654. https://doi.org/10.1016/j.jpowsour.2014.05.076.

(127) Liu, T. C.; Pell, W. G.; Conway, B. E.; Roberson, S. L. Behavior of Molybdenum Nitrides as Materials for Electrochemical Capacitors Comparison with Ruthenium Oxide. *J. Electrochem. Soc.* **1998**, *145* (6), 1882–1888. https://doi.org/10.1149/1.1838571.

(128) Wang, J.; Polleux, J.; Lim, J.; Dunn, B. Pseudocapacitive Contributions to Electrochemical Energy Storage in TiO 2 (Anatase) Nanoparticles. *J. Phys. Chem. C* **2007**, *111* (40), 14925–14931. https://doi.org/10.1021/jp074464w.

(129) Chao, D.; Zhu, C.; Yang, P.; Xia, X.; Liu, J.; Wang, J.; Fan, X.; Savilov, S. V.; Lin, J.; Fan, H. J.; et al. Array of Nanosheets Render Ultrafast and High-Capacity Na-Ion Storage by Tunable Pseudocapacitance. *Nat. Commun.* **2016**, *7*, 1–8. https://doi.org/10.1038/ncomms12122.

(130) Huang, Q.; Choi, D.; Cosimbescu, L.; Lemmon, J. P. Multi-Electron Redox Reaction of an Organic Radical Cathode Induced by a Mesopore Carbon Network with Nitroxide Polymers. *Phys. Chem. Chem. Phys.* **2013**, *15* (48), 20921–20928. https://doi.org/10.1039/c3cp54358g.

(131) Chmiola, J.; Yushin, G.; Gogotsi, Y.; Portet, C.; Simon, P.; Taberna, P. L. Anomalous Increase in Carbon at Pore Sizes Less than 1 Nanometer. *Science (80-.).* **2006**, *313* (5794), 1760–1763. https://doi.org/10.1126/science.1132195.

(132) Oschatz, M.; Boukhalfa, S.; Nickel, W.; Hofmann, J. P.; Fischer, C.; Yushin, G.; Kaskel, S. Carbide-Derived Carbon Aerogels with Tunable Pore Structure as Versatile Electrode Material in High Power Supercapacitors. *Carbon N. Y.* **2017**, *113*, 283–291.

https://doi.org/10.1016/j.carbon.2016.11.050.

(133) Yan, R.; Antonietti, M.; Oschatz, M. Toward the Experimental Understanding of the Energy Storage Mechanism and Ion Dynamics in Ionic Liquid Based Supercapacitors. *Adv. Energy Mater.* **2018**, *8* (18), 1–12. https://doi.org/10.1002/aenm.201800026.

(134) Love, B. E.; Simmons, A. L. Substituent Effects in the Oxidation of 2-Alkyl-1,4-Dialkoxybenzenes with Ceric Ammonium Nitrate. *Tetrahedron Lett.* **2016**, *57* (50), 5712–5715. https://doi.org/10.1016/j.tetlet.2016.11.042.

(135) Morimoto, N.; Kubo, T.; Nishina, Y. Tailoring the Oxygen Content of Graphite and Reduced Graphene Oxide for Specific Applications. *Sci. Rep.* **2016**, *6*, 4–11. https://doi.org/10.1038/srep21715.

(136) Jia, M. Y.; Xu, L. S.; Li, Y.; Yao, C. L.; Jin, X. J. Synthesis and Characterization of Graphene/carbonized Paper/tannic Acid for Flexible Composite Electrodes. *New J. Chem.* **2018**, *42* (17), 14576–14585. https://doi.org/10.1039/c8nj02898b.

(137) Nakahara, K.; Iriyama, J.; Iwasa, S.; Suguro, M.; Satoh, M.; Cairns, E. J. High-Rate Capable Organic Radical Cathodes for Lithium Rechargeable Batteries. *J. Power Sources* **2007**, *165* (2), 870–873. https://doi.org/10.1016/j.jpowsour.2006.11.045.

(138) Jeon, I. Y.; Shin, Y. R.; Sohn, G. J.; Choi, H. J.; Bae, S. Y.; Mahmood, J.; Jung, S. M.; Seo, J. M.; Kim, M. J.; Chang, D. W.; et al. Edge-Carboxylated Graphene Nanosheets via Ball Milling. *Proc. Natl. Acad. Sci. U. S. A.* **2012**, *109* (15), 5588–5593. https://doi.org/10.1073/pnas.1116897109.

(139) Xu, J.; Shui, J.; Wang, J.; Wang, M.; Liu, H. K.; Dou, S. X.; Jeon, I. Y.; Seo, J. M.; Baek, J. B.; Dai, L. Sulfur-Graphene Nanostructured Cathodes via Ball-Milling for High-Performance Lithium-Sulfur Batteries. *ACS Nano* **2014**, *8* (10), 10920–10930. https://doi.org/10.1021/nn5047585.

(140) Leistenschneider, D.; Zürbes, K.; Schneidermann, C.; Grätz, S.; Oswald, S.; Wegner, K.; Klemmed, B.; Giebeler, L.; Eychmüller, A.; Borchardt, L. Mechanochemical Functionalization of Carbon Black at Room Temperature. *Carbon N. Y.* **2018**, *4* (1), 14. https://doi.org/10.3390/c4010014.

(141) Mardix, S.; Alexander, E.; Brafman, O.; Steinberger, I. T. Polytype Families in Zinc Sulphide Crystals. *Acta Crystallogr.* **1967**, *22* (6), 808–812. https://doi.org/10.1107/s0365110x67001616.

(142) Howarth, A. J.; Peters, A. W.; Vermeulen, N. A.; Wang, T. C.; Hupp, J. T.; Farha, O. K. Best Practices for the Synthesis, Activation, and Characterization of Metal–Organic Frameworks. *Chem. Mater.* **2016**, *29*, 26–39. https://doi.org/10.1021/acs.chemmater.6b02626.

(143) Wiberley, S. E.; Aikens, D. A. Chemical Lnstrumentation. *J. Chem. Educ.* **1964**, *41* (2).

(144) Hieftje, G. M. Atomic Emission Spectroscopy - It Lasts and Lasts and Lasts. *J. Chem. Educ.* **2000**, *77* (5), 577–583. https://doi.org/10.1021/ed077p577.

(145) Cychosz, K. A.; my Guillet-Nicolas, R.; Garcí a-Martí nez, J.; Thommes, M. Recent Advances in the Textural Characterization of Hierarchically Structured Nanoporous Materials. *Chem. Soc. Rev.* **2017**, *46*, 389–414. https://doi.org/10.1039/c6cs00391e.

(146) Hector, D.; Olivero, S.; Orange, F.; Duñach, E.; Gal, J. F. Quality Control of a Functionalized Polymer Catalyst by Energy Dispersive X-Ray Spectrometry (EDX or EDS). *Anal. Chem.* **2019**, *91* (3), 1773–1778. https://doi.org/10.1021/acs.analchem.8b04170.

(147) Pal, R.; Sikder, A. K.; Saito, K.; Funston, A. M.; Bellare, J. R. Electron Energy Loss Spectroscopy for Polymers: A Review. *Polym. Chem.* **2017**, *8* (45), 6927–6937. https://doi.org/10.1039/c7py01459g.

(148) Fish, V. B. Chemical Instrumentation. *J. Chem. Educ.* **1969**, *46* (5), A323–A346. https://doi.org/10.1021/cen-v056n004.p031.

(149) Yu, B.-Y.; Chen, Y.-Y.; Wang, W.-B.; Hsu, M.-F.; Tsai, S.-P.; Lin, W.-C.; Lin, Y.-C.; Jou, J.-H.; Chu, C.-W.; Shyue, J.-J. Depth Profiling of Organic Films with X-Ray Photoelectron Spectroscopy Using C60+ and Ar+ Co-Sputtering. *Anal. Chem.* **2008**, *80* (9), 3412–3415. https://doi.org/10.1021/ac702626n.

(150) Adnadjević, B.; Vukićević, J.; Filipović-Rojka, Z.; Marković, V. The Influence of NaX Zeolite Particle Size on Crystallinity Measured by the XRD Method. *Zeolites* **1990**, *10*, 699–702. https://doi.org/10.1016/0144-2449(90)90083-4.

(151) ASTM Inter- national, West Conshohocken, P. ASTM Standard D5357-03(2013), Standard Test Method for Determination of Relative Crystallinity of Zeolite Sodium a by X-Ray Diffraction. 2013.

(152) Altman, M.; Shukla, A. D.; Zubkov, T.; Evmenenko, G.; Dutta, P.; Van Der Boom, M. E. Controlling Structure from the Bottom-up: Structural and Optical Properties of

Layer-by-Layer Assembled Palladium Coordination-Based Multilayers. *J. Am. Chem. Soc.* **2006**, *128* (22), 7374–7382. https://doi.org/10.1021/ja061026e.

(153) Yang, G.; Zhang, Y.; Huang, Y.; Shakir, M. I.; Xu, Y. Incorporating Conjugated Carbonyl Compounds into Carbon Nanomaterials as Electrode Materials for Electrochemical Energy Storage. *Phys. Chem. Chem. Phys.* **2016**, *18* (46), 31361–31377. https://doi.org/10.1039/c6cp06754a.

(154) Zhang, S.; Pan, N. Supercapacitors Performance Evaluation. *Adv. Energy Mater.* **2015**, *5* (6), 1–19. https://doi.org/10.1002/aenm.201401401.

10. Acknowledgements

I would like to thank Prof. Dr. Markus Antonietti for giving me an exciting opportunity of doing my PhD in his group. During the time in his group I expanded my knowledge greatly and I gained a lot of practical skills in the lab. Secondly, I'd like to thank Dr. Clemens Liedel for the direct supervision of my work and for helping me to achieve my goal.

Furthermore I would like to thank Dr. Steffen Tröger-Müller, Dr. Saowaluk Chaleawlert-umpon and Jinyeon Hwang for explaining me many new concepts regarding electrochemistry. Also to Jessica Brandt for the great help in the lab and performing of ICP-OEC measurements, to Antje Völkel for measuring TGA and combustive analysis and to Heike Runge and Rona Pitschke for measuring SEM samples.

Furthermore, I would like to thank all my colleagues who engaged in many scientific discussion with me heling me to develop new ideas in the first place to Martin Oschatz, Nieves Lopez Salas, Baris Kumru, Majd Al-Naji, Valerio Molinari, Paolo Giusto, Karen Leus, Francesco Brandi, Milena Perovic, Konstantin Schutjajew, Ralf Walczak, Runyu Yan and Julya Stein Siena, but also to many many others. I would like to thank Julya once again, for proofreading my thesis.

However, my colleagues were also my friends and many hours I have spent with them outside of work so I also thank them for keeping me company and keeping me sane. Additionally, I would like to thank my friends from all over the world for keeping me company, my friends from my hometown, from bachelor, from master, from the dorm and many others.

I would like to thank my family who always supported me and especially to my grandmothers, Marija Rakasic and Tereza Ilic for putting me on the way of science. To two of them I would like to dedicate my PhD thesis. Furthermore, I would like to thank my mom who sparked my interest in science when I was a child. Also, I would like to thank my girlfriend for unconditional support.